

Radionuclide Incorporation and Long Term Performance of Apatite Waste Forms

Fuel Cycles

Jianwei Wang

Louisiana State University

In collaboration with:

Rensselaer Polytechnic Institute

Kimberly Gray, Federal POC

John Vienna, Technical POC

Project Title:**Radionuclide Incorporation and Long Term Performance of Apatite
Waste Forms 11-3105****Project Principal Investigators**

Prof. Jianwei Wang
Department of Geology and Geophysics
Louisiana State University
Baton Rouge, Louisiana 70803-0001

Prof. Jie Lian
Department of Mechanical and Nuclear Engineering
Rensselaer Polytechnic Institute
Troy, New York 12180-3590, USA

Prof. Fei Gao
Nuclear Engineering and Radiological Sciences
University of Michigan
Ann Arbor, MI 48109-2104

Project Recipient:

Louisiana State University
Baton Rouge, Louisiana 70803

Award Number: DE-AC07-05ID14517_00118430

Date of Report: December 31, 2015

I. Overall objectives and results

A. Project objectives:

This project aims to combine state-of-the-art experimental and characterization techniques with atomistic simulations based on density functional theory (DFT) and molecular dynamics (MD) simulations. With an initial focus on long-lived I-129 and other radionuclides such as Cs, Sr in apatite structure, specific research objectives include the atomic scale understanding of: (1) incorporation behavior of the radionuclides and their effects on the crystal chemistry and phase stability; (2) stability and microstructure evolution of designed waste forms under coupled temperature and radiation environments; (3) incorporation and migration energetics of radionuclides and release behaviors as probed by DFT and molecular dynamics (MD) simulations; and (4) chemical durability as measured in dissolution experiments for long term performance evaluation and model validation.

B. Project results:

Apatite waste forms to incorporate iodine have been developed, and their properties were characterized and their performance and structural stability under radiation and durability in solution were evaluated. A new solid state approach using high energy ball milling and SPS was developed at room temperature for synthesizing iodine-load lead-vanadate apatites with stoichiometric iodine incorporation, and without the loss of volatile iodine, leading to a dense ceramic iodine waste form with high thermal stability. A new theoretical method was developed to predict unknown apatite compositions and understand known apatites using a crystal chemistry approach and Artificial Neural Network simulation, leading to a number of new apatite possible apatites that incorporate iodine. Chemical durability test at high temperature based on accelerated leaching protocols was performed over an extended time, and the results suggest iodine-lead-vanadium apatite is durable with a long term leaching rate of below ~2 mg/m²/d at 90°C. Iodine release is incongruent and controlled by both a diffusive in the channel of the crystal structure and constant dissolution of crystal. A new approach of synthesizing graphene-based iodoapatite nanocomposites and a new absorbent material for iodine have been developed. The results provide a scientific basis for apatite waste forms and long term performance for nuclear fuel cycle program.

II. Efforts performed and the accomplishments achieved

A. Efforts performed on objectives (1) and (2) (lead by Rensselaer Polytechnic Institute)

At Rensselaer Polytechnic Institute, the research team led by Prof. Jie Lian (two postdocs and two Ph.D. students) are mainly focus on the development of advanced waste forms based apatite structures that can incorporate iodine, and properties characterization and performance evaluation. A new solid state approach was developed at room temperature for synthesizing iodine-load lead-vanadate apatites, and dense apatite pellets were consolidated by a low temperature spark plasma process without the loss of volatile iodine. Temperature effects on densification and grain coarsening of the SPS densified iodoapatite pellets, and microstructure evolution during sintering

were studied. The mechanical properties and structural integrity of the SPS densified iodoapatite at low temperatures were also characterized. We also explore the possibility of synthesizing graphene-based iodoapatite nanocomposites in order to improve the thermal-mechanical properties. Radiation performance of the designed iodine loaded apatite was also tested by ion beam irradiation. A new absorbent material was also developed at Rensselaer Polytechnic Institute based on high surface area graphene and graphene-based aerogel which show excellent iodine absorption and kinetics.

Major accomplishments achieved:

- Lead phosphate-vanadate fluoroapatites with different P/V ratios were synthesized, and a complete solid solution of phosphate-vanadate can be obtained from the pure end vanadate to the pure end phosphate members.
- We performed ion beam irradiation using 1 MeV Kr^{2+} on the series of vanadate-phosphate fluorapatite with the goal in understanding the effects of V/P ratio on the damage production and defect annealing processes. Materials with the lower V/P ratio display enhanced stability against intense radiation.
- A novel approach in synthesizing I-incorporated apatite was developed by high energy ball milling, in which a pure apatite phase was obtained with the loading of Iodine up to 9 wt%, close to the maximum waste loading defined by the apatite structure. The successful development of this new approach opens up the opportunity for synthesizing a wide range of different I-bearing apatite compositions as stable waste forms for immobilizing long-lived I-129.
- Systematic materials characterizations establish the correlation among morphological and microstructural evolution, microchemical composition variation and materials processing conditions. Specifically, highly crystalline and single phase I-apatite can be achieved by high energy ball milling and thermal annealing above a recrystallization temperature. The grain size, structure and phase composition can be controlled upon the interplay of milling time, annealing temperature and duration.
- Elevated temperature will result in I-loss and decomposition of I-apatite, leading to the formation of secondary phase, presenting a major challenge in developing advanced waste forms for confining highly volatile elements such as I-129. Conventional sintering approaches will inevitably result in I-loss, and novel rapid densification methods are needed in order to develop highly dense and stable apatite for I-incorporation. The potential of spark plasma sintering will be explored in the near future to demonstrate the feasibility in densifying materials and meanwhile mitigating I-volatilization.
- Optimized SPS processes and low temperature synthesis of fully dense iodine apatite without phase decomposition and iodine loss, and the correlation between sintering conditions and properties of sintered apatite ceramic including microstructure, grain size and density was established.
- The low temperature SPS process (400 °C for 5mins under pressure of 60 MPa) was developed, allowing consolidation of iodine apatite below phase decomposition temperature, and fully dense apatite pellets consisting of nano-scale grain in nano-ceramics were obtained as confirmed by SEM images.

- The consolidation of dense iodoapatite pellets above 95% theoretical density can be achieved by spark plasma sintering at temperature as low as 350 °C for 20 mins, and microstructure analysis indicates a nanocrystalline ceramic with the grain average size less than 100 nm. Grain coarsening and growth dominates the sintered microstructure at higher temperature and longer duration.
- The effects of various sintering temperature (350 °C, 400 °C, 500 °C, and 700 °C) and durations (0 ~20 mins) on the microstructure, density, fracture morphology and mechanical properties including Young's modulus and hardness were investigated. Due to dense and nano-sized grain structure, the dense nanoceramic display a significantly improved fracture toughness of pellet $1.302 \text{ MPa m}^{0.5}$, as compared with bulk pellets with coarsened structure.
- Greatly enhanced thermal stability and mechanical properties of the SPS-densified pellets at low temperature was observed, and the irradiation behavior of the pellet sample sintered was evaluated by intense low energy ion bombardments. Results show SPS-sintered pellets can have significantly enhanced radiation tolerance of the iodine apatite against displacive radiation induced amorphization, owing to the improved crystallinity as a result of the highly efficient sintering process.
- Graphene powder and graphene-aerogels show excellent absorption capability and fast kinetics for capturing and sequestering radioactive iodine, and can be used as effective absorbent for off-gas process.
- Graphene-based apatite composites have been synthesized by spark plasma sintering in order to further enhance thermal-mechanical properties.
- Further concepts of encapsulation of the iodine apatites or iodine-loaded graphene powders embedded into the hydroxyapatite as a core-shell structure were explored in order to enhance the corrosion resistance and chemical durability.
- Radiation damage of the nano-sized iodapatites synthesized by SPS with different microstructure and grain size was conducted by ion beam irradiation using IVEM-tandem facility at Argonne National Laboratory.

B. Efforts on objectives (3) and (4) (lead by Louisiana State University)

At Louisiana State University, the research team led by Prof. Wang has two postdocs and one graduate student worked during the project period. They mainly focus on the incorporation of radionuclides into apatite structure, using theoretical approaches -- objective (2) and chemical durability as measured in dissolution experiments, using accelerated leaching tests protocols -- objective (4). Theoretically, Artificial Neuron Network simulations were used to understand the crystal chemistry of apatite chemical compositions and the approach was used this technique for iodine-apatite. A number of unknown iodine-apatite compositions were predicted. Using DFT calculations, thermodynamic properties of a number of apatite compositions (known and unknown compositions) were performed. We also focused on the mechanical properties and structure properties of apatites. Both of the efforts were used to facilitate the interatomic potential parameterization of the apatites. The durability test of $\text{Pb}_5(\text{VO}_4)_3\text{I}$ apatite was based on the procedure described in the Standard Test Method for Accelerated Leach Test (ALT), ASTM C-1308. With over a hundred of composition analysis from the leached samples, and microscopic and spectroscopic analyses, the results show that both time-dependent diffusion of iodine and

constant dissolution of apatite control the leaching of iodine from the waste form. In short term, iodine release is controlled by diffusion from the structural channels, dissolution in long term, which becomes constant at given conditions – temperature, pH, and solution concentrations. Lead and vanadium releases are controlled by constant dissolution and are congruent.

Major accomplishments achieved:

- A new theoretical method was developed to predict unknown apatite chemical compositions, and understand known ones, based on Artificial Neuron Network simulation. This crystal chemistry approach combined the numerical simulation allowed us to predict unit cell parameters, channel size of the crystal structure, and other structural details of any possible chemical compositions with the apatite structure.
- The method was applied to $\text{Pb}_5(\text{VO}_4)_3\text{I}$, the results show that the simulation correctly predicted the unit cell length and channel size of the structure, indicating the iodide ion fits in the structural channel, consistent with x-ray diffraction result.
- For unknown apatite composition with a formula - $\text{A}_5(\text{XO}_4)_3\text{Z}$, we considered any possible elements in A and X site from periodic table and with Z site occupied by iodine for possible iodine-apatite composition. Using the Artificial Neuron Network method, our simulations suggest that combinations of A site cations of Ag^+ , K^+ , Sr^{2+} , Pb^{2+} , Ba^{2+} , and Cs^+ , and X site cations, mostly formed tetrahedron, of Mn^{5+} , As^{5+} , Cr^{5+} , V^{5+} , Mo^{5+} , Si^{4+} , Ge^{4+} , and Re^{7+} are possible apatite compositions that are able to incorporate iodide. The charge balance of different apatite compositions can be achieved by multiple substitutions at a single site or coupled substitutions at both A and X sites.
- DFT using program CRYSTAL09. Electron charge calculation of $\text{Pb}_5(\text{VO}_4)_3\text{I}$ apatite shows that main ionic nature of the bonding between iodide and coordinating Pb. The calculated vibrational frequencies compare well with experimental observation, suggesting the computational methods is suitable for free energy calculations.
- Two reaction procedures were considered for calculations of the thermodynamic of apatite formation. The results show that formation of $\text{Pb}_5(\text{VO}_4)_3\text{I}$ apatite from oxides is more favorable as temperature increase, but less favorable from vanadate. Using the methodology that is tested for $\text{Pb}_5(\text{VO}_4)_3\text{I}$ apatite, we have calculated thermodynamic properties of other known and unknown apatites with various chemical compositions, including Pb-As-I and other apatites.
- Crystal structure and mechanical properties including bulk modulus and elastic constants of $\text{Ca}_5(\text{VO}_4)_3\text{F}$, $\text{Ca}_5(\text{VO}_4)_3\text{I}$, $\text{Pb}_5(\text{VO}_4)_3\text{I}$ are calculated. The results were used to fit the interatomic interaction potentials for large scale molecular dynamics simulations at our collaborating institution - University of Michigan.
- Apatite structure show significant flexibility and resilience to the structure and chemical changes induced by Beta decay from fission products such as radioactive Sr, Cs, and I, by DFT based theoretical calculations.
- The electron(s) generated by β -decay of radioactive fission products, $\text{Cs}^+ \rightarrow \text{Ba}^{2+}$, $\text{Sr}^{2+} \rightarrow \text{Y}^{3+} \rightarrow \text{Zr}^{4+}$, and $\text{I} \rightarrow \text{Xe} \rightarrow \text{vacancy}$ can be balanced by the $\text{Fe}^{3+} \rightarrow \text{Fe}^{2+}$ reduction process. Fe^{3+} can be a qualified charge balancer in the typical apatite.

- The studies indicate $\text{Ca}_{10}(\text{PO}_4)_6\text{F}_2$ with Cs^+ and Fe^{3+} coupled substitution could be a promising waste-form for $\text{Cs}^+ \rightarrow \text{Ba}^{2+}$ transmutation; $\text{Ca}_4\text{Y}_6(\text{SiO}_4)_6\text{F}_2$ with Sr^{2+} and Fe^{3+} substitution may involve a structural unstable in the $\text{Y}^{3+} \rightarrow \text{Zr}^{4+}$ process due to the change of the coordination number for Zr^{4+} to oxygen ligands; and a structural distortion may be expected for I^- decay in $\text{AgFePb}_8(\text{VO}_4)_6\text{I}_2$ due to the alteration of the tetrahedral $(\text{VO}_4)^{3-}$.
- Durability of $\text{Pb}_5(\text{VO}_4)_3\text{I}$ apatite, a dense ceramic form, sintered using SPS method and provided by our collaborator at Rensselaer Polytechnic Institute, was tested based on the procedure described in the Standard Test Method for Accelerated Leach Test (ALT), ASTM C-1308. The normalized release rate of iodine is below $\sim 2 \text{ mg/m}^2/\text{d}$ at the conditions of 90°C in DI water, sample surface/leachant volume ratio of 1.0 m^{-1} , and one day exchange interval.
- A normalization procedure was developed to account the leaching tests at different test parameters: surface/volume ratio, leachant change interval, and time history of leaching experiment. By applied this procedure, all the test at different test parameters can be compared and modeled as a function of leaching time, leading to a greater understanding of leaching kinetics.
- The short term iodine release is controlled by diffusion of iodine from structural channel, and long term lease is controlled by constant dissolution, based on the results on modeling of normalized iodine release rate as a function of time.
- The molar ratios of dissolved species reveal that V and Pb are dissolved in congruent, controlled by constant dissolution at a given condition. But iodine is released incongruently, and is a function of time, which is independent on the number of batch experiments and whether the surface is polished between the experiments.
- The durability tests also show the leaching of the apatite is affected by the chemistry of its constitute elements, Pb, and V. At high pH (e.g., 9), the dissolution is very low, below the detecting limit of the ICP-MS spectrometer, and there might be some $\text{Pb}(\text{OH})_2$ precipitation. At low pH, i.e., 6, the dissolution is \sim two orders of magnitudes higher than with DI water at 90°C . At lower pH, i.e., 4, a new phase is precipitated at the sample surface, and identified as chervetite – $\text{Pb}_2\text{V}_2\text{O}_7$, based on SEM and Raman spectroscopic results.
- Activation energy of iodine release is estimated to be $\sim 21 \pm 1.6 \text{ kJ/mol}$, based temperature dependent leaching tests and Arrhenius plot.
- Long term durability can be well resented using analytical equation of **Rate** = $k_0 \cdot 10^{\eta \cdot \text{pH}} \cdot \exp(-\frac{E_a}{RT})$, which is parameterized with the experimental datasets on tests of surface/volume ratio, exchange interval, temperature, pH, and time history.

C. Efforts on objectives (3) (lead by University of Michigan)

At Pacific Northwest National Laboratory (PNNL), the research team led by Dr. Fei Gao (a high school student and a visiting scholar) mainly focused on developing next generation interatomic potentials for apatites (that is based on the data from FT calculations). These potentials are used in the atomistic simulations that provide a theoretical basis for the design and optimization

of apatite ceramics with a desired physical and chemical durability and appropriate waste loading capability. Large-scale molecular dynamics method has been used to simulate diffusion properties, phase stability, radiation effects from alpha-decay damage of the incorporated radionuclides and fission track formation. Effects on the local bonding environment of iodine at surface, interface, and grain boundaries of the apatites are investigated, as segregation of the impurities at such places can be common. We model radiation damage and defect accumulation due to alpha-decay of the incorporated radionuclides and fission track formation, as well as phase stability under irradiation, in apatites phase. At University of Michigan (UM), with graduate student, the research has been focused on simulations of displacement cascades in $\text{Ca}_5(\text{VO}_4)_3\text{F}$ using LAMMPS code, and understanding defect production. Also, we have developed a new set of interatomic potentials for $\text{Pb}_5(\text{VO}_4)_3\text{I}$ apatite, and determined threshold energies, defect generation and defect clustering in $\text{Pb}_5(\text{VO}_4)_3\text{I}$ apatite.

Major accomplishments achieved:

- Based on DFT calculations, new interatomic potentials for $\text{Ca}_5(\text{VO}_4)_3\text{F}$ and $\text{Pb}_5(\text{VO}_4)_3\text{I}$ have been developed using a genetic algorithm developed at PNNL. These potential are validated against DFT calculations and experimental data. Also, these potentials have been refined to avoid unrealistic attraction due to the dominance of the dispersion term that is encountered in radiation damage simulations.
- These potentials are used to study the defect properties of $\text{Ca}_5(\text{VO}_4)_3\text{I}$, including defect formation energies, migration energies and incorporation energies of iodine ion, as well as thermodynamic and mechanical properties of $\text{Ca}_5(\text{VO}_4)_3\text{I}$.
- A similar approach has been applied to study defect formation, defect migration, incorporation energies of iodine ion, and thermodynamic and mechanical properties of $\text{Pb}_5(\text{VO}_4)_3\text{I}$.
- The threshold energies, E_d , of different species along different crystalline directions in $\text{Ca}_5(\text{VO}_4)_3\text{F}$ and $\text{Pb}_5(\text{VO}_4)_3\text{I}$ are determined. The results indicate strong anisotropic along different directions for both cations and anions. However, the E_d values of cations are much larger than anions.
- In addition, large scale MD simulations have been carried out to investigate displacement cascades in $\text{Ca}_5(\text{VO}_4)_3\text{F}$ and $\text{Pb}_5(\text{VO}_4)_3\text{I}$ using LAMMPS code, understanding defect production and defect clustering and evaluating microstructural evolution and studying phase stability under irradiation. The comparison between $\text{Ca}_5(\text{VO}_4)_3\text{F}$ and $\text{Pb}_5(\text{VO}_4)_3\text{I}$ provide significant insights into how the different compositions, with the same structures, affect defect generation and clustering.
- A new method has been developed to identify defects and defect structures in $\text{Ca}_5(\text{VO}_4)_3\text{F}$ and $\text{Pb}_5(\text{VO}_4)_3\text{I}$, which is based on the occupation of Voronoi polyhedra centered on lattice sites instead of simply counting the number of displaced atoms. This method can be applied to other apatites and ceramic waste forms.
- We have initiated to simulate the fission track formation in $\text{Ca}_5(\text{VO}_4)_3\text{F}$, understanding the track geometry, defect annealing and heat transformation, as well as the core structures of fission tracks, and wish that these studies will be continued.

III. Publications and conference presentations

A. Publications in Peer-reviewed Journals:

2013

1. Fengyuan Lu, Zhili Dong, Jiaming Zhang, Timothy White, Rodney C. Ewing and Jie Lian, Tailoring the Radiation Tolerance of Vanadate-phosphate Fluorapatites by Chemical Composition Control, **RCS Advances** 3 (2013) 15178-15184.

2014

2. Tiankai Yao, Fengyuan Lu, Hongtao Sun, Jianwei Wang, Rodney C. Ewing, and Jie Lian, “Bulk Iodoapatite Ceramic Densified by Spark Plasma Sintering with Exceptional Thermal Stability”, **J. Am. Ceram. Soc.**, 97 (2014) 2409–2412 (Rapid Communication and selected as a Key Scientific Articles on Advances in Engineering).
3. Fengyuan Lu, Tiankai Yao, Jinling Xu, Jingxian Wang, Spencer Scott, Zhili Dong, Rodney C. Ewing and Jie Lian, Facile Low Temperature Solid State Synthesis of Iodoapatite by High Energy Ball Milling, **RSC Advances** 2014, 4, 38718-38725.

2015

4. Spencer M. Scott, Tao Hu, Tiankai Yao, Guoqing Xin, and Jie Lian, Graphene-Based Sorbents for Iodine-129 Capture and Sequestration, **Carbon** 90 (2015) 1-8.
5. Fengyuan Lu, Tiankai Yao, Jianren Zhou, Rodney C. Ewing, and Jie Lian, (2015) Radiation Stability of Spark Plasma Sintered Lead Vanadate Iodoapatite, **Journal of American Ceramic Society** 98 (2015) 3361-3366.
6. Jianwei Wang, (2015) Incorporation of iodine into apatite structure: a crystal chemistry approach using Artificial Neural Network. **Frontiers in Earth Science**, volume 3, article 20.
7. Tiankai Yao, Spencer Scott, Guoqing Xin, Fengyuan Lu, and Jie Lian, Dense Iodapatite Ceramics Consolidated by Low Temperature Spark Plasma Sintering, **J. American Ceram. Soc** (2015) 98, 3733-3739.

In draft manuscript

8. Ge Yao and Jianwei Wang (2015) Effect of beta-decay on the structure and energetics of apatite-structured nuclear waste forms. (Physical Chemistry Chemical Physics)
9. Zelong Zhang, Aubrey Heath, Kalliat T. Valsaraj, Tiankai Yao, Jie Lian, and Jianwei Wang (2015) Dual-Mode Mechanisms of Iodine Release and Long-term Chemical Durability of Iodine Apatite $\text{Pb}_{9.85}(\text{VO}_4)_6\text{I}_{1.7}$ (Geochimica et Cosmochimica Acta)

10. Structure, vibrational spectroscopy, and thermodynamics of apatites from a first-principles study. Manuscript in preparation.

In preparation

11. Fei Gao, et al., Development of New Interatomic Potentials for $\text{Ca}_5(\text{VO}_4)_3\text{F}$ and $\text{Pb}_5(\text{VO}_4)_3\text{I}$, Defect Properties and Thermal Dynamics Properties, under preparation.
12. Fei Gao, et al., Threshold Hold Energies and Displacement Energy Surface in $\text{Ca}_5(\text{VO}_4)_3\text{F}$ and $\text{Pb}_5(\text{VO}_4)_3\text{I}$, under preparation.
13. Fei Gao, et al., Comparison Study of Displacement Cascades, Defect Production and Defect Clustering in $\text{Ca}_5(\text{VO}_4)_3\text{F}$ and $\text{Pb}_5(\text{VO}_4)_3\text{I}$, under preparation.

B. Talks and Presentations

2012

1. Jianwei Wang, Jie Lian, and Fei Gao (2012) Radionuclide Incorporation and Long Term Performance of Apatite Waste Forms. Fundamental WF Science Web Conference. Organized by John D. Vienna. Pacific Northwest National Laboratory. July 16, 2012.

2013

2. Jianwei Wang (2013) Crystal chemistry and thermodynamics of apatite for iodine incorporation from a first-principles study. GLOBAL 2013: International Nuclear Fuel Cycle Conference. Sept. 29-Oct. 3, 2013 in Salt Lake City, Utah
3. Jianwei Wang, Fei Gao, and Jie Lian (2013) Apatite Waste Forms: Synthesis, Crystal Chemistry, and Thermodynamics for Iodine Incorporation. SWF working group meeting, April 2-4, 2013, Albuquerque, NM.
4. **(Invited)** Jianwei Wang, Fei Gao, and Jie Lian (2013) Electronic Structure, Vibrational Spectroscopy, and Thermodynamics of I-Apatite from a First-Principles Study. TMS 2013, March 3-7, San Antonio, Texas, USA.
5. Jianwei Wang, Jie Lian, and Fei Gao (2013) Radionuclide Incorporation and Long Term Performance of Apatite Waste Forms. Durability Test Discussion – Apatite. Organized by John D. Vienna. Testing Needs Discussion, Web Conference Call, Feb. 6, 2013.
6. Jie Lian, Ion irradiation-induced Amorphization in vanadate phosphate apatites, symposium “Materials Science of Nuclear Waste Management”, 2013 TMS Annual Meeting & Exhibition.
7. Jie Lian, Materials Behavior under Extreme Environments – Nuclear Energy and Nano-scale Materials Design, Workshop on Nanomaterials & Engineered Microstructures for Nuclear Applications (NEMNA), Feb. 28-March 1, 2013, Brookhaven National Laboratory.
8. **(Invited)** Jie Lian, Nanostructured Materials for Nuclear Applications: Opportunities and

Challenges, Department of Materials and Chemical Engineering, University of Irvine, Nov. 13, 2013

2014

9. Jianwei Wang, Jie, Lian, and Fei Gao. Crystal chemistry, thermodynamics, and durability of apatite for iodine incorporation. Geochemistry of Nuclear Waste Storage and Disposition 247th ACS National Meeting, Dallas, TX. March 16-20, 2014
10. Jianwei Wang, Jie, Lian, and Fei Gao. Modeling crystal chemistry and thermodynamics of apatite for iodine incorporation. Goldschmidt 2014, Sacramento, June 8-13th, 2014.
11. Jie Lian, Apatite-Based Ceramic Waste Forms by High Energy Ball Milling and Spark Plasma Sintering for Iodine Confinement, MRS Fall meeting, Dec. 1, 2014, Boston, oral presentation.
12. Jie Lian, Apatite-Based Ceramic Waste Forms by High Energy Ball Milling and Spark Plasma Sintering for Iodine Confinement, TMS 2015, Florida, oral presentation.
13. J.W. Wang. Computational Earth Materials for Environmental and Energy. Molecular Simulations of Earth Materials for Environmental and Energy Applications, HPC 3rd Annual HPC User Symposium. LSU Digital Media Center, Louisiana State University, June 4-5, 2014.

2015

14. J.W. Wang. (2015). Two Modes of Iodine Release of Iodine-apatite in Aqueous Solution: Diffusion and Dissolution. 250th ACS National Meeting, Boston, MA. August 16-20, 2015.
15. Jianwei Wang (2015) Radionuclide Incorporation and Long Term Performance of Apatite Waste Form. MRWFD working group meeting, August 11-12, 2015 Gaithersburg, Washingtonian, Maryland.
16. **(Invited)** J.W. Wang. (2015) Computational earth materials & geochemistry. Department of Chemistry. Louisiana State University March 31, 2015.
17. **(Invited)** J.W. Wang. (2015) Molecular simulations of earth materials and geochemistry for environment and energy applications. The University of Southern Mississippi, Department of Geography & Geology, March 20th, 2015

IV. Published papers and manuscripts

Most of the results obtained toward achievement of the objective of this project have been published in journal forms or in manuscripts for publication in peer-reviewed journals. This section next is a compilation of published papers, and manuscripts.

PAPER

[View Article Online](#)
[View Journal](#) | [View Issue](#)

Tailoring the radiation tolerance of vanadate–phosphate fluorapatites by chemical composition control

Fengyuan Lu,^a Zhili Dong,^b Jiaming Zhang,^c Timothy White,^b Rodney C. Ewing^c and Jie Lian^{*a}Cite this: *RSC Advances*, 2013, **3**, 15178Received 7th May 2013,
Accepted 12th June 2013

DOI: 10.1039/c3ra42246a

www.rsc.org/advances

The apatite-type structure of $A_4A''_6(BO_4)_6(OH, F, Cl)_2$ ($A^I, A^{II} = Ca, Na$, rare earths, fission product elements such as I and Tc, and/or actinides; $B = Si, P, V$, or Cr) offers unique structural advantages as an advanced nuclear waste form because a wide variety of actinides and fission products can be incorporated into the structure through coupled cation and anion substitutions. However, apatite undergoes a radiation-induced crystalline-to-amorphous transition, and previously, the effect of composition on the radiation-induced transformation has not been well understood. In this study, we demonstrate that vanadate–phosphate fluorapatite's radiation tolerance can be controlled by varying the composition. Enhanced radiation tolerance is achieved by replacing vanadium with phosphorus at the B-site or by replacing Pb with Ca at the A-site. Correlations among chemical composition, radiation performance and electronic to nuclear stopping power ratio were demonstrated and suggest that the ionization process resulting from electronic energy loss may enhance annealing of defects upon radiation damage.

1. Introduction

The apatite-type structure of $A_4A''_6(BO_4)_6X_2$ ($A^I, A^{II} = Ca, Na$, rare earths, fission products such as Tc and I, and/or actinides; $B = Si, P, V$, or Cr; and $X = OH, F, Cl, I$ or O) has a relatively open structure with six equivalent BO_4 tetrahedra corner-connected to AO_6 metaprism columns to form one-dimensional tunnels as the frame. The two distinct cationic sites, A^I and A^{II} , differ in their atomic-scale environments and local symmetries, for each A^I cation has nine O atoms as nearest neighbors and each A^{II} cation is surrounded by one anion and six O atoms of three distinct types. The A^{II} cations and anions are located in the flexible tunnels. The apatite structure can be changed by adjusting the chemical composition, particularly the A-site cations and the B-site element. Trivalent cations (e.g. lanthanides) at the A-sites can result in nonstoichiometric composition and disordered anions in the channels at interstitial sites, which may be responsible for the high ion conductivity of apatite.^{1–3} Large atoms at the A-site or B-site usually result in an expanded apatite unit cell, as apatites with large atoms like Pb (A-site) and V (B-site) generally have large

unit cell parameters. Likewise, the replacement of smaller atoms by larger atoms will lead to a larger apatite unit cell. In phosphate–vanadate chlorapatites, $A_{10}(V_xP_{1-x}O_4)_6Cl_2$, the unit cell expansion caused by increasing V-content follows Vegard's Law with $x < 0.5$, but becomes quite erratic with $x > 0.5$;⁴ while in $(Pb_xCa_{1-x})_{10}(VO_4)_6F_2$, upon the substitution of Pb for Ca, the unit cell parameter a increases linearly and the increase in c follows a binomial function.⁵

Besides potential applications in fast ion conductor,^{1–3} catalyst⁶ and luminescent materials,^{7,8} the uniquely flexible and chemically durable structure of apatite offers great advantages as an advanced waste form for the immobilization of toxic heavy metals,^{9,10} actinides¹¹ and anionic fission products.¹² For instance, the apatite channel cross-section can be tuned through substitutions of A-site cations or BO_4 tetrahedral groups to accommodate voluminous ions, such as iodine-129, a typical fission product of uranium-235.¹² The radioactive decay of the incorporated radionuclides in nuclear waste will generate displacive and ionizing irradiations, which may cause damage to the host material and consequently affect their long term durability. Radiation stability may be associated with different energy loss mechanism,^{13,14} chemical compositions,¹⁵ structural disorder¹⁶ and grain size.^{17–19} As a result, the radiation effects in different apatite compositions are of great interest, and efforts have been made to study the radiation stability of apatite as a nuclear waste form, specifically using natural apatite minerals and fluorapatite. Generally, apatite-based ceramics anneal defects easily, such

^aDepartment of Mechanical, Aerospace & Nuclear Engineering, Rensselaer Polytechnic Institute, Troy, NY 12180, U.S.A. E-mail: lianj@rpi.edu; Fax: +1 518-276-6025; Tel: +1 518-276-6081

^bSchool of Materials Science and Engineering, Nanyang Technological University, Singapore 639798

^cDepartments of Earth & Environmental Sciences and Materials Science & Engineering, University of Michigan, Ann Arbor, MI 48109-1005, U.S.A

that their radiation durability is not compromised even under high radiation fluxes at low temperatures ($\sim 60^\circ\text{C}$) during storage or disposal for waste form applications.^{20–23} However, it has been reported that synthetic apatites, *e.g.* fully phosphate fluorapatite,^{24,25} mono-silicate fluorapatite,^{25,26} synthetic britholite¹⁴ and fully silicate apatite,^{27,28} can be amorphized by intense ion irradiations, and $(\text{Pb}_5\text{Ca}_5)(\text{VO}_4)_6\text{F}_2$ apatite may transform to CaVO_3 perovskite by high flux 200 keV electron beams.²⁹

One approach to improving a material's radiation stability is to control the composition, as this affects the energetics of defect production and annealing. Such effects have been reported in pyrochlores,^{15,30–32} perovskites,³³ A_2TiO_5 structures (A = lanthanides),³⁴ spinels,³⁵ zircon, ³⁶ monazites,³⁶ as well as apatite.²⁵ The effect of chemical composition on radiation tolerance may be associated with different anti-site defect formation energies caused by changes in cation radius ratio,^{15,37} or with the ratio of electronic-to-nuclear stopping power (ENSP).³⁶ Previously, Soulet *et al.* reported that silicate-phosphate apatite shows a decrease in α -annealing efficiency upon increasing SiO_4/PO_4 group ratio, but little explanation was given.²⁵ To understand the chemical composition effects on apatite structure radiation stability, we performed ion beam irradiation using 1 MeV Kr^{2+} on a series of vanadate-phosphate fluorapatite $\text{Ca}_{10}(\text{P}_x\text{V}_{1-x}\text{O}_4)_6\text{F}_2$ ($x = 0, 0.2, 0.4, 0.5, 0.6, 0.8, 1.0$) and $(\text{Pb}_x\text{Ca}_{1-x})_{10}(\text{VO}_4)_6\text{F}_2$ ($x = 0, 0.4, 0.6, 0.8$), in order to understand the effects of A-site and B-site compositions on the radiation damage and defect annealing processes in the apatite structure.

2. Experiments

The calcium-lead vanadate fluorapatite powders with different compositions were synthesized by solid state reaction between CaO (prepared by firing AR grade CaCO_3 at 900°C), PbO , V_2O_5 and CaF_2 powders mixed in corresponding proportions and fired at 800°C in alumina boats at ambient atmosphere for 10 h, as described in an earlier work.⁴ These precursor powders were then ball-milled and treated again at 800°C for about 2.5 days to allow the reaction to proceed to completion. To synthesize calcium vanadate-phosphate fluorapatite, CaO , V_2O_5 and CaF_2 powders were mixed in appropriate proportions in diluted orthophosphoric acid and stirred for more than 2 h. The sludge was dried at about 95°C in oven for 2 days, followed by heat treatment at 900°C for 24 h. By controlling the ratio between different reagents, we deliberately synthesized vanadate-phosphate fluorapatite $\text{Ca}_{10}(\text{P}_x\text{V}_{1-x}\text{O}_4)_6\text{F}_2$ with different PO_4/VO_4 tetrahedral group ratios and calcium-lead vanadate fluorapatite $(\text{Pb}_x\text{Ca}_{1-x})_{10}(\text{VO}_4)_6\text{F}_2$ with different Pb/Ca cation ratios. Such a replacement of the PO_4 groups by the larger VO_4 groups or calcium by the larger lead cation results in a larger unit cell and a larger channel cross-section with which to accommodate larger anions such as iodine, which make the vanadate-phosphate fluorapatite a promising host phase for the immobilization of the fission product I-129.

Iodine-containing apatite in the form of $\text{Pb}_{10}(\text{VO}_4)_6\text{I}_2$ was previously reported,^{12,38} displaying the same crystal structure as the $\text{Pb}_{10}(\text{VO}_4)_6\text{F}_2$ apatite.

For the investigation of the fluorapatite radiation performance affected by the different compositions, 1 MeV Kr^{2+} ions were used to irradiate the different $\text{Ca}_{10}(\text{P}_x\text{V}_{1-x}\text{O}_4)_6\text{F}_2$ and $(\text{Pb}_x\text{Ca}_{1-x})_{10}(\text{VO}_4)_6\text{F}_2$ samples. The ion irradiations were conducted using the IVEM-tandem facility at Argonne National Laboratory, which consists of a Hitachi H-9000NAR TEM interfaced to ion accelerators, and monitored with *in situ* TEM for the irradiation induced structural evolution of apatite. Both *in situ* high resolution TEM (HRTEM) and selected area electron diffraction (SAED) techniques were used to track the changes of the apatite structure under intense ion bombardments. The synergetic temperature and radiation effects were also studied by using the heating TEM stage in a temperature range from 300 to 700 K. The Kr^{2+} fluences were converted to the universal radiation damage unit of displacements per atom (dpa) calculated by the SRIM 2008 program, using an estimated 50 eV displacement energy (E_d) for all the atoms, which was adopted by previous studies based on theoretical computations.^{28,39}

3. Results and discussion

3.1 Room temperature ion irradiation of vanadate-phosphate fluorapatite

Vanadate-phosphate fluorapatites with different PO_4/VO_4 ratios, $\text{Ca}_{10}(\text{P}_x\text{V}_{1-x}\text{O}_4)_6\text{F}_2$ ($x = 0, 0.2, 0.4, 0.6, 0.8$ and 1), were irradiated by 1 MeV Kr^{2+} at room temperature (300 K) with a dose rate of 6.25×10^{10} ions $\text{cm}^{-2} \text{s}^{-1}$. In general, all of these fluorapatites underwent a crystalline-to-amorphous transition under 1 MeV Kr^{2+} irradiation, as a result of the ballistic interaction and the subsequent atomic displacements. However, the critical ion fluences for the amorphization varied with the chemical composition, *i.e.* the PO_4/VO_4 ratio, indicating that the radiation stability depends on the composition of the B-site. Fig. 1 shows a series of SAED patterns (inset) and corresponding high resolution TEM (HRTEM) images taken at different ion fluences for pure vanadate fluorapatite $\text{Ca}_{10}(\text{VO}_4)_6\text{F}_2$ with $x = 0$. The HRTEM lattice image and SAED inset in Fig. 1a clearly show a hexagonal structure typical for the fluorapatite. Small amorphous domains began to appear at a low fluence of 6.25×10^{13} ions cm^{-2} (Fig. 1b), suggesting that direct impact process may be responsible for amorphization. At a fluence of 1.25×10^{14} ions cm^{-2} , extended damage was observed by HRTEM, and a significant diffuse halo appeared in SAED, accompanying the weakening of the diffraction pattern (Fig. 1c). Finally, the lattice image showed a fully amorphous matrix with a SAED diffuse halo completely replacing the diffraction spot pattern when the fluence exceeded 1.6×10^{14} ions cm^{-2} or 0.21 dpa (Fig. 1d), which is the critical amorphization dose (D_c) for $\text{Ca}_{10}(\text{VO}_4)_6\text{F}_2$ at room temperature. A higher D_c indicates higher resistance to radiation-induced amorphization.

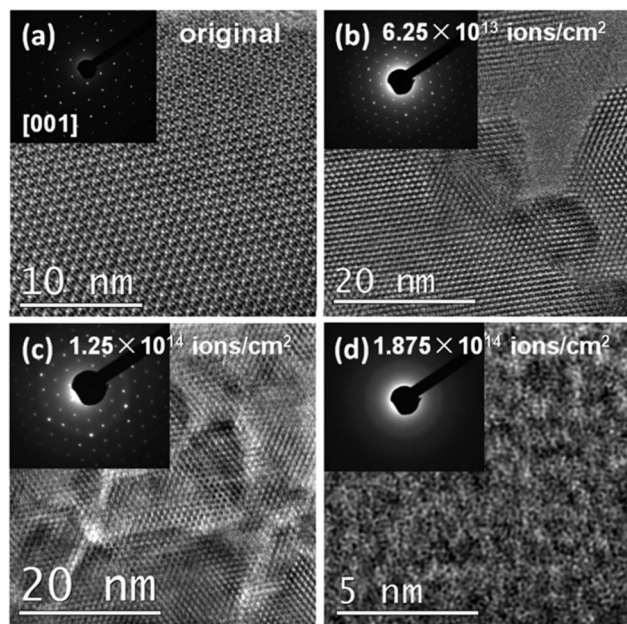


Fig. 1 TEM images showing the amorphization process of $\text{Ca}_{10}(\text{VO}_4)_6\text{F}_2$ induced by 1 MeV Kr^{2+} irradiation: (a) original crystalline apatite, (b) radiation damage at a fluence of $6.25 \times 10^{13} \text{ ions cm}^{-2}$ and (c) $1.25 \times 10^{14} \text{ ions cm}^{-2}$, (d) complete amorphization at $1.875 \times 10^{14} \text{ ions cm}^{-2}$.

When 20 at% vanadium was substituted by phosphorus, resulting in a chemical composition of $\text{Ca}_{10}(\text{P}_{0.2}\text{V}_{0.8}\text{O}_4)_6\text{F}_2$ ($x = 0.2$) with a decreased unit cell, the radiation tolerance of apatite increased. As shown in the TEM images in Fig. 2, the complete amorphization of $\text{Ca}_{10}(\text{P}_{0.2}\text{V}_{0.8}\text{O}_4)_6\text{F}_2$ only occurred after the fluence exceeded $2 \times 10^{14} \text{ ions cm}^{-2}$ ($\sim 0.26 \text{ dpa}$), which is about 25% higher than the D_c of $\text{Ca}_{10}(\text{VO}_4)_6\text{F}_2$. Further increase in x and hence the PO_4/VO_4 ratio leads to a more radiation tolerant apatite structure with higher D_c . A complete substitution of phosphorus for vanadium ($x = 1$), which results in a pure phosphate apatite of $\text{Ca}_{10}(\text{PO}_4)_6\text{F}_2$, brings the highest D_c of $6 \times 10^{14} \text{ ions cm}^{-2}$ (0.73 dpa) among all $\text{Ca}_{10}(\text{P}_x\text{V}_{1-x}\text{O}_4)_6\text{F}_2$ compositions, as shown by the series of SAED patterns taken at different ion fluences (Fig. 3). The vanadate-phosphate fluorapatite D_c dependence as a function of x (Fig. 4a) indicates that the radiation tolerance of $\text{Ca}_{10}(\text{P}_x\text{V}_{1-x}\text{O}_4)_6\text{F}_2$ increases monotonically with the P occupancy at the B-site. As the composition changes from a vanadate fluorapatite of $\text{Ca}_{10}(\text{VO}_4)_6\text{F}_2$ ($x = 0$) to a phosphate

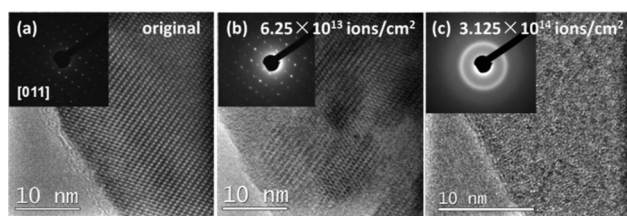


Fig. 2 TEM images showing the amorphization process of $\text{Ca}_{10}(\text{P}_{0.2}\text{V}_{0.8}\text{O}_4)_6\text{F}_2$: (a) original, (b) at a fluence of $6.25 \times 10^{13} \text{ ions cm}^{-2}$, (c) amorphization at a fluence of $3.125 \times 10^{14} \text{ ions cm}^{-2}$.

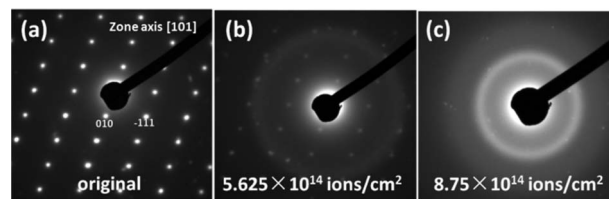


Fig. 3 SAED patterns showing the amorphization process of $\text{Ca}_{10}(\text{PO}_4)_6\text{F}_2$: (a) original, (b) at a fluence of $5.625 \times 10^{14} \text{ ions cm}^{-2}$, (c) amorphization at a fluence of $8.75 \times 10^{14} \text{ ions cm}^{-2}$.

fluorapatite of $\text{Ca}_{10}(\text{PO}_4)_6\text{F}_2$ ($x = 1$), the D_c increases to over three times the original value. Therefore, the substitution of PO_4 tetrahedral groups for VO_4 groups can enhance the radiation stability of fluorapatite, although it may reduce of the capacity to incorporate iodine into the structure.

3.2 Temperature dependence of the radiation tolerance of vanadate-phosphate fluorapatite

Temperature is an important factor that directly affects the defect dynamics and hence the radiation damage process. Generally, at elevated temperatures, increased mobility of radiation-induced defects results in a higher Frenkel pair recombination rate and defect interaction with the materials microstructure, leading to the suppression of radiation damage as a result of a dynamic annealing effect. Materials that are subject to radiation-induced amorphization at room temperature can become highly radiation resistant when the temperature exceeds a critical value when the enhanced defect annealing rate is greater than the radiation defect production, such that the amorphization cannot occur even at extremely high doses. Thus, the critical temperature (T_c) is a distinctive property and a good measure of the radiation tolerance of materials, as a higher T_c is associated with higher tendency towards radiation-induced amorphization and lower radiation tolerance.

In order to understand the temperature dependence of the radiation tolerance of vanadate-phosphate fluorapatite, $\text{Ca}_{10}(\text{P}_x\text{V}_{1-x}\text{O}_4)_6\text{F}_2$, a series of 1 MeV Kr^{2+} irradiation experiments were conducted at different temperatures from 300 K to 700 K for 3 different compositions: $\text{Ca}_{10}(\text{VO}_4)_6\text{F}_2$, $\text{Ca}_{10}(\text{P}_{0.5}\text{V}_{0.5}\text{O}_4)_6\text{F}_2$ and $\text{Ca}_{10}(\text{PO}_4)_6\text{F}_2$. *In situ* TEM observation confirmed the enhanced radiation tolerance at elevated

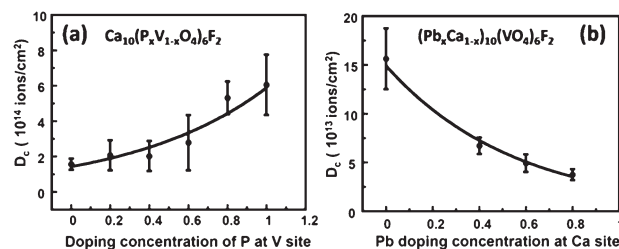


Fig. 4 Dependence of critical amorphization dose (D_c) on (a) P concentration x at V site in $\text{Ca}_{10}(\text{P}_x\text{V}_{1-x}\text{O}_4)_6\text{F}_2$ and (b) Pb concentration x at Ca site in $(\text{Pb}_x\text{Ca}_{1-x})_{10}(\text{VO}_4)_6\text{F}_2$.

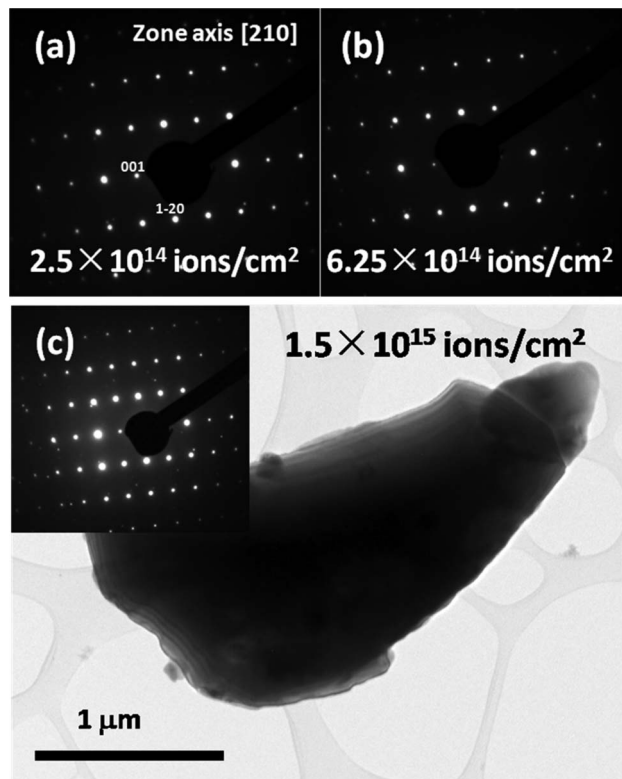


Fig. 5 SAED patterns showing $\text{Ca}_{10}(\text{VO}_4)_6\text{F}_2$ remained while the ion fluence increased from (a) 2.5×10^{14} ions cm^{-2} , (b) 6.25×10^{14} to (c) 1.5×10^{15} ions cm^{-2} .

temperatures for these fluorapatites. For instance, at 673 K, $\text{Ca}_{10}(\text{VO}_4)_6\text{F}_2$ remains highly crystalline at a high fluence of 1.5×10^{15} ions cm^{-2} (Fig. 5), which is an order of magnitude higher than its room temperature D_c of 1.6×10^{14} ions cm^{-2} . However, *in situ* TEM also revealed distinct amorphization at higher temperatures for fluorapatites with different PO_4/VO_4 ratio at the B-site. The phosphate fluorapatite $\text{Ca}_{10}(\text{PO}_4)_6\text{F}_2$ already becomes extremely resistant to amorphization above ~ 440 K; in contrast, the vanadate $\text{Ca}_{10}(\text{VO}_4)_6\text{F}_2$ can still be amorphized at nearly 600 K. The D_c values of the three different apatite compositions at different temperatures are shown in Fig. 6a; and based on a direct impact model,^{40,41} their temperature dependence curves were fit by an empirical exponential function in the form of

$$D_c = \frac{D_0}{1 - \exp[(E_a/k)(1/T_c - 1/T)]},$$

in which D_0 is the critical amorphization dose extrapolated at $T = 0$ K, E_a is the activation energy for defect annealing, and T_c is the critical amorphization temperature. The fitted T_c values, which are 441 ± 17 K for $\text{Ca}_{10}(\text{PO}_4)_6\text{F}_2$, 562 ± 16 K for $\text{Ca}_{10}(\text{P}_{0.5}\text{V}_{0.5}\text{O}_4)_6\text{F}_2$ and 603 ± 1 K for $\text{Ca}_{10}(\text{VO}_4)_6\text{F}_2$, steadily decreases with P concentration at the B-site as shown in Fig. 6b, indicating enhanced radiation tolerance with higher PO_4/VO_4 ratio, which is consistent with the room temperature irradiation data.

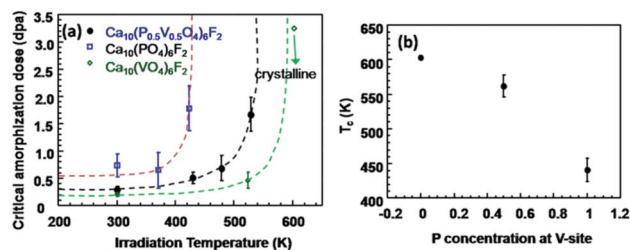


Fig. 6 (a) Temperature dependence of D_c for three different vanadate–phosphate fluorapatite compositions; (b) T_c dependence on P concentration x at the V site in $\text{Ca}_{10}(\text{P}_x\text{V}_{1-x}\text{O}_4)_6\text{F}_2$.

3.3 Ion irradiation of calcium–lead vanadate fluorapatite ($\text{Pb}_x\text{Ca}_{1-x}\text{}_{10}(\text{VO}_4)_6\text{F}_2$)

Similar to the substitution of VO_4 for PO_4 tetrahedral groups in fluorapatite, substitution of Pb for Ca at the fluorapatite A-site causes unit cell expansion, with an increase of the a lattice parameter from 9.7068 Å to 9.7526 Å and c from 7.0118 Å to 7.0415 Å.⁵ Such a substitution not only increases apatite structure unit cell volume, but also changes its radiation tolerance. The ion irradiation experiments for calcium–lead vanadate fluorapatites ($\text{Pb}_x\text{Ca}_{1-x}\text{}_{10}(\text{VO}_4)_6\text{F}_2$) were conducted at room temperature with 1 MeV Kr^{2+} beams in a similar way as the vanadate–phosphate apatites in Section 3.1. The TEM images in Fig. 7 show that by increasing the Pb occupation at the Ca A-site from 0 to 40 at%, the D_c decreases from 1.6×10^{14} ions cm^{-2} (0.21 dpa) as in $\text{Ca}_{10}(\text{VO}_4)_6\text{F}_2$ to 6.875×10^{13} ions cm^{-2} (0.11 dpa) as in $\text{Pb}_4\text{Ca}_6(\text{VO}_4)_6\text{F}_2$.

The dependence of the radiation tolerance for ($\text{Pb}_x\text{Ca}_{1-x}\text{}_{10}(\text{VO}_4)_6\text{F}_2$) fluorapatite on the Pb content is indicated by the D_c curve as a function of Pb doping concentration x at Ca site (Fig. 4b). The Pb-content exhibits a negative impact on the radiation performance of fluorapatite. By replacing 80 at% of the Ca atoms with Pb, resulting in a composition of $\text{Pb}_8\text{Ca}_2(\text{VO}_4)_6\text{F}_2$, the critical amorphization dose at room temperature is reduced to nearly 20% of that of pure calcium apatite $\text{Ca}_{10}(\text{VO}_4)_6\text{F}_2$. Similar to the D_c dependence on P concentration in phosphate–vanadate apatite, the D_c dependence curve for ($\text{Pb}_x\text{Ca}_{1-x}\text{}_{10}(\text{VO}_4)_6\text{F}_2$) decreases with increasing Pb-concentration, x .

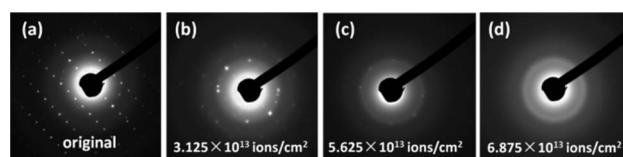


Fig. 7 SAED patterns showing the amorphization process of $\text{Pb}_4\text{Ca}_6(\text{VO}_4)_6\text{F}_2$ at room temperature: (a) original crystalline sample, (b) radiation damage at a fluence of 3.125×10^{13} ions cm^{-2} and (c) 5.625×10^{13} ions cm^{-2} , (d) amorphization at a fluence of 6.875×10^{13} ions cm^{-2} , which is significantly lower than the D_c of $\text{Ca}_{10}(\text{VO}_4)_6\text{F}_2$.

3.4 The effect of ENSP on the radiation tolerance of fluorapatites with different compositions

The energy loss mechanism of the energetic ions is crucial in determining the irradiation damage process. The ballistic effect of nuclear energy loss (or nuclear stopping power: S_n) causes atomic displacements that can lead to amorphization of the irradiated materials. The effect of electronic energy loss (or electronic stopping power: S_e) may depend on its intensity. Moderate S_e is capable of promoting defect recombination or recovery, even recrystallization of materials.^{42–45} In contrast, very high S_e , which occurs in swift heavy ion irradiations, can induce thermal spikes that are responsible for the phase transition,^{46–49} damage or even amorphization.^{13,49,50} Since the competition between radiation damage production and defect recovery determines the amorphization process, the ratio of electronic to nuclear stopping power (ENSP) can be a significant factor that affects a materials' radiation stability. A higher ENSP value may result in higher radiation defect recovery rate as compared with radiation damage accumulation, and hence enhanced radiation resistance.

Previously, Meldrum *et al.* demonstrated that, under 800 keV Kr^{2+} irradiation, the T_c trend in phosphate zircons and monazites of different cation compositions (LnPO_4) correlates well with the ENSP.³⁶ As for the radiation stability of apatite structure, an early study reported that crystalline $\text{Ca}_2\text{Nd}_8(\text{SiO}_4)_6\text{O}_2$ is unaffected by ionizing radiation, but undergoes amorphization due to displacement mechanisms caused by recoil nuclei emitted in alpha decay.⁵¹ Utsunomiya *et al.* also used ENSP to explain the T_c variation of synthetic britholite $\text{Ca}_{4-x}\text{REE}_{6+x}(\text{SiO}_4)_6\text{O}_2$ (REE = rare earth elements), which had an inverse correlation.¹⁴ Amorphous apatite can even recrystallize under 200 keV electron beam due to ionization effects.^{52,53} Recently, Weber *et al.* demonstrated that the D_c increases and the T_c decreases for silicate apatite with increasing ratio of in-cascade ionization to displacement rates, which can be explained and predicted by a dynamic model.²⁸ In light of the importance of the energy loss mechanisms, we calculated the ENSP for the different fluorapatite compositions using SRIM 2008. The ENSP calculation results reveal that the steady increase of room temperature D_c (Table 1) and decrease of T_c (Fig. 8) upon decreasing V- and Pb-contents correlates with the increase of ENSP of the fluorapatites. The influence of electronic loss indicated by higher ENSP is responsible for the enhanced defect recovery and suppression of radiation-induced amorphization in fluorapatite, which is consistent with previous studies.³² The increasing D_c and enhanced radiation tolerance of vanadate-phosphate fluorapatite with increasing PO_4/VO_4

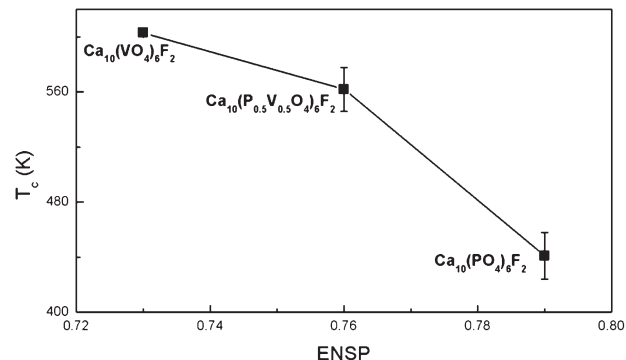


Fig. 8 T_c vs. ENSP plot indicates decreasing T_c with increasing ENSP.

ratios may also be attributed to the easier rearrangement of the PO_4 tetrahedral group upon ion irradiation as compared with the larger VO_4 group. The rearrangement of the PO_4 tetrahedra may improve the radiation defect annealing efficiency in a similar way to the enhancement of radiation tolerance of pyrochlores by reducing the A-site to B-site cation radius ratio to lower the cation anti-site defect energy.³⁷

In the use of the apatite structure as a nuclear waste form, the important factors are waste loading, radiation tolerance, and chemical durability. For $\text{Ca}_{10}(\text{P}_x\text{V}_{1-x}\text{O}_4)_6\text{F}_2$ and $(\text{Pb}_x\text{Ca}_{1-x})_{10}(\text{VO}_4)_6\text{F}_2$, although the replacement of PO_4 group by the larger VO_4 group, or Ca by the larger Pb, leads to a larger channel that can accommodate larger ions, such as iodine, the resulting structure also has a lower radiation stability. In addition, the replacement of the smaller and lighter atoms by heavier atoms also reduces the weight percentage of waste loading. This problem is especially remarkable for Pb which is about five times heavier than Ca, so that a complete substitution of Pb for Ca in $(\text{Pb}_x\text{Ca}_{1-x})_{10}(\text{VO}_4)_6\text{F}_2$ adds over 100% weight to the waste form, as compared with only 12 wt% for complete substitution of V for P in $\text{Ca}_{10}(\text{P}_x\text{V}_{1-x}\text{O}_4)_6\text{F}_2$. Therefore, it is important to balance factors such as iodine loading, waste form weight and radiation stability, by adjusting the chemical composition of the fluorapatite, to achieve an optimized waste form design. The current data show that a vanadate-phosphate fluorapatite $\text{Ca}_{10}(\text{P}_x\text{V}_{1-x}\text{O}_4)_6\text{F}_2$ with moderate V content may be more favorable than a lead-rich vanadate fluorapatite $(\text{Pb}_x\text{Ca}_{1-x})_{10}(\text{VO}_4)_6\text{F}_2$ in terms of optimal nuclear waste form performance.

4. Conclusions

The radiation tolerance of fluorapatite $\text{A}^{\text{I}}_4\text{A}^{\text{II}}_6(\text{BO}_4)_6\text{F}_2$, a proposed nuclear waste form, can be tailored by controlling the species of cation at the A-site and the BO_4 tetrahedral group at the B-site. Substituting Pb for Ca at the A-site or VO_4 for PO_4 at the B-site, a method used to enhance the accommodation of I-129 in apatite, can also significantly reduce apatite's tolerance against radiation-induced amorphization. A complete substitution of V for P in $\text{Ca}_{10}(\text{P}_x\text{V}_{1-x}\text{O}_4)_6\text{F}_2$

Table 1 Comparison of ENSP and D_c for fluorapatites with different compositions

Composition	S_e (eV nm ⁻¹)	S_n (eV nm ⁻¹)	ENSP	D_c (ions cm ⁻²)
$\text{Pb}_4\text{Ca}_6(\text{VO}_4)_6\text{F}_2$	774	1143	0.68	0.11
$\text{Ca}_{10}(\text{VO}_4)_6\text{F}_2$	736	1010	0.73	0.21
$\text{Ca}_{10}(\text{P}_{0.5}\text{V}_{0.5}\text{O}_4)_6\text{F}_2$	775	1022	0.76	0.30
$\text{Ca}_{10}(\text{PO}_4)_6\text{F}_2$	823	1043	0.79	0.73

results in an exponential reduction of room temperature critical dose by about 70% and an increase in critical temperature from 441 ± 17 K to 603 ± 1 K; whereas, a replacement of 80 at% of Ca by Pb results in an exponential reduction of room temperature critical dose by about 80%. The reduced radiation stability upon atomic substitution at the A- or B-site can be attributed to the decreasing ENSP ratio and the more difficult rearrangement of the VO_4 tetrahedral group. The tailoring of fluorapatite's radiation stability by controlling the chemical composition enables optimal nuclear waste form design for enhanced performance, which should balance the waste loading and the radiation stability of fluorapatite.

Acknowledgements

This work is supported by the Energy Frontier Research Center–Materials Science of Actinides (DE SC0001089). JL also acknowledges the financial support of the DOE NEUP (Nuclear Engineering University Program) with the award number of DE-AC07-05ID14517. ZD acknowledges the support of a NTU AcRF grant (RG11/04). The authors thank the staff of the IVEM-tandem Facility at the Argonne National Laboratory for their assistance during ion irradiation and *in situ* TEM characterization.

References

- 1 A. Najib, J. E. H. Sansom, J. R. Tolchard, P. R. Slater and M. S. Islam, *Dalton Trans.*, 2004, 3106–3109.
- 2 A. Orera, E. Kendrick, D. C. Apperley, V. M. Orera and P. R. Slater, *Dalton Trans.*, 2008, 5296–5301.
- 3 J. E. H. Sansom, J. R. Tolchard, M. S. Islam, D. Apperley and P. R. Slater, *J. Mater. Chem.*, 2006, **16**, 1410–1413.
- 4 J. Y. Kim, Z. L. Dong and T. J. White, *J. Am. Ceram. Soc.*, 2005, **88**, 1253–1260.
- 5 Z. L. Dong, T. J. White, B. Wei and K. Laursen, *J. Am. Ceram. Soc.*, 2002, **85**, 2515–2522.
- 6 T. Wakabayashi, S. Kato, Y. Nakahara, M. Ogasawara and S. Nakata, *Catal. Today*, 2011, **164**, 575–579.
- 7 S. Ferdov, R. A. S. Ferreira and Z. Lin, *Chem. Mater.*, 2006, **18**, 5958–5964.
- 8 L. Leon-Reina, E. R. Losilla, M. Martinez-Lara, S. Bruque and M. A. G. Aranda, *J. Mater. Chem.*, 2004, **14**, 1142–1149.
- 9 T. A. Ioannidis and A. I. Zouboulis, *J. Hazard. Mater.*, 2003, **97**, 173–191.
- 10 Q. Y. Ma, S. J. Traina, T. J. Logan and J. A. Ryan, *Environ. Sci. Technol.*, 1993, **27**, 1803–1810.
- 11 R. C. Ewing, *Proc. Natl. Acad. Sci. U. S. A.*, 1999, **96**, 3432–3439.
- 12 F. Audubert, J. Carpena, J. L. Lacout and F. Tetard, *Solid State Ionics*, 1997, **95**, 113–119.
- 13 F. Y. Lu, J. W. Wang, M. Lang, M. Toulemonde, F. Namavar, C. Trautmann, J. M. Zhang, R. C. Ewing and J. Lian, *Phys. Chem. Chem. Phys.*, 2012, **14**, 12295–12300.
- 14 S. Utsunomiya, S. Yudinsev, L. M. Wang and R. C. Ewing, *J. Nucl. Mater.*, 2003, **322**, 180–188.
- 15 S. X. Wang, B. D. Begg, L. M. Wang, R. C. Ewing, W. J. Weber and K. V. G. Kutty, *J. Nucl. Mater.*, 1999, **14**, 4470–4473.
- 16 J. M. Zhang, J. Lian, F. X. Zhang, J. W. Wang, A. F. Fuentes and R. C. Ewing, *J. Phys. Chem. C*, 2010, **114**, 11810–11815.
- 17 J. Lian, J. M. Zhang, V. Pointeau, F. X. Zhang, M. Lang, F. Y. Lu, C. Poinssot and R. C. Ewing, *J. Nucl. Mater.*, 2009, **393**, 481–486.
- 18 F. Y. Lu, M. B. Huang, F. Yaqoob, M. Lang, F. Namavar, C. Trautmann, H. T. Sun, R. C. Ewing and J. Lian, *Appl. Phys. Lett.*, 2012, **101**, 041904.
- 19 J. M. Zhang, J. Lian, A. F. Fuentes, F. X. Zhang, M. Lang, F. Y. Lu and R. C. Ewing, *Appl. Phys. Lett.*, 2009, **94**, 243110.
- 20 A. J. W. Gleadow and P. G. Fitzgerald, *Earth Planet. Sci. Lett.*, 1987, **82**, 1–14.
- 21 P. F. Green, I. R. Duddy, A. J. W. Gleadow, P. R. Tingate and G. M. Laslett, *Earth Planet. Sci. Lett.*, 1986, **59**, 237–253.
- 22 P. F. Green, I. R. Duddy, G. M. Laslett, K. A. Hegarty, A. J. W. Gleadow and J. F. Lovering, *Chemical Geology*, 1989, **79**, 155–182.
- 23 W. J. Weber, R. C. Ewing and A. Meldrum, *J. Nucl. Mater.*, 1997, **250**, 147–155.
- 24 S. Miro, D. Grebille, D. Chateigner, D. Pelloquin, J. P. Stoquert, J. J. Grob, J. M. Costantini and F. Studer, *Nucl. Instrum. Methods Phys. Res., Sect. B*, 2005, **227**, 306–318.
- 25 S. Soulet, J. Carpena, J. Chaumont, O. Kaitasov, M. O. Ruault and J. C. Krupa, *Nucl. Instrum. Methods Phys. Res., Sect. B*, 2001, **184**, 383–390.
- 26 S. Soulet, J. Carpena, J. Chaumont, J. C. Krupa and M. O. Ruault, *J. Nucl. Mater.*, 2001, **299**, 227–234.
- 27 L. M. Wang and W. J. Weber, *Philos. Mag. A*, 1999, **79**, 237–253.
- 28 W. J. Weber, Y. W. Zhang, H. Y. Xiao and L. M. Wang, *RSC Adv.*, 2012, **2**, 595–604.
- 29 Z. L. Dong, T. J. White, K. Sun, L. M. Wang and R. C. Ewing, *J. Am. Ceram. Soc.*, 2004, **88**, 184–190.
- 30 J. Lian, J. Chen, L. M. Wang, R. C. Ewing, J. M. Farmer, L. A. Boatner and K. B. Helean, *Phys. Rev. B: Condens. Matter*, 2003, **68**, 134107.
- 31 J. Lian, K. B. Helean, B. J. Kennedy, L. M. Wang, A. Navrotsky and R. C. Ewing, *J. Phys. Chem. B*, 2006, **110**, 2343–2350.
- 32 F. Y. Lu, M. Nyman, Y. Q. Shen, Z. L. Dong, G. K. Wang, F. X. Zhang, R. C. Ewing and J. Lian, *MRS Online Proc. Libr.*, 2011, **1298**, mrsf10-1298-r06-02, DOI: 10.1557/opl.2011.373.
- 33 K. L. Smith, G. R. Lumpkin, M. G. Blackford, M. Colella and N. J. Zaluzec, *J. Appl. Phys.*, 2008, **103**, 083531.
- 34 C. L. Tracy, M. Lang, J. M. Zhang, F. X. Zhang, Z. W. Wang and R. C. Ewing, *Acta Mater.*, 2012, **60**, 4477–4486.
- 35 G. Baldinozzi, D. Simeone, D. Gosset, S. Surble, L. Mazerolles and L. Thome, *Nucl. Instrum. Methods Phys. Res., Sect. B*, 2008, **266**, 2848–2853.
- 36 A. Meldrum, L. A. Boatner and R. C. Ewing, *Phys. Rev. B: Condens. Matter*, 1997, **56**, 13805–13814.
- 37 K. E. Sickafus, L. Minervini, R. W. Grimes, J. A. Valdez, M. Ishimaru, F. Li, K. J. McClellan and T. Hartmann, *Science*, 2000, **289**, 748–751.
- 38 S. Le Gallet, L. Campayo, E. Courtois, S. Hoffmann, Y. Grin, F. Bernard and F. Bart, *J. Nucl. Mater.*, 2010, **400**, 251–256.
- 39 C. Meis, *J. Nucl. Mater.*, 2001, **289**, 167–176.
- 40 S. X. Wang, L. M. Wang and R. C. Ewing, *Phys. Rev. B: Condens. Matter*, 2000, **63**, 024105.
- 41 W. J. Weber, R. C. Ewing and L. M. Wang, *J. Mater. Res.*, 1994, **9**, 688–698.

- 42 J. Lian, J. M. Zhang, F. Namavar, Y. W. Zhang, F. Y. Lu, H. Haider, K. Garvin, W. J. Weber and R. C. Ewing, *Nanotechnology*, 2009, **20**, 245303.
- 43 F. Y. Lu, J. M. Zhang, M. B. Huang, F. Namavar, R. C. Ewing and J. Lian, *J. Phys. Chem. C*, 2011, **115**, 7193–7201.
- 44 A. Meldrum, L. A. Boatner and R. C. Ewing, *J. Mater. Res.*, 1997, **12**, 1816–1827.
- 45 W. J. Weber, Y. W. Zhang and L. M. Wang, *Nucl. Instrum. Methods Phys. Res., Sect. B*, 2012, **277**, 1–5.
- 46 A. Benyagoub, *Phys. Rev. B: Condens. Matter Mater. Phys.*, 2005, **72**, 094114.
- 47 A. Benyagoub, F. Levesque, F. Couvreur, C. Gibert-Mougel, C. Dufour and E. Paumier, *Appl. Phys. Lett.*, 2000, **77**, 3197–3199.
- 48 M. Lang, J. Lian, J. M. Zhang, F. X. Zhang, W. J. Weber, C. Trautmann and R. C. Ewing, *Phys. Rev. B: Condens. Matter Mater. Phys.*, 2009, **79**, 224105.
- 49 J. M. Zhang, M. Lang, J. Lian, J. Liu, C. Trautmann, S. Della-Negra, M. Toulemonde and R. C. Ewing, *J. Appl. Phys.*, 2009, **105**, 113510.
- 50 G. Szenes, *J. Nucl. Mater.*, 2005, **336**, 81–89.
- 51 W. J. Weber, *J. Am. Ceram. Soc.*, 1982, **65**, 544–548.
- 52 I. T. Bae, Y. W. Zhang, W. J. Weber, M. Higuchi and L. A. Giannuzzi, *Appl. Phys. Lett.*, 2007, **90**, 021912.
- 53 I. T. Bae, Y. W. Zhang, W. J. Weber, M. Ishimaru, Y. Hirotsu and M. Higuchi, *J. Mater. Res.*, 2008, **23**, 962–967.

Bulk Iodoapatite Ceramic Densified by Spark Plasma Sintering with Exceptional Thermal Stability

Tiankai Yao,[‡] Fengyuan Lu,[‡] Hongtao Sun,[‡] Jianwei Wang,[§] Rodney C. Ewing,[¶] and Jie Lian^{‡,†}

[‡]Department of Mechanical, Aerospace, and Nuclear Engineering, Rensselaer Polytechnic Institute, Troy, New York 12180

[§]Department of Geology & Geophysics, Center for Computation and Technology, Louisiana State University, Baton Rouge, Louisiana 70803

[¶]Department of Geological & Environmental Sciences, Stanford University, Stanford, California 94305-2115

Iodoapatite powder prepared by high-energy ball milling is densified by Spark Plasma Sintering to ~96% theoretical density. X-ray Diffraction and First-principle Calculation indicates the sintered phase is iodine-deficient apatite with chemical composition of $\text{Pb}_{9.85}(\text{VO}_4)_6\text{I}_{1.7}$ and iodine confinement over 8 wt%. Thermogravimetric analysis shows the bulk iodoapatite displays exceptionally stability without iodine release until 670°C. The greatly improved iodine confinement can be attributed to the dense matrix upon rapid consolidation from highly activated powders by mechanical attrition.

I. Main Article

As a byproduct of uranium fission, radioactive I-129, has detrimental effect on both environment and human beings due to its involvement in metabolic process and extremely long half-life around 15.7 million yr.¹ Iodine is extremely mobile and highly volatile, unreactive with many silicate minerals and rocks, and no engineering barriers can be used to confine iodine. Therefore, the capture and immobilization of I-129 into a durable waste form that can retain its integrity in deep geological disposal environment is of particular importance for effective nuclear waste management. Glass waste form is currently adopted for its versatile incorporation of complex nuclear waste streams,² and recent composite glass waste forms were developed, based on Bi–Zn-oxide³ and Bi–Si–Zn-oxide,⁴ in confining iodine. However, the vitrification of conventional glass waste forms requires elevated temperature and relatively long processing duration, and thus is less desirable for volatile elements such as I-129, necessitating the development of new waste forms that can be processed and consolidated at relatively low temperature without or minimal iodine loss.

Apatite is an earth abundant mineral, normally denoted as $\text{A}_{10}(\text{BO}_4)_6\text{C}_2$, displaying extraordinary structural flexibility and crystal chemistry. A wide range of radionuclides can be incorporated into apatite structure through coupled cation and anion substitutions (e.g., $A = \text{Ca}, \text{Na}, \text{Pb}$, rare earth, fission product elements, or actinides; $B = \text{P}$ or V ; $C = \text{F}, \text{Cl}, \text{I}$). Among these, $\text{Pb}_{10}(\text{VO}_4)_6\text{I}_2$ was proposed as a potential waste form for iodine immobilization due to its high chemical durability evidenced by its mineral analogue, a measured

rate of dissolution of 0.0025 g/m²d at pH 6 and 90°C,⁵ and high iodine loading of around 8 wt% as inferred from its crystal structure.^{5–7}

However, it is a great challenge to consolidate lead vanadate iodoapatite into dense ceramics due to the highly volatile nature of iodine. $\text{Pb}_{10}(\text{VO}_4)_6\text{I}_2$ also experiences a phase decomposition to $\text{Pb}_3(\text{VO}_4)_2$ at a low temperature less than 300°C, and a complete iodine loss occurred at ~400°C.⁸ Conventionally, it was synthesized by confined reactive high-pressure sintering in which PbI_2 as the core part is encapsulated by $\text{Pb}_3(\text{VO}_4)_2$. The vanadinite not only acts as reaction reagent but also a barrier to prevent the release of iodine as the sintering temperature (700°C) is significantly higher than the melting point of PbI_2 (400°C).^{5,9} Recently, microwave heating was used to fabricate bulk lead vanadate iodoapatite. However, highly dense pellets cannot be achieved and voids at the order of 10 μm dominated the microstructure of sintered pellets.¹⁰ Spark plasma sintering (SPS) was also utilized to sinter Pb–P–V iodoapatite by both nonreactive and reactive sintering,¹¹ in which iodoapatite powders as the starting materials were synthesized by solid-state reaction and calcination at 720°C for 15 h in a sealed quartz ampoule. Thermal stability and iodine confinement were not reported on the SPS-densified pellets. Consolidation of iodoapatite into dense bulk form with minimal iodine loss is critical for the development of durable waste forms for iodine confinement.

In this work, iodoapatite powders were fabricated by solid-state reaction at room temperature using high-energy ball milling (HEBM) of powders of the constituent chemicals¹² followed by a low-temperature annealing (200°C), in which the iodine can be well confined in the powders. HEBM greatly improve the sinter ability of the synthesized powder samples, and thus dense iodoapatite pellets with a relative density of 96% can be consolidated by spark plasma at 700°C at very short durations (several minutes). The low temperature synthesis of iodoapatite and rapid consolidation by SPS greatly mitigate the iodine loss associated with synthesis and densification processes. The SPS-densified iodoapatite pellets shows exceptional thermal stability and no iodine release occurs until 670°C. Those features underline that SPS combining with HEBM is promising in fabricating advanced waste form materials with greatly improved thermal stability for incorporation of highly volatile element I-129.

Lead vanadate iodoapatite powder were firstly prepared by HEBM (Fritsch, Pulverisette 7, Idar-Oberstein, Germany) of the stoichiometric quantity of constituent compounds including PbO (99.9% purity; Alfa Aesar, Ward Hill, MA), V₂O₅ (98% purity; Sigma-Aldrich, St. Louis, MO), and PbI₂ (99% purity; ACROS, Fair Lawn, NJ) to target a chemical composition of $\text{Pb}_{10}(\text{VO}_4)_6\text{I}_2$. The HEBM was performed in

R. Ballarini—contributing editor

Manuscript No. 35047. Received May 23, 2014; approved June 5, 2014.

[†]Author to whom correspondence should be addressed. e-mail: lian@rpi.edu

a sealed environment at room temperature to avoid the potential loss of volatile iodine during the solid-state reaction process. In this study, 10 g of constituent powders was mixed with 100 g of 2 mm ZrO_2 ball in an 80 ml ZrO_2 milling bowl. The mixture was milled for 10 h at a speed of 500 rpm with a pulse of 10 mins on and 5 min off. The highest temperature in the milling bowl during HEBM was around 50°C. Iodoapatite in the form of amorphous matrix embedded with nm-sized crystalline clusters formed upon HEBM, as shown by the broad characteristic diffraction peak (112) of iodoapatite centered at 2θ of 28° (see Fig. 1). Scanning electron microscopy by a Carl Zeiss Supra SEM (Jena, Germany) shows a typical feature of micron-sized granular for samples prepared by HEBM (inset in Figure). Energy dispersive spectroscopy (EDS) spectrum was acquired with an OXFORD INCA EDS detector equipped with the SEM (Oxfordshire, UK). Semiquantitative elemental analysis based on SEM-EDS indicates that a high content of iodine (above 9.1 ± 0.6 wt%) can be incorporated into as-milled powder. The as-milled iodoapatite powder was thermally treated at 200°C for 1 h in order to achieve a single phase of crystalline iodoapatite, and no iodine loss was identified upon low-temperature annealing. The effects of ball milling and thermal treatment parameters on the microstructure, phase, and chemical composition and iodine confinement were reported separately.¹²

For consolidation, 1.5 g of the annealed powder was loaded into a graphite die (15 mm inside diameter) and sintered by SPS system (Model 10-3, Thermal Tech. LLC., Santa Rosa, CA) with a direct current of 25 ms plus on and 5 ms off. Applied pressure increased to 40 MPa with the sintering temperature increased to 700°C at a heating rate of 200°C/min. A K-type thermal couple was used to monitor the sintering temperature. The sintering durations of 1 and 3 min were employed (hereafter referred to as 700-1 and 700-3 samples). Upon release of the pressure and cool down with furnace after sintering, densified pellets by SPS were obtained. Archimedes density of the sintered sample was measured by using ethanol as the immersion media at room temperature. A color change occurred from the starting powder (light yellow) to the sintered pellet (black green), similar to materials consolidated by SPS previously reported.^{13,14} The thermal stability of the sintered sample was evaluated by thermogravimetric analysis (TGA) in inert gas environment (nitrogen) with a temperature ramp rate of 5°C/min.

Figure 2(a) shows the x-ray diffraction patterns of the thermally annealed powders and SPS-densified pellets at 700°C for 1 and 3 min. A dominated well-crystalline iodoapatite phase with the diffraction peaks corresponding to iodoapatite was identified, suggesting that iodoapatite phase was well preserved without significant phase decomposition and iodine loss during densification at elevated temperature due to the rapid consolidation process of SPS. To better elucidate the phase constitution of the sintered pellet, first-principle calculation was also employed to simulate the XRD patterns of possible structure and compositions, and compared with the experimental XRD patterns. No structural data of stoichiometric $\text{Pb}_{10}(\text{VO}_4)_6\text{I}_2$ were reported in literature. Consequently, its crystal structure is constructed by replacing chlorine in $\text{Pb}_{10}(\text{VO}_4)_6\text{Cl}_2$ with iodine atoms, and the geometry was fully optimized within the framework of density functional theory as implanted by the CASTEP package.¹⁵ The exchange and correlation functional were treated by the Generalized Gradient Approximation of Perdew-Burke-Ernzerhof (GGA-PBE).¹⁶ A $2 \times 2 \times 2$ k -points and cut-off energy of 820 eV were adapted to guarantee the high accuracy of lattice parameter and thus the consequently calculated XRD pattern [Fig. 2(b)]. A XRD pattern [Fig. 2(c)] was also simulated for the previously reported substoichiometric phase, $\text{Pb}_{9.85}(\text{VO}_4)_6\text{I}_{1.7}$.¹⁷ A perfect match was observed between the experimental patterns and that of a slightly iodine-deficient composition $\text{Pb}_{9.85}(\text{VO}_4)_6\text{I}_{1.7}$, and thus the chemical phase

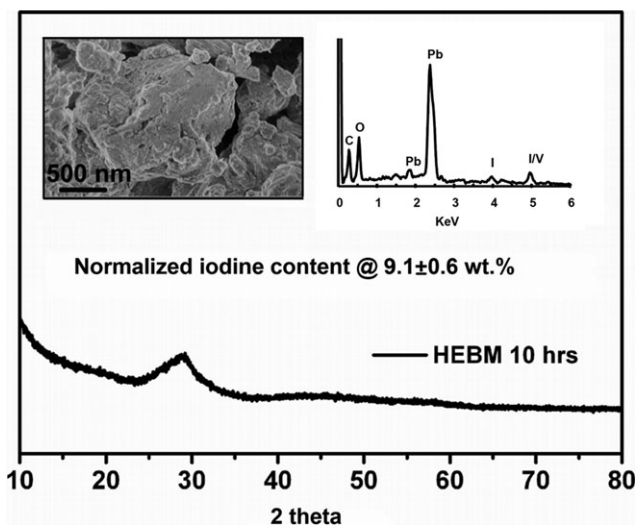


Fig. 1. Iodoapatite fabricated by a low-temperature solid-state reaction by high-energy ball milling and their phase, morphology, and microchemical compositions characterized by X-ray diffraction, SEM and EDS.

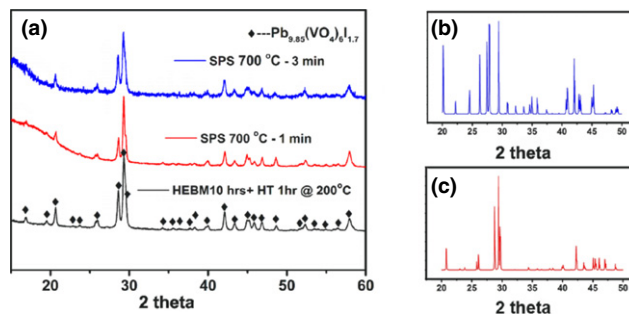


Fig. 2. XRD patterns of the 200°C thermally annealed iodoapatite and spark plasma sintering densified pellets at 700°C for 1 and 3 min (a); and simulated patterns by DFT calculations of stoichiometric $\text{Pb}_{10}(\text{VO}_4)_6\text{I}_2$ (b) and that of substoichiometric $\text{Pb}_{9.85}(\text{VO}_4)_6\text{I}_{1.7}$ (c).

of the SPS-densified sample could be better described by substoichiometric $\text{Pb}_{9.85}(\text{VO}_4)_6\text{I}_{1.7}$. The slightly iodine-deficient composition is also consistent with the Reitveld refinement of the XRD pattern for 200°C thermally annealed powders, suggesting no significant iodine loss occurred during SPS densification process.

For potential applications of nuclear waste forms eventually disposed in a deep geological environment, highly dense and durable matrices are desired with minimized loss of radionuclides and enhanced chemical durability. Particularly, highly density (e.g., greater than 92% theoretical value) may effectively reduce the open surface¹¹ directly contacting with leaching environments. Thus, a dense and uniform microstructure favors the preserving of radionuclide confined in the waste form. The densities of 700-1 and 700-3 samples are found to be 95.9% and 94.6%, respectively, suggesting that iodine apatite can be consolidated into dense bulk forms by SPS at very short durations (e.g., several minutes). SEM images [Figs. 3(b) and (c)] show a dense and uniform microstructure and small amount of submicron voids existing in the sintered pellet. Quantitative analysis of the SEM-EDS patterns of the SPS-densified pellets indicates a very minor reduction in the normalized iodine content from the as-milled powders to dense bulk form, as shown by a high iodine loading above 8 wt% for the 700-3 sample [Fig. 3(e)]. This is reasonable because the sample was sintered at a longer time at a high temperature of 700°C. A uniform elemental distribution of iodine was also identified from the periphery to the center of the SPS-densified pellets (data not shown here). These

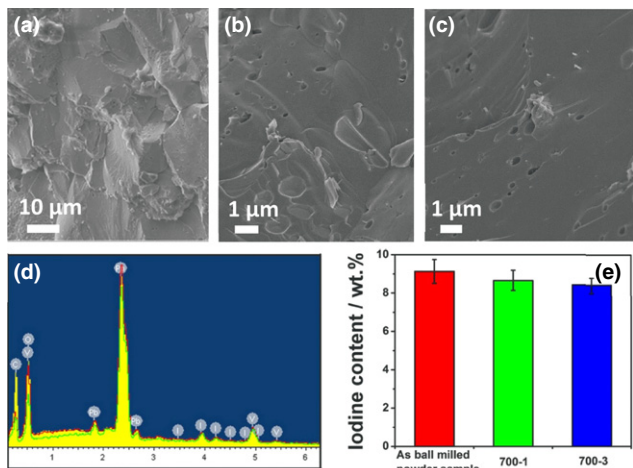


Fig. 3. Microstructure and elemental analysis of spark plasma sintering (SPS)-densified pellets: SEM image of bulk sample densified by SPS at 700°C at different durations of 1 min (a), a close-up image (b) and 3 min (c); (d)EDS of the 700-3 sample; and (e) Normalized iodine content of the as-milled powder and SPS- densified pellets.

results indicate that the iodine loss typically occurred at high-temperature sintering without buffer layers can be greatly mitigated by rapid SPS consolidation process using extremely high heating rate, very short duration, and applied stress. SEM image of microstructure also shows a dominating trans-granular fracture feature for the SPS pellet, indicating its brittle nature.

The SPS-densified pellets display greatly improved thermal stability and iodine confinement as a result of dense microstructure and larger grain size in which iodine release can be effectively prevented. Figure 4 shows the TGA testing of the SPS-densified pellets in a nitrogen inert gas environment at a heating rate of 5°C/min. An *in-situ* XRD diffraction study⁸ reported that high temperature-synthesized iodoapatite decomposes to lead ortho-vanadate $\text{Pb}_3(\text{VO}_4)_2$ at only 270°C and completely loses its iodine at above 407°C. For as-milled powdered samples by HEBM, the onset of phase decomposition and associated weight loss occurs at ~330°C and the iodine loss completes at 500°C. Thermal annealing of the as-milled powders at 200°C increases the phase decomposition temperature to 400°C due to improved crystallinity and larger grain size. The densification of the bulk iodoapatite by

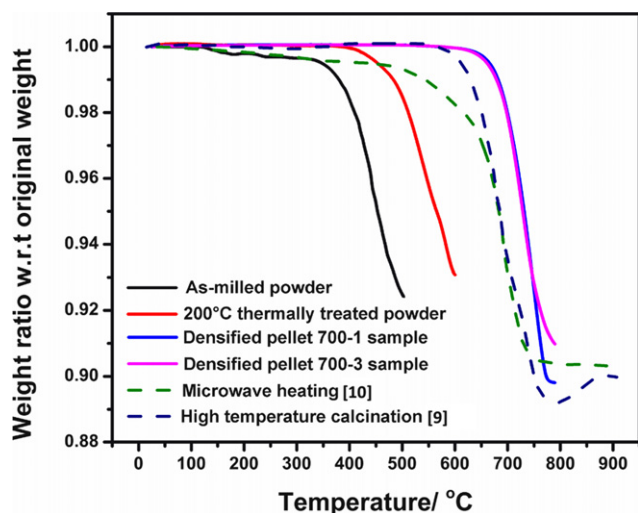


Fig. 4. Greatly improved thermal stability and iodine confinement of the spark plasma sintering densified pellets as characterized by thermogravimetric analysis. As-milled powder and 200°C thermally treated powdered samples, and densified pellets by microwave, and high-temperature sintering are included for comparison.

SPS significantly enhances the thermal stability and no iodine loss occurs at temperature till 670°C, significantly higher than the phase decomposition temperature for powdered iodoapatite. Iodine loss completes at 800°C, and the total weight loss for both 700-1 and 700-3 exceeds 8 wt%, consistent with iodine content defined by EDS measurements and TGA studies previously reported. Within experimental uncertainties of EDS measurement and TGA testing (carbon contamination from graphite die may contribute to additional weight loss), a slightly less weight loss was observed for the 700-3 sample, consistent with its slightly lower density. These results imply that partial decomposition of $\text{Pb}_{9.85}(\text{VO}_4)_6\text{I}_{1.7}$ and very minor iodine loss may occur at a longer duration (3 min) at elevated temperature despite that the phase decomposition and iodine loss are effectively mitigated by the rapid consolidation process.

Of particular significance, our SPS-densified pellets consolidated from iodoapatite powders prepared by HEBM show an improved thermal stability as compared previously densified pellets by high-temperature sintering in a sealed environment or microwave sintering. For example, a mass loss temperature of 500°C was reported for the iodoapatite pellets prepared by microwave dielectric heating, in which a 10% of $\text{Pb}_3(\text{VO}_4)_2$ buffer phase was used for TGA testing.¹⁰ Similarly, iodoapatite prepressed pellet calcinated at 700°C for 5 h in a sealed environment is stable up to about 527°C.⁹ The greatly improved thermal stability and iodine confinement of the SPS-densified pellet in this work can be attributed a much denser sintered microstructure and significantly reduced porosity as compared with pellets by microwave¹⁰ or high-temperature sintering⁹ with the relative density of ~80%.

II. Conclusions

Dense bulk lead vanadate iodoapatite ceramic with a density of 95.9% TD was successfully fabricated by combination of HEBM and SPS. Its chemical composition was determined by using XRD and first-principle calculation to be substoichiometric, $\text{Pb}_{9.85}(\text{VO}_4)_6\text{I}_{1.7}$. Also, the SPS-densified pellet displays enhanced thermal stability without iodine loss till 670°C, showing great promising as durable waste forms for confining long-lived iodine for effective waste management. Future work will focus on manipulating microstructure and grain size by changing SPS parameters and explore the possibility to further improve mechanical toughness, structural integrity, and thermal stability and investigate their microstructure evolution upon intensive radiation environment for potential waste form application.

Acknowledgments

This work was financially supported by DOE NEUP (Nuclear Engineering University Program) under award DE-AC07-05ID14517 and a NSF career award DMR 1151028.

References

- B. L. Cohen, "High-Level Radioactive-Waste from Light-Water Reactors," *Rev. Mod. Phys.*, **49**, 1–20 (1977).
- B. Grambow, "Nuclear Waste Glasses - How Durable?" *Elements*, **2**, 357–64 (2006).
- D. F. Sava, T. J. Garino, and T. M. Nenoff, "Iodine Confinement into Metal-Organic Frameworks (MOFs): Low-Temperature Sintering Glasses to Form Novel Glass Composite Material (GCM) Alternative Waste Forms," *Ind. Eng. Chem. Res.*, **51**, 614–20 (2012).
- T. J. Garino, T. M. Nenoff, J. L. Krumhansl, and D. X. Rademacher, "Low-Temperature Sintering Bi-Si-Zn-Oxide Glasses for Use in Either Glass Composite Materials or Core/Shell I-129 Waste Forms," *J. Am. Ceram. Soc.*, **94**, 2412–9 (2011).
- F. Audubert, J. Carpena, J. L. Lacout, and F. Tetard, "Elaboration of an Iodine-Bearing Apatite - Iodine Diffusion into a $\text{Pb}_3(\text{VO}_4)_2$ Matrix," *Solid State Ionics*, **95**, 113–9 (1997).
- W. J. Weber, A. Navrotsky, S. Stefanovsky, E. R. Vance, and E. Vernaz, "Materials Science of High-Level Nuclear Waste Immobilization," *MRS Bull.*, **34**, 46–53 (2009).

⁷P. Patel, "United States Launches New Direction to Manage Nuclear Waste," *MRS Bull.*, **38**, 206–7 (2013).

⁸S. A. T. Redfern, S. E. Smith, and E. R. Maddrell, "High-Temperature Breakdown of the Synthetic Iodine Analogue of Vanadinite, Pb-5(VO₄)(3)I: An Apatite-Related Compound for Iodine Radioisotope Immobilization?" *Mineral. Mag.*, **76**, 997–1003 (2012).

⁹M. Uno, M. Shinohara, K. Kurosaki, and S. Yamanaka, "Some Properties of a Lead Vanado-Iodoapatite Pb-10(VO₄)(6)I-2," *J. Nucl. Mater.*, **294**, 119–22 (2001).

¹⁰M. C. Stennett, I. J. Pinnock, and N. C. Hyatt, "Rapid Synthesis of Pb-5(VO₄)(3)I, for the Immobilisation of Iodine Radioisotopes, by Microwave Dielectric Heating," *J. Nucl. Mater.*, **414**, 352–9 (2011).

¹¹S. Le Gallet, L. Campayo, E. Courtois, S. Hoffmann, Y. Grin, F. Bernard, and F. Bart, "Spark Plasma Sintering of Iodine-Bearing Apatite," *J. Nucl. Mater.*, **400**, 251–6 (2010).

¹²L. Campayo, S. Le Gallet, Y. Grin, E. Courtois, F. Bernard, and F. Bart, "Spark Plasma Sintering of Lead Phosphovanadate Pb-3(VO₄)(1).(6)(PO₄)(0.4)," *J. Eur. Ceram. Soc.*, **29**, 1477–84 (2009).

¹³C. Wang and Z. Zhao, "Transparent MgAl₂O₄ Ceramic Produced by Spark Plasma Sintering," *Scripta Mater.*, **61**, 193–6 (2009).

¹⁴S. R. Casolco, J. Xu, and J. E. Garay, "Transparent/Translucent Polycrystalline Nanostructured Yttria Stabilized Zirconia with Varying Colors," *Scripta Mater.*, **58**, 516–9 (2008).

¹⁵M. D. Segall, P. J. D. Lindan, M. J. Probert, C. J. Pickard, P. J. Hasnip, S. J. Clark, and M. C. Payne, "First-Principles Simulation: Ideas, Illustrations and the CASTEP Code," *J. Phys.-Condensed Matter*, **14**, 2717–44 (2002).

¹⁶J. P. Perdew, J. A. Chevary, S. H. Vosko, K. A. Jackson, M. R. Pederson, D. J. Singh, and C. Fiolhais, "Atoms, Molecules, Solids, and Surfaces: Applications of the Generalized Gradient Approximation for Exchange and Correlation," *Phys. Rev. B*, **46**, 6671–87 (1992).

¹⁷F. Audubert, J. M. Savariault, and J. L. Lacout, "Pentalead Tris(Vanadate) Iodide, a Defect Vanadinite-Type Compound," *Acta Crystallogr. Sect. C-Cryst. Struct. Comm.*, **55**, 271–3 (1999). □


 Cite this: *RSC Adv.*, 2014, 4, 38718

Facile low temperature solid state synthesis of iodoapatite by high-energy ball milling

 Fengyuan Lu,^a Tiankai Yao,^a Jinling Xu,^a Jingxian Wang,^b Spencer Scott,^a Zhili Dong,^b Rodney C. Ewing^c and Jie Lian^{*a}

The apatite structure-type has been proposed as a potential waste form for the immobilization of long-lived fission products, such as I-129; however, it is difficult to synthesize iodoapatite without significant iodine loss due to its high volatility. In this study, we report a facile low temperature ($\sim 50^\circ\text{C}$) solid-state method for successfully synthesizing lead-vanadate iodoapatite by high-energy ball milling (HEBM) of constituent compounds: PbI_2 , PbO and V_2O_5 . As-milled iodoapatite is in the form of an amorphous matrix embedded with nanocrystals and can be readily crystallized by subsequent thermal annealing at a low temperature of 200°C with minimal iodine loss. Rietveld refinement of the X-ray diffraction patterns indicates that the thermally-annealed iodoapatite is iodine deficient with an iodine concentration of $\sim 4.2\%$. Thermal gravimetric analysis (TGA) indicates that low temperature annealing greatly improves the thermal stability and iodine confinement. This novel approach, using HEBM and thermal annealing, is a very promising method for synthesizing advanced materials that can confine highly volatile radionuclides, such as I-129, which pose significant challenges for the successful disposal of high-level nuclear waste.

 Received 4th June 2014
Accepted 20th August 2014

DOI: 10.1039/c4ra05320f

www.rsc.org/advances

1. Introduction

The immobilization and disposal of I-129, a long-lived fission product element ($t_{1/2} = 15.7$ million years), is critical to the effective management of high-level radioactive waste.¹ I-129 is highly mobile because it forms negatively charged species in solution; thus, it requires a specially-designed, durable waste form for its immobilization. There have been a number of efforts to incorporate I-129 into a durable matrix for deep geological disposal.^{1–5} The apatite-type structure $\text{A}_4\text{A}^{\text{II}}_6(\text{BO}_4)_6\text{X}_2$ ($\text{A}^{\text{I}}, \text{A}^{\text{II}} = \text{Ca}, \text{Na}, \text{rare earths}, \text{fission products such as Sr, and/or actinides}$; $\text{B} = \text{Si}, \text{P}, \text{V}, \text{or Cr}$; and $\text{X} = \text{OH}, \text{F}, \text{Cl}, \text{or O}$) offers the advantages of high waste loading, high chemical durability and “tunable” radiation stability.^{3,6} A wide range of actinides and fission products can be incorporated into apatite structure as a result of its structural flexibility and complex crystal chemistry upon coupled cation and anion substitutions. Particularly, apatite has an open frame structure consisting of six equivalent BO_4 tetrahedra corner-connected to AO_6 metaprisim columns, forming a one-dimensional channel parallel to the c axis of the hexagonal structure. Large A-site cations create a larger channel capable of accommodating X-anions, such as iodine. In

contrast, smaller A-site cations reduce channel size, which may lead to X anion vacancies and non-stoichiometric apatite compositions.^{7,8} Lead vanadate iodoapatite $\text{Pb}_{10}(\text{VO}_4)_6\text{I}_2$ has large A- and B-site atoms of Pb and V that enable the accommodation of the high concentrations of iodine anions in the tunnel and has thus been proposed as a promising waste form for the immobilization of I-129. The theoretical iodine loading estimated from the stoichiometric composition is $\sim 8.4\text{ wt}\%$.

Extensive research has been conducted on the synthesis and testing of $\text{Pb}_{10}(\text{VO}_4)_6\text{I}_2$ type iodoapatite for iodine confinement and disposition. A previous *ab initio* calculation estimated the standard enthalpy of formation for stoichiometric iodoapatite to be $-1298.471\text{ kcal mol}^{-1}$, suggesting that the iodoapatite may be thermodynamically stable at room temperature.⁹ Efforts to synthesize iodine-bearing apatite date back to the 1950s,¹⁰ and are currently attracting renewed interests due to the increasing concerns over the waste management of I-129.^{3,11,12} Conventional hot pressing method has been used to synthesize the lead vanadate iodoapatite at sintering temperatures of approximately 700°C , and structural analysis by Audubert *et al.*¹³ showed an iodine-deficient, Pb-apatite structure-type with a composition of $\text{Pb}_{9.85}(\text{VO}_4)_6\text{I}_{1.7}$ and a theoretical density of 6.935 g cm^{-3} . A significant iodine loss may occur during synthesis process due to the high volatility of iodine and a phase decomposition of lead-vanadate iodoapatite (e.g., $\text{Pb}_{10}(\text{VO}_4)_6\text{I}_2$ or $\text{Pb}_{9.85}(\text{VO}_4)_6\text{I}_{1.7}$) to orthovanadate $\text{Pb}_3(\text{VO}_4)_2$ at $\sim 270^\circ\text{C}$ and a complete iodine loss occurs at $\sim 400^\circ\text{C}$.¹⁴ As a result, highly isolated systems such as sealed containers or

^aDepartment of Mechanical, Aerospace, and Nuclear Engineering, Rensselaer Polytechnic Institute, Troy, NY 12180, USA. E-mail: lianj@rpi.edu

^bSchool of Materials Science and Engineering, Nanyang Technological University, Singapore 639798, Singapore

^cDepartment of Geological & Environmental Sciences, Stanford University, Stanford, CA 94305-2115, USA

encapsulating ceramics are needed for the synthesis of iodoapatite by solid state reaction at elevated temperature in order to prevent potential iodine loss.^{1,3,15} Recently, novel techniques such as reactive microwave dielectric heating¹² and spark plasma sintering (SPS)¹¹ have been developed for the synthesis of lead vanadate iodoapatite. Rapid heating of the materials resulting from field assisted sintering helps to prevent significant iodine loss. However, these methods still involve chemical reaction at elevated temperatures by heating the samples. As a result, the development of a low temperature solid state approach for synthesizing iodoapatite without release of radioactive iodine is critical for safe immobilization and disposal of problematic I-129.

In the present work, we demonstrate a one-step facile route for synthesizing iodoapatite *via* a low temperature solid-state reaction by a high energy ball mill (HEBM). The solid-state reaction, targeting the $\text{Pb}_{10}(\text{VO}_4)_6\text{I}_2$ -based iodoapatite structure, was energized solely by mechanical attrition induced by HEBM without any heating, leading to nanocrystals embedded into an amorphous matrix. The ball-milled, amorphous iodoapatite can be crystallized by subsequent thermal annealing at a relatively low temperature of 200 °C. Chemical analysis indicated that no iodine loss occurred upon low temperature thermal annealing, and the iodine waste loading is above 7 wt%, close to the maximum waste loading defined by the structural stoichiometry. The efficient synthesis of iodoapatite by HEBM and subsequent annealing provides a new pathway for the development of advanced iodine bearing waste forms with minimum iodine-loss.

2. Experimental procedure

The HEBM process was carried out in a Fritsch Pulverisette 7 Premium Line planetary ball mill following simple and efficient procedures. Specifically, commercially-available micron-sized PbI_2 (99.5% purity), PbO (99.3% purity) and V_2O_5 (99.1% purity) powders were mixed in a molar ratio of 1 : 9 : 3 as the starting materials. In a typical run, 10 g of these powders were milled with 5 ml of ethanol by 100 g of 2 mm diameter ZrO_2 milling balls in an 80 ml ZrO_2 milling bowl. The mixtures were milled at a speed of 500 rpm at varied durations of 5, 10 and 20 hours, respectively. During the milling process, the temperature and pressure inside the milling bowl were monitored by an Easy GTM sensor. After the milling, the powders were dried and separated from the milling balls, and subsequent thermal annealing was performed on as-milled powders at different temperatures of 200, 300, 400 and 550 °C in air for 1 hour, respectively.

The morphology, microstructure and chemical composition of as-milled and thermally-treated samples were characterized by a JEOL 2010 transmission electron microscopy (TEM) and by a Zeiss Supra 55 scanning electron microscopy (SEM). Crystal structures were analyzed by X-ray diffraction (XRD) with a PANalytical X'pert Pro X-ray diffractometer, and the Rietveld structural refinement of the XRD data was done with TOPAS software. To determine the phase transition temperature of the as-milled samples, differential scanning calorimetry (DSC) was

conducted in a DSC-Q100 instrument (TA instrument, US). The powder samples were loaded into a covered aluminum pan in a nitrogen atmosphere with a nitrogen flow rate of 50 ml min⁻¹, followed by a thermal cycle of heating to 510 °C at a heating rate of 5 °C min⁻¹ and then cooling down to room temperature at 10 °C min⁻¹. Thermal gravimetric analysis (TGA) was performed in a TGA-Q50 (TA instrument, US) system to determine the weight loss during heating from room temperature to 510 °C under flowing air at a heating rate of 5 °C min⁻¹.

3. Results and discussion

3.1 Materials synthesis by high energy ball milling

Simple binary oxides and iodide of PbI_2 , PbO and V_2O_5 in a molar ratio of 1 : 9 : 3 were selected as the starting materials for HEBM synthesis of iodoapatite in order to target the stoichiometric composition of $\text{Pb}_{10}(\text{VO}_4)_6\text{I}_2$. Ethanol was used for wet grinding to improve the milling efficiency and prevent agglomeration and chunk formation. During the high energy ball milling, the temperature and pressure inside the bowl slightly increased to ~50 °C and ~1.5 bars as monitored by the Easy GTM sensor. The high impact velocities and frequencies of the grinding media bring the materials into a highly non-equilibrium state, consequently inducing a solid state chemical reaction among the ingredients: $\text{PbI}_2 + 9\text{PbO} + 3\text{V}_2\text{O}_5 \rightarrow \text{Pb}_{10}(\text{VO}_4)_6\text{I}_2$.

The XRD data in Fig. 1a indicate that the iodoapatite began to form after 5 hours of milling, and the appearance of a diffraction peak at $2\theta = 28^\circ$ suggested the formation of intended phase assemblage of iodoapatite. However, due to the short ball milling duration, there are still unreacted PbI_2 , PbO and V_2O_5 traced in the obtained powders. A complete reaction was achieved after 10 hours of milling, as the original binary oxide and iodide peaks fully disappeared and the characteristic iodoapatite (112) peak, centered at 2θ of ~28°, became

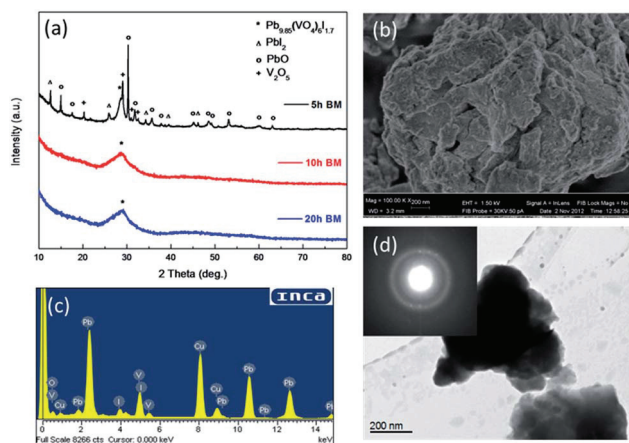


Fig. 1 (a) XRD patterns of ball-milled powders with different milling times; (b) a SEM image of an as-milled sample (20 h milling) displaying micron-sized granules consisting of consolidated nano-sized particles; (c) and (d): a EDS spectrum and a bright field TEM image showing the successful fabrication of I-apatite by high-energy ball milling and nano-sized -microstructures in the as-milled sample.

prominent. An increase in milling time to 20 hours has no significant effects on the phase assemblage and structure. Significant peak broadening and overlapping of the iodoapatite (121), (112) and (300) diffractions centered at 2θ of $\sim 28^\circ$ were observed in both 10 h and 20 h milled samples, implying the formation of nanostructure. Fig. 1b is a SEM image of the as-milled sample (after 20 h milling) showing the morphology of micron-sized granular consisting of consolidated nanoparticles for the I-apatite, and the morphology is typically observed for the materials prepared by high energy ball milling.

Energy-dispersive X-ray spectroscopy (EDS) measurements of the as-milled samples were performed using TEM (as shown in Fig. 1c). Signal of iodine can be clearly seen in the EDS spectrum, indicating the confinement of iodine upon the formation of the single-phase apatite after high energy ball milling. Quantification analysis of EDS data (see Table 1) indicates that the 10 h milled sample is an iodine-bearing phase with ~ 4.2 at% iodine content. The waste loading of iodine is close to the atomic percentage in the previously-reported $\text{Pb}_{9.85}(\text{VO}_4)_6\text{I}_{1.70}$ iodoapatite synthesized *via* reactive sintering.¹³ The 20 h milled sample shows an iodoapatite structure similar to that of the 10 h milled sample as confirmed by XRD and EDS. These results highlight a very effective approach in confining highly volatile iodine into apatite structure-type upon solid-state reaction at room temperature with greatly enhanced reaction kinetics and minimized I-volatilization by high energy ball milling.

Bridge-field TEM image (Fig. 1d) shows nano-sized particles embedded into a larger sized cluster, consistent with the SEM observation. High resolution TEM (HRTEM) images (Fig. 2a) of the 10 h milled sample reveal that materials exist in the form of nanocrystals embedded in a predominantly-amorphous matrix.

This is consistent with the discrete weak diffraction spots, mostly corresponding to apatite (112), in an amorphous halo background in the selected area electron diffraction (SAED) pattern (inset in Fig. 2a). The nanocrystals are mostly 4–10 nm in size and often isolated from each other by the amorphous matrix. Accompanying with the solid state reaction, the intense mechanical attrition by the high energy ball milling also caused solid-state amorphization, leading to the formation of amorphous matrix embedded with only residual nano-sized crystallites.

3.2 Thermally-activated crystallization and phase stability

As crystalline ceramic waste form may display enhanced chemical durability and thus reduced radionuclide release by incorporating and confining radionuclides into the atomic

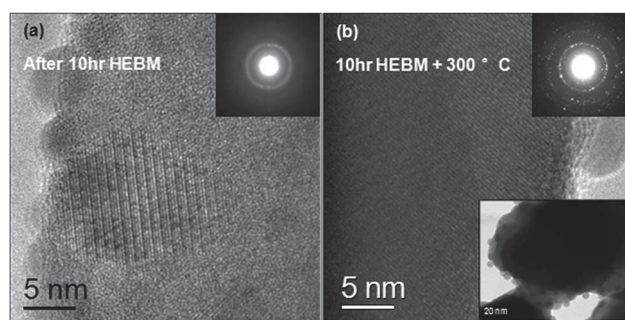


Fig. 2 (a) HRTEM image and SAED pattern (inset) of the 10 h ball milled sample showing iodoapatite nanocrystals embedded in an amorphous matrix; (b) HRTEM image inset with a lower magnification image and SAED pattern of the 300 °C treated sample showing significant crystallization and grain growth.

structure,^{16,17} crystalline iodoapatite is preferred for the confinement of iodine. Previous reports showed that thermal crystallization of amorphous hydroxyapatite and fluoroapatite usually occurred at temperature higher than 600 °C.^{18–21} However, such relatively high temperatures may be unfavorable for iodoapatite, because of phase decomposition due to iodine loss.¹⁴ In contrast, the as-milled iodoapatite can be well recrystallized at temperature as low as 200 °C without significant iodine loss as a result of enhanced reactivity of the powders upon mechanical attrition.

Thermal stability and recrystallization of the as-milled I-apatite were first probed by differential scanning calorimetry (DSC) at a heating rate of 5 °C min^{−1}, as shown in Fig. 3. A strong endothermic peak for the 10 h milled sample was observed at 228 °C extending from ~ 190 to ~ 250 °C, corresponding to the recrystallization from almost amorphized I-apatite. The minor extended peak between 88 °C and 100 °C of the 20 h milled sample may be attributed to the endothermic peak of adsorbed water as a result of higher moisture adsorption due to significant grain size reduction. The calculated enthalpy of transition for the 10 h milled sample is ~ 24.38 J g^{−1}. Similarly, the 20 h milled iodoapatite undergoes an exothermic process from ~ 180 to ~ 220 °C that peaked at 209 °C, indicating an exothermic crystallization with an enthalpy of transition of ~ 27.57 J g^{−1}. The lower exothermic peak and higher enthalpy of transition for the 20 h milled iodoapatite can be attributed to excess free surface energy and possible higher defect density resulting from the longer mechanical milling duration. Such an excess of free surface energy may greatly facilitate the

Table 1 EDS element analysis (at%) of the 10 h as-milled sample and thermally treated samples (3 columns on the left), as compared to the element compositions for stoichiometric $\text{Pb}_{10}(\text{VO}_4)_6\text{I}_2$, non-stoichiometric $\text{Pb}_{9.85}(\text{VO}_4)_6\text{I}_{1.7}$ and lead vanadate $\text{Pb}_3(\text{VO}_4)_2$

Element at%	10 h HEBM	10 h HEBM + 200 °C	10 h HEBM + 200 °C	10 h HEBM + 400 °C	Stoichiometric $\text{Pb}_{10}(\text{VO}_4)_6\text{I}_2$	$\text{Pb}_{9.85}(\text{VO}_4)_6\text{I}_{1.7}$	$\text{Pb}_3(\text{VO}_4)_2$
V	12.00	12.54	12.27	11.78	14.28	14.44	15.38
I	4.18	4.14	3.58	1.12	4.76	4.09	0
Pb	26.91	25.98	26.73	28.83	23.81	23.71	23.08
O	56.91	57.34	57.42	58.27	57.15	57.76	61.54

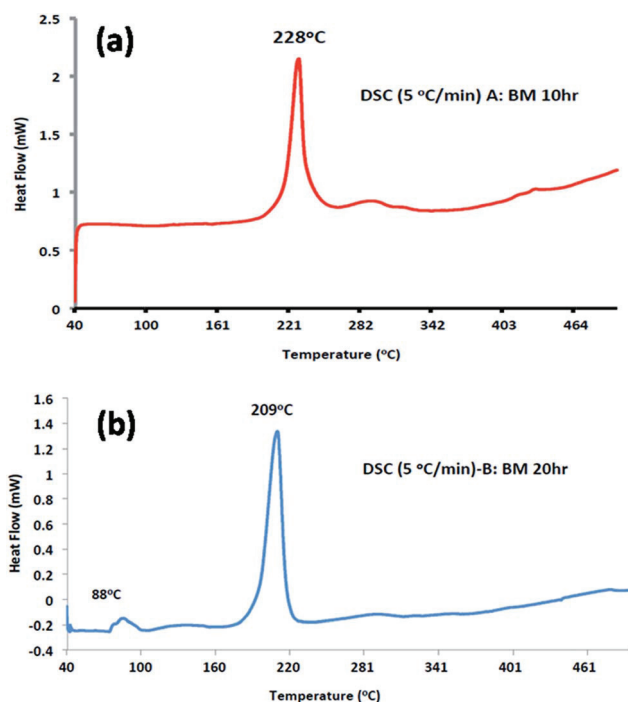


Fig. 3 DSC curves of the as-milled iodoapatite samples: (a) 10 h milled and (b) 20 h milled with a heating rate of 5 °C min⁻¹.

crystallization process by reducing the energy difference between the amorphous and crystalline phases to achieve a lower transition temperature.

The as-milled iodoapatite powders were thermally treated in air at temperatures of 200, 300, 400 and 550 °C for 1 hour, and the thermal stability and microstructure evolution were investigated by XRD diffraction. As shown in Fig. 4, significant peak sharpening and increase in intensity of the diffraction peaks in the XRD patterns can be observed after thermal treatment at 200 °C and 300 °C for both 10 and 20 h milled samples, indicating remarkable crystallization and grain growth due to the thermal treatment. In addition to the strongest peaks of (121), (112) and (300) at ~28° of two-theta, diffraction peaks corresponding to other crystal planes of lead vanadate iodoapatite also emerged after 200 and 300 °C thermal treatments. Further increasing the heat treatment temperature at 400 °C, dual phases form with non-iodine bearing phase Pb₃(VO₄)₂ dominated, as a result of iodine volatilization and decomposition of iodine apatite into lead vanadate for both samples milled at 10 and 20 h.

The thermally-activated crystallization and grain growth was also observed by both *in situ* and *ex situ* TEM and SEM. *In situ* TEM was performed while heating the as-milled sample to 200 °C with a heating stage, showing that the originally amorphous matrix rapidly crystallized with grain coarsening to ~30 nm in only tens of seconds. This is also evident by *ex situ* TEM characterization of the 300 °C treated sample which exhibits a well-crystalline grain structure with an average size of 30–50 nm (Fig. 2b). The enhanced crystallinity of the ball milled sample upon thermal treatment is also evidenced by the

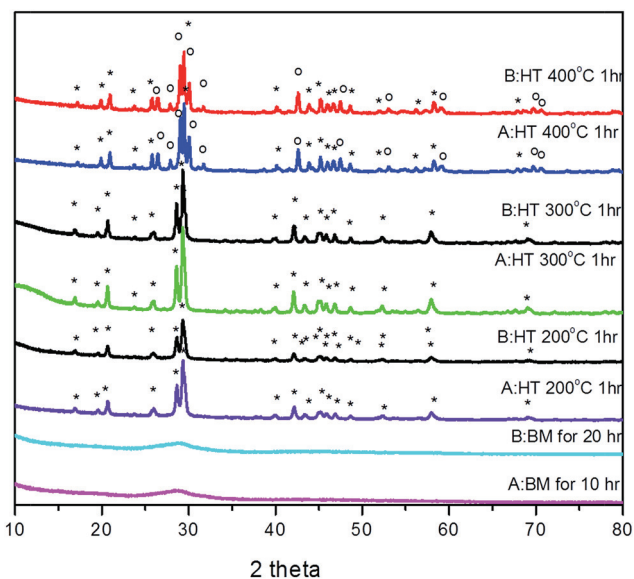


Fig. 4 XRD patterns of thermally treated samples at 200 °C, 300 °C and 400 °C for 1 hour for both 10 h and 20 h ball milled samples. Amorphous-dominant iodoapatite began to form after 10 h and 20 h ball milling. A pure and highly crystalline iodoapatite was obtained by 200 °C and 300 °C thermal treatments; and a further increase in temperature to 400 °C led to the formation of Pb₃(VO₄)₂ as a result of iodoapatite phase decomposition and iodine loss.

selected area diffraction pattern (inset in Fig. 2b). *Ex situ* SEM images show that the micron-sized granules consisting of consolidated nanoparticles are clearly observed as compared with the rough surface of the mainly amorphous, as-milled sample in Fig. 1b and d, the thermally-treated samples shown in Fig. 5 exhibit equant grains with well-identified grain boundaries. In addition, the larger grain size can be observed at higher annealing temperatures as a result of thermally-activated grain boundary migration and coarsening. A qualitative assessment of microstructures indicates that the thermally-

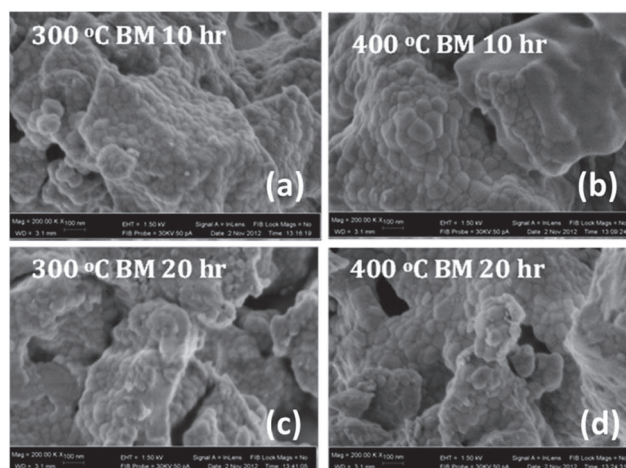


Fig. 5 High magnification SEM images of the 20 h ball milled sample after (a) 300 °C and (b) 400 °C thermal treatment; and the 20 h ball milled sample after (c) 300 °C and (d) 400 °C thermal treatment.

treated samples, resulting from longer ball-milling times, has a finer grain size, consistent with the smaller initial particle size prior to thermal treatment. An increase of thermal treatment temperature to 400 °C leads to further grain growth.

In brief, the ball milling and thermal treatment mainly affect the grain size and crystallinity of the samples. On one hand, high energy ball milling induces solid state chemical reaction to form the iodoapatite; on the other, it reduces the grain size and crystallinity of the sample *via* mechanical attrition. Post-milling thermal treatment below 400 °C improves the crystallinity and induces a grain growth in the sample; however, thermal treatment temperature at 400 °C or above induces significant decomposition of the iodoapatite phase.

3.3 Structural characteristics of iodoapatite by Rietveld refinement

Rietveld refinements were performed on the XRD data revealing detailed structural characteristics of the thermally treated samples. The successful XRD data refinement of the 200, 300 and 400 °C treated samples, as indicated by the good fit of the patterns in Fig. 6, suggests that the 200 and 300 °C treated samples are a pure, iodine-bearing apatite structure. The structural parameters and the key bond lengths of the 200 and 300 °C treated pure iodoapatites are summarized in Table 2 and

3. The iodoapatite samples, treated at 200 °C and 300 °C, are identical to the hexagonal apatite structure ($P6_3/m$). There are two types of Pb atoms (the columnar Pb1 and axial Pb2), tightly bonded to VO_4 tetrahedra and I atoms that are aligned in the channel formed by the VO_4 tetrahedra corner-connected to PbO_6 metaprism columns along the c -axis, as shown in Fig. 7. The VO_4 unit is comprised of one V and four crystallographically nonequivalent O atoms, O1, O2, O3 and O4, with 6 sites for O1 and O2, and 12 sites for O3 and O4. The Rietveld refinement indicates that the pure iodoapatite phase in the 200 °C and 300 °C treated samples contain certain iodine and lead deficiencies, with slightly different compositions of $\text{Pb}_{9.85}(\text{VO}_4)_6\text{I}_{1.70}$ (200 °C) and $\text{Pb}_{9.84}(\text{VO}_4)_6\text{I}_{1.68}$ (300 °C). This iodine-deficient structure is similar to the non-stoichiometric iodoapatite $\text{Pb}_{9.85}(\text{VO}_4)_6\text{I}_{1.70}$ reported by Audubert *et al.*¹³ The 200 °C treated sample has a smaller lattice parameter a but a larger c -parameter than the sample treated at 300 °C. This suggests that the large iodine atom competes with the Pb for the sites in the tunnel along the c -axis. The bond lengths of V–O in the VO_4 tetrahedra (Table 3) range from 1.631 to 1.802 Å for the 200 °C treated sample, and 1.567 to 1.877 Å for the 300 °C treated one, respectively. The more distorted VO_4 tetrahedra in the 200 °C treated sample may be attributed to the slightly higher iodine occupancy, as inferred by the calculated chemical formula.

The two phases in the sample treated at 400 °C are evident in the XRD pattern (Fig. 4) and were also determined by the Rietveld refinement as 15 wt% of $\text{Pb}_3(\text{VO}_4)_2$ and 85 wt% of highly iodine-deficient $\text{Pb}_{9.45}(\text{VO}_4)_6\text{I}_{0.9}$, with anion vacancies along c -axis. The dominant phase of $\text{Pb}_{9.45}(\text{VO}_4)_6\text{I}_{0.9}$ exhibits a low iodine occupancy of 0.0745 as compared with 0.1424 in the 300 °C treated sample, and the total iodine content in the double-phase sample is estimated to be ~1.4 at% accordingly. The highly iodine-deficient $\text{Pb}_{9.45}(\text{VO}_4)_6\text{I}_{0.9}$ is a metastable phase that results from the partial decomposition of $\text{Pb}_{9.84}(\text{VO}_4)_6\text{I}_{1.68}$ and can further decompose to $\text{Pb}_3(\text{VO}_4)_2$ by release of all the iodine at higher temperatures. The complete breakdown of $\text{Pb}_{9.45}(\text{VO}_4)_6\text{I}_{0.9}$ was observed when the as-milled powders were heated at 550 °C for 1 hour.

3.4 Micro-chemical composition variation upon thermal annealing and iodine confinement

Confinement of iodine is critical for the immobilization of long-lived iodine in a stable matrix because of its highly volatility. Quantitative analysis of EDX spectra of the as-milled and thermally-treated materials was performed in order to determine the correlation among microchemical composition, phase transformation, I-loss and thermal annealing, in order to establish the mechanism of the phase decomposition of I-apatite at elevated temperature as a result of I-volatilization. Table 1 summarizes the elemental analysis of P, V, O and I for the ball-milled samples before and after thermal treatment by an EDX attached with a TEM. The iodine confinement in the synthesized powdered samples and upon thermal annealing was compared with that of ideal stoichiometric composition and iodine deficient iodoapatite determined by Rietveld refinement.

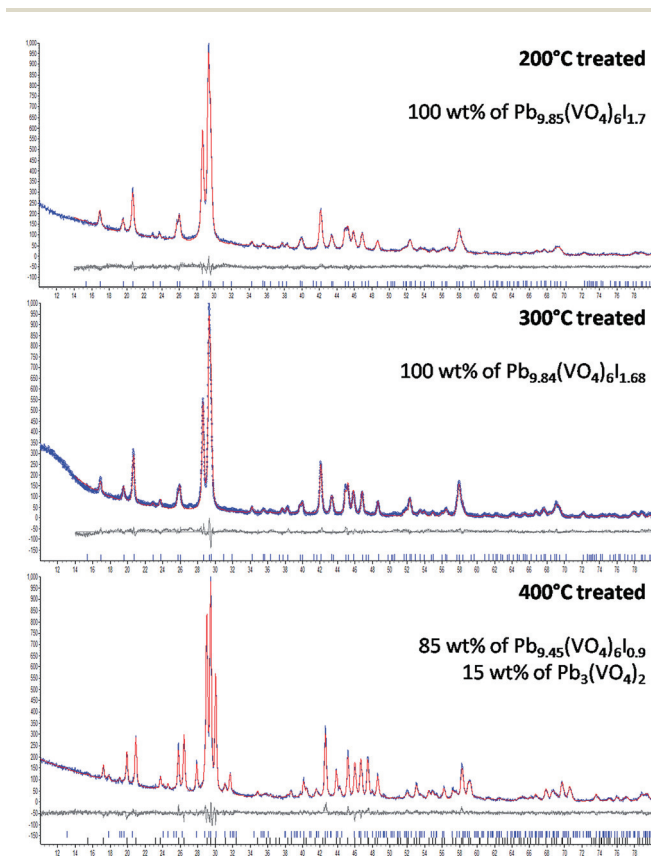


Fig. 6 Refinement fitting of the XRD patterns of 200 °C, 300 °C and 400 °C treated iodoapatite, with blue lines representing the fit curves, red lines are the XRD patterns, gray lines are the fit to the data, and the tick marks show peak positions for the refined phases.

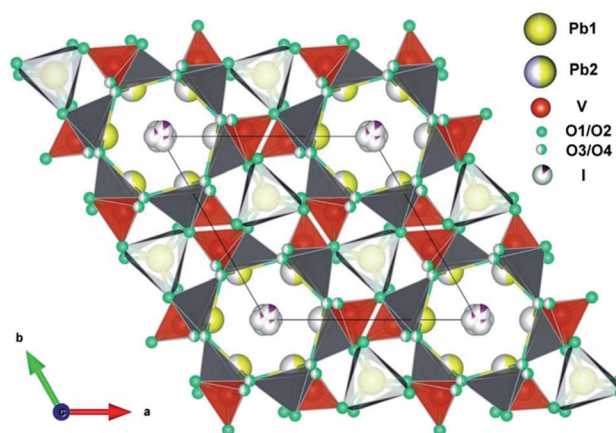
Table 2 Refined structural parameter of iodoapatite after 200 °C and 300 °C heat treatment

	Atom	Site	x	y	z	Occupancy
200 °C treated $a = 10.4486 \text{ \AA}$ $c = 7.4782 \text{ \AA}$	Pb1	4f	1/3	2/3	0.0064	0.9828
	Pb2	12i	0.0090	0.2673	0.2743	0.4934
	V	6h	0.3815	0.4030	1/4	1
	O1	6h	0.4532	0.3347	1/4	1
	O2	6h	0.4610	0.5599	1/4	1
	O3	12i	0.2524	0.3344	0.0627	0.5
	O4	12i	0.3239	0.4901	0.0823	0.5
	I	12i	0.0331	0.0465	0.00047	0.1424
300 °C treated $a = 10.4627 \text{ \AA}$ $c = 7.4773 \text{ \AA}$	Pb1	4f	1/3	2/3	0.0066	0.9587
	Pb2	12i	0.0049	0.2665	0.2762	0.5
	V	6h	0.3886	0.4048	1/4	1
	O1	6h	0.4918	0.3362	1/4	1
	O2	6h	0.4854	0.6118	1/4	1
	O3	12i	0.2299	0.3501	0.1776	0.5
	O4	12i	0.3212	0.3813	0.0497	0.5
	I	12i	0.2394	0.03233	0.0006	0.1419

Table 3 Refined key bond lengths of iodoapatite after 200 °C and 300 °C heat treatment

200 °C treated		300 °C treated	
Bond	Length (Å)	Bond	Length (Å)
Pb1–O1	2.886	Pb1–O1	2.591
Pb1–O1	2.886	Pb1–O1	2.591
Pb1–O1	2.886	Pb1–O1	2.591
Pb1–O2	2.861	Pb1–O2	2.730
Pb1–O2	2.861	Pb1–O2	2.730
Pb1–O2	2.861	Pb1–O2	2.730
Pb1–O3	3.177	Pb1–O3	2.955
Pb1–O3	3.177	Pb1–O3	2.955
Pb1–O3	3.177	Pb1–O3	2.955
Pb2–O1	3.159	Pb2–O1	3.159
Pb2–O2	2.512	Pb2–O2	2.257
Pb2–O3	2.330	Pb2–O3	2.090
Pb2–O3	2.670	Pb2–O3	2.189
Pb2–O4	3.120	Pb2–O4	2.316
Pb2–O4	3.174	Pb2–O4	2.668
Pb2–I	2.7898	Pb2–I	3.054
Pb2–I	2.925	Pb2–I	2.985
V–O1	1.782	V–O1	1.567
V–O2	1.802	V–O2	1.877
V–O3	1.631	V–O3	1.558

Quantitative EDS analysis indicates that iodine is well confined in the fully-crystalline iodoapatite at a low thermal annealing temperature of 200 °C and no iodine loss is observed. The iodine contents are ~4.2 at% and 4.1 at% for the 10 h as-milled and 200 °C thermally-treated powders, respectively. This iodine content is consistent with the chemical formula $\text{Pb}_{9.85}(\text{VO}_4)_6\text{I}_{1.7}$ (~4.1 at%) as defined by the Rietveld refinement and is also similar to that previously reported by Audubert *et al.*¹³ The iodine atomic percentage decreases slightly to ~3.6 at% for the 300 °C thermally-treated sample, consistent with the chemical formula of $\text{Pb}_{9.84}(\text{VO}_4)_6\text{I}_{1.68}$. These results highlight a very effective approach of high energy ball milling in

Fig. 7 View of the $\text{Pb}_{9.85}(\text{VO}_4)_6\text{I}_{1.7}$ crystal structure showing the I atoms in the V–O and Pb1–O polyhedral channel.

synthesizing I-bearing apatite and great iodine confinement. No significant I-loss occurs during ball milling due to the low temperature solid state reaction and post thermal annealing at a relatively-low temperature. Majority of iodine can be incorporated in the single phase apatite, which is of particular significance for the confinement of long-lived iodine.

A drastic reduction of iodine content occurs at higher annealing temperatures with a reduction of iodine level from ~3.6 at% in the 300 °C treated sample to ~1.1 at% after the 400 °C thermal treatment. Such a reduced iodine content at 400 °C indicates the loss of iodine due to the decomposition of the iodoapatite structure to lead vanadate $\text{Pb}_3(\text{VO}_4)_2$, consistent with the XRD data. The decomposition of iodoapatite observed at 400 °C releases the highly volatile free iodine, of which the low boiling point of iodine (184.3 °C) and strong tendency of sublimation can lead to I_2 gas release.

TGA was utilized to investigate the decomposition and iodine loss of the iodoapatite at elevated temperatures. The TGA curves in Fig. 8a showed the weight changes of the 10 h and 20

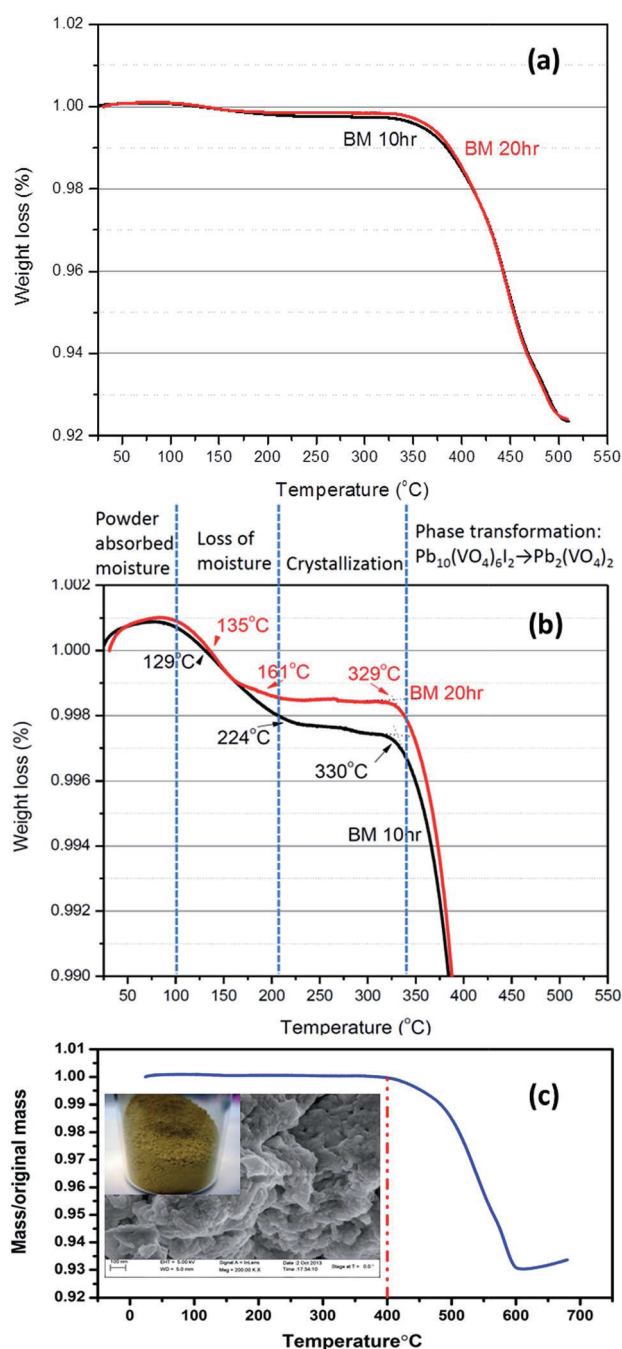


Fig. 8 TGA curves of ball-milled samples: (a) as-milled iodoapatite samples, with the black line showing the 10 h milled sample and the red line showing the 20 h milled sample; (b) a close-up of the TGA curves of (a); and (c) crystalline iodoapatite powders upon 10 h ball milling and thermal treated at 200 °C for 1 h. Significant enhancement in the thermal stability and phase decomposition temperature are identified. A high iodine loading (~ 7 wt%) was observed in the thermally annealed samples.

milled powder samples in a temperature range from 25 to 510 °C. Both samples were generally stable up to ~ 330 °C in air with no significant weight change. A close-up TGA spectrum is shown in Fig. 8b, in which different stages of crystallization and phase decomposition can be clearly identified. Particularly, the

onset of weight loss began at ~ 330 °C, followed by a steep edge at ~ 380 °C that extends and saturates afterward to 500 °C. The total loss of weight was ~ 7.6 wt% for both samples, close to the weight percentage of iodine (~ 7.3 wt%) in the $\text{Pb}_{9.85}(\text{VO}_4)_6\text{I}_{1.70}$ and $\text{Pb}_{9.84}(\text{VO}_4)_6\text{I}_{1.68}$ iodoapatite structures. Therefore, we conclude that the decomposition and iodine loss for the HEBM synthesized iodoapatite occur mainly between 330 and 500 °C, and the phase decomposition and the release of gaseous I_2 account for most of the weight loss.

The subsequent annealing process at a low temperature 200 °C greatly improves the thermal stability and increases the phase decomposition temperature due to the high crystalline feature and noticeable grain coarsening. The on-set temperature for iodine loss increases to 400 °C and no significant weight loss (only ~ 1 wt%) was observed above 500 °C for the loosely-packed powders (as shown in Fig. 8c) upon 200 °C thermally treatment. Complete iodine loss (~ 7 wt%) occurs at the temperature above 600 °C. As compared with Fig. 8a, no moisture absorption is found in Fig. 8c because the significant grain growth upon thermal annealing dramatically reduced the specific surface area of the iodoapatite sample and hence the moisture absorption.

3.5 Impact and significance of HEBM process for iodine immobilization

The HEBM synthesis of high-iodine iodoapatite demonstrated in this study features a facile one-step solid state reaction at low temperature (~ 50 °C) with a high iodine loading. The as-milled sample in the form of amorphous-dominated matrix can readily be crystallized at temperatures as low as 200 °C without any iodine loss. This simple and efficient synthesis approach allows large scale processing iodine-bearing waste forms for the immobilization of long lived fission product I-129.

The low temperature solid state reaction by HEBM and subsequent low temperature annealing offer distinct advantages for developing durable waste forms for effective confinement of volatile radionuclides. Previous methods, *e.g.*, 500–700 °C for conventional hot pressing and ~ 500 °C for microwave heating,^{1,3,12,15} inevitably require heating the samples to relatively high temperatures, leading to significant phase decomposition and iodine release.¹⁴ In such cases, the chemical processing system must be confined, such as with sealed containers or embedding the reactants in an orthovanadophosphate matrix.^{1,3,15} In contrast, high-loading of iodine can be achieved for the single phase iodoapatite by the facile, low-temperature approach by HEBM.

It is worth noting that the our HEBM synthesized iodoapatite exhibits improved thermal stability as compared with the previously reported high temperature sintered iodoapatite, which begins to decompose to lead ortho-vanadate $\text{Pb}_3(\text{VO}_4)_2$ at only 270 °C and completely loses its iodine at above 407 °C.¹⁴ Although a higher mass loss temperature of 500 °C was reported for the iodoapatite prepared by microwave dielectric heating, it is noted that dense iodoapatite pellets with 10% of $\text{Pb}_3(\text{VO}_4)_2$ buffer phase was used for TGA testing in that study,¹² rather than the loosely packed nano-sized powders as the current

work. The thermal stability improvement for HEBM synthesized iodoapatite may be due to the low reaction temperature ($\sim 50^\circ\text{C}$) during the ball milling process as compared with the $500\text{--}700^\circ\text{C}$ temperature for the various heating techniques as previously reported.^{3,12} At such a low temperature, thermal decomposition and destabilization of the iodoapatite can be greatly mitigated, resulting in enhanced thermal stability of the powdered samples with a complete iodine loss above 500°C . In addition, the subsequent annealing process at low temperature 200°C will further improve the thermal stability due to the high crystalline feature and noticeable grain coarsening. No significant weight loss (only $\sim 1\text{ wt}\%$) was observed above 500°C for the loosely-packed powders (as shown in Fig. 8c) upon 200°C thermally treatment and complete iodine loss occurs at 600°C .

For consolidation of iodoapatite into durable waste forms, very rapid heating techniques such as spark plasma sintering (SPS) and microwave heating^{11,12} will be particularly useful in order to minimize iodine release associated with the densification. The nano-scale features and surface activation upon mechanical attrition of HEBM will greatly improve the sinterability and reactivity of the ball-milled powders, beneficial for the densification and consolidation process. The improved sinterability and reactivity of the ball milled samples were already demonstrated by the enhanced kinetics for rapid recrystallization and grain growth at temperature (200°C), far below the decomposition temperature of iodoapatite. Using ball-milled powders and spark plasma sintering, we have fabricated fully dense iodoapatite ceramic pellets at temperatures of 700°C within a very short duration (e.g., several minutes) with greatly-improved thermal stability and iodine confinement, as compared with previously-fabricated iodoapatite pellets by SPS or microwaving sintering.^{11,12} The study on rapid consolidation of iodoapatite will be reported elsewhere.²²

4. Conclusions

In summary, we report a novel low temperature solid-state approach of synthesizing iodine-bearing apatite by high-energy ball milling combining with low temperature post thermal annealing. In contrast to previously reported synthesis methods which required heating at elevated temperature, the HEBM approach is a facile and one-step solid reaction at low temperature driven by mechanical attrition such that the iodine loss occurring at elevated temperatures can be greatly mitigated. The as-milled samples exist in the form of nanocrystals embedded in an amorphous matrix, and the crystals can be readily recrystallized into a pure, single-phase iodoapatite at 200°C . As compared to iodoapatite obtained by conventional methods, the ball-milled iodoapatite has a lower crystallization temperature, improved thermal stability, a higher decomposition temperature and excellent iodine confinement. The successful development of this new approach opens up the opportunity for synthesizing a wide range of different iodine-bearing apatite compositions as stable waste forms for the immobilization and safe disposal of long-lived, radiotoxic fission product I-129.

Acknowledgements

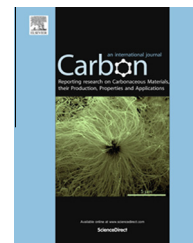
This work is supported by DOE NEUP (Nuclear Engineering University Program) under the award DE-AC07-05ID14517 and a NSF career award DMR 1151028. ZL Dong acknowledges the support from a Singapore NTU AcRF grant RG11/04.

Notes and references

- 1 C. Guy, F. Audubert, J. E. Lartigue, C. Latrille, T. Advocat and C. Fillet, *C. R. Phys.*, 2002, **3**, 827.
- 2 N. C. Hyatt, J. A. Hriljac, A. Choudhry, L. Malpass, G. P. Sheppard and E. R. Maddrell, *Mater. Res. Soc. Symp. Proc.*, 2004, **807**, 359.
- 3 F. Audubert, J. Carpena, J. L. Lacout and F. Tetard, *Solid State Ionics*, 1997, **95**, 113.
- 4 G. Lefevre, J. Bessiere, J. J. Ehrhardt and A. Walcarius, *J. Environ. Radioact.*, 2003, **70**, 73.
- 5 S. Wu, S. Wang, A. Simonetti, F. Chen and T. E. Albrecht-Schmitt, *Radiochim. Acta*, 2011, **99**, 573.
- 6 F. Y. Lu, Z. L. Dong, J. M. Zhang, T. White, R. C. Ewing and J. Lian, *RSC Adv.*, 2013, **3**, 15178.
- 7 Z. L. Dong, T. J. White, B. Wei and K. Laursen, *J. Am. Ceram. Soc.*, 2002, **85**, 2515.
- 8 T. J. White and Z. L. Dong, *Acta Crystallogr., Sect. B: Struct. Sci.*, 2003, **59**, 1.
- 9 J. L. Fleche, *Phys. Rev. B: Condens. Matter Mater. Phys.*, 2002, **65**, 245116.
- 10 L. Merker and H. Wondratschek, *Z. Anorg. Allg. Chem.*, 1959, **300**, 41.
- 11 S. Le Gallet, L. Campayo, E. Courtois, S. Hoffmann, Y. Grin, F. Bernard and F. Bart, *J. Nucl. Mater.*, 2010, **400**, 251.
- 12 M. C. Stennett, I. J. Pinnock and N. C. Hyatt, *J. Nucl. Mater.*, 2011, **414**, 352.
- 13 F. Audubert, J. M. Savariault and J. L. Lacout, *Acta Crystallogr., Sect. C: Cryst. Struct. Commun.*, 1999, **55**, 271.
- 14 S. A. T. Redfern, S. E. Smith and E. R. Maddrell, *Mineral. Mag.*, 2012, **76**, 997.
- 15 M. Uno, M. Shinohara, K. Kurosaki and S. Yamanaka, *J. Nucl. Mater.*, 2001, **294**, 119.
- 16 R. C. Ewing, W. J. Weber and W. Lutze, *Disposal of Weapon Plutonium*, 1996, vol. 4, p. 65.
- 17 G. R. Lumpkin, *Elements*, 2006, **2**, 365.
- 18 I. Cacciotti, A. Bianco, M. Lombardi and L. Montanaro, *J. Eur. Ceram. Soc.*, 2009, **29**, 2969.
- 19 K. A. Gross, V. Gross and C. C. Berndt, *J. Am. Ceram. Soc.*, 1998, **81**, 106.
- 20 M. Hidouri, K. Bouzouita, F. Kooli and I. Khattech, *Mater. Chem. Phys.*, 2003, **80**, 496.
- 21 P. Layrolle, A. Ito and T. Tateishi, *J. Am. Ceram. Soc.*, 1998, **81**, 1421.
- 22 T. K. Yao, F. Y. Lu, H. T. Sun, J. W. Wang, R. C. Ewing and J. Lian, *J. Am. Ceram. Soc.*, 2014, **97**, 2409.

Available at www.sciencedirect.com

ScienceDirect

journal homepage: www.elsevier.com/locate/carbon

Graphene-based sorbents for iodine-129 capture and sequestration

Spencer M. Scott, Tao Hu, Tiankai Yao, Guoqing Xin, Jie Lian *

Department of Mechanical, Aerospace and Nuclear Engineering, Rensselaer Polytechnic Institute, 110, 8th Street, Troy, NY 12180, USA

ARTICLE INFO

Article history:

Received 4 January 2015

Accepted 30 March 2015

Available online 2 April 2015

ABSTRACT

The capture and sequestration of iodine-129 (^{129}I), a long-lived byproduct of nuclear fission, is essential to the implementation of advanced nuclear fuel cycles and effective nuclear waste management. Current state-of-the-art technologies inherently require silver to bind iodine, *e.g.*, silver-loaded silica aerogels or silver-loaded zeolite (AgZ), which are very expensive and an environmental concern. It is highly desirable to develop alternative cost-effective adsorbents for iodine capture and sequestration. Herein, we report graphene-based nanomaterials including graphene powder and graphene aerogel as novel iodine sorbents showing exceptional adsorption capability and kinetics. By measuring iodine sorption capacities and uptake rates in an $\text{I}_{2(\text{g})}$ saturated environment, graphene sorbents display impressive iodine sorption capacities with powdered samples achieving mass gains in excess of 85 mass%, and aerogels exceeding 100% mass gains. A direct correlation among specific surface area, defect concentration, and maximum sorption capacity has been established, and the sorption kinetics of the graphene for iodine capture was determined.

© 2015 Elsevier Ltd. All rights reserved.

1. Introduction

Iodine-129 (^{129}I), a long-lived (1.6×10^7 year half-life) radionuclide, is of significant concern to the implementation of spent nuclear fuel reprocessing [1]. This can be attributed to the environmental mobility and biological affinity of iodine, which when combined with the radioactive nature of ^{129}I , presents a threat to public safety due to the potential for serious health issues [2]. Due to these concerns, the Environmental Protection Agency (EPA) has implemented strict regulations on the release of ^{129}I from the reprocessing facilities, which require an effective capture efficiency in excess of 99% (decontamination factor > 167) [3]. This has created a demand for iodine sorbents and waste forms which will be suitable for use in reprocessing systems and geologic disposal [4].

The most common methods of iodine management involve $^{129}\text{I}_{2(\text{g})}$ being passed through silver-exchanged-zeolite (AgZ), which due to its silver content is highly selective for elemental iodine [5,6]. However, due to issues associated with densification into a durable waste form, and the relatively high cost of silver, implementation has lagged. Other sorbents currently being investigated include Ag-functionalized silica aerogels, and chalcogen-based aerogels, both of which have been relatively successful for iodine capture but may be costly to produce, either due to fabrication techniques or precursor materials [7,8].

Graphene, the two-dimensional basal plane of graphite, has become the focus of extensive interest for a wide range of applications including composite materials, semiconductors, and energy storage, due to its impressive mechanical, electrical, and thermal properties [9,10]. However, the

* Corresponding author.

E-mail address: lianj@rpi.edu (J. Lian).

<http://dx.doi.org/10.1016/j.carbon.2015.03.070>

0008-6223/© 2015 Elsevier Ltd. All rights reserved.

extremely-large theoretical specific surface area ($2630 \text{ m}^2 \text{ g}^{-1}$) for single layer graphene, in combination with its highly controllable defect and functional group concentration, has generated interests for graphene as a sorbent material for gasses, albeit primarily for potential gas detectors [11,12].

This work presents graphene-based materials including graphene powder and aerogel as potential sorbents for ^{129}I in spent nuclear fuel reprocessing off-gas, and investigates the sorption capacities of several varieties of graphene for $\text{I}_{2(\text{g})}$ in a saturated iodine environment. The synthesis and characterization techniques for the graphene sorbents are provided, in addition to analysis on the sorption capacity and thermal stability of the iodine-loaded samples. The correlation among surface area, defect concentration, and temperature as to how they affect the sorption/desorption interaction between graphene and elemental iodine was determined.

The graphene-based sorbents address several key challenges associated with the capture of ^{129}I in the reprocessing of spent nuclear fuel. The most prominent challenge, the reliance on silver in sorbent materials, presents a significant financial hurdle facing several current technologies. The high specific surface area of graphene-based materials enable improvements in the maximum sorption capacity and rapid kinetics of iodine adsorption over conventional methods which utilize a chemical affinity for iodine as opposed to physical adsorption of iodine. The relatively simple fabrication of graphene may also address issues associated with some of the more highly engineered sorbent materials, which require more complicated processes to synthesize [6–9]. Thus, graphene-based absorbents are more cost effective for iodine capture and sequestration.

2. Experimental section

2.1. Graphene synthesis

Graphite oxide (GO) was synthesized using a modified Hummers method [13]. Graphite flake (10 g) was mixed with sodium nitrate (5 g) and concentrated sulfuric acid (18 M, 230 mL). The mixture was carefully stirred in an ice bath (0°C), and potassium permanganate (30 g) was slowly added to the solution to ensure that the temperature did not exceed 20°C . The solution was then heated to 35°C for 30 min. Deionized water (460 mL) was added and the solution was then heated to 98°C for 15 min. A weak hydrogen peroxide solution was then added (3 wt, 710 mL). A series of centrifugation (3200 rpm, 5 min) with repeated deionized water, dilute hydrochloric acid, and ethanol washing produced the GO powder which was vacuum dried at 40°C for 12 h.

Thermal shock graphene powder was obtained through a thermal exfoliation process, in which GO powder (200 mg) was loaded in an argon filled, quartz tube furnace (GSL1100X, MTI, USA) at 1050°C for 30 s [14]. Pristine graphene powder, which demonstrated remarkably high specific surface area and defect concentration was commercially available and purchased from Shanghai Xinchu Energy Technology Co. Ltd. Pristine graphene powder was annealed to reduce the defect concentration, and in turn the specific

surface area, through the use of an electric furnace [15]. By annealing at 3000°C defects were completely eliminated, resulting in a specific surface area reduction from $1272 \text{ m}^2 \text{ g}^{-1}$ for the pristine highly defective graphene to $88.5 \text{ m}^2 \text{ g}^{-1}$ for the defect-free graphene.

Graphene aerogels were synthesized using a hydrothermal process in which a GO solution (3 mg/mL) was heated in an autoclave at 120°C for 10 h to produce a graphene hydrogel [16]. The hydrogel was then freeze-dried overnight to produce the final aerogel.

2.2. Iodine uptake

The graphene powders with different defect concentrations and surface areas samples were exposed to a saturated iodine environment through the use of a desiccator, in which solid iodine crystals were placed in lieu of the desiccant. Iodine uptake was determined through the change in mass of the tested samples before and after exposure to the saturated iodine environment. Due to the sublimation of iodine, the chamber quickly reached a saturated state, which helped drive the adsorption of $\text{I}_{2(\text{g})}$ to reach the maximum sorption capacity within reasonable times. Exposure to a saturated-iodine environment allows for simple comparison of graphene to other sorbent materials currently being considered for iodine capture [17]. The iodine uptake experiment in a saturated iodine environment was also performed on graphene aerogel.

2.3. Characterization techniques

Brunauer–Emmett–Teller (BET) surface area measurements were conducted using a Micromeritics ASAP 2000 instrument. The microstructure of samples was observed with a field-emission SEM on a Zeiss Supra 55. Raman spectroscopy was carried out using a LabRAM HR800 Raman microscope using a 532.18 nm green laser with 600 g-mm^{-1} grating. Thermogravimetric analysis (TGA) was carried out with a TA Instrument (TGA-Q50 instrument), and was utilized as a primary method for confirming the iodine uptake of the samples. TGA was also used to demonstrate the thermal stability of the sorbent, and indicate the temperature threshold for iodine desorption. XPS was conducted using a PHI 5000 Versa Probe system.

3. Results and discussion

Graphene shows great potential as an advanced absorbent material for capturing iodine with an extremely fast adsorption kinetics, as demonstrated by the iodine uptake results of the graphene powders (Fig. 1A). SEM images (Fig. 1B and C) show the morphology of the graphene sheets and the presence of adsorbed iodine on graphene. The iodine in these images appears to adhere to the surface of the graphene, forming discrete particles. The mass gain curve shows an initial stage with a linear iodine uptake rate and very fast adsorption kinetics, followed by a gradual increase until reaching the maximum sorption capacity. The adsorption of iodine on the surface of graphene is further demonstrated

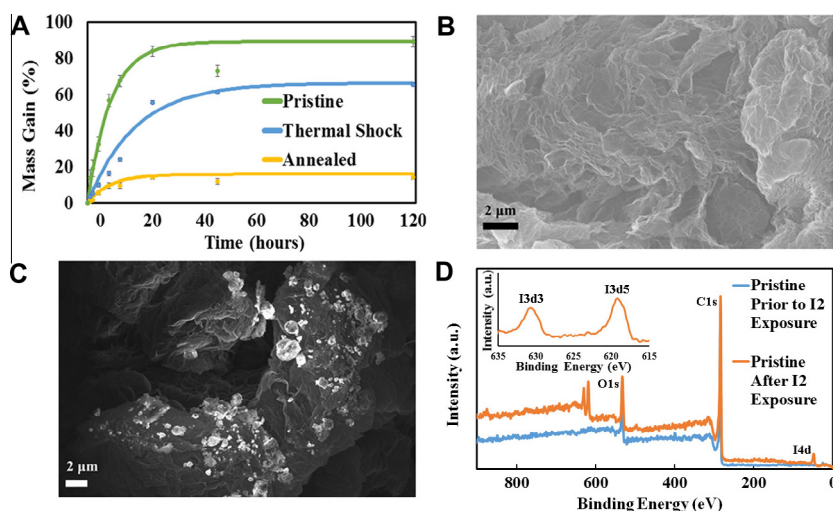


Fig. 1 – Iodine capture by graphene: (A) iodine uptake curves for the investigated graphene powders at 25 °C; (B) SEM image of the pristine highly defective graphene; (C) iodine particulates upon absorbed on the surface of pristine graphene sheets; (D) XPS of pristine graphene before and after I₂ exposure, indicating the presence of adsorbed iodine, XPS of I3d3 and I3d5 peaks (inset). (A color version of this figure can be viewed online.)

by XPS (Fig. 1D and the inset), in which the characteristic peaks of iodine, I3d3, I3d5, and I4d are clearly observed at 630.8, 619.2, and 49.9 eV, respectively. Quantitative analysis of XPS spectra reinforces the iodine uptake findings, with iodine peaks attributed to 45% of the total mass in pristine graphene powders after exposure. The total amount of adsorbed iodine in pristine graphene powders after exposure corresponds to 80% mass gain, consistent with the iodine uptake results.

The linear uptake rate and maximum I₂ sorption capacity for graphene powders with different defect concentrations and surface areas are tabulated in Table 1. A direct relationship between specific surface area (Fig. 2A) and the elemental iodine sorption capacity can be identified. For example, the ‘thermal shock’ graphene (400 m² g^{−1}) displayed a maximum sorption capacity >65%; while the annealed graphene sample (88 m² g^{−1}) displayed a maximum sorption capacity >15%. The exceptional performance of the ‘pristine’ highly defective graphene (1272 m² g^{−1}), with over 80% mass gain within the first 24-h and a maximum sorption capacity exceeding 85%, made it the optimal choice for further investigation regarding the adsorption kinetics. This demonstrates a direct relationship between specific surface area and iodine sorption capacity in graphene powders.

Raman spectroscopy of the samples (Fig. 2B) indicates a direct relationship between the defect concentrations and the specific surface areas of the samples. The pristine highly defective graphene sample, which possessed the highest

specific surface area, displayed the most intense D-band (~1350 cm^{−1}) as compared to its G-band (~1580 cm^{−1}), with an I_D/I_G ratio of 1.32, indicating the highest defect concentration of the samples measured. The thermal shock graphene with specific surface area of 400 m² g^{−1} displays a notable D-band, indicating a significant defect concentration, with an I_D/I_G ratio of 1.11; while the annealed graphene does not display an observable D-band (I_D/I_G ratio of 0), indicating the elimination of defects due to the heat treatment. The presence of a 2D-band (~2700 cm^{−1}) in annealed graphene indicates a degree of graphitization, further contributing to the reduction in specific surface area. This demonstrates a direct relationship between defect concentration and specific surface area in graphene powders, and by extension a direct relationship between defect concentration and iodine sorption capacity.

The pore size distribution and concentration of the graphene powders (Fig. 2C) followed a similar trend as observed between specific surface area and defect concentration, with pores both increasing the specific surface area and acting as adsorption sites for iodine. This is exemplified through the disparity between the pristine and annealed graphene powders in these categories. The heat treatment effectively eliminates defects and pores from the pristine graphene, resulting in a severe loss of iodine sorption capacity.

The role of functional groups in the physisorption of iodine on graphene powders was also investigated. Differences in functional group concentrations on graphene

Table 1 – Properties and iodine sorption capacities of the investigated graphene powders.

Sample	Specific surface area (m ² g ^{−1})	Carbon to oxygen ratio (C:O)	Defect concentration (I _D /I _G)	Linear uptake rate (%/h)	Maximum I ₂ sorption capacity (%)
Annealed	88.5	44.45	0	1.2 ± 0.1	15.8 ± 1.4
Thermal shock	400	4.52	1.11	2.2 ± 0.2	66.2 ± 0.8
Pristine	1272	5.20	1.32	6.8 ± 0.7	89.2 ± 2.9

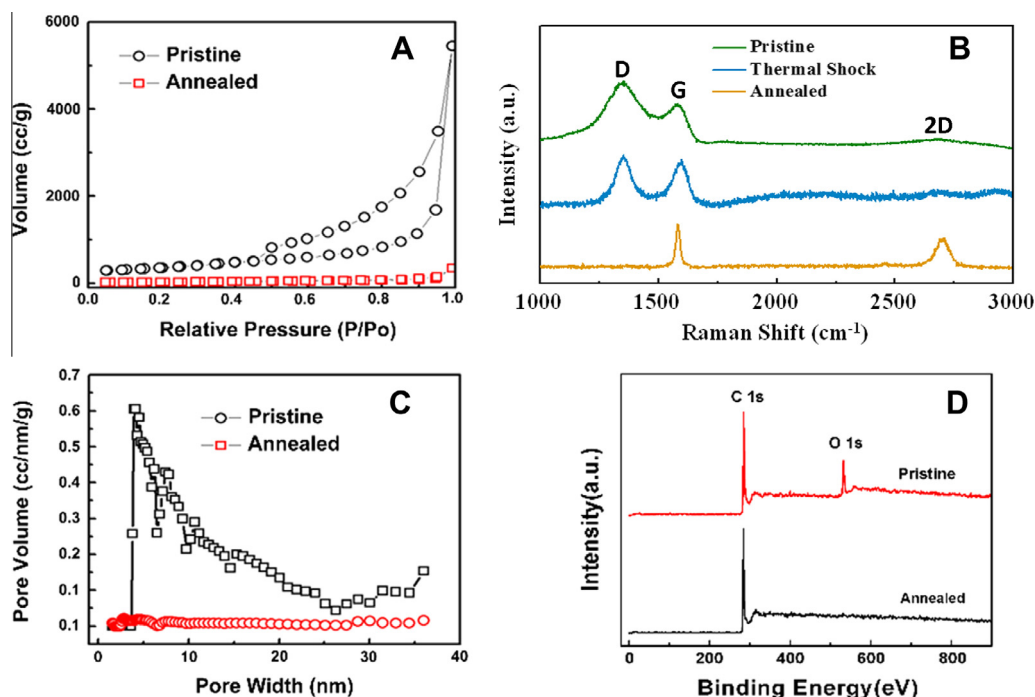


Fig. 2 – Characterization of selected graphene powders. (A) BET surface area analysis (B) Raman spectroscopy (C) pore size distribution (D) XPS. (A color version of this figure can be viewed online.)

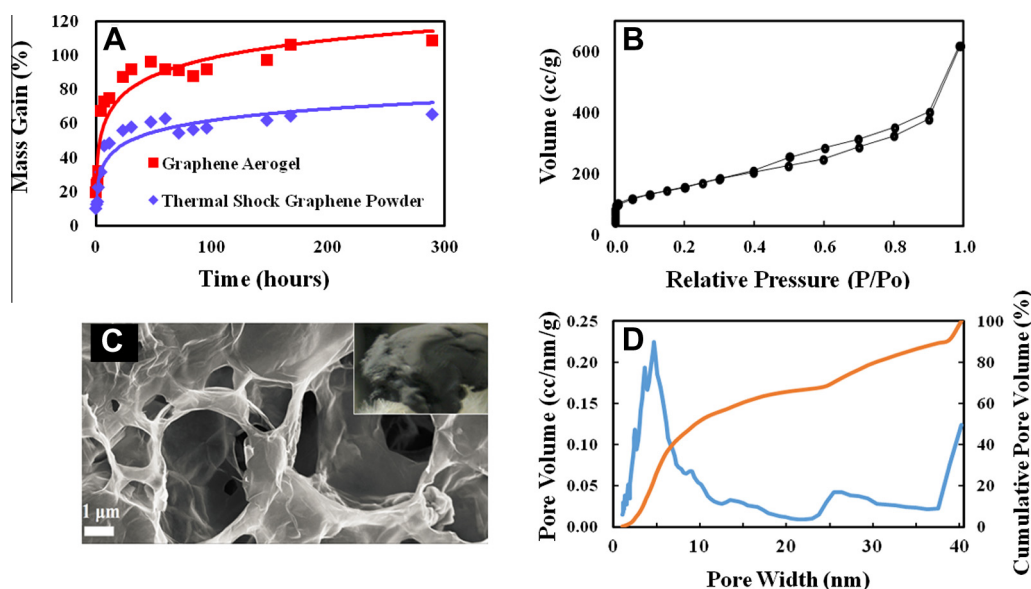


Fig. 3 – (A) Iodine uptake of graphene aerogel as compared to graphene powder; (B) N_2 adsorption-desorption isotherm for graphene aerogel; (C) SEM image of graphene aerogel porous structure, optical image of graphene aerogel (inset); and (D) Pore size distribution of graphene aerogel. (A color version of this figure can be viewed online.)

powders are best observed through their relative carbon and oxygen contents (C:O ratios) obtained via XPS measurements (Fig. 2C). No relationship was observed between oxygen functional group concentration and the rate of iodine uptake or the maximum sorption capacity of iodine, with specific surface area and defects being the primary factors in both the linear uptake rate and the maximum iodine sorption capacity in graphene powders.

By a hydrothermal approach from GO solution, graphene aerogel was prepared and tested as the adsorbent material for iodine capture. Graphene aerogels have demonstrated an improved iodine sorption capacity ($>100\%$ mass gain) as compared with pristine graphene powders with a high specific area ($1272\text{ m}^2\text{ g}^{-1}$), and thermal shock graphene powders ($400\text{ m}^2\text{ g}^{-1}$) [18]. (See the iodine uptake curve for graphene aerogel in Fig. 3A). BET measurement (Fig. 3B) of graphene

aerogel also show a very high surface area up to ($508 \text{ m}^2 \text{ g}^{-1}$), suggesting great potential of graphene aerogel as an advanced absorbent materials. The increased iodine sorption capacity observed in graphene aerogel despite a relatively-lower specific surface area, as compared to pristine graphene, is indicative of a structural factor, attributed to the pore shape and size of the highly porous graphene aerogel (Fig. 3C). Specifically, over 50% of the pore volume and 85% of the pore surface area are contributed by pores under 10 nm in width (see Fig. 3D and Supporting information). This demonstrates while there are larger pores in the aerogel structure, they contribute very little to the overall pore volume and specific surface area of the bulk material. The pore profile for graphene aerogels was best fit by a cylindrical pore non-local density functional theory (NLDFT) equilibrium model, as opposed to the slit pore model the graphene powder samples followed. While surface area and defect concentration may dominate the maximum iodine adsorption capacity and kinetics as determined from the powder samples, the pore size and structure may affect the iodine adsorption process as well, in which a dedicated balance between iodine adsorption and desorption is achieved under the saturated testing environment. The macropores of the graphene aerogel enable rapid diffusion of the gas molecules such that large surface area of the aerogel can be accessible. On the other hand, the dominate mesopores less than 10 nm may help to confine adsorbed iodine, consistent with the thermal stability testing of the iodine-loaded samples. The unique pore structure (meso- and micron-pores) is thought to improve not only the maximum sorption capacity of iodine, but the thermal stability of adsorbed iodine, while maintaining identical sorption kinetics at the initial stage as observed in graphene powders.

We further studied the effects of temperature on iodine uptake capacity and adsorption kinetics (see Fig. 4) of the graphene powders. No significant change in the maximum iodine uptake capacity was observed at elevated temperatures (Fig. 4A); however significant increases in the sorption rate were observed. The linear sorption rate in pristine graphene powders drastically increased with temperature, with 63.6%/h observed at 70 °C, and 22.8%/h observed at 50 °C, as compared to the 6.8%/h observed at 25 °C. The mass gain upon iodine adsorption also saturated within 4 h at 70 °C. While the uptake rate dramatically increased, the maximum sorption capacity remained unchanged within the experimental error. These results indicate that the effect of temperature on the performance of graphene-based iodine

sorbents is primarily on the sorption kinetics in which greatly-enhanced adsorption kinetics occurs for iodine uptake with increased temperature. By fitting the linear iodine uptake rates to Arrhenius' equation [19]:

$$k = Ae^{-E_a/RT} \quad (1)$$

where k is the linear sorption rate, A is the pre-exponential factor, E_a is the activation energy, R is the universal gas constant, and T is the temperature. The apparent activation energy of iodine adsorption can be determined by plotting $\ln(k)$ against $1/T$ (as shown in Fig. 4B):

$$\ln k = -\frac{E_a}{R} \frac{1}{T} + \ln A \quad (2)$$

This enables the graphical determination of the apparent activation energy, calculated to be 70.63 kJ/mole. Incorporating the energy release associated with iodine's deposition (61.1 kJ/mole) yielded a total adsorption energy (E_{ads}) of 131.73 kJ/mole (1.365 eV/ I_2). This value is in excellent agreement with density functional theory (DFT) calculations on the iodine-graphene system, which found the E_{ads} to be between 1.21 and 1.265 eV [20,21]. This also agrees with prior work, stating the iodine-graphene interaction has an ionic contribution, and is caused by charge transfer between the iodine and graphene [22].

The weight gain of the iodine-loaded graphene samples and their thermal stability were further tested by TGA (Fig. 5). A weak bonding between the I_2 molecules and the graphene structure can be identified, which reinforces the asserted physisorption of the I_2 on the powders. The sharp mass losses before 200 °C agree with prior DFT calculations on graphene-halogen adsorption, indicating a dependence on *van der Waals* forces to stabilize the system despite having a significant ionic contribution [21]. The weight loss is consistent with the iodine uptake results (Fig. 1). This may limit the practicality of implementation of unfunctionalized graphene powders as absorbents in waste streams below a temperature of 200 °C for iodine capture.

The enhanced thermal stability of graphene aerogels as demonstrated by TGA results (Fig. 5B) suggest the same mechanisms improving the sorption capacity allow for enhanced retention of physisorbed iodine, in which the highly-confined meso-pores in the three-dimensional macroscopic graphene aerogels allows the confinement of adsorbed iodine. The most notable feature of this TGA curve is the lack of a decisive iodine release temperature, a significant departure from the sharp mass losses before 200 °C observed in

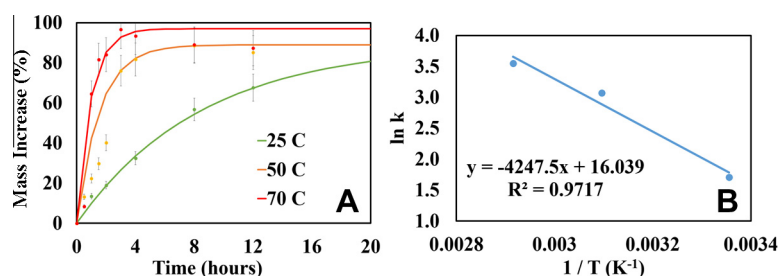


Fig. 4 – (A) Iodine uptake of pristine graphene at elevated temperatures (B) Arrhenius plot of I_2 uptake. (A color version of this figure can be viewed online.)

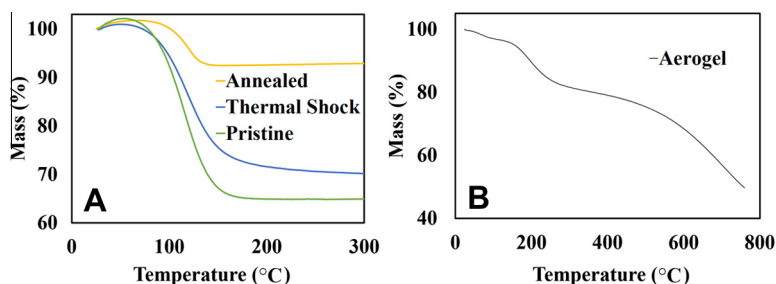


Fig. 5 – Thermogravimetric analysis for (A) graphene powders (B) graphene aerogels. (A color version of this figure can be viewed online.)

powdered samples. The lack of a temperature for major iodine release suggests another mechanism for the capture of physisorbed iodine in graphene aerogels. The mass decrease to 80% demonstrates a loss similar to that observed in powders, but the gradual decrease from 200 °C to 500 °C may demonstrate the migration of iodine contained in the mesoporous structure; while the more significant release of iodine occurs within the temperature range of 500–750 °C.

Upon the capture of iodine off-gas from the spent fuel processing plant, it is of necessity to confine the iodine into durable waste forms for direct deposition. At first glance, the weak bonding observed with graphene powders and the nature of physisorption present a challenge in direct consolidation of the iodine-absorbed graphene into a durable waste form material. However, the exceptional maximum sorption capability and extremely fast kinetics present a unique opportunity of using graphene-based materials as absorbents for capturing iodine not only for direct consolidation, but as an intermediate storage medium for ^{129}I in spent nuclear fuel reprocessing systems. The physisorption of the iodine potentially allows the recycling of the graphene absorbent at relatively low temperature (<200 °C). Due to the relatively low temperature of iodine release, it is expected that graphene will retain its high specific surface area without undergoing graphitization which occurs at temperatures exceeding 600 °C. This would allow for use in other waste forms, such as lead orthovanadophosphate – iodoapatite ceramics, which may have precursors less suitable for spent nuclear fuel reprocessing systems [23,24].

Another possibility is to encapsulate the iodine-loaded graphene into a proven durable ceramic matrix such as apatite [25]. While the incorporation of iodine loaded graphene into a ceramic matrix would prove difficult for conventional densification techniques, novel densification and consolidation techniques such as field-assisted sintering technologies, *e.g.*, spark plasma sintering (SPS), may allow for iodine incorporation into apatite ceramic matrix with minimal iodine loss. This has been demonstrated in our previous work related to iodine waste forms [23,26]. Iodine confinement in a durable ceramic matrix, such as apatite, is a promising path for this work. Recently, our group has decreased the densification temperature of lead vanadate iodoapatite to 350 °C highlighting the possibility of iodine retention during the incorporation into a durable ceramic matrix. The

consolidation of the iodine-loaded graphene into the durable apatite matrix is currently under exploration and will be reported separately.

This work differs from the previously mentioned approaches to ^{129}I management in that it relies on the physisorption of the gaseous iodine; whereas other approaches such as silver-exchanged-zeolites, silver-functionalized aerogels, and chalcogen-based aerogels utilize chemisorption or a chemical affinity for iodine to capture ^{129}I . Despite this lack of chemical affinity for binding with iodine, this approach enables significant mass loadings, as demonstrated in Table 2, up to 51 wt % in graphene aerogels, as compared to the 32 wt % in silver-functionalized silica aerogels, and 68 wt % demonstrated in chalcogen aerogels [17,27]. The improvement in I_2 sorption capacity demonstrated over silver-based materials are encouraging to the elimination of silver from iodine sorbent materials. It should be noted that while chalcogen aerogels outperformed graphene aerogels in their maximum I_2 sorption capacities, the fabrication of such materials may prove difficult for large scale production, in addition to issues associated with consolidation into a durable waste form.

Due to the comparable I_2 sorption capacities of the graphene-based sorbents, further investigation into the capture efficiency and associated decontamination factor (DF), defined as the amount of iodine present upstream from the sorbent divided by the amount of iodine downstream from the sorbent, should be conducted to determine if graphene-based sorbents are compliant with EPA regulations regarding breakthrough efficiency and decontamination factor.

Further work regarding graphene-based iodine sorbents should consider the densification of sorbents into durable waste forms, in addition to the performance of sorbents in adsorption beds to meet EPA regulations regarding breakthrough efficiency. Graphene aerogels are expected to perform well in these aspects due to their high mass loadings, physical stability, and impressive thermal stability which may be further enhanced when coupled with novel densification techniques such as spark plasma sintering. This uptake in combination with the rapid sorption kinetics makes graphene-based materials promising candidates for further iodine sorption tests including deep-bed sorption, functionalization, and waste form consolidation.

Table 2 – Comparison of iodine-129 sorbent materials capacities and decontamination factors.

Sorbent material	Maximum I ₂ content (wt %)	Decontamination factor (DF)
Pristine graphene powder	45	–
Graphene aerogel	51	–
SnS chalcogel	68	250–500
Ag-exchanged mordenite	17	10 ² –10 ⁵
Ag-functionalized silica aerogel	32	10 ⁴

4. Conclusion

In summary, we report graphene-based materials as novel absorbents for iodine absorption with exceptional maximum iodine uptake capacity and kinetics. A direct correlation among specific surface area, defects and I₂ sorption capacity has been demonstrated through uptake experiments. Defects in the graphene structure may act as potential binding sites for the physisorption of iodine on the surface of graphene sheets. Temperature has been shown to have a direct relationship with the iodine sorption kinetics, with increasing temperature significantly increasing the iodine uptake rate, while having little-to-no impact on the maximum sorption capacity of the graphene. Due to the exceptional iodine sorption capacity demonstrated, graphene-based materials particularly graphene aerogels, are well-suited for further development as ¹²⁹I sorbents. The high iodine mass gain (over 100 wt %), improved physical stability as compared to graphene powders, and the enhanced thermal stability well above the boiling point of iodine (184.3 °C) make graphene aerogel a promising candidate for iodine capture and sequestration from spent nuclear fuel reprocessing systems.

Acknowledgments

This work was financially supported by DOE NEUP (Nuclear Engineering University Program) under award DE-AC07-05ID14517 (iodine adsorption experiment) and a NSF award DMR 1151028 (synthesis of graphene-based absorbents and structural characterization).

Appendix A. Supplementary data

Supplementary data associated with this article can be found, in the online version, at <http://dx.doi.org/10.1016/j.carbon.2015.03.070>.

REFERENCES

- [1] Croff A, Alexander C. Decay characteristics of once-through LWR and LMFBR spent fuels, high-level wastes, and fuel-assembly structural material wastes. Oak Ridge National Laboratory, ORNL/TM-7431; 1980.
- [2] Whitehead D. The distribution and transformations of iodine in the environment. *Environ Int* 1984;10(4):321–39.
- [3] Kelly J. Assessment of the technical basis of 40CFR190. 40CFR190 Briefing, Sandia National Laboratory, March 2009;25:9.
- [4] Todd T, Vienna J. Separations and waste forms campaign implementation plan. Pacific Northwest National Laboratory, PNNL-21453; 2012.
- [5] Haefner DR, Tranter TJ. Methods of gas phase capture of iodine from fuel reprocessing off-gas: a literature survey. Idaho National Laboratory, INL/EXT-07-12299; 2007.
- [6] Chapman KW, Chupas PJ, Nenoff TM. Radioactive iodine capture in silver-containing mordenites through nanoscale silver iodide formation. *J Am Chem Soc* 2010;132(26):8897–9.
- [7] Matyas J, Fryxell G, Busche B, Wallace K, Fifield L. Functionalised silica aerogels: advanced materials to capture and immobilise radioactive iodine. *Ceramic Engineering and Science Proceedings: American Ceramic Society Inc*, 735 Ceramic Place Westerville OH 43081 United States; p. 23–32.
- [8] Riley BJ, Chun J, Um W, Lepry WC, Matyas J, Olszta MJ, et al. Chalcogen-based aerogels as sorbents for radionuclide remediation. *Environ Sci Technol* 2013;47(13):7540–7.
- [9] Schedin F, Geim A, Morozov S, Hill E, Blake P, Katsnelson M, et al. Detection of individual gas molecules adsorbed on graphene. *Nat Mater* 2007;6(9):652–5.
- [10] Zhu Y, Murali S, Cai W, Li X, Suk JW, Potts JR, et al. Graphene and graphene oxide: synthesis, properties, and applications. *Adv Mater* 2010;22(35):3906–24.
- [11] Zhang Y-H, Chen Y-B, Zhou K-G, Liu C-H, Zeng J, Zhang H-L, et al. Improving gas sensing properties of graphene by introducing dopants and defects: a first-principles study. *Nanotechnology* 2009;20(18):185504–11.
- [12] Dai J, Yuan J, Giannozzi P. Gas adsorption on graphene doped with. *Appl Phys Lett* 2009;95(23).
- [13] Hummers Jr WS, Offeman RE. Preparation of graphitic oxide. *J Am Chem Soc* 1958;80(6):1339.
- [14] McAllister MJ, Li J-L, Adamson DH, Schniepp HC, Abdala AA, Liu J, et al. Single sheet functionalized graphene by oxidation and thermal expansion of graphite. *Chem Mater* 2007;19(18):4396–404.
- [15] Jin M, Kim TH, Lim SC, Duong DL, Shin HJ, Jo YW, et al. Facile physical route to highly crystalline graphene. *Adv Funct Mater* 2011;21(18):3496–501.
- [16] Xu Y, Sheng K, Li C, Shi G. Self-assembled graphene hydrogel via a one-step hydrothermal process. *ACS Nano* 2010;4(7):4324–30.
- [17] Strachan DM, Chun J, Matyas J, Lepry WC, Riley BJ, Ryan JV, et al. Summary report on the volatile radionuclide and immobilization research for FY2011 at PNNL: Environmental Molecular Sciences Laboratory, Pacific Northwest National Laboratory, Richland, WA (United States). Funding organisation: US Department of Energy (United States); 2011.
- [18] Worsley MA, Pauzauskie PJ, Olson TY, Biener J, Satcher Jr JH, Baumann TF. Synthesis of graphene aerogel with high electrical conductivity. *J Am Chem Soc* 2010;132(40):14067–9.
- [19] Laidler KJ. The development of the Arrhenius equation. *J Chem Educ* 1984;61(6):494–8.

-
- [20] Klintenberg M, Lebegue S, Katsnelson M, Eriksson O. Theoretical analysis of the chemical bonding and electronic structure of graphene interacting with Group IA and Group VIIA elements. *Phys Rev B* 2010;81(8):085433. 5pp.
- [21] Medeiros PV, Mascarenhas AJ, de Brito Mota F, de Castilho CMC. A DFT study of halogen atoms adsorbed on graphene layers. *Nanotechnology* 2010;21(48):485701–8.
- [22] Rudenko A, Keil F, Katsnelson M, Lichtenstein A. Adsorption of diatomic halogen molecules on graphene: a van der Waals density functional study. *Phys Rev B* 2010;82(3):03542. 7pp.
- [23] Yao T, Lu F, Sun H, Wang J, Ewing RC, Lian J. Bulk iodoapatite ceramic densified by spark plasma sintering with exceptional thermal stability. *J Am Ceram Soc* 2014;97(8):2409–12.
- [24] Lu F, Yao T, Xu J, Wang J, Scott S, Dong Z, et al. Facile low temperature solid state synthesis of iodoapatite by high-energy ball milling. *RSC Adv* 2014;4(73):38718–25.
- [25] Guy C, Audubert F, Lartigue J-E, Latrille C, Advocat T, Fillet C. New conditionings for separated long-lived radionuclides. *CR Phys* 2002;3(7):827–37.
- [26] Matyáš J, Engler R. Assessment of methods to consolidate iodine-loaded silver-functionalized silica aerogel. Pacific Northwest National Laboratory, PNNL-22874; 2013.
- [27] Riley BJ, Pierce DA, Chun J, Chun J, Matyáš J, Lepry WC, Garn TG, et al. Polyacrylonitrile–chalcogel hybrid sorbents for radioiodine capture. *Environ Sci Technol* 2014;48(10):5832–9.

Radiation Stability of Spark-Plasma-Sintered Lead Vanadate Iodoapatite

Fengyuan Lu,^{‡,†} Tiankai Yao,[§] Yaron Danon,[§] Jianren Zhou,[‡] Rodney C. Ewing,[¶] and Jie Lian^{§,†}

[‡]Department of Mechanical and Industrial Engineering, Louisiana State University, Baton Rouge, Louisiana 70803

[§]Department of Mechanical, Aerospace, and Nuclear Engineering, Rensselaer Polytechnic Institute, Troy, New York 12180

[¶]Department of Geological & Environmental Sciences, Stanford University, Stanford, California 94305-2115

Spark-plasma-sintered lead vanadate iodoapatite $\text{Pb}_{9.85}(\text{VO}_4)_6\text{I}_{1.7}$, a promising nuclear waste form for the immobilization of I-129, was irradiated with energetic ions, electrons, and gamma rays, to investigate its radiation stability. *In situ* TEM observation of the 1 MeV Kr^{2+} irradiation shows that lead vanadate iodoapatite generally exhibits higher tolerance against ion irradiation-induced amorphization than lead vanadate fluorapatite, and the spark plasma sintering can further enhance its radiation stability attributed to the enhanced crystallinity, reduced defect concentration, and denser microstructure. The critical amorphization dose and critical temperature for the SPS-densified iodoapatite at 700°C are determined to be 0.25 dpa at room temperature and 230°C, respectively. No significant phase transformation or microstructural damage occurred under energetic electron and gamma irradiations. Raman spectra of gamma-ray-irradiated iodoapatite indicate improved V–O bond order at 500 kGy dose. Generally, the spark-plasma-sintered iodoapatite exhibits excellent radiation stability for nuclear waste form applications. The significantly enhanced radiation stability of the SPS-densified iodoapatite suggests that SPS holds great promise for fabricating iodoapatite waste form with minimum iodine loss and optimized radiation tolerance for effective management of highly volatile I-129.

I. Introduction

THE management of radioactive wastes, particularly the long-lived actinides such as Pu, Np, and Am, and various types of fission products (FP) such as Cs-135, Sr-90, and I-129, is crucial to the development of safe nuclear energy. The volatile I-129 is a particularly troublesome FP due to its high mobility, volatility, and extremely long half-life of 15.7 million years, which requires a specially designed waste form for its long-term immobilization and disposal in geological repositories. The apatite structure-type $\text{A}^{\text{I}}_4\text{A}^{\text{II}}_6(\text{BO}_4)_6\text{X}_2$ (A^{I} , A^{II} = alkali, alkaline earths, rare earths, fission products, or actinides, B = Si, P, V, or Cr, and X = OH, O, or halogens) has an open-frame structure, in which six equivalent BO_4 tetrahedra are corner-connected to AO_6 metaprism columns to form one-dimensional tunnels that can accommodate large anionic species, such as iodine. Its high structural flexibility and excellent chemical durability make it a promising host phase for the immobilization of a wide range of radionuclides, especially the volatile I-129.^{1–3} Extensive efforts have been made to effectively incorporate I-129^{1,4–6}

and several other FPs^{7–9} and actinides^{10–15} into the apatite structure for long-term geological disposal.

Lead vanadate iodoapatite $\text{Pb}_{10}(\text{VO}_4)_6\text{I}_2$, whose large A- and B-site atoms of Pb and V enable high loading of iodine anions in the tunnel, is a particularly suitable waste form candidate for the immobilization of I-129, along with other FPs and actinides. As a result, various experimental methods have been adopted to fabricate iodoapatite with purpose of improving I-129 waste management.^{1,4,6,16,17} Due to the high mobility of iodine, the stability of the incorporated I-129 in the lead vanadate iodoapatite is of particular concern because the complex thermal and radiation environment of the waste form could potentially cause the release of I-129 to the surrounding environment. The iodine leaching rates in iodoapatite fabricated by conventional hot-pressing method were reported to be either higher than or comparable to AgI glass waste form.^{18,19} Recently, a fabrication method combining low-temperature high-energy ball milling (HEBM) synthesis and spark plasma sintering (SPS) consolidation has been reported, which significantly reduces iodine loss during fabrication and greatly improves the thermal stability of the iodoapatite.^{16,17} Specifically, as compared with previously reported methods, the HEBM synthesis method exhibits lower crystallization temperature, improved thermal stability, a higher decomposition temperature, and excellent iodine confinement for the iodoapatite.¹⁶ The SPS consolidation further improves the thermal stability of the bulk iodoapatite, such that the structure remains highly stable up to a high temperature of 670°C, and the complete iodine loss does not occur until a very high temperature of 800°C is reached.¹⁷

The apatite-based nuclear waste form can incorporate a wide range of radionuclides including Pu-239, Am-241, Np-237, Sr-90, Tc-99, Cs-135, Cs-137, and I-129.^{1,8,9,11,15} These radionuclides decay in different modes that generate energetic alpha-particles and alpha-recoils (in actinides), beta particles (in most FPs), and gamma rays (in FPs like I-129 and Cs-137), which can create complex radiation environments in the waste form. Considering the extremely long period required for geological disposition, the accumulation of radiation damage could potentially amorphize iodoapatite, reduce its durability and cause the release of the incorporated radionuclides,²⁰ particularly the volatile I-129. Therefore, the radiation tolerance of iodoapatite must be carefully evaluated. The radiation stability of various apatite compositions has been investigated previously, including natural F-rich apatite,²¹ oxyapatite,^{22–24} hydroxyapatite,²⁵ and fluorapatite.^{25–27} However, the radiation stability of the I-129-bearing iodoapatite waste form has not been investigated. In this work, systematic irradiation experiments on the HEBM-synthesized and SPS-densified iodoapatite samples were performed to simulate the radiation effects caused by alpha, beta, and gamma decays, and the phase stability of the samples under the different radiation conditions was studied for evaluating their long-term performance as nuclear waste forms. The results show significantly enhanced radiation sta-

W. E. Lee—contributing editor

Manuscript No. 36582. Received March 17, 2015; approved May 31, 2015.

[†]Authors to whom correspondence should be addressed. e-mails: luf@lsu.edu and lianj@rpi.edu

bility in SPS-densified iodoapatite, indicating that SPS holds great promise for optimizing the fabrication of iodoapatite waste form with minimum iodine loss and maximized radiation tolerance.

II. Experimental Procedure

(1) Sample Preparation

Iodoapatite powders were prepared using low temperature ($\sim 50^\circ\text{C}$) HEBM-induced solid-state synthesis in a Fritsch Pulverisette 7 Premium Line planetary ball mill, as described in a previous report.¹⁶ The starting powder ingredients of PbI_2 , PbO , and V_2O_5 were ball-milled by 2-mm-sized ZrO_2 balls at 500 rpm for 20 h to form iodoapatite $\text{Pb}_{9.85}(\text{VO}_4)_6\text{I}_{1.7}$, which has a minor iodine deficiency and hence a slight deviation from the ideal stoichiometry of $\text{Pb}_{10}(\text{VO}_4)_6\text{I}_2$. The as-milled iodoapatite samples existed in the form of nanocrystals, mostly 4–10 nm in size, embedded in an amorphous matrix. The subsequent 1-hour heat treatment at 300°C resulted in a significant crystallization of the amorphous matrix and grain coarsening to 30–50 nm in size [shown in Fig. 1(a)], which exhibits a high iodine loading (>8 wt%) and greatly improved thermal stability, as compared with conventionally high-temperature-sintered iodoapatite.^{1,18,19,28} This ball-milled and heat-treated sample is denoted by BM-300C. Consolidation of the thermally treated iodoapatite powders was achieved by SPS with a very high heating rate of $200^\circ\text{C}/\text{min}$ and a short temperature holding time of 1 min at the maximum temperature of 700°C ,¹⁷ and the consolidated sample is denoted by SPS-700C. Such a fast heating rate and short sintering duration enable the maintenance of the chemical composition and structure of the lead vanadate apatite without iodine loss, which usually occurs at this high-temperature range.

(2) Irradiation Experiments

The irradiations of the iodoapatite samples were carried out in three different ways: energetic ion irradiation, electron

irradiation, and gamma ray irradiation. Energetic 1 MeV Kr^{2+} irradiation was utilized to simulate the radiation damage caused by the alpha decay events of the incorporated actinides in apatite waste forms. Generally, alpha decay is the radiation source of greatest concern, because it is responsible for the major radiation damages in ceramic waste forms, such as radiation-induced amorphization and phase separation that have direct impact on the retention of the incorporated radionuclides, especially the highly mobile I-129. The 1 MeV Kr^{2+} irradiation was conducted using the IVEM-Tandem facility at Argonne National Laboratory, which combines a Hitachi H-9000NAR transmission electron microscope (TEM) with ion accelerators to allow *in situ* TEM observation of the radiation damage process. The SPS-700C sample was ground and dispersed on a carbon-coated TEM grid, before loaded in the TEM and irradiated by 1 MeV Kr^{2+} , and the radiation-induced phase change was closely monitored by selected area electron diffraction (SAED). During ion irradiations, the TEM electron beam was intentionally turned off to minimize the electron irradiation effects. The BM-300C powder sample was also irradiated and monitored in the same manner for comparison. A TEM heating stage was used for irradiations at elevated temperatures, to obtain the temperature dependence of the radiation-induced amorphization. The Kr^{2+} fluences were converted into the universal displacive radiation damage unit of displacements per atom (dpa) by the SRIM 2008 program using a displacement energy (E_d) of 50 eV for all the atoms, as previously suggested by other studies based on theoretical calculations.^{24,26,29}

To simulate the effects of beta decay on iodoapatite, 200 keV, electron irradiations were conducted using the focused electron beam and monitored in the same TEM. Gamma irradiation was conducted on the SPS-densified pellets using the LINAC facility at Rensselaer Polytechnic Institute, where a gamma ray with a continuous energy spectrum in the MeV range was generated by deceleration (Bremsstrahlung) of a 15 MeV electron beam by a metal target,

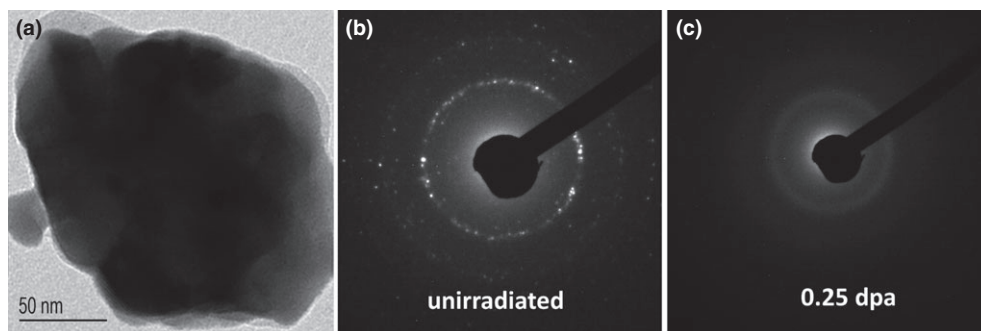


Fig. 1. (a) A bright-field TEM image of the nanocrystalline BM-300C; (b) SAED pattern showing the diffraction rings of the unirradiated BM-300C; (c) SAED pattern showing the amorphous halo of the BM-300C at irradiated by 1 MeV Kr^{2+} to 0.25 dpa at room temperature.

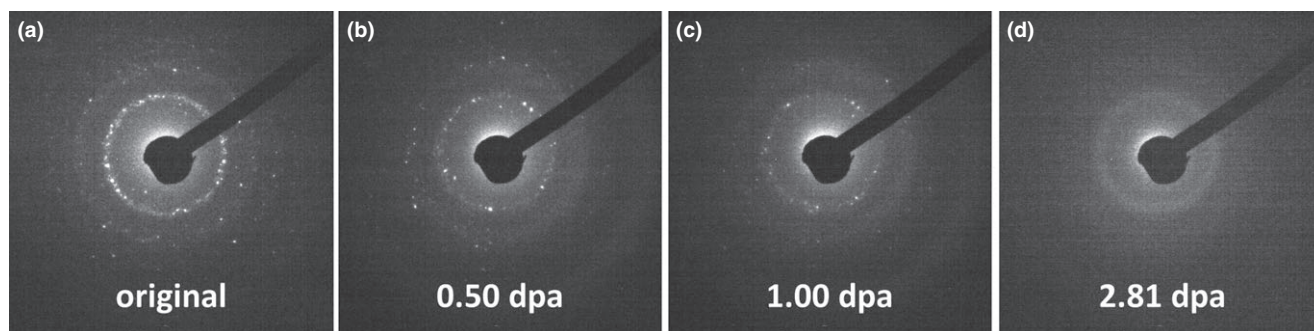


Fig. 2. A sequence of SAED patterns showing the 1 MeV Kr^{2+} irradiation-induced amorphization process of BM-300C at 513 K: (a) unirradiated crystalline sample; (b) 0.50 dpa; (c) 1.00 dpa; (d) complete amorphization at 2.81 dpa.

with doses up to 500 kGy, a level known to cause structural, microstructural and property changes in ceramic nuclear wastes.^{30–32} *Ex situ* X-ray diffraction (XRD) and Raman spectroscopy were conducted on the gamma-ray-irradiated iodoapatite samples to determine the radiation effects.

III. Results and Discussion

(1) Ion Irradiation

The highly flexible, open frame structure of apatite allows the incorporation of not only the voluminous I-129, but also various actinides and FPs in the structure to achieve a very high waste loading. When actinides are incorporated, their alpha decay events will cause damage to the apatite host phase mainly through elastic collisions and displacements of the lattice atoms. In extreme cases, under long-term alpha decay irradiations, the originally crystalline apatite waste form can undergo a crystalline-to-amorphous transformation, which may lead to increased migration and eventual release of radionuclide, especially I-129. Such displacive radiation-induced amorphization have been reported in a wide range of ceramic waste forms like monazite,^{33,34} pyrochlore,^{35,36} garnet,^{37,38} and zircon.^{34,39} Recent studies have revealed that the radiation tolerance of crystalline ceramics depends on various factors including chemical composition,^{26,35} structural ordering,⁴⁰ grain size,^{33,41} and radiation condition.^{22,42} The purpose of the 1 MeV Kr²⁺ irradiation experiments is to investigate the radiation stability of the SPS-consolidated iodoapatite samples and determine the underlying factor that contributes to the radiation tolerance. The two iodoapatite sample types of BM-300C and SPS-700C were irradiated at different temperatures

and the data were compared, to determine the effect of SPS on the radiation stability of iodoapatite.

Under 1 MeV Kr²⁺ irradiation at room temperature, BM-300C underwent a radiation-induced amorphization as the irradiation dose reached a critical dose (D_c) of 0.25 dpa (1×10^{14} ions/cm²). As shown in the SAED patterns in Figs. 1(b) and (c), before irradiation, the SAED pattern of BM-300C shows clear diffraction rings from the 30–50-nm-sized nanocrystalline particles [Fig. 1(b)]; at 0.25 dpa, the diffraction rings completely disappeared and the diffuse halo appeared [Fig. 1(c)], indicating a completely amorphous state. At elevated temperature, the BM-300C exhibits significant defect annealing, such that the D_c increased dramatically when the temperature exceeded 500 K (227°C). Figure 2 shows a sequence of SAED patterns taken at different irradiation doses at 513 K (240°C), in which the clear diffraction rings from the unirradiated sample [Fig. 2(a)] gradually dimmed upon increasing dose until they were completely replaced by the amorphous halo at a D_c of 2.81 dpa [Figs. 2(b)–(d)], 10 times higher than that at room temperature. The temperature dependence of the critical amorphization dose D_c as shown in Fig. 3 was fit and plotted based on a direct-impact-model-based empirical exponential equation:^{39,43}

$$D_c = \frac{D_0}{1 - \exp\left[\left(\frac{E_a}{k}\right)\left(\frac{1}{T_c} - \frac{1}{T}\right)\right]}$$

where D_0 is the critical amorphization dose extrapolated at $T = 0$ K, E_a is the activation energy for defect annealing, and T_c is the critical amorphization temperature. The physical meaning of T_c is the upper temperature limit for the radiation-induced amorphization to occur. When the temperature exceeds T_c , all of the defects induced by irradiation can be annealed such that complete amorphization cannot occur. Therefore, T_c can also be used to indicate the radiation tolerance of materials, of which a lower T_c usually implies higher defect annealing capabilities at elevated temperatures and hence greater tolerance against radiation-induced amorphization. The temperature dependence curve of D_c for the BM-300C sample is plotted in Fig. 3, and its T_c is determined as 515 K. This T_c is confirmed by irradiation experiment conducted at 523 K, merely 8 K higher than the T_c , in which no complete amorphization was observed even at a high dose of 6.25 dpa.

The lead vanadate iodoapatite $\text{Pb}_{9.85}(\text{VO}_4)_6\text{I}_{1.7}$ BM-300C exhibits significantly higher radiation tolerance than the previously reported isostructural calcium and lead vanadate fluorapatite $(\text{Pb}_x\text{Ca}_{1-x})_{10}(\text{VO}_4)_6\text{F}_2$.²⁶ As a comparison, the temperature dependence curve of D_c of calcium vanadate fluorapatite $\text{Ca}_{10}(\text{VO}_4)_6\text{F}_2$ is also plotted in Fig. 3, showing a lower room temperature D_c of 0.21 dpa and a higher T_c of 603 K. As the radiation tolerance of $(\text{Pb}_x\text{Ca}_{1-x})_{10}(\text{VO}_4)_6\text{F}_2$ decreases with increasing Pb content,²⁶ it is apparent that

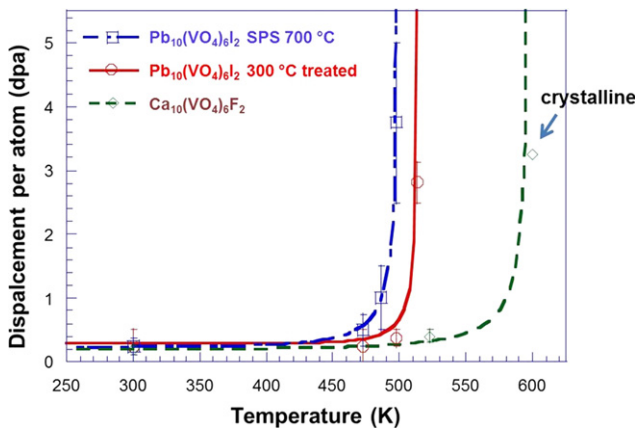


Fig. 3. Temperature dependence curves of D_c for SPS-700C, BM-300C and the previously reported $\text{Ca}_{10}(\text{VO}_4)_6\text{F}_2$,²⁶ showing a decreasing radiation tolerance from left to right. The open diamond on the far right side indicates that $\text{Ca}_{10}(\text{VO}_4)_6\text{F}_2$ is still crystalline at this point.

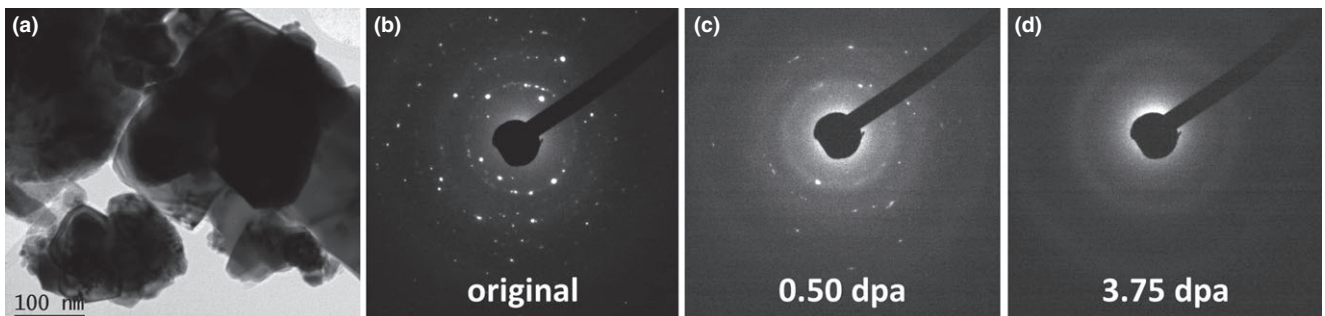


Fig. 4. (a) A bright TEM image of powders mechanically ground from dense SPS-700C; (b–d) sequence of SAED patterns showing the 1 MeV Kr²⁺ irradiation-induced amorphization of SPS-700C at 498 K: (b) unirradiated crystalline SPS-700C, (c) SPS-700C irradiated to 0.50 dpa; (d) complete amorphization of SPS-700C at 3.75 dpa.

lead vanadate iodoapatite $\text{Pb}_{9.85}(\text{VO}_4)_6\text{I}_{1.7}$ is much more radiation tolerant than lead vanadate fluorapatite $\text{Pb}_{10}(\text{VO}_4)_6\text{F}_2$, and the radiation tolerance order is $\text{Pb}_{9.85}(\text{VO}_4)_6\text{I}_{1.7} > \text{Ca}_{10}(\text{VO}_4)_6\text{F}_2 > \text{Pb}_{10}(\text{VO}_4)_6\text{F}_2$. The higher radiation tolerance of iodoapatite than fluorapatite may be attributed to difference in energy loss upon energetic charge particle interaction. The energy loss of the incident ions is mainly due to two mechanisms: the ballistic effect of nuclear energy loss or nuclear stopping power (S_n) which can cause atomic displacements and consequently amorphization of the irradiated crystalline ceramics, and the electronic energy loss or electronic stopping power (S_e), of which a moderate value may benefit the defect recovery process and enhance the radiation tolerance.^{44–46} Therefore, higher ratios of electronic-to-nuclear stopping power (ENSP) may result in higher radiation tolerance. The substitution of iodine for fluorine in the anionic position of apatite leads to a higher ENSP (0.626 vs. 0.613) as estimated by the SRIM-2008 program, which may explain the higher radiation stability occurred in iodoapatite.

The SPS-densification process resulted in improved crystallinity, dense microstructure and a significant grain growth in iodoapatite. The grain size grew from below 10 nm in BM-300C to hundreds of nm or microns in SPS-700C, as shown in Fig. 4(a). SPS-700C also exhibits even higher radiation tolerance than BM-300C. At room temperature, radiation-induced amorphization occurred at 0.25 dpa in SPS-700C, similar to that in BM-300C. However, at elevated temperature, the D_c of SPS-700C increases more dramatically than BM-300C. At 498 K, SPS-700C was not completely amorphized until the dose reached 3.75 dpa, as evidenced by the sequence of SAED patterns taken at different doses in Figs. 4(b)–(d). The irradiation experiments were also carried out at elevated temperatures to obtain a set of D_c data points used to generate a temperature dependence curve plotted in Fig. 3. The T_c of SPS-700C is 502 K, lower than that of BM-300C. A comparison of the radiation response of SPS-700C iodoapatite, BM-300C iodoapatite, $\text{Ca}_{10}(\text{VO}_4)_6\text{F}_2$, and $\text{Pb}_{10}(\text{VO}_4)_6\text{F}_2$ is given in Fig. 3, indicating the radiation stability in the order of $\text{SPS-700C} > \text{BM-300C} > \text{Ca}_{10}(\text{VO}_4)_6\text{F}_2 > \text{Pb}_{10}(\text{VO}_4)_6\text{F}_2$. Further enhancement in the radiation tolerance by SPS is likely attributed to improved crystallinity and structural ordering in the iodoapatite by high-temperature sintering and SPS rapid consolidation.

(2) Electron and Gamma Irradiations

The 200 keV electron beam irradiation was used to simulate the beta decay events associated with the incorporated I-129 and other FPs. As compared to 1 MeV Kr^{2+} , the 200 keV electrons are much less likely to cause atomic displacement cascades in iodoapatite, as the energy is mostly lost to electronic stopping power S_e and ionization in the materials. In some cases, the electron beam irradiation can assist the defect recovery and even facilitate the crystallization and grain growth of displacive-radiation-damaged materials.^{24,33,44} *In situ* TEM observation confirmed that no significant amorphization, phase change or major microstructural damage occurred in the electron beam irradiated BM-300C and SPS-700C TEM samples.

The effects of gamma ray emission on the iodoapatite waste form were investigated by gamma ray irradiation of SPS-700C to different dose levels of 50, 100, and 500 kGy. *Ex situ* XRD patterns of the irradiated SPS-700C showed very little changes even at the highest dose of 500 kGy, indicating that the crystal structure of iodoapatite remained the same. However, Raman spectroscopic analysis revealed subtle changes in the chemical bonding of iodoapatite upon gamma irradiation. Raman spectra of the original and irradiated samples are shown in Fig. 5(a), in which significant changes are found in two regions: one in the higher wave number range 750–850 cm^{-1} associated with the stretching

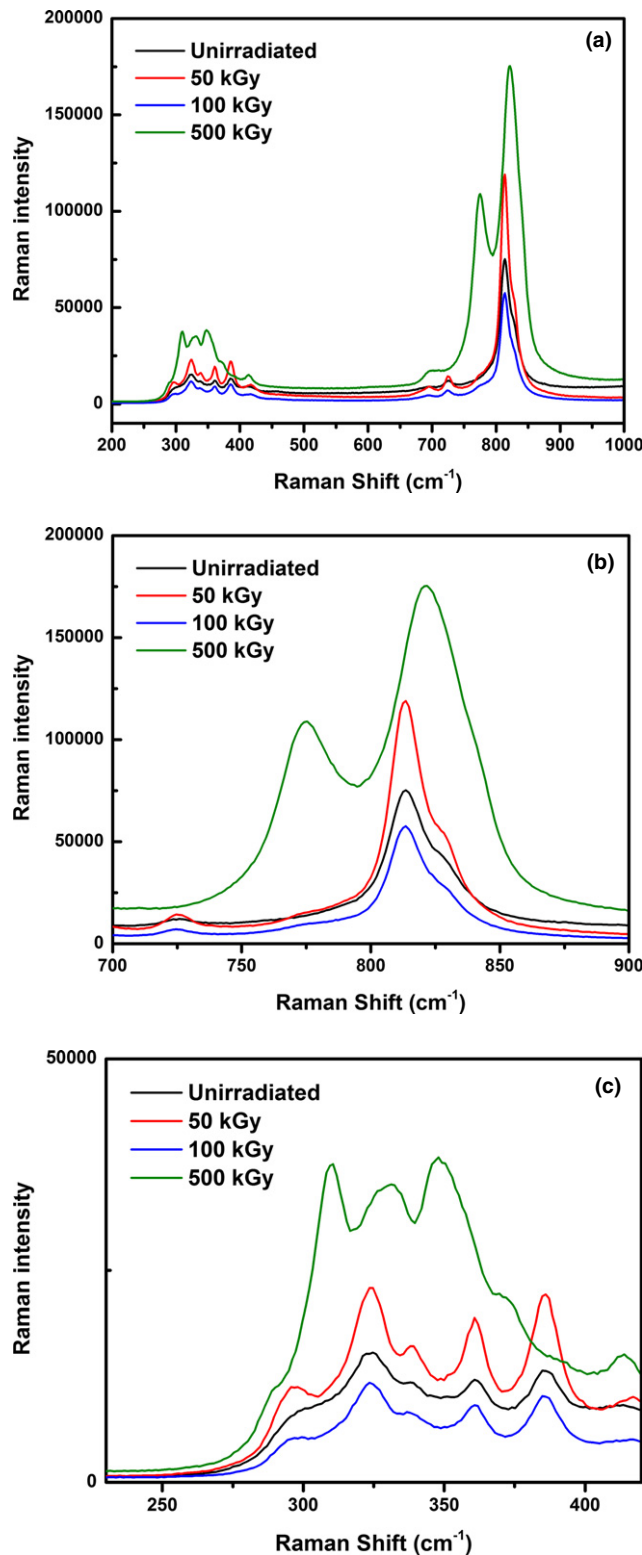


Fig. 5. Raman spectra of the unirradiated SPS-700C and samples irradiated with 50, 100, and 500 kGy gamma ray: (a) overall wave number range 200–1000 cm^{-1} ; (b) higher wave number range 750–850 cm^{-1} ; (c) lower wave number range 300–400 cm^{-1} .

vibration of VO_4 tetrahedra [Fig. 5(b)], and the other in the lower wave number range 300–400 cm^{-1} associated with the bending of the O–V–O bond [Fig. 5(c)].⁴⁷ In Fig. 5(b), the original sample shows the strongest peak centered around 813 cm^{-1} , which is attributed to the A_g symmetric stretching mode of the VO_4 tetrahedra. The E_{2g} asymmetric stretching vibrational peak at 776 cm^{-1} is abnormally low as compared to those previously reported.^{47–49} Upon gamma irradiation,

the changes in the VO_4 stretching modes remained insignificant until the dose reached 500 kGy, when the E_{2g} asymmetric stretching peak at 776 cm^{-1} showed a remarkable increase in intensity by two times, and the A_g symmetric stretching mode shifted from 813 cm^{-1} to a higher wave number of 823 cm^{-1} . By adopting the empirical method presented by Hardcastle and Wachs,⁵⁰ the changes in V–O bond length and bond strength of iodoapatite at the highest gamma ray dose can be related to the shifting of the A_g stretching frequency, and their values were estimated by using the following empirical functions. The bond length R is given in

$$\nu = 21349 \exp(-1.9176R)$$

and the bond strength $s(\text{V–O})$ is given by

$$s(\text{V–O}) = \left[0.2912 \ln \left(\frac{21349}{\nu} \right) \right]^{-5.1}$$

where ν is the vibrational frequency. As the A_g stretching mode shifted from 813 to 823 cm^{-1} , the V–O bond length decreased from 1.704 to 1.698 Å, and the bond strength increased from 1.2876 to 1.3124 vu (vu is the valence unit). As the bond strength indicates the bond order, the vibration frequency shift implies improved iodoapatite V–O bond order upon gamma irradiation. In the lower wave number range in Fig. 5(c), vibrational bands at ~ 305 , 330, and 350 cm^{-1} corresponding to the asymmetric O–V–O bending vibrational modes emerged at the highest dose of 500 kGy. All these changes in the Raman spectra point to a more ordered bonding structure in gamma-irradiated vanadate iodoapatite, which suggests that high dose gamma irradiation may improve the V–O bond order in the SPS-700C sample.

Generally, the systematic ion, electron and gamma irradiations indicate excellent radiation stability of the SPS-densified iodoapatite used as a nuclear waste form. Under displacive 1 MeV Kr^{2+} irradiation, iodoapatite exhibits a T_c lower than many types of apatites,^{26,36} garnet,³⁷ pyrochlores,³⁵ and zirconia⁵¹ proposed as nuclear waste forms, implying great defect annealing at elevated temperatures. Furthermore, the SPS processing further enhances the radiation tolerance of iodoapatite and reduces the T_c from 515 K in BM-300C to 502 K in SPS-700C. Therefore, other than an effective consolidation and densification technique for the fabrication of iodine-bearing ceramic waste forms, SPS also has the advantage of improving the radiation tolerance against alpha-decay-induced amorphization. The electron irradiations show insignificant effects of beta decay events on the phase and microstructure of iodoapatite. Intense gamma irradiation dose may enhance the V–O bond order in the SPS-densified iodoapatite, probably due to an ionization-assisted process. Overall, the spark-plasma-sintered iodoapatite is a promising waste form that can remain stable under complex radiation conditions in the long term.

IV. Conclusions

Systematic irradiations of the SPS-densified lead vanadate iodoapatite were conducted to investigate its radiation stability in the presence of different radiation sources of alpha-, beta-, and gamma decays. The experimental results generally indicate excellent radiation stability of the iodoapatite. Under energetic ion irradiations, the SPS-700C iodoapatite shows enhanced tolerance against radiation-induced amorphization, as compared with as-milled lead vanadate iodoapatite, conventionally synthesized lead vanadate fluorapatite, and many other types of ceramic waste forms. The enhanced radiation performance for the SPS-densified iodoapatite may be attributed to the improved crystallinity and dense microstructure. In addition, the SPS-densified pellet is also largely stable

under beta irradiation and even shows improved bond ordering under intense gamma rays. Owing to its radiation stability, the SPS-densified iodoapatite holds great promise for the immobilization and disposal of I-129.

Acknowledgments

This work is supported by DOE NEUP (Nuclear Engineering University Program) under the award DE-AC07-05ID14517. JL also acknowledges a NSF career award DMR 1151028 in the synthesis of iodoapatite by high energy ball milling and consolidation by spark plasma sintering. FL acknowledges the support of the U.S. Nuclear Regulatory Commission Faculty Development Grant (NRC-38-10-933). The authors also thank the staff of the IVEM-tandem facility at the Argonne National Laboratory and the staff of the LINAC facility at Rensselaer Polytechnic Institute for their assistance with the irradiation experiments.

References

- ¹F. Audubert, J. Carpena, J. L. Lacout, and F. Tetard, "Elaboration of an Iodine-Bearing Apatite - Iodine Diffusion into a $\text{Pb}_3(\text{VO}_4)_2$ Matrix," *Solid State Ionics*, **95** [1–2] 113–9 (1997).
- ²R. C. Ewing, "Nuclear Waste Forms for Actinides," *P. Natl. Acad. Sci. USA*, **96** [7] 3432–9 (1999).
- ³R. C. Ewing, "The Design and Evaluation of Nuclear-Waste Forms: Clues from Mineralogy," *Can. Miner.*, **39**, 697–715 (2001).
- ⁴S. Le Gallet, et al., "Spark Plasma Sintering of Iodine-Bearing Apatite," *J. Nucl. Mater.*, **400** [3] 251–6 (2010).
- ⁵L. Merker and H. Wondratschek, "Bleiverbindungen Mit Apatitstruktur, Insbesondere Blei Jod-Apatite Und Blei Brom-Apatite," *Z. Anorg. Allg. Chem.*, **300** [1–2] 41–50 (1959).
- ⁶M. C. Stennett, I. J. Pinnock, and N. C. Hyatt, "Rapid Synthesis of $\text{Pb}_3(\text{VO}_4)_2$ for the Immobilisation of Iodine Radioisotopes, by Microwave Dielectric Heating," *J. Nucl. Mater.*, **414** [3] 352–9 (2011).
- ⁷N. Gmati, K. Boughzala, A. Chaabene, N. Fattah, and K. Bouzouita, "Mechanochemical Synthesis of Strontium Apatites Doped with Lanthanum and Cesium," *Cr. Chim.*, **16** [8] 712–20 (2013).
- ⁸S. P. Kumar and G. Buvanawari, "Synthesis of Apatite Phosphates Containing Cs^+ , Sr^{2+} and RE^{3+} Ions and Chemical Durability Studies," *Mater. Res. Bull.*, **48** [2] 324–32 (2013).
- ⁹C. Gaillard, C. Den Auwer, and S. D. Conradson, "An X-ray Absorption Near Edge Spectroscopy Study of Trace Amount Technetium Implanted in Apatite," *Phys. Chem. Chem. Phys.*, **4** [12] 2499–500 (2002).
- ¹⁰R. El Ouenzerfi, M. T. Cohen-Adad, C. Goutaudier, and G. Panczer, "Uranium-Doped Britholites $\text{Ca}_x\text{La}_y(\text{SiO}_4)_{6-x}(\text{PO}_4)_y\text{O}_2$: U Synthesis, Characterization and Preliminary Study of Uranium Diffusion," *Solid State Ionics*, **176** [1–2] 225–31 (2005).
- ¹¹V. Natarajan, T. K. Seshagiri, R. Veeraraghavan, and M. D. Sastry, "Radiation Effects in Plutonium and Carbonate co-Doped Calcium Hydroxy Apatite: An EPR Study," *J. Radioanal. Nucl. Ch.*, **256** [3] 445–9 (2003).
- ¹²K. Popa, et al., "Thermodynamic Properties of $\text{CaTh}(\text{PO}_4)_2$ Synthetic Cheralite," *Am. Miner.*, **93** [8–9] 1356–62 (2008).
- ¹³J. Rakovan, R. J. Reeder, E. J. Elzinga, D. J. Cherniak, C. D. Tait, and D. E. Morris, "Structural Characterization of U(VI) in Apatite by X-ray Absorption Spectroscopy," *Environ. Sci. Technol.*, **36** [14] 3114–7 (2002).
- ¹⁴O. Terra, F. Audubert, N. Dacheux, C. Guy, and R. Podor, "Synthesis and Characterization of Uranium-Bearing Britholites," *J. Nucl. Mater.*, **366** [1–2] 70–86 (2007).
- ¹⁵F. Goubard, P. Griesmar, and A. Tabuteau, "Alpha Self-Irradiation Effects in Ternary Oxides of Actinides Elements: The Zircon-Like Phases $\text{Am}^{\text{III}}\text{VO}_4$ and $\text{A}^{\text{IV}}\text{Np}^{\text{IV}}(\text{VO}_4)_2$ ($\text{A} = \text{Sr}, \text{Pb}$)," *J. Solid State Chem.*, **178** [6] 1898–902 (2005).
- ¹⁶F. Y. Lu, et al., "Facile Low Temperature Solid State Synthesis of Iodoapatite by High-Energy Ball Milling," *Rsc. Adv.*, **4** [73] 38718–25 (2014).
- ¹⁷T. K. Yao, F. Y. Lu, H. T. Sun, J. W. Wang, R. C. Ewing, and J. Lian, "Bulk Iodoapatite Ceramic Densified by Spark Plasma Sintering with Exceptional Thermal Stability," *J. Am. Ceram. Soc.*, **97** [8] 2409–12 (2014).
- ¹⁸C. Guy, F. Audubert, J. E. Lartigue, C. Latrille, T. Advocat, and C. Fillet, "New Conditionings for Separated Long-Lived Radionuclides," *C.R. Phys.*, **3** [7–8] 827–37 (2002).
- ¹⁹M. Uno, M. Shinohara, K. Kurosaki, and S. Yamanaka, "Some Properties of a Lead Vanado-Iodoapatite $\text{Pb}_{10}(\text{VO}_4)_6\text{I}_2$," *J. Nucl. Mater.*, **294** [1–2] 119–22 (2001).
- ²⁰W. J. Weber, et al., "Radiation Effects in Crystalline Ceramics for the Immobilization of High-Level Nuclear Waste and Plutonium," *J. Mater. Res.*, **13** [6] 1434–84 (1998).
- ²¹A. Meldrum, L. M. Wang, and R. C. Ewing, "Electron-Irradiation-Induced Phase Segregation in Crystalline and Amorphous Apatite: A TEM Study," *Am. Miner.*, **82** [9–10] 858–69 (1997).
- ²²S. Utsunomiya, S. Yudinsev, L. M. Wang, and R. C. Ewing, "Ion-Beam and Electron-Beam Irradiation of Synthetic Britholite," *J. Nucl. Mater.*, **322** [2–3] 180–8 (2003).
- ²³L. M. Wang and W. J. Weber, "Transmission Electron Microscopy Study of Ion-Beam-Induced Amorphization of $\text{Ca}_2\text{La}_8(\text{SiO}_4)_6\text{O}_2$," *Philos. Mag. A*, **79** [1] 237–53 (1999).
- ²⁴W. J. Weber, Y. W. Zhang, H. Y. Xiao, and L. M. Wang, "Dynamic Recovery in Silicate-Apatite Structures Under Irradiation and Implications for Long-Term Immobilization of Actinides," *Rsc. Adv.*, **2** [2] 595–604 (2012).

- ²⁵S. Soulet, J. Carpena, J. Chaumont, O. Kaitasov, M. O. Ruault, and J. C. Krupa, "Simulation of the Alpha-Annealing Effect in Apatitic Structures by He-Ion Irradiation: Influence of the Silicate/Phosphate Ratio and of the OH⁻/F⁻ Substitution," *Nucl. Instrum. Meth. B*, **184** [3] 383–90 (2001).
- ²⁶F. Y. Lu, Z. L. Dong, J. M. Zhang, T. White, R. C. Ewing, and J. Lian, "Tailoring the Radiation Tolerance of Vanadate-Phosphate Fluorapatites by Chemical Composition Control," *Rsc. Adv.*, **3** [35] 15178–84 (2013).
- ²⁷S. Miro, et al., "X-ray Diffraction Study of Damage Induced by Swift Heavy Ion Irradiation in Fluorapatite," *Nucl. Instrum. Meth. B*, **227** [3] 306–18 (2005).
- ²⁸S. A. T. Redfern, S. E. Smith, and E. R. Maddrell, "High-Temperature Breakdown of the Synthetic Iodine Analogue of Vanadinite, Pb₅(VO₄)₃I: An Apatite-Related Compound for Iodine Radioisotope Immobilization?" *Miner. Mag.*, **76** [4] 997–1003 (2012).
- ²⁹C. Meis, "Computational Study of Plutonium-Neodymium Fluorobrotholite Ca₉Nd_{0.5}Pu_{0.5}(SiO₄)(PO₄)₅F₂ Thermodynamic Properties and Threshold Displacement Energies," *J. Nucl. Mater.*, **289** [1–2] 167–76 (2001).
- ³⁰S. Baccaro, N. Catallo, A. Cemmi, and G. Sharma, "Radiation Damage of Alkali Borate Glasses for Application in Safe Nuclear Waste Disposal," *Nucl. Instrum. Meth. B*, **269** [2] 167–73 (2011).
- ³¹N. Deng, et al., "Effects of Gamma-Ray Irradiation on Leaching of Simulated ¹³³Cs⁺ Radionuclides from Geopolymer Wasteforms," *J. Nucl. Mater.*, **459**, 270–5 (2015).
- ³²C. Jegou, et al., "Effect of External Gamma Irradiation on Dissolution of the Spent UO₂ Fuel Matrix," *J. Nucl. Mater.*, **341** [1] 62–82 (2005).
- ³³F. Y. Lu, Y. Q. Shen, X. Sun, Z. L. Dong, R. C. Ewing, and J. Lian, "Size Dependence of Radiation-Induced Amorphization and Recrystallization of Synthetic Nanostructured CePO₄ Monazite," *Acta Mater.*, **61** [8] 2984–92 (2013).
- ³⁴A. Meldrum, L. A. Boatner, and R. C. Ewing, "Displacive Radiation Effects in the Monazite- and Zircon-Structure Orthophosphates," *Phys. Rev. B*, **56** [21] 13805–14 (1997).
- ³⁵J. Lian, et al., "Radiation-Induced Amorphization of Rare-Earth Titanate Pyrochlores," *Phys. Rev. B*, **68** [1] 3 (2003).
- ³⁶S. X. Wang, B. D. Begg, L. M. Wang, R. C. Ewing, W. J. Weber, and K. V. G. Kutty, "Radiation Stability of Gadolinium Zirconate: A Waste Form for Plutonium Disposition," *J. Mater. Res.*, **14** [12] 4470–3 (1999).
- ³⁷J. M. Zhang, T. S. Livshits, A. A. Lizin, Q. N. Hu, and R. C. Ewing, "Irradiation of Synthetic Garnet by Heavy Ions and Alpha-Decay of Cm-244," *J. Nucl. Mater.*, **407** [3] 137–42 (2010).
- ³⁸S. Utsunomiya, L. M. Wang, S. Yudinsev, and R. C. Ewing, "Ion Irradiation-Induced Amorphization and Nano-Crystal Formation in Garnets," *J. Nucl. Mater.*, **303** [2–3] 177–87 (2002).
- ³⁹W. J. Weber, R. C. Ewing, and L. M. Wang, "The Radiation-Induced Crystalline-to-Amorphous Transition in Zircon," *J. Mater. Res.*, **9** [3] 688–98 (1994).
- ⁴⁰J. M. Zhang, et al., "Enhanced Radiation Resistance of Nanocrystalline Pyrochlore Gd₂(Ti_{0.65}Zr_{0.35})₂O₇," *Appl. Phys. Lett.*, **94** [24] 243110 (2009).
- ⁴¹T. D. Shen, S. Feng, M. Tang, J. A. Valdez, Y. Wang, and K. E. Sickafus, "Enhanced Radiation Tolerance in Nanocrystalline MgGa₂O₄," *Appl. Phys. Lett.*, **90** [26] 263115 (2007).
- ⁴²F. Y. Lu, et al., "Amorphization of Nanocrystalline Monoclinic ZrO₂ by Swift Heavy Ion Irradiation," *Phys. Chem. Chem. Phys.*, **14** [35] 12295–300 (2012).
- ⁴³S. X. Wang, L. M. Wang, and R. C. Ewing, "Irradiation-Induced Amorphization: Effects of Temperature, Ion Mass, Cascade Size, and Dose Rate," *Phys. Rev. B*, **63** [2] 024105 (2001).
- ⁴⁴F. Y. Lu, J. M. Zhang, M. B. Huang, F. Namavar, R. C. Ewing, and J. Lian, "Phase Transformation of Nanosized ZrO₂ Upon Thermal Annealing and Intense Radiation," *J. Phys. Chem. C*, **115** [15] 7193–201 (2011).
- ⁴⁵A. Meldrum, L. A. Boatner, and R. C. Ewing, "Electron-Irradiation-Induced Nucleation and Growth in Amorphous LaPO₄, ScPO₄, and Zircon," *J. Mater. Res.*, **12** [7] 1816–27 (1997).
- ⁴⁶W. J. Weber, Y. W. Zhang, and L. M. Wang, "Review of Dynamic Recovery Effects on Ion Irradiation Damage in Ionic-Covalent Materials," *Nucl. Instrum. Meth. B*, **277**, 1–5 (2012).
- ⁴⁷R. L. Frost, M. Crane, P. A. Williams, and J. T. Klopogge, "Isomorphic Substitution in Vanadinite [Pb₅(VO₄)₃Cl] - a Raman Spectroscopic Study," *J. Raman Spectrosc.*, **34** [3] 214–20 (2003).
- ⁴⁸J. G. Eon, C. B. Boechat, A. M. Rossi, J. Terra, and D. E. Ellis, "A Structural Analysis of Lead Hydroxyvanadinite," *Phys. Chem. Chem. Phys.*, **8** [15] 1845–51 (2006).
- ⁴⁹Q. He, X. Liu, X. M. Hu, S. C. Li, and H. J. Wang, "Solid Solution Between Lead Fluorapatite and Lead Fluorvanadate Apatite: Mixing Behavior, Raman Feature and Thermal Expansivity," *Phys. Chem. Miner.*, **38** [10] 741–52 (2011).
- ⁵⁰F. D. Hardcastle and I. E. Wachs, "Determination of Vanadium Oxygen Bond Distances and Bond Orders by Raman-Spectroscopy," *J. Phys. Chem.-Us*, **95** [13] 5031–41 (1991).
- ⁵¹A. Meldrum, S. J. Zinkle, L. A. Boatner, and R. C. Ewing, "Heavy-Ion Irradiation Effects in the ABO₄ Orthosilicates: Decomposition, Amorphization, and Recrystallization," *Phys. Rev. B*, **59** [6] 3981–92 (1999). □

Incorporation of iodine into apatite structure: a crystal chemistry approach using Artificial Neural Network

Jianwei Wang *

Department of Geology and Geophysics, Center for Computation and Technology, Louisiana State University, Baton Rouge, LA, USA

OPEN ACCESS

Edited by:

Zhicheng Jing,
Case Western Reserve University,
USA

Reviewed by:

Alexander F. Goncharov,
Carnegie Institution of Washington,
USA

Geoffrey David Bromiley,
The University of Edinburgh, UK

*Correspondence:

Jianwei Wang,
Department of Geology and
Geophysics, Louisiana State
University, E235 Howe-Russell
Building, Baton Rouge, LA 70803,
USA
jianwei@lsu.edu

Specialty section:

This article was submitted to
Earth and Planetary Materials,
a section of the journal
Frontiers in Earth Science

Received: 25 February 2015

Accepted: 08 May 2015

Published: 03 June 2015

Citation:

Wang J (2015) Incorporation of iodine
into apatite structure: a crystal
chemistry approach using Artificial
Neural Network.
Front. Earth Sci. 3:20.
doi: 10.3389/feart.2015.00020

Materials with apatite crystal structure have a great potential for incorporating the long-lived radioactive iodine isotope (^{129}I) in the form of iodide (I^-) from nuclear waste streams. Because of its durability and potentially high iodine content, the apatite waste form can reduce iodine release rate and minimize the waste volume. Crystal structure and composition of apatite ($\text{A}_5(\text{XO}_4)_3\text{Z}$) was investigated for iodide incorporation into the channel of the structure using Artificial Neural Network. A total of 86 experimentally determined apatite crystal structures of different compositions were compiled from literature, and 44 of them were used to train the networks and 42 were used to test the performance of the trained networks. The results show that the performances of the networks are satisfactory for predictions of unit cell parameters a and c and channel size of the structure. The trained and tested networks were then used to predict unknown compositions of apatite that incorporates iodide. With a crystal chemistry consideration, chemical compositions that lead to matching the size of the structural channel to the size of iodide were then predicted to be able to incorporate iodide in the structural channel. The calculations suggest that combinations of A site cations of Ag^+ , K^+ , Sr^{2+} , Pb^{2+} , Ba^{2+} , and Cs^+ , and X site cations, mostly formed tetrahedron, of Mn^{5+} , As^{5+} , Cr^{5+} , V^{5+} , Mo^{5+} , Si^{4+} , Ge^{4+} , and Re^{7+} are possible apatite compositions that are able to incorporate iodide. The charge balance of different apatite compositions can be achieved by multiple substitutions at a single site or coupled substitutions at both A and X sites. The results give important clues for designing experiments to synthesize new apatite compositions and also provide a fundamental understanding how iodide is incorporated in the apatite structure. This understanding can provide important insights for apatite waste forms design by optimizing the chemical composition and synthesis procedure.

Keywords: apatite, iodine, nuclear waste forms, fission products, crystal chemistry, Artificial Neural Network, unit cell parameters, channel size

Introduction

Production of nuclear energy generates radioactive nuclear wastes. Depending on the fuel cycle option, novel chemical reprocessing and transmutation strategies can result in complicated waste streams with a number of radionuclides including heavy alkaline and alkaline earth elements,

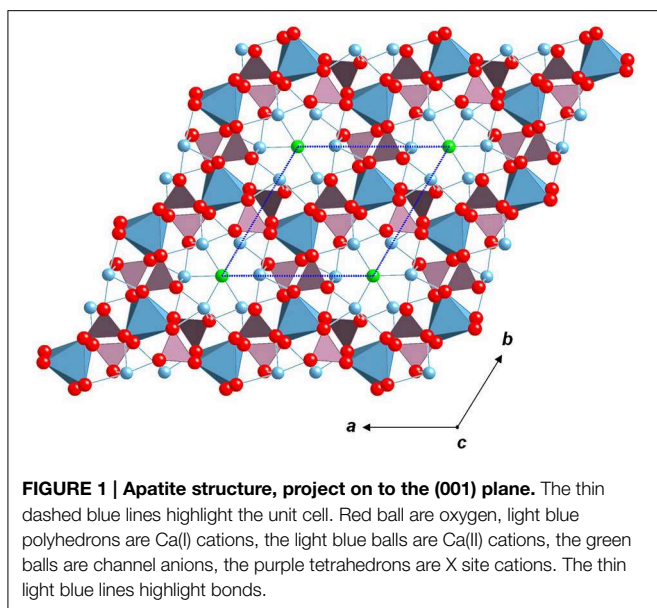
transition metals, minor actinides, and lanthanides. Among volatile radionuclides, ^{129}I is particular challenging because iodine is highly mobile either in gas form or in its reduced form, with a long a half-life of 1.57×10^7 years. In its reduced oxidation state, i.e., I^- , iodide is highly mobile in the environment because it is stable in a wide range of redox potential and pH conditions, and is weakly bounded to the surfaces of silicate minerals and rocks commonly occurring in the environment. Because of these unique properties, iodine deserves special attention for designing durable waste forms for long-term disposal in a geological setting.

A number of waste forms have been considered for ^{129}I . Silver iodide (AgI), with a melting point of 558°C , density of 5.7 g/cm^3 , has a very low solubility in water, with a solubility product constant of 8.52×10^{-17} at standard condition (Lide, 2014), which suggests it could be a good candidate for long-term storage. However, AgI itself is not a waste form, and it must be incorporated and packaged into a dense and mechanically durable solid waste form for long-term disposal. Its relatively high vapor pressure at moderate temperature is an issue that limits the thermal processing temperature (Garino et al., 2011a). Because of its low melting point, the temperatures to reach a vapor pressure of 1, 10, 100 Pa are 594, 686, and 803°C respectively (Lide, 2014). The vapor pressures are considered high in terms of the waste processing at high temperature (often greater than 800°C). In addition, AgI is photosensitive, and the ionic silver in AgI may be reduced to metallic silver upon exposed to light. This photochemical process reduces the stability of AgI and increases the cost and environmental risk during the processing, transport, and disposal. Borosilicate glasses have been the most widely adopted material at industrial scales for the immobilization of nuclear wastes (Donald et al., 1997), but it is not a choice for iodine because high iodine loss at the required processing temperature (Garino et al., 2011a). In order to use a glass waste form for iodine, low temperature sintering glasses, which can be processed below the melting point of AgI , are recommended. There are a number of glass waste forms proposed for iodine in the literature including vanadium and lead oxide glasses (Nishi et al., 1996), low temperature sintering Bi-Si-Zn-oxide glasses (Garino et al., 2011b), Bi-P-Zn-oxide glasses (Yang et al., 2013), AgI and $\text{Ag}_4\text{P}_2\text{O}_7$ glass (Sakuragi et al., 2008), and silver aluminophosphate glasses (Lemesle et al., 2014). In many of those low temperature sintering glasses, AgI is still the phase that contains iodine and the glass functions as a matrix that encapsulates AgI . In addition to glasses, other waste forms for iodine have also been considered, including iodide sodalite (Sheppard et al., 2006; Maddrell et al., 2014), hydrotalcite-like layered bismuth-iodine-oxide (Krumhansl and Nenoff, 2011), organic frameworks (MOFs) materials (Sava et al., 2012), cyclodextrins compounds (Szente et al., 1999), uranyl borates (Wu et al., 2011), and apatites (Audubert et al., 1997; Carpena et al., 2001; Uno et al., 2001; Zhang et al., 2007; Le Gallet et al., 2010; Campayo et al., 2011; Stennett et al., 2011; Redfern et al., 2012; Lu et al., 2013; Yao et al., 2014). Each of above proposed waste forms for iodine has its unique advantages and limitations that in some part depend on the disposal condition. Since conditions and settings of a long-term geological disposal may vary, more than one candidate waste form for iodine would

be ideal, which would provide flexibility in choosing the strategy for a disposal of the nuclear waste.

Among ceramic waste forms for iodine, materials with apatite structure have a number of advantageous properties including long-term durability and structural and chemical flexibility. Its long-term durability is demonstrated by stability of natural apatite samples over billions of years in earth's history (Gauthier-Lafaye et al., 1996). Its structural and chemical flexibilities are shown in a wide range of chemical substitutions at both a single and different crystallographic sites, and its adaptability of symmetries other than hexagonal symmetry (White and ZhiLi, 2003; White et al., 2005). These flexibilities offer an opportunity to incorporate multiple radionuclides in a single phase ceramics. Because apatite waste forms are single phase, it is relatively simpler to characterize its durability and to evaluate its performance than a multiphase waste form. In addition, the flexibility of chemical substitutions in apatite may be beneficial for incorporating both radionuclides and their decay products. Because its multiple crystallographic sites can be occupied by elements with different charges, changes associated with the valance and identity of the radioactive elements resulting from radioactive decay of those β emitters, e.g., ^{137}Cs and ^{90}Sr , could be potentially offset by a charge transfer between the sites and structural distortions within the same phase. This charge transfer and structural distortion, preferably local within a couple of bond distance, would prevent likely phase transition or decomposition due to radioactive decay without compromising the integrity of the phase. For ^{129}I , the isotope β decays to ^{129}Xe . The emitted electron could be captured by a variable valance metal ion in the structure and the ^{129}Xe could remain in the structure as a defect or diffuse away as a gas molecule. Thus, apatite-structured phases may be tolerant against or has potential to mitigate the aging effect of radionuclides from a process so-called radioparagenesis (Jiang et al., 2009, 2010), a structural and chemical transformation process resulting from radioactive decay of radionuclides in a solid phase.

Natural mineral apatite has a chemical composition of $\text{Ca}_5(\text{PO}_4)_3(\text{OH}, \text{F}, \text{Cl})$ (Naray-Szabo, 1930; Pan and Fleet, 2002; White et al., 2005; Pasero et al., 2010). Apatite is also one of few minerals produced and used by biological systems. Hydroxyleapatite is the major mineral component of tooth and bone (Wopenka and Pasteris, 2005). The extended apatite subgroup describes minerals with the same crystal structure as apatite but with different compositions by chemical substitutions. There are a large collection of synthetic materials with apatite structure. In this paper, apatite-structured material, or simply apatite, is used for materials having apatite structure. The general formula for apatite-structured materials is $\text{A}_5(\text{XO}_4)_3\text{Z}$, often with hexagonal $P6_3/m$ symmetry (space group number 176). Apatite could also adapt symmetries of $P6_3$, $P-3$, $P-6$, $P2_1/m$, and $P2_1$ while keeping the same structural topology (White and ZhiLi, 2003). The crystal structure is depicted in **Figure 1**. The A cation occupies two crystallographic sites Ca(I) and Ca(II). The molar ratio Ca(I)/Ca(II) is 2:3. The A cation can be substituted by a number of cations including Na^+ , K^+ , Cs^+ , Mg^{2+} , Ca^{2+} , Ba^{2+} , Sr^{2+} , Cd^{2+} , Pb^{2+} , Fe^{2+} , Fe^{3+} , REE^{3+} , and Ac^{4+} (REE: rare earth elements, Ac: actinides). For $\text{Ca}_5(\text{PO}_4)_3\text{F}$, Ca(I) site has



a coordination number of six at Ca(I)-O distance of 2.5 Å and nine at 2.8 Å, and Ca(II) site has a coordination number of six at Ca(I)-O/F distance of 2.5 Å and seven at 2.7 Å (Hughes et al., 1989; White and ZhiLi, 2003). The X cation often forms a tetrahedron with four oxygen atoms and can be substituted by P^{5+} , Si^{4+} , S^{6+} , V^{5+} , Cr^{5+} , As^{5+} , Mn^{5+} , Ge^{4+} . In some cases, the tetrahedron anion group can be replaced by non-tetrahedron anions such as ReO_5^{3-} (Baud et al., 1979) and BO_3^{3-} (Campayo et al., 2011). The Z anion in the structural channel can be substituted by OH^- , F^- , Cl^- , Br^- , I^- , O^{2-} , CO_3^{2-} , and IO_3^- . The chemical substitutions are often coupled between multiple sites. For instance, Ca^{2+} substitution by RE^{3+} at Ca(I)/Ca(II) site is coupled with tetrahedron cation substitution of PO_4^{3-} by SiO_4^{4-} (e.g., $Ca^{2+} + PO_4^{3-} = RE^{3+} + SiO_4^{4-}$). This kind of coupled substitutions involving multiple crystallographic sites is common for apatite and gives apatite-structured materials a unique property that can lead to simultaneous incorporations of multiple radionuclides. For instance, $Sr_8CsNd(PO_4)_6F_{2.3}$, including both Sr and Cs in its structure, was synthesized by a precipitation reaction method (Burakov, 2005). In addition to be used as a host material for storage of nuclear wastes (Audubert et al., 1997; Carpena et al., 2001; Ewing, 2001; Uno et al., 2001; Carpena and Lacout, 2005; Kim et al., 2005; Zhang et al., 2007; Le Gallet et al., 2010; Campayo et al., 2011; Stennett et al., 2011; Redfern et al., 2012; Lu et al., 2013), apatite materials have a number of other applications including bone tissues (Vallet-Regi and Gonzalez-Calbet, 2004), ionic conductors (Arikawa et al., 2000; Kharton et al., 2004), fertilizer (Easterwood et al., 1989), and fission track dating of geological record (Gallagher, 1995; Gallagher et al., 1998). For nuclear waste applications, apatite has been suggested for storage of a number of nuclear wastes including I, Cs, Sr, rare earth elements, and actinides (e.g., U, Th) (Rakovan and Hughes, 2000; Ewing, 2001; Pan and Fleet, 2002; Rakovan et al., 2002; Luo et al., 2009). For iodine incorporation, a lead vanado-iodoapatite $Pb_{10}(VO_4)_6I_2$, a synthetic apatite inspired by a chemically

similar natural apatite, lead vanado-chlorapatite (mineral name vanadinite) $Pb_{10}(VO_4)_6Cl_2$, was prepared from $Pb_3(VO_4)_2$ and PbI_2 in stoichiometric amounts using hot-pressing method at a temperature above the melting temperature of PbI_2 (Audubert et al., 1997). Later, lead vanado-iodoapatite was also synthesized by a microwave dielectric heating method using a modified domestic microwave (Stennett et al., 2011). $AgPb_9(VO_4)_6I$ and $AgBa_9(VO_4)_6I$ were synthesized using a solid state reaction method starting with stoichiometric amounts of $Pb_3(VO_4)_2$ and AgI, and $Ba_3(VO_4)_2$ and AgI in a sealed quartz vessels in vacuum and heat-treated at 973 K for 5 h (Uno et al., 2004). Since mineral mimetite ($Pb_5(AsO_4)_3Cl$) has a similar chemical composition as vanadinite, its iodide form, $Pb_5(AsO_4)_3I$, may also be synthesized. Recently, iodate (IO_3^-) was incorporated in hydroxyapatite structure by precipitation in water (Campayo et al., 2011). High-temperature breakdown of the synthetic $Pb_5(VO_4)_3I$ was characterized and the apatite was observed to be stable until temperature reaches as high as 540°C. A new development of synthesizing iodide-apatite was to combine high energy ball milling and Sparking plasma Sintering (SPS) to synthesize a single phase, almost stoichiometric $Pb_5(VO_4)_3I$ apatite at low temperature with minimum iodine loss (Yao et al., 2014). Excellent radiation resistant and thermal recovery properties were reported for vanadate-phosphate fluorapatite (Lu et al., 2013), silicate-apatite structures (Weber et al., 2012a,b), and actinide-bearing apatites (Weber et al., 1997). A low iodine leach rate of 0.0025 g/m²/day was reported for synthetic $Pb_5(VO_4)_3I$ apatite at pH 6 and 90°C (Stennett et al., 2011).

As these studies show, apatite has a great potential for storage of a number of radioactive nuclear waste elements because of its long-term durability and irradiation stability. Although materials with apatite structure show excellent properties for various radionuclides, these properties may vary with their chemical compositions. In order to optimize the nuclear waste performance, there is a need to explore the chemical and physical properties and durability of different apatite compositions. However, the chemical substitutions occur at all sites in apatite (i.e., A, X, and Z sites of $A_5(XO_4)_3Z$) and each of these sites can be occupied by a number of elements. The possible apatite compositions could easily reach an unmanageable number only for the end-members. Even for iodide apatite where the iodide is the only Z anion, there are over a hundred possible end-member compositions. It is expected that not all of them are thermodynamically stable and are suitable as waste forms. Experimentally, trying all the combinations would be not only expensive but also time consuming. Thus, it is necessary to be selective by ruling out those that do not meet some basic requirements of the structure and crystal chemistry of apatite. For iodide incorporation in the structural channel, size of the channel in the apatite structure has to fit the size of iodide ion. Currently, only a few iodide apatite compositions have been synthesized experimentally (Audubert et al., 1997; Uno et al., 2004; Campayo et al., 2011; Stennett et al., 2011; Yao et al., 2014). In order to explore other possible compositions, all combinations of elements from the periodic table that meet a basic consideration of the crystal structure and chemical formula should be considered. One of efficient methods to explore a large

number of apatite compositions is Artificial Neural Network (ANN). The method has been previously used to predict the crystallographic cell parameters (Wu et al., 2004; Kockan and Evis, 2010; Kockan et al., 2014) and hardness and fracture toughness (Evis and Arcaklioglu, 2011) of apatite using the average ionic radii of ions at different crystallographic sites. The method has also been used for other crystalline phases (Asadi-Eydivand et al., 2014).

Purpose of this study is to apply Artificial Neural Network method for apatite to predict the size of the structural channel and unknown iodide apatite compositions. By including electron negativity as an additional input parameter in addition to ionic radius, the accuracy of predicted channel size is improved. The simulations provide an understanding of crystal chemistry of apatite and explore unknown apatite with iodide as the channel anion. The results demonstrate that Artificial Neural Network simulation is an effective tool to explore large number of apatite chemical compositions and can be used to predict unknown apatite chemical compositions.

Method—Artificial Neural Networks Simulation

Artificial Neural Network (ANN) approach is inspired from biological neuron assemblies and their way of encoding and solving problems. The philosophy of the approach is to abstract some key ingredients from biology and out of those to construct simple mathematical models. The network consists of an input layer, one or more hidden layers, and an output layer. First, the input data are passed to the input layer with a weight and a bias, and then the results are passed to the neurons in the hidden layers and processed by a training function, and finally the data are passed to the output neuron. There are weighting factors between the neurons of each layer. The predicted output results are compared with actual results, which are used to adjust the weights and biases till the difference between predicted and actual results reaches a predefined criterion (Zhang and Friedrich, 2003). For function approximation, in order to deduce the relationship between the input and the output, a neural network is first trained using a given set of input-output data (typically through supervised learning). After training, such a network can be used as a trained network with an input-output characteristic approximately equal to the relationship of the training problems. Because of the modular and non-linear nature of Artificial Neural Networks, they are considered to be able to approximate any arbitrary function to an arbitrary degree of accuracy, which is particularly useful for non-linear relations. Typically, available data are divided to two subsets, training set and testing set. Validation is needed to calculate the error after each epoch (one cycle of training data). The testing dataset is used to check the ability of the network to predict new data at the end of the training process before the network can be used for predictions (Zhang and Friedrich, 2003; Samarasinghe, 2006; Lucon and Donovan, 2007).

In this study, the available data were divided roughly to half and half, and the training dataset was strategically selected in order to cover the end members of available chemical

compositions and some important solid solutions of apatite. A multilayer perception model with supervised learning and batch training was used. A single hidden layer with different numbers of processing units and various learning methods were tested in order to achieve the best network performance and prediction reliability. In the hidden layer, there are a number of commonly used non-linear activation functions. And in this study, hyperbolic tangent sigmoid transfer function was used. The backpropagation algorithm was used. A linear function was used for the output layer. The sigmoid function has a number of advantages for the transfer function in the hidden layer. Its continuity makes it differentiable and minimization of the mean-square error with respect to the weighted sums can be used to adjust the weights of the network during the backpropagation of errors. It has upper and lower bounds, which means even if the inputs are very large, the outputs will never reach large values. Non-linearity makes the functions a natural choice for complex non-linear correlations between inputs and outputs (Samarasinghe, 2006).

The Artificial Neural Network toolbox from Matlab program package was used (The MathWorks, 2011; Demuth and Beale, 2013). A number of training functions have been tried. Levenberg-Marquardt backpropagation is a network training function that updates weight and bias values according to Levenberg-Marquardt optimization. It is often the fastest backpropagation algorithm in the toolbox, and was tested first. Other algorithms tested include resilient backpropagation, BFGS quasi-Newton backpropagation, and Bayesian regulation backpropagation among other algorithms. Using mean-square error with respect to weight and bias as the performance function, the Bayesian regulation backpropagation has the best performance. Bayesian regularization minimizes a linear combination of squared errors and weights. It also modifies the linear combination so that at the end of training, the resulting network has good generalization qualities.

Results and Discussion

Crystallographic Data Set of Apatite-Structured Materials

In order for ANNs to predict properties of unknown apatite of various chemical compositions, a dataset, including chemical composition and crystal structure, of known apatite compositions has to be constructed. The dataset is based on a large number of publications in the open literature and crystal structure databases about apatite. For the iodide incorporation, the channel size is important since the iodide radius is large, 2.2 Å (Shannon, 1976). In order for iodide to be incorporated in the structural channel, the channel size has to be compatible with the size of the ion. Since the coordinates of Ca(II) site in the crystal structure is needed to calculate the channel size, crystal structure information, i.e., chemical composition, occupancies and coordinates of the sites, are needed for the construction of the dataset.

A dataset of 86 apatite compositions was compiled from inorganic crystal structure database (ICSD) and the literature (Wu et al., 2004; ICSD, 2010; Kockan and Evis, 2010), listed in

Supplementary Table 1. The average ion radius is calculated based on the chemical formula and is molar fraction weight-averaged. Because the interaction between the channel anion and Ca(II) site cation in apatite structure is mainly ionic, ionic radii for A and Z ions are used. Ionic radii of all the elements in the periodic table have been compiled in the literature (Shannon, 1976; Henderson, 2000). Ionic radius depends on the coordination number, which in turn is dependent on cutoff bond distance. For apatite, coordination numbers of Ca(I) and Ca(II) sites in $\text{Ca}_5(\text{PO}_4)_3\text{F}$ are 6 at 2.5 Å, or 9 and 7 at 2.8 Å respectively. For this study, two A cation sites are not distinguished. For the consistency between the two sites and across different apatite compositions, coordination number of 6 was used for the ionic radius of A cation when choosing the ionic radius values from the literature. For X site, crystal radius was used, largely because the X cation has a strong covalent bond with oxygen and coordination number is 4 in most of the cases. However, the use of crystal radius should not make difference in ANN simulations because crystal radius differs from ionic radius by a constant of 0.14 Å (Shannon, 1976). The coordination number of the channel Z anion depends on the location of the channel ion, and it is 3 if the ion is positioned in the same (001) plane of the Ca(II) or 6 if in the plane of the Ca(I). Some channel anions can have multiple occupies positioned in a range between the two planes, which are largely dependent on the relative size of the channel anion with respect to the channel size and interactions between the channel anion and Ca(II) cations. For consistency, coordination number of 6 was used for ionic radius parameter of the channel anion. In the previous ANNs studies of apatite (Wu et al., 2004; Kockan and Evis, 2010), ionic radius with a coordination number of 6 was used for the tetrahedron-forming cations, which is not consistent with the structure and coordination of the cations. In the present study, the size of ions was based on the actual coordination and bonding character of the concerned ions, resulting in better overall predictions of the cell parameters. In addition to ionic radius, electronegativity was used as an input parameter because it is important for defining chemical bonding character between the atoms, which in turn affects both the unit cell parameters and channel size. Electronegativity was not used previously in predicting the unit cell parameters (Wu et al., 2004; Kockan and Evis, 2010). We will show in the next section that using electronegativity as an additional input improves the accuracies of the predictions of the channel size and the unit cell parameters. Electron configuration, valence electron, electron localization and delocalization, and electron spin state are all important when considering chemical bonding. However, since these properties are already largely reflected in ionic radius and electronegativity, they are not considered in the present study.

Artificial Neural Network Simulations

The dataset from experimental crystal structure data is divided to two, one for training the networks (i.e., the first 44 apatites in Supplementary Table 1) and one for testing the networks (i.e., the rest, 42 apatites). The training dataset includes the end members of apatite compositions and some of the solid solutions, and the rest of them are included in the testing dataset. This strategy

allows the ANNs to be well trained for the predictions of apatite compositions.

Figure 2 illustrates the ANN method used to simulate the cell parameters and channel size of apatite. There are six input parameters, average radius and average electronegativity for each of the three cation sites. There is a hidden layer with four neurons and an output layer. The output has one parameter. The ANN simulations were carried out separately for unit cell parameters a , c , and channel size.

Using Bayesian regularization (BR) algorithm, the training simulation runs until the algorithm is converged, which is indicated by the convergence of the effective number of simulation parameters, maximum MU (a parameter for controlling convergence algorithms), convergence of the summed square error, and sum squared parameter. For unit cell parameter a , the simulation took 130 epochs, and the sum of squared errors (SSE) was converged to 0.0613. The effective number of parameters was found to be 21, and the sum squared parameter was converged to 7.08. These results indicate the BR method successfully minimized the error function and a higher generalization was achieved. Similar results were obtained for unit cell parameter c and channel size.

The performance of the ANNs is judged by the errors and the error distributions between predicted and target experimental values. It can be evaluated by the coefficient (i.e., R) of a linear regression between predicted and target experimental values. In contrast to previously studies (Wu et al., 2004; Kockan and Evis, 2010), electronegativity was used as an input in the present study for each of the ions in the ANNs. The results show that, by including the electronegativity, with the same settings of the ANN simulations, the R values are increased by 1.2, 1.3, and 8.8% for the testing set of cell parameters a , c , and channel size respectively, suggesting that the performance of the ANNs is improved over without using electronegativity as an input parameter. This improvement is especially true for the prediction of the channel size, which is more sensitive to the electronegativity of the atoms.

Prediction of Unit Cell Parameters

For unit cell parameter a , the ANN simulation result is shown in **Figure 3** and listed in Supplementary Table 1. The dashed-lines are perfect prediction lines and solid lines are linear regression lines. The fitting coefficient R values of the linear regression

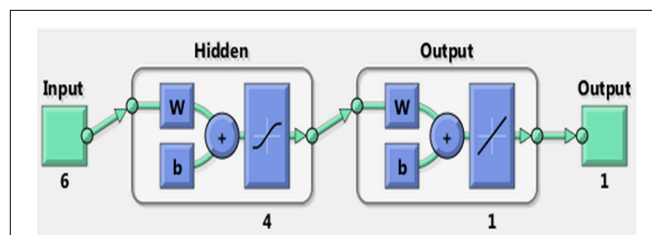


FIGURE 2 | The Artificial Neural Network used for the predictions of apatite compositions and structure parameters. There are six input parameters and one output parameter, one output layer, and one hidden layer. There are 4 neurons used in the hidden layer for the networks.

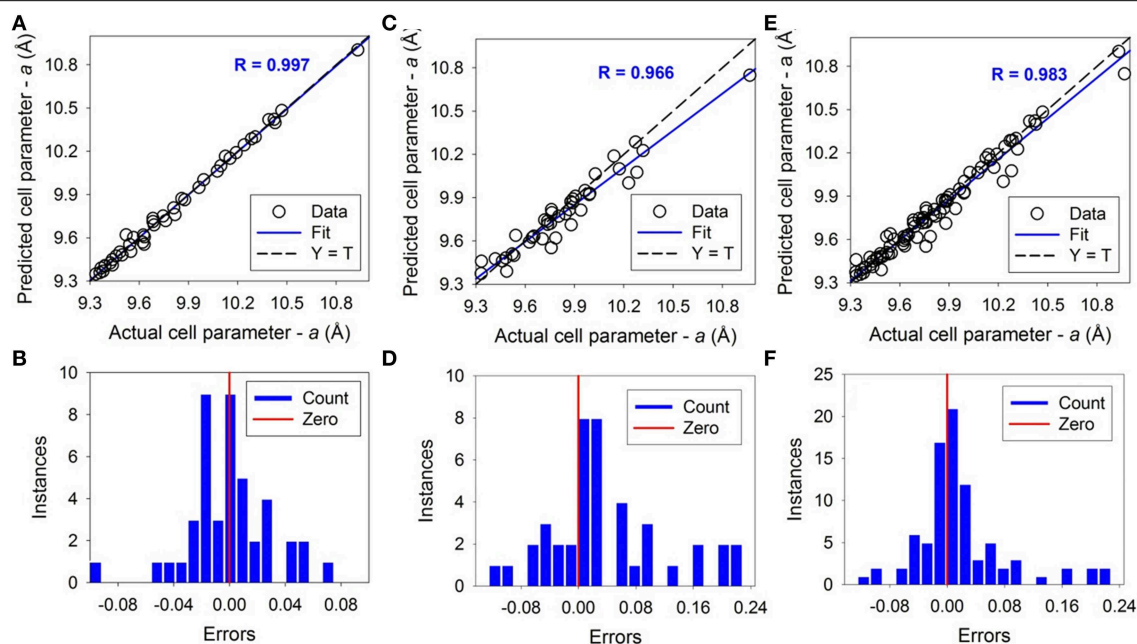


FIGURE 3 | The results of Artificial Neural Network simulations of unit cell parameter *a*. The upper figures show the correlations between predicted and actual values. The bottom figures show the error distributions around the vertical red bars of zero error. The dashed lines

correspond to $Y = T$ when the predicted and actual are the same. The solid lines correspond to linear fitting with a fitting coefficient of R . Open circles are experimental data. (A,B) are the result of training, (C,D) are of testing, and (E,F) are of the total.

between the predicted and actual value are 0.997, 0.966, and 0.983 for the training, testing, and overall ANN simulations respectively. The average error between the predicted and actual value is 0.22%, 0.65%, and 0.43% for training, testing and overall dataset respectively. The maximum error is 1.05% for the training dataset and 2.23% for the testing dataset. For unit cell parameter *c*, results are shown in Figure 4 and also listed in Supplementary Table 1. The coefficient R values are 0.998, 0.977, and 0.989 for the training, testing, and overall ANN simulations respectively. The average errors are 0.20%, 0.67%, and 0.43% for training, testing and overall dataset respectively. The maximum error is 1.35% for the training dataset and 2.29% for the testing. As shown by the error distributions in Figures 3, 4, the errors for the predictions of *a* and *c* are distributed around the averages normally, except a couple of exceptions. These results suggest that the trained and tested ANNs are satisfactory for predicting the apatite cell parameters *a* and *c* of unknown apatite compositions. The results are similar to previous studies using average ionic radii at different sites (i.e., A, X, Z of $A_5(XO_4)_3Z$) to predict the crystallographic unit cell parameters (Wu et al., 2004; Kockan and Evis, 2010).

Figure 5 illustrates how a trained and tested ANN is used for predicting unit cell parameter *a* of unknown apatite compositions with iodide in the channel of the structure. As shown, for any given average radii of A and X site cations, the cell parameter *a* (or *c*) can be predicted by reading into the figure. Since the A and X cations are unknown, their electronegativities have to be assumed (i.e., 2.33 and 1.63 for A and X respectively), which will need to be adjusted for an actual composition. For instance, for A site radius

of 1.2 Å and X site radius of 0.4, the predicted *a* cell parameter is ~10.17 Å. For an actual prediction, compositions have to be given and average radii and electronegativities at all sites will need to be calculated and supplied to the trained and tested ANN. This approach is applicable to any apatite compositions with or without iodide in the channel. Giving the flexibility of apatite structure, there is a large number of cations that can occupy A and X sites. Similar figures like Figure 5 can be generated from ANN simulations to show predictions of the cell parameters as a function of the cation radius.

Although trained and tested ANNs could take any chemical compositions for predicting properties of the apatite, constraints exist as not any combinations of elements at A, X, and Z sites are possible apatite compositions. First, any substitutions at one site or coupled substitutions at multiple sites are constrained by charge balance. For the Z anion, in addition to F, OH, Cl, Br, I, O and vacancy are also possible, and poly-oxyanion are also possible but rare. For the A cation, the valance can deviate from +2 to +1, +3 and +4, indicating a great flexibility of the site incorporating various charged species. For the X cation, in addition to tetrahedral forming cations, cations that can form pyramidal polyhedron like ReO_5^{3-} (Baud et al., 1979) and trigonal pyramidal iodate IO_3^- are also possible in the tetrahedral site (Campayo et al., 2011).

Prediction of Channel Size of Apatite Structure for Iodide Incorporation

For iodide apatite, the channel size of the structure has to be large enough to incorporate iodide ion. For instance, the synthetic

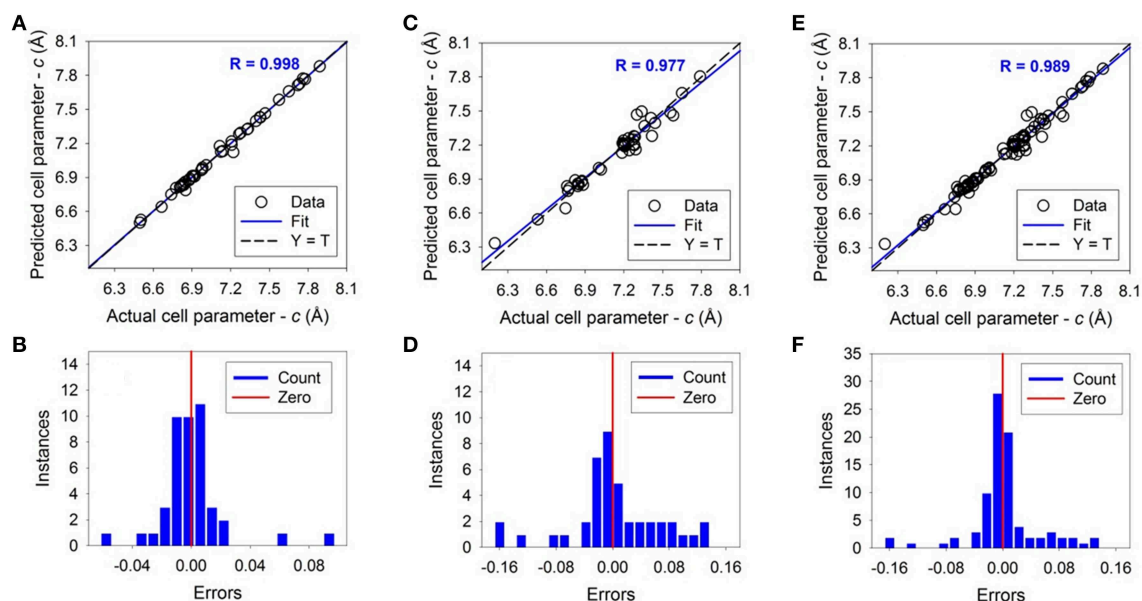


FIGURE 4 | The results of Artificial Neural Network simulations of unit cell parameter c . The upper figures show the correlations between predicted and actual values. The bottom figures show the error distributions around the vertical red bars of zero error. The dashed lines

correspond to $Y = T$ when the predicted and actual are the same. The solid lines correspond to linear fitting with a fitting coefficient of R . Open circles are experimental data. (A,B) are the result of training, (C,D) are of testing, and (E,F) are of the total.

iodide apatite (i.e., $\text{Pb}_5(\text{VO}_4)_3\text{I}$) has relatively large ion Pb^{2+} in the Ca(I)/Ca(II) sites and VO_4 in the tetrahedron site, leading to a large channel size (Audubert et al., 1997). The success of the synthesis is largely inspired by a natural mineral, vanadinite - $\text{Pb}_5(\text{VO}_4)_3\text{Cl}$, a structurally inflated apatite. The hypothesis is that apatite compositions resulting in the size of the structural channel matching with the size of iodide ion are mostly possible chemical compositions for incorporating iodide. This hypothesis is based on an observation that large channel hosts large anions and small channel hosts small anions. **Figure 6** shows such a correlation between the channel size (predicted and actual) and different anions for a collection of apatites. As shown, the ionic radii of I, Br, Cl, OH, and F are correlated with their respective channel sizes in the apatite structure. If the channel is too small for a given composition, iodide ion would not be able to fit in. Thus, the ability to predict the channel size is necessary for predicting unknown iodide apatite compositions.

The ANN simulation for the channel size was carried out similarly to those of the lattice parameters. The channel size is defined as the radius of the largest sphere held in the channel defined by Ca(II) site cations. The training and testing results of the ANN for prediction of channel size are shown in **Figure 7**. As shown, the ANN is well trained with the R values of 0.981, 0.901, and 0.945 for the training, testing and overall respectively. The average errors are 0.75%, 1.45%, and 1.10% for training, testing and overall dataset respectively. The maximum error is 4.10% for the training dataset and 6.29% for the testing. The error distributions are mostly distributed around the averages normally. Although the testing dataset is challenging, extreme outliers are rare. Only two cases are predicted with over 4% off

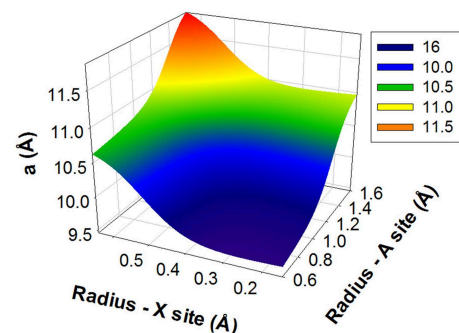


FIGURE 5 | An Artificial Neural Network for the prediction of unit cell parameter a . The figure is color coded with red color for high value and blue color for small value. For any given average radii of A and X site cations, the cell parameter a can be predicted by just reading the value at the surface of predicted cell parameter a .

the experimental values. These results suggest that the trained and tested ANN is satisfactory and can be used to predict the channel size for unknown chemical compositions with iodide in the channel.

To illustrate how to use the trained and tested ANN, **Figure 8** shows a prediction of possible iodide apatite compositions. The optimal radius of the channel should match the combined radius of iodide ion and Ca(II) site cation. For the ionic radius of iodide 2.20 Å and 3.5% flexibility of the structure and error of the ANN prediction, which is set to approximately the maximum error excluding the two extreme cases out of 86 cases, the possible

iodide chemical compositions are those that their X and A site cation average radii fall within the pink curves at X-A plane in **Figure 8**. The corresponding channel size falls at the surface within the pink curves. As it is projected on to the radius-X and radius-A plane, the region between the pink lines is possible average X and A site cations. Thus, possible A site cations include: Ag^+ , Sr^{2+} , Pb^{2+} , K^+ , Ba^{2+} , and Cs^{2+} and possible X site

cations include Si^{4+} , Mn^{5+} , As^{5+} , Cr^{5+} , V^{5+} , Re^{7+} , Ge^{4+} , and Mo^{5+} , which are mainly tetrahedron forming cations. Therefore, combinations of A site = Sr^{2+} , Pb^{2+} , Cd^{2+} , Ba^{2+} of 2+ charged cations with ionic radius larger than or close to 1.2 Å, and X site = V^{5+} , As^{5+} , Cr^{5+} , and Mo^{5+} of 5+ charged tetrahedral anion may provide suitable channel size for iodide. In addition, if Si and Ge form the X site tetrahedrons, 3+ charge cations are needed for charge balance at A site. Rare earth cations of the first few elements such as La with ionic radius close or larger

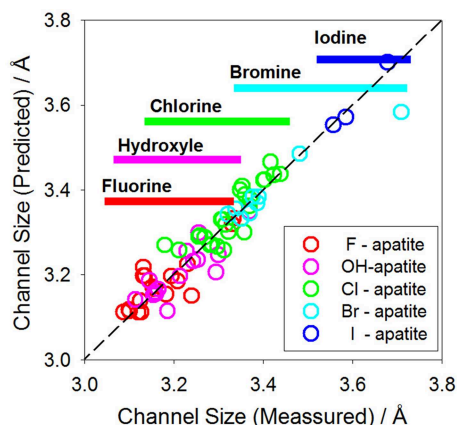


FIGURE 6 | Correlation between the channel size and ionic radius of the channel anion. The open circles are actual experimental data. The horizontal bars correspond to the range of channel size of experimental determined crystal structures. The dashed line corresponds to when predicted and actual values are equal.

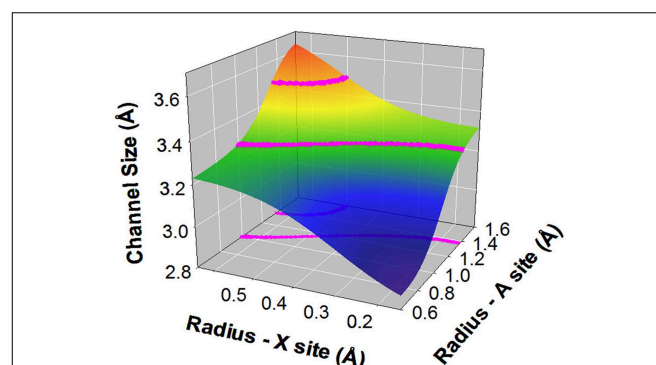


FIGURE 8 | Prediction of unknown apatite compositions with iodine in the structural channel. The region between pink lines is possible average radii of A and X cations. The two pink lines define channel size that fits iodine in the structure, which is calculated based on ionic radius of iodine 2.20 Å and 3.5% error prediction. The region is also both projected on to the radius-A and radius-X plane and on to the surface of predicted channel size.

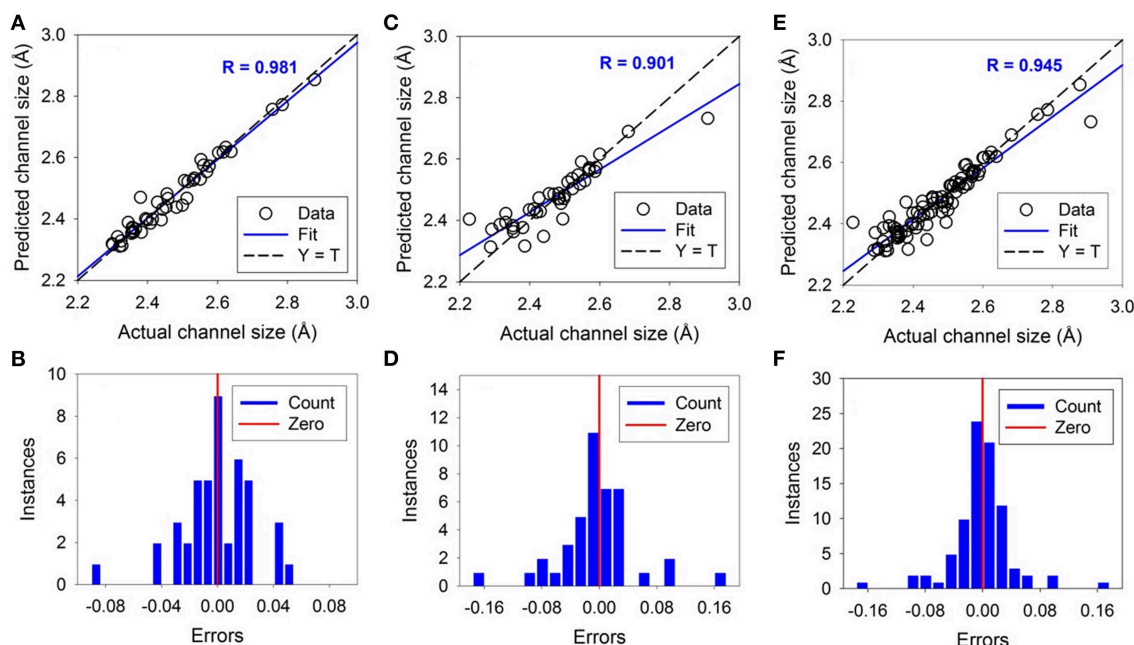


FIGURE 7 | The results of Artificial Neural Network simulations of the channel size. The upper figures show the correlations between predicted and actual values. The bottom figures show the error distributions around the vertical red bars of zero error. The dashed lines

correspond to $Y = T$ when the predicted and actual are the same. The solid lines correspond to linear fitting with a fitting coefficient of R . Open circles are experimental data. **(A,B)** are the result of training, **(C,D)** are of testing, and **(E,F)** are of the total.

than 1.2 Å are considered. It is also possible that 1+ charged cations such as Ag^+ , Cs^+ , K^+ at A site should be able to be incorporated in the apatite structure by coupled substitutions in one or more sites with higher charged ions. Indeed, Ag-Pb-V-I apatite was synthesized using a solid state reaction method (Uno et al., 2004) with the topology of the apatite structure but with a monoclinic symmetry, which is not unusual for apatite group materials (White and ZhiLi, 2003).

Concluding Remarks

Artificial Neural Network simulations of apatite show that the unit cell parameters and the detail of crystal structure (i.e., channel size) can be predicted from its chemical compositions. The results lead to a prediction of a number of possible apatite compositions with iodide incorporated in the structure. Although it is yet to see the accuracy of the prediction, the results provide important clues for designing experiments to synthesize new apatite compositions. It needs to be mentioned that the Artificial Neural Network simulations only consider crystallographic information and doesn't explicitly predict thermodynamics stability of the predicted compositions. The purpose of the simulations is to narrow down potential apatite chemical compositions from over hundreds of possibilities. These small groups of compositions are expected to be manageable by experiments. In order to further narrow down the list using a computational approach, thermodynamic stability of the predicted chemical compositions will need to be estimated by, for instance, first-principles thermodynamics calculations.

The ability to predict the properties of apatite structure using Artificial Neural Network is originated from the fact that there is a strong correlation, although non-linear, between the structure and chemical composition of apatite. In addition, a large structural and compositional database of apatite allows adequate training and testing of the Artificial Neural Networks before predictions can be made. The availability of a large database stems from the facts that there is a wide range of applications of apatite structured materials, and structural and compositional flexibilities of apatite structure, which are demonstrated from the fact that the apatite structure can even be deviated from hexagonal symmetry while maintaining the topology of apatite structure. However, such flexibilities, both

structural and compositional, are not unique to apatite structure. Many natural minerals with potential interests to nuclear waste forms have structural and compositional flexibilities similar to apatite, such as powellite related minerals—scheelite and fergusonite ABO_4 ($\text{A} = \text{Ca}, \text{Pb}, \text{Ba}, \text{Y}, \text{La}, \text{Ce}, \text{Nd}$, $\text{B} = \text{Mo}, \text{W}, \text{Nb}, \text{Ti}$), hollandite AB_8O_{16} ($\text{A} = \text{Cs}, \text{Sr}, \text{Ba}, \text{Rb}$, $\text{B} = \text{Al}, \text{Ti}, \text{Fe}, \text{Mn}$), crichtonite ($\text{Ca}, \text{Sr}, \text{La}, \text{Ce}, \text{Y}$) $(\text{Ti}, \text{Fe}, \text{Mn})_{21}\text{O}_{38}$, murataite $(\text{Y}, \text{Na})_6(\text{Zn}, \text{Fe})_5(\text{Ti}, \text{Nb})_{12}\text{O}_{29}(\text{O}, \text{F})_{14}$, to name a few. It is expected that the approach of using Artificial Neural Network to predict possible compositions of apatite of incorporating iodide could also be useful for the understanding of the relationship between chemical composition and crystal structure of other crystalline phases including those aforementioned for incorporating various fission products. For non-crystalline materials such as glass nuclear waste form, the structure is often defined at short and intermediate ranges. The local structure surrounding incorporated radionuclides is expected to vary with the composition of the glass as well as the waste composition and level of waste loading. Such variations of the local structure, mostly defined by coordination, bond distances and angles of the glass structural units, suggest structural flexibility of the glasses. The relationship between the structure and incorporated radionuclides in the glasses could then be modeled using similar approaches like Artificial Neural Network as for crystalline phases. This kind of modeling, although often challenging for glasses, is practical for crystalline phases and is imperative to the understanding of the composition-structure-property relation. The results could provide important insights for nuclear waste forms design by optimizing the chemical composition and properties for optimal performance for various nuclear waste elements.

Acknowledgments

This research is being performed using funding received from the DOE Office of Nuclear Energy's Nuclear Energy University Programs under award DE-AC07-05ID14517.

Supplementary Material

The Supplementary Material for this article can be found online at: <http://journal.frontiersin.org/article/10.3389/feart.2015.00020/abstract>

References

- Arikawa, H., Nishiguchi, H., Ishihara, T., and Takita, Y. (2000). Oxide ion conductivity in Sr-doped $\text{La}_{10}\text{Ge}_6\text{O}_{27}$ apatite oxide. *Solid State Ionics* 136, 31–37. doi: 10.1016/S0167-2738(00)00386-6
- Asadi-Eydivand, M., Solati-Hashjin, M., Farzadi, A., and Osman, N. A. A. (2014). Artificial neural network approach to estimate the composition of chemically synthesized biphasic calcium phosphate powders. *Ceramics Int.* 40, 12439–12448. doi: 10.1016/j.ceramint.2014.04.095
- Audubert, F., Carpena, J., Lacout, J. L., and Tetard, F. (1997). Elaboration of an iodine-bearing apatite Iodine diffusion into a $\text{Pb}_3(\text{VO}_4)_2$ matrix. *Solid State Ionics* 95, 113–119. doi: 10.1016/S0167-2738(96)00570-X
- Baud, G., Besse, J. P., Sueur, G., and Chevalier, R. (1979). Structure de nouvelles apatites au rhenium contenant des anions volumineux: $\text{Ba}_{10}(\text{ReO}_5)_6\text{X}_2$ ($\text{X} = \text{Br}, \text{I}$). *Mater. Res. Bull.* 14, 675–682. doi: 10.1016/0025-5408(79)90051-5
- Burakov, B. E. (2005). *Development of Fluorapatite as a Waste Form: Final Report*. Las Vegas, NV: University of Nevada.
- Campayo, L., Grandjean, A., Coulon, A., Delorme, R., Vantelon, D., and Laurencin, D. (2011). Incorporation of iodates into hydroxyapatites: a new approach for the confinement of radioactive iodine. *J. Mater. Chem.* 21, 17609–17611. doi: 10.1039/c1jm14157k
- Carpena, J., Donazzon, B., Ceraulo, E., and Prene, S. (2001). Composite apatitic cement as material to retain cesium and iodine. *Comptes Rendus De L Academie Des Sciences Serie Ii Fascicule C-Chimie*, 4, 301–308. doi: 10.1016/S1387-1609(01)01229-4

- Carpena, J., and Lacout, J. L. (2005). Calcium phosphate nuclear materials: apatitic ceramics for separated wastes. *Actual. Chim.* 37, 66–71.
- Demuth, H., and Beale, M. (2013). *Neural Network Toolbox for use with MATLAB, User's Guide*. Massachusetts: The MathWorks, Inc.
- Donald, I. W., Metcalfe, B. L., and Taylor, R. N. J. (1997). The immobilization wastes using ceramics and glasses. *J. Mater. Sci.* 32, 5851–5887. doi: 10.1023/A:1018646507438
- Easterwood, G. W., Sartain, J. B., and Street, J. J. (1989). Fertilizer effectiveness of three carbonate apatites on an acid ultisol. *Commun. Soil Sci. Plant Anal.* 20, 789–800. doi: 10.1080/00103628909368117
- Evis, Z., and Arcaklioglu, E. (2011). Artificial neural network investigation of hardness and fracture toughness of hydroxylapatite. *Ceramics Int.* 37, 1147–1152. doi: 10.1016/j.ceramint.2010.10.037
- Ewing, R. C. (2001). The design and evaluation of nuclear-waste forms: clues from mineralogy. *Can. Miner.* 39, 697–715. doi: 10.2113/gscanmin.39.3.697
- Gallagher, K., Brown, R., and Johnson, C. (1998). Fission track analysis and its applications to geological problems. *Annu. Rev. Earth Planet. Sci.* 26, 519–572. doi: 10.1146/annurev.earth.26.1.519
- Gallagher, K. (1995). Evolving temperature histories from apatite fission-track data. *Earth Planet. Sci. Lett.* 136, 421–435. doi: 10.1016/0012-821X(95)00197-K
- Garino, T. J., Nenoff, T. M., Krumhansl, J. L., and Rademacher, D. (2011a). “Development of iodine waste forms using low-temperature sintering glass,” in *Materials Challenges in Alternative and Renewable Energy Vol. 224*, eds G. Wicks, J. Simon, R. Zidan, E. LaraCurzio, T. Adams, J. Zayas, et al. (Westerville, OH: Amer Ceramic Soc.), 305–312.
- Garino, T. J., Nenoff, T. M., Krumhansl, J. L., and Rademacher, D. X. (2011b). Low-temperature sintering Bi-Si-Zn-oxide glasses for use in either glass composite materials or core/Shell I-129 waste forms. *J. Am. Ceramic Soc.* 94, 2412–2419. doi: 10.1111/j.1551-2916.2011.04542.x
- Gauthier-Lafaye, F., Holliger, P., and Blanc, P. L. (1996). Natural fission reactors in the Franceville basin, Gabon: a review of the conditions and results of a “critical event” in a geologic system. *Geochim. Cosmochim. Acta* 60, 4831–4852. doi: 10.1016/S0016-7037(96)00245-1
- Henderson, W. (2000). *Main Group Chemistry*. Hoboken, NJ: Royal Society of Chemistry.
- Hughes, J. M., Cameron, M., and Crowley, K. D. (1989). Structural variations in natural F, OH, and Cl apatites. *Am. Mineral.* 74, 870–876.
- ICSD. (2010). *Inorganic Crystal Structure Database*. Fachinformationszentrum Karlsruhe. FIZ Karlsruhe: National Institute of Standards and Technology.
- Jiang, C., Stanek, C. R., Marks, N. A., Sickafus, K. E., and Uberuaga, B. P. (2009). Predicting from first principles the chemical evolution of crystalline compounds due to radioactive decay: the case of the transformation of CsCl to BaCl. *Phys. Rev. B* 79:132110. doi: 10.1103/PhysRevB.79.132110
- Jiang, C., Uberuaga, B. P., Sickafus, K. E., Nortier, F. M., Kitten, J. J., Marks, N. A., et al. (2010). Using “radioparagenesis” to design robust nuclear waste forms. *Energy Environ. Sci.* 3, 130–135. doi: 10.1039/B915493K
- Kharton, V. V., Marques, F. M. B., and Atkinson, A. (2004). Transport properties of solid oxide electrolyte ceramics: a brief review. *Solid State Ionics* 174, 135–149. doi: 10.1016/j.ssi.2004.06.015
- Kim, J. Y., Dong, Z. L., and White, T. J. (2005). Model apatite systems for the stabilization of toxic metals: II, cation and metalloid substitutions in chlorapatites. *J. Am. Ceramic Soc.* 88, 1253–1260. doi: 10.1111/j.1551-2916.2005.00136.x
- Kockan, U., and Evis, Z. (2010). Prediction of hexagonal lattice parameters of various apatites by artificial neural networks. *J. Appl. Crystallogr.* 43, 769–779. doi: 10.1107/S0021889810018133
- Kockan, U., Ozturk, F., and Evis, Z. (2014). Artificial-neural-network prediction of hexagonal lattice parameters for non-stoichiometric apatites. *Mater. Tehnol.* 48, 73–79.
- Krumhansl, J. L., and Nenoff, T. M. (2011). Hydrotalcite-like layered bismuth-iodine-oxides as waste forms. *Appl. Geochem.* 26, 57–64. doi: 10.1016/j.apgeochem.2010.11.003
- Le Gallet, S., Campayo, L., Courtois, E., Hoffmann, S., Grin, Y., Bernard, F., et al. (2010). Spark plasma sintering of iodine-bearing apatite. *J. Nucl. Mater.* 400, 251–256. doi: 10.1016/j.jnucmat.2010.03.011
- Lemesle, L., Méar, F. O., Campayo, L., Pinet, O., Revel, B., and Montagne, L. (2014). Immobilization of radioactive iodine in silver aluminophosphate glasses. *J. Hazard. Mater.* 264, 117–126. doi: 10.1016/j.jhazmat.2013.11.019
- Lide, R. D. (2014). “Fluid properties - Vapor pressure,” in *CRC Handbook of Chemistry and Physics, 95th Edn*, ed W. M. Haynes (Boca Raton, FL: CRC Press), 6–66.
- Lu, F. Y., Dong, Z. L., Zhang, J. M., White, T., Ewing, R. C., and Lian, J. (2013). Tailoring the radiation tolerance of vanadate-phosphate fluorapatites by chemical composition control. *RSC Adv.* 3, 15178–15184. doi: 10.1039/c3ra42246a
- Lucon, P. A., and Donovan, R. P. (2007). An artificial neural network approach to multiphase continua constitutive modeling. *Composites B Eng.* 38, 817–823. doi: 10.1016/j.compositesb.2006.12.008
- Luo, Y., Hughes, J. M., Rakovan, J., and Pan, Y. (2009). Site preference of U and Th in Cl, F, and Sr apatites. *Am. Mineral.* 94, 345–351. doi: 10.2138/am.2009.3026
- Maddrell, E., Gandy, A., and Stennett, M. (2014). The durability of iodide sodalite. *J. Nucl. Mater.* 449, 168–172. doi: 10.1016/j.jnucmat.2014.03.016
- Naray-Szabo, S. (1930). The structure of apatite $\text{Ca}_5(\text{PO}_4)_3\text{F}$. *Z. Kristallographie* 75, 387–398.
- Nishi, T., Noshita, K., Naitoh, T., Namekawa, T., Takahashi, K., and Matsuda, M. (1996). Applicability of $\text{V}_2\text{O}_5\text{-P}_2\text{O}_5$ glass system for low-temperature vitrification. *MRS Proc.* 465, 221. doi: 10.1557/PROC-465-221
- Pan, Y. M., and Fleet, M. E. (2002). “Compositions of the apatite-group minerals: substitution mechanisms and controlling factors,” in *Phosphates: Geochemical, Geobiological, and Materials Importance*, Vol. 48, eds M. J. Kohn, J. Rakovan, and J. M. Hughes (Hoboken, NJ: Wiley-Blackwell), 13–49.
- Pasero, M., Kampf, A. R., Ferraris, C., Pekov, I. V., Rakovan, J., and White, T. J. (2010). Nomenclature of the apatite supergroup minerals. *Eur. J. Mineral.* 22, 163–179. doi: 10.1127/0935-1221/2010/0022-2022
- Rakovan, J., Reeder, R. J., Elzinga, E. J., Cherniak, D. J., Tait, C. D., and Morris, D. E. (2002). Structural characterization of U(VI) in apatite by X-ray absorption spectroscopy. *Environ. Sci. Technol.* 36, 3114–3117. doi: 10.1021/es015874f
- Rakovan, J. F., and Hughes, J. M. (2000). Strontium in the apatite structure: strontian fluorapatite and belovite-(Ce). *Can. Mineral.* 38, 839–845. doi: 10.2113/gscanmin.38.4.839
- Redfern, S. A. T., Smith, S. E., and Maddrell, E. R. (2012). High-temperature breakdown of the synthetic iodine analogue of vanadinite, $\text{Pb}_5(\text{VO}_4)_3\text{I}$: an apatite-related compound for iodine radioisotope immobilization? *Mineral. Mag.* 76, 997–1003. doi: 10.1180/minmag.2012.076.4.15
- Sakuragi, T., Nishimura, T., Nasu, Y., Asano, H., Hoshino, K., and Iino, K. (2008). Immobilization of radioactive iodine using AgI vitrification technique for the TRU wastes disposal: evaluation of leaching and surface properties. *MRS Proc.* 1107:279. doi: 10.1557/PROC-1107-279
- Samarasinghe, S. (2006). *From Data to Models. Neural Networks for Applied Sciences and Engineering*. Boca Raton, FL: Auerbach Publications.
- Sava, D. F., Garino, T. J., and Nenoff, T. M. (2012). Iodine confinement into Metal-Organic Frameworks (MOFs): low-temperature sintering glasses to form novel Glass Composite Material (GCM) alternative waste forms. *Ind. Eng. Chem. Res.* 51, 614–620. doi: 10.1021/ie200248g
- Shannon, R. (1976). Revised effective ionic radii and systematic studies of interatomic distances in halides and chalcogenides. *Acta Crystallogr. Sect. A* 32, 751–767. doi: 10.1107/S0567739476001551
- Sheppard, G. P., Hriliac, J. A., Maddrell, E. R., and Hyatt, N. C. (2006). Silver Zeolites: iodide Occlusion and conversion to Sodalite—a potential 129I waste form? *MRS Proc.* 932, 7. doi: 10.1557/PROC-932-36.1
- Stennett, M. C., Pinnock, I. J., and Hyatt, N. C. (2011). Rapid synthesis of $\text{Pb}_5(\text{VO}_4)_3\text{I}$ for the immobilisation of iodine radioisotopes, by microwave dielectric heating. *J. Nucl. Mater.* 414, 352–359. doi: 10.1016/j.jnucmat.2011.04.041
- Szente, L., Fenyvesi, E., and Szejtli, J. (1999). Entrapment of iodine with cyclodextrins: potential application of cyclodextrins in nuclear waste management. *Environ. Sci. Technol.* 33, 4495–4498. doi: 10.1021/es981287r
- The MathWorks, I. (2011). *MATLAB and Artificial Neural Network Toolbox Release 2011a*. Massachusetts: The MathWorks, Inc.
- Uno, M., Kosuga, A., Masuo, S., Imamura, M., and Yamanaka, S. (2004). Thermal and mechanical properties of $\text{AgPb}_9(\text{VO}_4)_6\text{I}$ and $\text{AgBa}_9(\text{VO}_4)_6\text{I}$. *J. Alloys Comp.* 384, 300–302. doi: 10.1016/j.jallcom.2004.04.094
- Uno, M., Shinohara, M., Kurosaki, K., and Yamanaka, S. (2001). Some properties of a lead vanado-iodoapatite $\text{Pb}_{10}(\text{VO}_4)_6\text{I}_2$. *J. Nucl. Mater.* 294, 119–122. doi: 10.1016/S0022-3115(01)00462-7

- Vallet-Regi, M., and Gonzalez-Calbet, J. M. (2004). Calcium phosphates as substitution of bone tissues. *Prog. Solid State Chem.* 32, 1–31. doi: 10.1016/j.progsolidstchem.2004.07.001
- Weber, W. J., Ewing, R. C., and Meldrum, A. (1997). The kinetics of alpha-decay-induced amorphization in zircon and apatite containing weapons-grade plutonium or other actinides. *J. Nucl. Mater.* 50, 147–155. doi: 10.1016/S0022-3115(97)00271-7
- Weber, W. J., Zhang, Y. W., and Wang, L. M. (2012a). Review of dynamic recovery effects on ion irradiation damage in ionic-covalent materials. *Nucl. Instrum. Methods Phys. Res. Sect. B Beam Interac. Mater. Atoms* 277, 1–5. doi: 10.1016/j.nimb.2011.12.043
- Weber, W. J., Zhang, Y. W., Xiao, H. Y., and Wang, L. M. (2012b). Dynamic recovery in silicate-apatite structures under irradiation and implications for long-term immobilization of actinides. *RSC Adv.* 2, 595–604. doi: 10.1039/C1RA00870F
- White, T., Ferraris, C., Kim, J., and Madhavi, S. (2005). “Apatite—an adaptive framework structure,” in *Micro- and Mesoporous Mineral Phases*, Reviews in Mineralogy & Geochemistry, Vol. 57, eds G. Ferraris and S. Merlino (Chantilly, VA: Mineralogical Society of America), 307–401.
- White, T. J., and ZhiLi, D. (2003). Structural derivation and crystal chemistry of apatites. *Acta Crystallogr. Sect. B*, 59, 1–16. doi: 10.1107/S0108768102019894
- Wopenka, B., and Pasteris, J. D. (2005). A mineralogical perspective on the apatite in bone. *Mater. Sci. Eng. C Biomimetic Supramol. Syst.* 25, 131–143. doi: 10.1016/j.msec.2005.01.008
- Wu, P., Zeng, Y. Z., and Wang, C. M. (2004). Prediction of apatite lattice constants from their constituent elemental radii and artificial intelligence methods. *Biomaterials* 25, 1123–1130. doi: 10.1016/S0142-9612(03)00617-3
- Wu, S., Wang, S., Simonetti, A., Chen, F., and Albrecht-Schmitt, T. E. (2011). Incorporation of iodate into uranyl borates and its implication for the immobilization of I-129 in nuclear waste repositories. *Radiochim. Acta* 99, 573–579. doi: 10.1524/ract.2011.1864
- Yang, J. H., Shin, J. M., Park, J. J., and Park, G. (2013). Waste form of silver iodide (AgI) with low-temperature sintering glasses. *Sep. Sci. Technol.* 49, 298–304. doi: 10.1080/01496395.2013.817424
- Yao, T., Lu, F., Sun, H., Wang, J., Ewing, R. C., and Lian, J. (2014). Bulk iodoapatite ceramic densified by spark plasma sintering with exceptional thermal stability. *J. Am. Ceramic Soc.* 97, 2409–2412. doi: 10.1111/jace.13101
- Zhang, M., Maddrell, E. R., Abraitis, P. K., and Salje, E. K. H. (2007). Impact of leach on lead vanado-iodoapatite $Pb_5(VO_4)_3I$: an infrared and Raman spectroscopic study. *Mater. Sci. Eng. B Solid State Mater. Adv. Technol.* 137, 149–155. doi: 10.1016/j.mseb.2006.11.003
- Zhang, Z., and Friedrich, K. (2003). Artificial neural networks applied to polymer composites: a review. *Composites Sci. Technol.* 63, 2029–2044. doi: 10.1016/S0266-3538(03)00106-4

Conflict of Interest Statement: The author declares that the research was conducted in the absence of any commercial or financial relationships that could be construed as a potential conflict of interest.

Copyright © 2015 Wang. This is an open-access article distributed under the terms of the Creative Commons Attribution License (CC BY). The use, distribution or reproduction in other forums is permitted, provided the original author(s) or licensor are credited and that the original publication in this journal is cited, in accordance with accepted academic practice. No use, distribution or reproduction is permitted which does not comply with these terms.

Dense Iodoapatite Ceramics Consolidated by Low-Temperature Spark Plasma Sintering

Tiankai Yao,[‡] Spencer Scott,[‡] Guoqing Xin,[‡] Fengyuan Lu,[§] and Jie Lian^{‡,†}

[‡]Department of Mechanical, Aerospace, and Nuclear Engineering, Rensselaer Polytechnic Institute, Troy, New York 12180

[§]Mechanical & Industrial Engineering, Louisiana State University, Baton Rouge, Louisiana 70803

Pb_{9.85}(VO₄)₆I_{1.7}, a potential waste form for long-lived I-129 immobilization, experiences phase decomposition and thus iodine loss at an elevated temperature above 400°C, presenting a significant challenge for effective management of radioactive iodine. In this work, we report low-temperature consolidation of dense iodoapatite pellets with above 95% theoretical density by spark plasma sintering (SPS) at temperatures as low as 350°C for 20 min without iodine loss. Microstructure analysis indicates a nanocrystalline ceramic with an average grain size less than 100 nm. Grain growth dominates the sintered microstructure at higher temperatures and longer durations. The dense nanoceramics have significantly-improved fracture toughness as compared with bulk coarsened grain structures. The effects of sintering temperatures (350°C, 400°C, 500°C, and 700°C) and durations (0–20 min) on microstructure, density, fracture morphology, and mechanical properties including Young's modulus and hardness of bulk samples were investigated. Low temperature densified iodoapatites suggest immense potential of SPS as an advanced materials fabrication technology for the development of waste forms for immobilization of volatile radionuclides including radioactive iodine.

I. Introduction

RADIOACTIVE iodine isotope I-129, as a byproduct of uranium fission with a long half-life of 15.7 million years, has significant environmental and health impacts on metabolic process of human beings. Fukushima nuclear accident led to a significant amount of I-129 discharged into North Pacific sea.¹ Capture of iodine off-gas resulting from reprocessing of spent nuclear fuels and consolidation into durable waste forms are critical for the safe deposition of radioactive iodine.

Current waste form reference technology based on borosilicate glass is not suitable for iodine incorporation as glass formation and vitrification typically occur from elevated temperatures much higher than the melting temperature of iodide (e.g., 558°C for AgI and 400°C for PbI₂). Novel waste forms, such as glass-AgI composite,² iodine-bearing glass,³ metal-organic frameworks,⁴ are proposed to capture and confine I₂ gas into durable waste forms. Pure ceramic waste forms, based on iodoapatite [Pb_{9.85}(VO₄)₆I_{1.7}],⁵ are also proposed for immobilization of I-129 due to their high geological and chemical durability,⁶ thermal stability,⁷ and extreme high rate of iodine loading (~7.3 wt%, estimated from chemical formula).^{8,9} However, powder fabrication and consolidation of iodoapatite into

durable waste forms are challenging. Thermal calcination that transforms constituent oxides and iodide to iodoapatite was triggered at 700°C,^{10,11} above the decomposition temperature of iodoapatite. Therefore, a buffer layer was designed to prevent iodine release during fabrication. Reactive microwave sintering allows sintering of iodoapatite within several minutes and thus iodine loss is minimized,¹² however, the sintered sample exhibits porous microstructures; and minor relics of unreacted PbI₂.

Spark plasma sintering (SPS), a field-assisted sintering technology, allows sintering and densification of materials at much reduced temperatures and shorter durations than conventional sintering techniques.¹³ Its application in nuclear industry, such as fabrication of accident tolerance fuels,¹⁴ oxide-dispersion strengthened steel alloys,¹⁵ and nuclear waste forms¹⁶ is emerging. It has advantages of preserving fine grain structure and sustaining microstructure integrity due to the fast volumetric heating technique involved.

Both reactive SPS from co-milled Pb₃(VO₄)_{1.6}(PO₄)_{0.4} with PbI₂ powders and non-reactive SPS from iodoapatite powders were adopted to prepare ceramic waste forms.¹⁷ However, molten PbI₂ and abnormal grain growth were observed. An advanced powder fabrication method based on high-energy ball milling (HEBM), is developed to fabricate iodoapatite powders in our previous study.¹⁸ Encouraged by the extremely fast heating rate (200°C/min) of SPS, we attempted 700°C sintering from HEBMed powder and obtained dense sample (>96% TD); however, submicrometer voids exist, indicating slight decomposition of iodoapatite and iodine release. Very recently, Pb₁₀(VO₄)₆I₂ powder was fabricated by dry ball milling and subsequently densified by hot pressing at 400°C.¹⁹ Reactive SPS using Pb₃(VO₄)_{1.6}(PO₄)_{0.4} and PbI₂ as reactants was also studied and an optimized sintering temperature was identified to be 450°C.²⁰

Potential ceramic waste form materials should also have desired mechanical properties to retain their structural integrity and improve performance. However, apatite ceramics are typically brittle. For instance, hydroxyapatite (HA) has a relatively low fracture toughness (~0.58 MPa·m^{1/2})²¹ varies with sintering temperature and grain size.²² Ca₉Nd(PO₄)₅(SiO₄)F₂ has a fracture toughness of 0.75 MPa·m^{1/2},²³ similar to hydroxyapatite. Different approaches, including doping,²⁴ compositing,^{21,25} and microstructure control,²⁶ have been utilized to improve fracture toughness of apatite. For example, MgO-doped dense hydroxyapatite shows a greatly improved fracture toughness of 1.48 MPa·m^{1/2} because of enhanced crack deflection by nanoscale grain size.²⁴ Limited mechanical properties data are available for dense iodoapatite, and the only literature data for Pb₁₀(VO₄)₆I₂ is an elastic modulus and hardness of 26 and 4.3 GPa, respectively¹⁰ for sample with 82.3% TD prepared by high-pressure sintering at 500°C for 5 h.

This study presents the consolidation of HEBMed iodoapatite powders into dense pellets by SPS at temperatures as low as 350°C. The effects of different temperatures and dura-

C. Jantzen—contributing editor

tions on microstructure, sintering characteristics, and mechanical properties are explored. Dense (~97% TD) pure nanocrystalline iodoapatite samples with greatly enhanced fracture toughness were successfully fabricated at 350°C for 20 min under a pressure of 60 MPa. Effects of microstructure features on mechanical properties of sintered samples were also discussed.

II. Experimental Details

(1) Powder Fabrication by Solid-State Reaction

The iodoapatite powders were synthesized by a solid-state reaction at room temperature, in which the constituent oxides were processed by HEBM ((Fritsch, Pulverisette 7, Idar-Oberst, Germany). Specifically, 10 g of constituent powders of PbI_2 (99% purity; ACROS, Fair Lawn, NJ), V_2O_5 (98% purity; Sigma-Aldrich, St. Louis, MO), and PbO (99.9% purity; Alfa Aesar, Ward Hill, MA) according to stoichiometric $\text{Pb}_{10}(\text{VO}_4)_6\text{I}_2$ were mixed with 100 g ZrO_2 balls (2 mm) in an 80 mL vial. To facilitate particle break down and the chemical reaction, 10 mL of ethanol was added. Wet HEBM could also reduce volatility of produced powders through particle agglomeration in solution. Real-time monitor of HEBM showed the highest temperature within the vial approached 50°C at the end of HEBM. Amorphous particle matrix with 5–10 nm crystalline clusters was obtained after 10 h milling at a speed of 500 rpm with 10 min on and 5 min off.¹⁸ Obtained slurry was dried in fume hood overnight before thermal annealing at 200°C for 1 h prior to consequent consolidation. Thermal stability of annealed powder samples was characterized by thermogravimetric analysis (TGA; Q50, TA instruments, Inc. DE) in nitrogen atmosphere.

(2) Spark Plasma Sintering Processing

For each sintering, 1.5 g iodoapatite powders were loaded into a graphite die with an inner diameter of 14.75 mm. SPS (SPS 10-3; Thermal Technology, Santa Rosa, CA) consolidation was conducted at various temperatures between 300°C–700°C using a pulse cycle of 25 ms on and 3 ms off in helium atmosphere. Control temperature was monitored using a K-type thermal couple placed 2 mm beneath the powder sample within the graphite punch. Temperature increasing rate was fixed at 50°C per minute. A preloaded pressure of 3 MPa was increased linearly to 60 MPa with temperatures for all the sintering. After sintering, pressure was hold until the sample cool down with furnace to room temperature. Density of the sintered samples was measured according to Archimedes principle using deionized water as immersing media at room temperature.

(3) Structural Characterizations

Sectioned samples of the sintered samples were polished down using sand papers and final polishing was conducted by 0.3 μm alumina paste. To clearly reveal grain boundary, the polished samples were thermally etched at temperature 100°C lower than their sintering temperature for 0.5 h. Both thermal etched and fracture surfaces were analyzed using Carl Zeiss Supra55 scanning electron microscopy (SEM; Jena, Germany). Phase composition of the sintered samples was probed by XRD (PANalytical, Westborough, MA) using CuK_α ($\lambda = 1.5406 \text{ \AA}$) as the incident beam with a scanning step of 0.05° and a rate of 2 s per step.

(4) Mechanical Properties Measurement

The elastic modulus and hardness of the sintered samples were measured using Hysitron Triboindenter (Hysitron Inc. Minneapolis, MN) with a 100 nm Berkovich pyramidal tip. Before measurement, tip-area was calibrated using a standard fused quartz. Indentation was performed on the surface

polished by 0.3 μm alumina slurry with loading and unloading rates of 10 and a 3 s holding at the peak load of 500 mN. Oliver-Pharr model²⁷ was applied to calculate elastic modulus from the unloading curves. Hardness was also measured by nanoindentation.

Vickers microhardness indentation technique was utilized to estimate the fracture toughness of sintered samples. To produce well defined cracks, a 1 kg loading was applied on the mechanically-polished surface with 15 s holding time at the peak loading. Post indentation measurement was conducted right after using a Zeiss Microscopy. Indentation fracture toughness values were estimated using the following equation:²⁸

$$K_{\text{IC}} = 0.016 \left(\frac{E}{H} \right)^{0.5} \left(\frac{P}{C^{1.5}} \right)$$

where K_{IC} is estimated fracture toughness. E and H are the obtained elastic modulus and hardness from nanoindentation, respectively; P is applied loading during indentation; and C is measured crack length from center of indent.

III. Results and Discussion

(1) Densification and Grain Coarsening of Iodoapatite Samples

In a previous work,⁷ iodine-bearing apatite powders [$\text{Pb}_{9.85}(\text{VO}_4)_6\text{I}_{1.7}$] fabricated by dry HEBM and thermal annealing were consolidated into a bulk sample form at 700°C for 1 min with a density as high as 95.9% TD. However, this temperature is too high for iodoapatite to be stable as evidenced by submicrometer-sized pores even in samples sintered at this temperature without holding (Fig. 1). Those holes distribute on the facet-like transgranular fracture surface. Because the sintering temperature is too high, bubbles may form by phase decomposition during sintering. During cooling, those holes become the origin of cracks that break the sintered samples. Such a potential iodine release may require extra ventilation systems for radioactive I-129 processing. Therefore, one of the target for this study is to explore sintering conditions without iodine release.

Figure 2(a) shows the starting iodoapatite powders with an average grain size of $33 \pm 4 \text{ nm}$ (determined by manual measurements over more than 100 grains) synthesized by wet HEBM and subsequent thermal annealing at 200°C for 1 h.

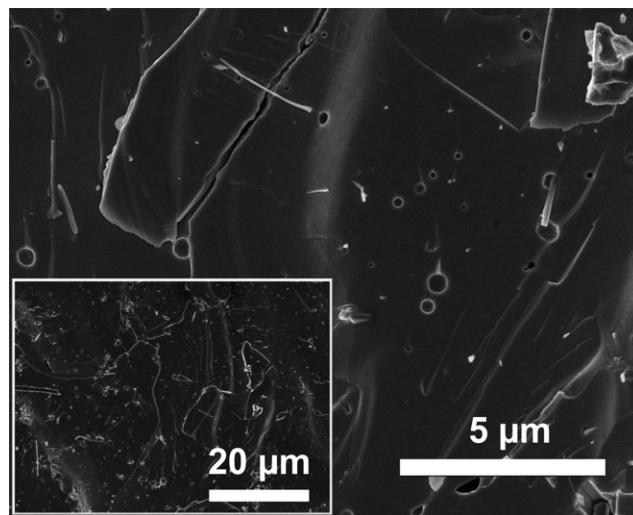


Fig. 1. Cross-sectional transgranular fracture surface with submicrometer pores in iodoapatite samples sintered at 700°C without holding under pressure of 40 MPa from powders fabricated by dry HEBM and subsequent thermal annealing at 200°C for 1 h.

TGA analysis¹⁸ indicated that the onset of significant weight loss is about 400°C. This temperature is relatively lower than that of sintered samples by microwave sintering (500°C)¹² and hot-pressed lead vanadate iodine apatite (520°C)¹⁹ possibly due to large free surface area of loosen powders. Powdered sample after TGA test from room temperature to 800°C was characterized to be $\text{Pb}_3(\text{VO}_4)_2$ [Fig. 2(b)], indicating phase decomposition of starting iodoapatite powders at elevated temperature to $\text{Pb}_3(\text{VO}_4)_2$ and PbI_2 . PbI_2 has a melting point of 402°C,¹⁰ and may exist as yellowish gaseous or solid forms, depending on temperatures. Accompanying the phase decomposition, a color change of powder samples was observed from dark yellow [inset in Fig. 2(a)] to yellowish [inset in Fig. 2(b)].

To eliminate the potential release of volatile iodine, consolidation of iodoapatite should be conducted at temperatures not higher than 400°C based on aforementioned TGA results. Therefore, SPS was conducted at a low temperature range of 300°C–400°C with the holding time from 0 to 20 min (Fig. 3). For comparison, higher temperature sintering at 500°C and 700°C was also attempted without holding to study effects of temperatures on powder densification and properties. Detailed sintering conditions, density and grain size, are presented in Table I and on the densification map [Fig. 3(c)].

Sample density increases with temperatures from 300°C ($68.3\% \pm 3.7\%$ TD) to 325°C ($81.1\% \pm 2.0\%$ TD) and further to 350°C ($96.4\% \pm 1.5\%$ TD) [Fig. 3(c)]. Despite the significant increase in density, the nanocrystalline grain size remained unchanged with respect to temperature. The increase in density with temperature indicates that densifica-

Table I. Summary of Sintering Conditions and Physical Properties of the SPS-densified Iodoapatite

Sample ID	Sintering temperature (°C)	Sintering time (min)	Density (TD)	Grain size (nm)
300-20	300	20	68.3 ± 3.8	71.8 ± 13.5
325-20	325	20	81.1 ± 2.0	67.5 ± 9.6
350-0	350	0	82.5 ± 1.4	73.5 ± 7.9
350-20	350	20	96.4 ± 1.6	87.8 ± 25.1
400-5	400	5	97.5 ± 0.7	157.4 ± 33.4
400-20	400	20	97.7 ± 0.4	220 ± 121.5
500-0	500	0	96.8 ± 1.8	224.0 ± 61.0
700-0	700	0	96.0 ± 1.4	477.5 ± 315.0

tion dominates the sintering process while grain size remains relatively unchanged.

Samples sintered at 400°C for 5 min are pure iodoapatite [$\text{Pb}_{9.85}(\text{VO}_4)_6\text{I}_{1.7}$] as suggested by the XRD pattern [Fig. 3(a)]. Samples sintered at 400°C for 20 min possess the highest density of 97.7% TD. Compared with samples sintered at 400°C for 5 min, there is an indistinguishable increase of density and an appreciable grain growth from 157 ± 33 nm to 220 ± 122 nm. In this case, grain growth dominates the sintering process at 400°C following densification after prolonged sintering time (e.g., after 5 min holding).

At higher temperature (above 400°C), a small reduction of density was observed with increase of sintering temperatures from 500°C to 700°C (Table I). However, grain size increases

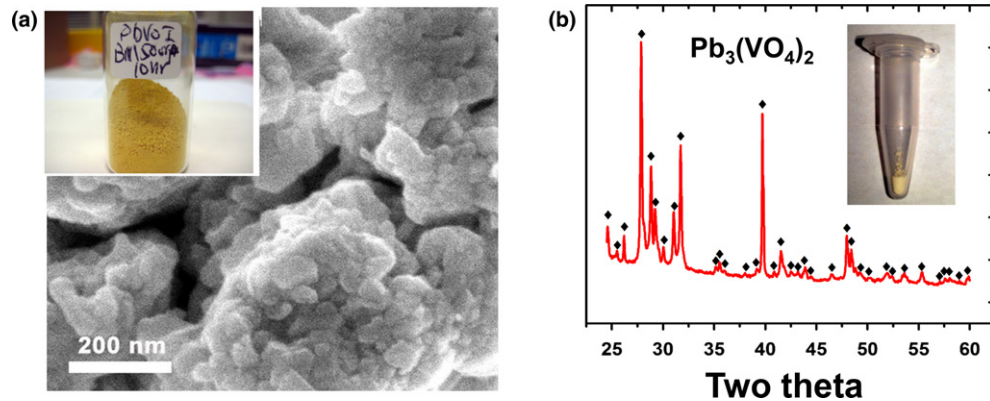


Fig. 2. (a) Nanosized lead vanadate iodoapatite powders fabricated by wet HEBM and subsequent thermal annealing at 200°C for 1 h (dark yellow powders in a glass vial); (b) After TGA experiment from room temperature to 800°C, debris (yellowish powders as shown in a plastic tub) were characterized by XRD to be $\text{Pb}_3(\text{VO}_4)_2$ phase mainly.

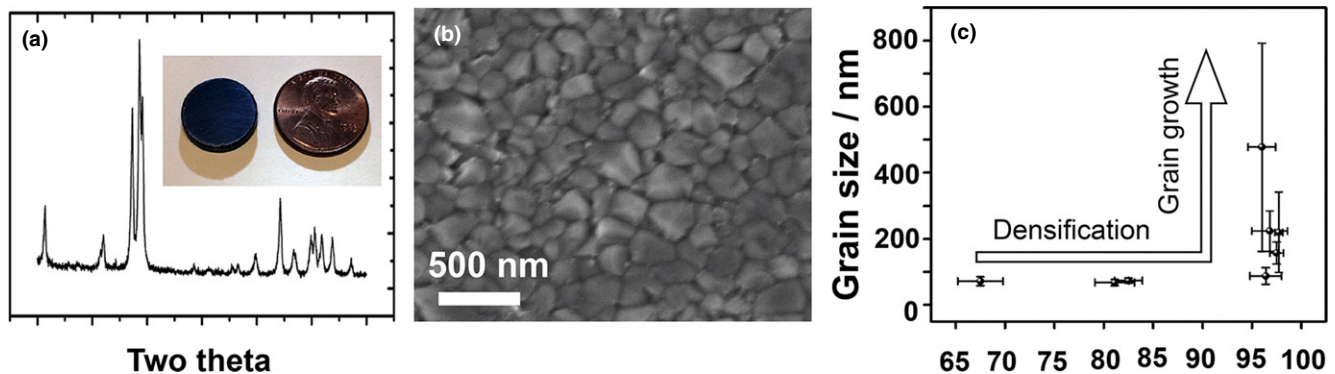


Fig. 3. (a) A XRD pattern for the 400-5 sample with picture inseted at upright corner where US penny is also presented as size reference; thickness is ~1 mm; (b) thermally etched surface of 500-0 sample; (c) a densification map for sintering conditions summarized in Table I.

dramatically, especially for 700-0 samples [Fig. 3(c)]. Yellow deposition on graphite spacers were also observed after sintering from phase decomposition and release of iodine through gaps of graphite tooling, and solidified on surface of cooler graphite spacers. However, nondetectable deposition on chamber face was found, suggesting the degree of phase decomposition is minor.

In a brief summary, densification dominates the sintering processes at temperature not higher than 400°C for the studied sintering time span (0–20 min). At higher sintering temperatures, grain growth dominates. Above 400°C, accompanying abnormal grain growth, a phase decomposition happened during sintering, and thus density of the sintered body is slightly decreased. These results indicate that by fine controlling SPS process, the densification and grain growth can be well separated, allowing the control of microstructure to obtain nanocrystalline ceramics.

(2) Microstructure Evolution and Fracture Morphology of the Sintered Samples

Cross section fracture surfaces of the samples sintered at low temperatures (300°C–350°C) and higher temperatures (400°C, 500°C, and 700°C) are presented in Figs. 4 and 5. Large open pores surrounding grain agglomerates as well as small closed pores are visible in the sample sintered at 300°C for 20 min [Fig. 4(a)], consistent with its low density (less than 70%) and suggesting minimal densification upon sintering. These large open pores inhibit grain boundary migration and thus grain growth. Also, small closed holes located at the tri-junction points of grains help to pin grain boundary migration.²⁹ Similar microstructure features are observed for samples sintered at 325°C for 20 min [Fig. 4(b)]. However, much denser microstructure was observed in the sample sintered at 350°C for 20 min [Figs. 4(c) and (d)]. Although large-sized open pores were completely eliminated, closed pores of tens nanometers embedded into a nanocrystalline matrix can still be observed on fracture surfaces. A mixture of inter- and trans-granular fracture models [Fig. 4(d)] suggests the strength of certain grain interior is superior to that of grain

boundary, and the latter becomes preferred crack propagation path.

When temperature is increased to 400°C for 5 min [Fig. 5(a)], sintering renders a finer microstructure than that of the sample sintered at 20 min at the same temperature [Fig. 5(b)]. A slightly abnormal grain growth is indicated by the coexistence of 50 and 200 nm grains in samples sintered for 20 min [Fig. 5(b)]. Fracture surface is dominated by inter-granular fracture model, underlining that grain boundary weakens with increasing of sintering temperatures.

Increasing temperatures further to 500°C [Figs. 5(c) and (d)], intergranular fracture surface was decorated by nanometer secondary phase particle. This secondary phase cannot be detected by XRD probably due to its limited quantity. However, based on the phase decomposition products of iodoapatite powders, those nanoparticles should be solidified PbI_2 or lead vanadium oxide. During sintering, when temperature is higher than 400°C, iodoapatite powders begin to decompose. PbI_2 was melted and can be released due to its relatively low melting point of 402°C. After bulk sample was cooled to temperature lower than 402°C, retained liquid phase within bulk sample begins to solidify and agglomerates to nanoparticle clusters.

Continue increasing sintering temperatures to 700°C [Figs. 5(e) and (f)] results in an appreciable abnormal grain growth with severely elongated prismatic grains embedded into a fine matrix, leading to a bimodal grain size distribution. Although the bimodal grain size microstructure is well-known for its capability to improve fracture toughness by deflecting cracks at fine grains,³⁰ long cracks [inset of Fig. 5(e)] still stretch tens of micrometers and can be easily observed in sintered pellet. Agglomerates of solidified lead iodide on grain boundaries indicate phase decomposition during sintering and degradation of iodine retention capability. Also, those agglomerates on grain boundary may also alter apatite performance under leaching condition.

In sum, sintering at elevated temperatures (500°C and 700°C) is not favorable for the development of apatite waste form for iodine immobilization due to possible phase decomposition, micro-crack generated, and potential release of

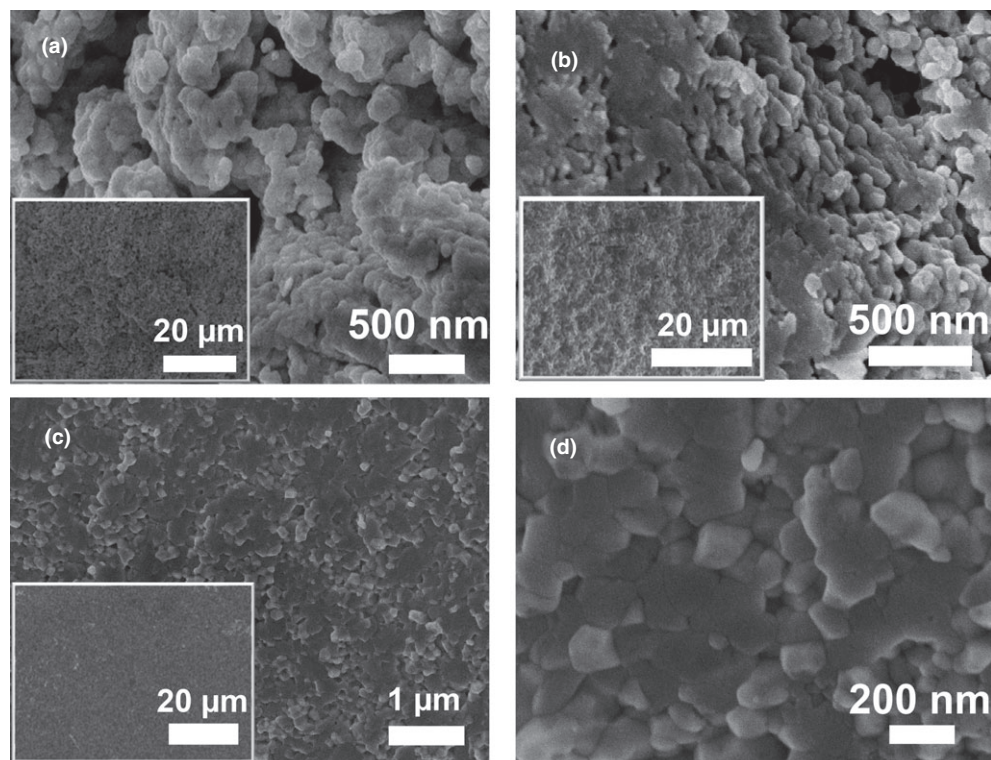


Fig. 4. Cross-sectional fracture surfaces for 300-20 (a), 325-20 (b), and 350-20 samples [(c) and (d)].

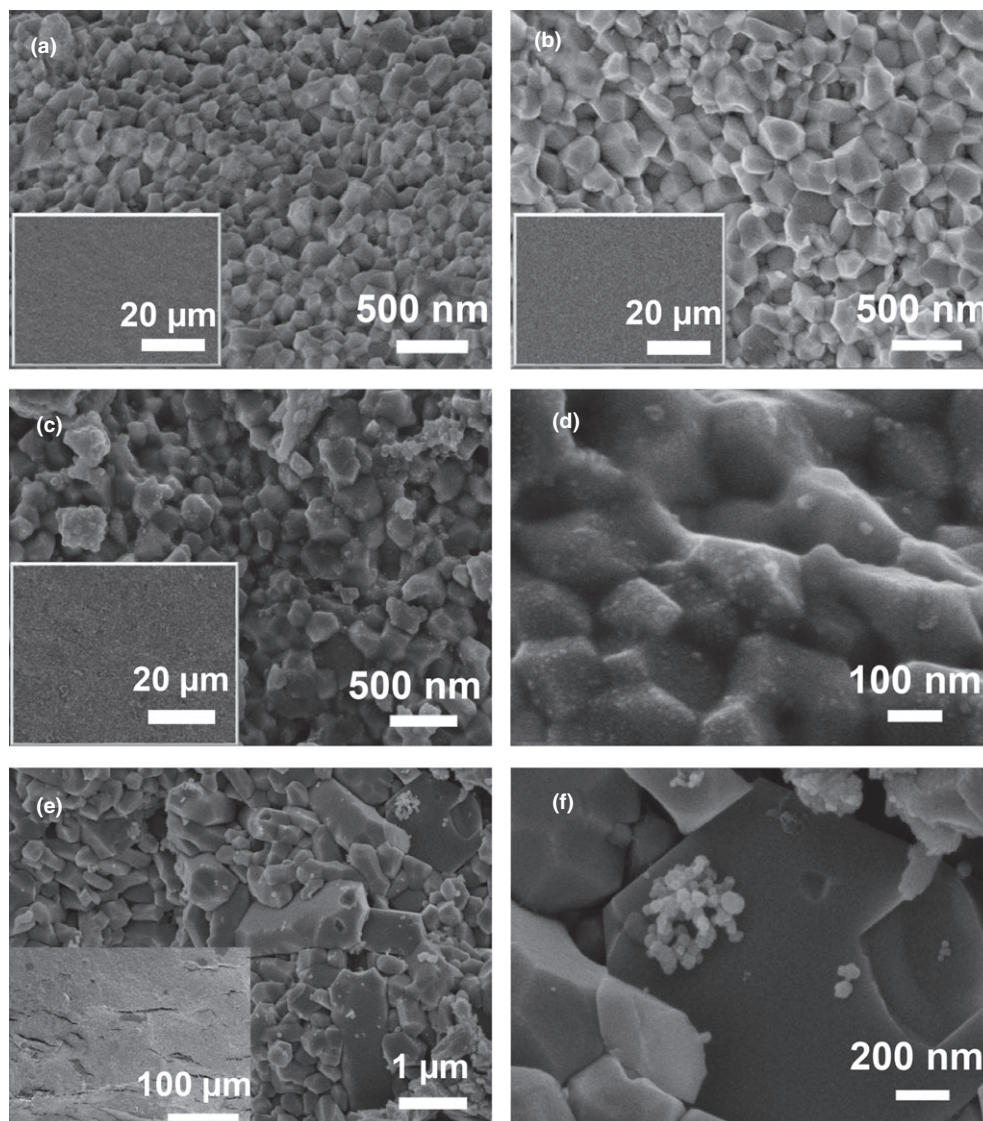


Fig. 5. Cross-sectional fracture surfaces for 400-5 (a), 400-20 (b), 500-0 [(c) and (d)], and 700-0 [(e) and (f)].

iodine containing phase (PbI_2). The extremely fast heating/cooling rates of SPS process mitigates the possible phase decomposition and gas release, allowing densification of HEBMed nanopowders at 350°C.

(3) Mechanical Properties

Mechanical properties of the sintered iodoapatite ceramic are substantially affected by microstructure features, especially densities and grain sizes. Those two factors are interdependent when grain coarsens with elimination of pores. Both Young's modulus and hardness increase with increased density exponentially. Additionally, for ceramics experiencing phase decomposition at elevated temperatures, decomposing phase could degrade mechanical properties. For example, HA samples sintered from nanopowders peaks its density at 1200°C but decreases at 1300°C due to phase decomposition; the newly formed secondary calcium phosphate phase and water vapor are responsible for the decreased hardness.³¹

In this study, phase decomposition in sintered pellets at 500°C and 700°C evidenced by observed secondary phases [Figs. 5(d) and (f)] and microcracks [inset of Fig. 5(e)] negatively impact mechanical integrity. The measured elastic modulus and hardness [Fig. 6(a)] of the single phase iodoapatite samples decreases sharply with decrease of density following the sequence of 400-20, 400-5, and 350-20 samples.

For 700-0 sample, much lower elastic modulus and hardness are observed, mainly caused by the detrimental effects from secondary phase and micro-cracks. The elastic modulus and hardness are similar to those of hot pressing samples sintered at 500°C for 5 h with a density of 82.3% TD.¹⁰ However, single phase iodoapatite samples sintered at lower temperature by SPS have much higher density and thus greater mechanical properties than the hot pressing samples. SPS is more effective of densifying HEBMed iodoapatite powders into dense pellets at low temperature without phase decomposition but extraordinary mechanical properties.

The well-known Hall-Petch relationship as observed in hydroxyapatite^{26,32,33} is not clearly identified for the iodoapatite samples in this study. Hardness first increases with larger grain sizes till 220 nm, followed by the reduction of hardness [Fig. 6(b)]. This tendency is consistent with change of sample density and a previous study³⁴ which shows the hardness of HA samples increases with sample density. These results suggest that porosity and phase purity governs the elastic and plastic behaviors of consolidated iodoapatite samples upon indentation, and thus hardness. The Hall-Petch effect may apply only to fully densified ceramic samples when the effect of porosity is diminished.

Apatite ceramics are typically brittle with low fracture toughness and thus are less resistant to crack propagation. As a potential nuclear waste form, apatite structure with

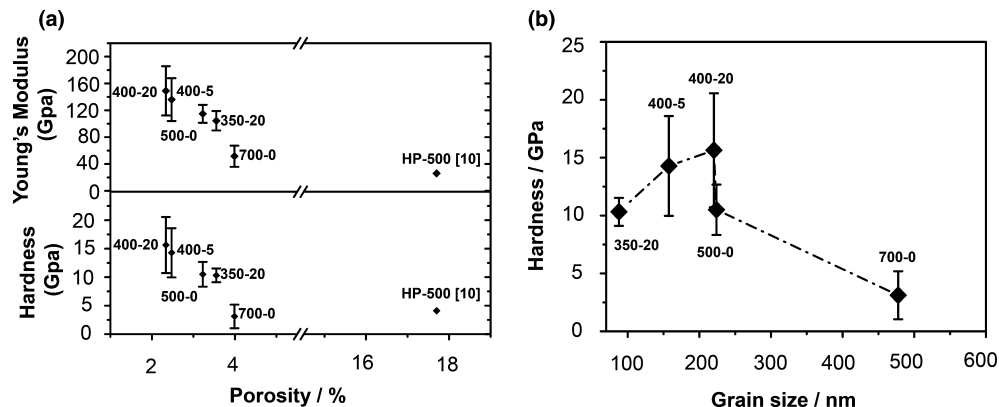


Fig. 6. Young's modulus and hardness of the sintered samples as a function of porosity (a); dependence of hardness on sample grain size (b).

higher fracture toughness would be a favorable property to maintain structural integrity. To investigate the variation of fracture toughness with sintering parameters, cracks are introduced by an indentation technique [Fig. 7(a)]. Indents are made on the surface plane perpendicular to the applied mechanical pressure on the sintered sample. Fracture patterns of the low-temperature sintered samples display intergranular fracture characters as shown in Fig. 7(b). Crack tips are harnessed by grain boundaries [Fig. 7(c)] as the fracture energy progressively consumed by crack propagating and is not sufficient to break bonding energy between adjacent grain boundaries.

Fracture toughness estimated based on the indentation as a function of grain size is shown in Fig. 7(d). No noticeable difference in the fracture toughness ($\sim 0.3\text{--}0.35\text{ MPa}\cdot\text{m}^{1/2}$) was observed for the sintered samples with grain size above 150 nm. Significant improvement in the fracture toughness as high as $0.5\text{ MPa}\cdot\text{m}^{1/2}$ occurs for the nanostructured iodoapatite ceramics synthesized at 350°C for 20 min with a grain size of $\sim 88\text{ nm}$. This result is similar to the trend for hydroxyapatite,²⁶ in which grain size has a profound effect on toughness only when grain size is smaller than 140 nm, and the highest fracture toughness is $1.06\text{ MPa}\cdot\text{m}^{1/2}$ achieved at a

grain size of 67 nm.²⁶ Particularly, grain-boundary affected zones were used to explain the extensive crack deflection and thus the enhancement of fracture toughness for hydroxyapatite with the grain size less than 100 nm. The significantly-enhanced fracture toughness for iodoapatite materials synthesized by the low-temperature SPS would greatly improve the structural integrity and thus the performance of the designed waste forms.

IV. Conclusions

Dense iodoapatite ceramic samples with a 96.5% TD can be consolidated by low temperature SPS at 350°C for 20 min, and microstructure analysis indicates a nanostructured feature with the mean grain size of $\sim 88\text{ nm}$. Higher sintering temperatures and prolonged durations for SPS sintering result in a significant grain coarsening, and phase decomposition is identified for samples sintered at temperature at 500°C and 700°C without holding. Elastic modulus and hardness are found to be closely related to the density of samples; while fracture toughness estimated by an indentation technique is governed more by grain size. Samples densified at 350°C for 20 min with nanosized grains show significant improvement of frac-

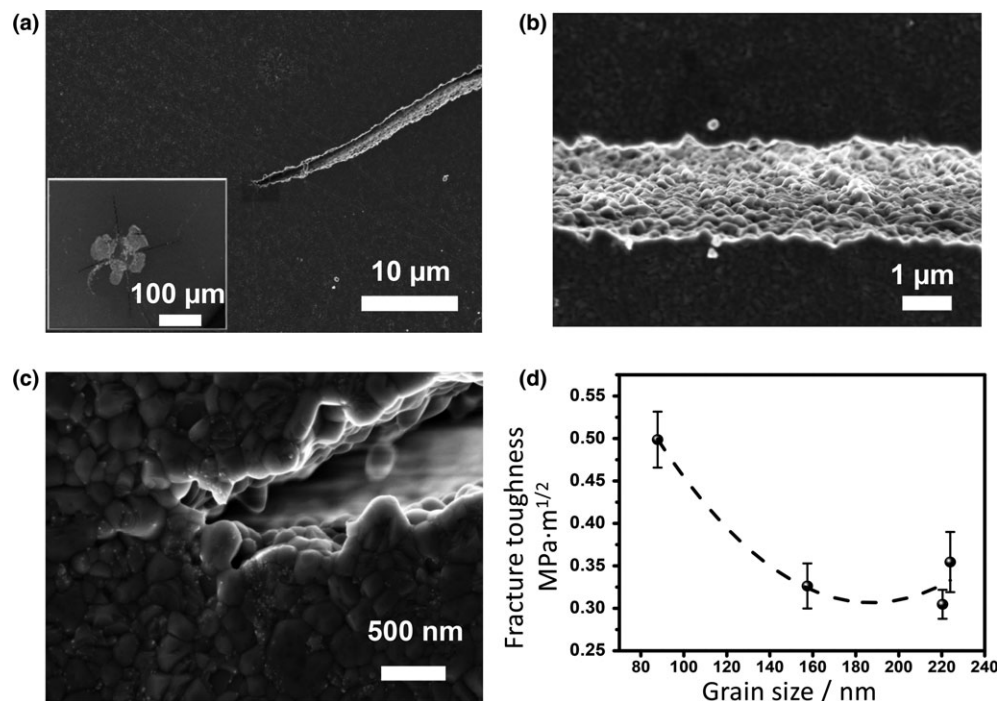


Fig. 7. Dent generated on polished surfaces perpendicular to the applied mechanical pressure of the 500-0 sample (a); a HRSEM image (b) shows crack propagation along grain boundaries and stopped at tip (c) and estimated fracture toughness as a function of grain size (d).

ture toughness over coarsened grain samples. The low-temperature SPS sintering capable of consolidating iodoapatite ceramic samples with greatly improved mechanical properties by microstructure manipulating has a significant impact in developing advanced materials for waste form application for effective nuclear waste management, particularly for highly volatile radionuclides including iodine-129.

Acknowledgment

This work was financially supported by DOE NEUP (Nuclear Engineering University Program) under award DE-AC07-05ID14517 and a NSF career award DMR 1151028.

References

- ¹X. Hou, et al., "Iodine-129 in Seawater Offshore Fukushima: Distribution, Inorganic Speciation, Sources, and Budget," *Environ. Sci. Technol.*, **47** [7] 3091–8 (2013).
- ²T. J. Garino, T. M. Nenoff, J. L. Krumhansl, and D. X. Rademacher, "Low-Temperature Sintering Bi-Si-Zn-Oxide Glasses for Use in Either Glass Composite Materials or Core/Shell 129I Waste Forms," *J. Am. Ceram. Soc.*, **94** [8] 2412–9 (2011).
- ³T. Lemesle, F. O. Méar, L. Campayo, O. Pinet, B. Revel, and L. Montagne, "Immobilization of Radioactive Iodine in Silver Aluminophosphate Glasses," *J. Hazard. Mater.*, **264** [0] 117–26 (2014).
- ⁴D. F. Sava, T. J. Garino, and T. M. Nenoff, "Iodine Confinement into Metal-Organic Frameworks (MOFs): Low-Temperature Sintering Glasses to Form Novel Glass Composite Material (GCM) Alternative Waste Forms," *Ind. Eng. Chem. Res.*, **51** [2] 614–20 (2012).
- ⁵F. Audubert, J.-M. Savariault, and J.-L. Lacout, "Pentalead Tris (Vanadate) Iodide, a Defect Vanadinite-Type Compound," *Acta Crystallogr. Sect. C: Cryst. Struct. Commun.*, **55** [3] 271–3 (1999).
- ⁶C. Guy, F. Audubert, J.-E. Lartigue, C. Latrille, T. Advocat, and C. Fillet, "New Conditionings for Separated Long-Lived Radionuclides," *C.R. Phys.*, **3** [7–8] 827–37 (2002).
- ⁷T. Yao, F. Lu, H. Sun, J. Wang, R. C. Ewing, and J. Lian, "Bulk Iodoapatite Ceramic Densified by Spark Plasma Sintering with Exceptional Thermal Stability," *J. Am. Ceram. Soc.*, **97** [8] 2409–12 (2014).
- ⁸W. J. Weber, A. Navrotsky, S. Stefanovsky, E. R. Vance, and E. Vernaz, "Materials Science of High-Level Nuclear Waste Immobilization," *MRS Bull.*, **34** [1] 46–53 (2009).
- ⁹P. Patel, "United States Launches New Direction to Manage Nuclear Waste," *MRS Bull.*, **38** [3] 206–7 (2013).
- ¹⁰M. Uno, M. Shinohara, K. Kurosaki, and S. Yamanaka, "Some Properties of a Lead Vanado-Iodoapatite $Pb_{10}(VO_4)_6I_2$," *J. Nucl. Mater.*, **294** [1–2] 119–22 (2001).
- ¹¹F. Audubert, J. Carpena, J. L. Lacout, and F. Tetard, "Elaboration of an Iodine-Bearing Apatite - Iodine Diffusion into a $Pb_3(VO_4)_2$ Matrix," *Solid State Ionics*, **95** [1–2] 113–9 (1997).
- ¹²M. C. Stennett, I. J. Pinnock, and N. C. Hyatt, "Rapid Synthesis of $Pb_5(VO_4)_3I$ for the Immobilisation of Iodine Radioisotopes, by Microwave Dielectric Heating," *J. Nucl. Mater.*, **414** [3] 352–9 (2011).
- ¹³Z. A. Munir, U. Anselmi-Tamburini, and M. Ohyanagi, "The Effect of Electric Field and Pressure on the Synthesis and Consolidation of Materials: A Review of the Spark Plasma Sintering Method," *J. Mater. Sci.*, **41** [3] 763–77 (2006).
- ¹⁴S. Yeo, E. McKenna, R. Baney, G. Subhash, and J. Tulenko, "Enhanced Thermal Conductivity of Uranium Dioxide-Silicon Carbide Composite Fuel Pellets Prepared by Spark Plasma Sintering (SPS)," *J. Nucl. Mater.*, **433** [1–3] 66–73 (2013).
- ¹⁵Q. X. Sun, T. Zhang, X. P. Wang, Q. F. Fang, T. Hao, and C. S. Liu, "Microstructure and Mechanical Properties of Oxide Dispersion Strengthened Ferritic Steel Prepared by a Novel Route," *J. Nucl. Mater.*, **424** [1–3] 279–84 (2012).
- ¹⁶Y. Watanabe, et al., "The Densification of Zeolite/Apatite Composites Using a Pulse Electric Current Sintering Method: A Long-Term Assurance Material for the Disposal of Radioactive Waste," *J. Eur. Ceram. Soc.*, **26** [4–5] 481–6 (2006).
- ¹⁷S. Le Gallet, et al., "Spark Plasma Sintering of Iodine-Bearing Apatite," *J. Nucl. Mater.*, **400** [3] 251–6 (2010).
- ¹⁸F. Lu, et al., "Facile Low Temperature Solid State Synthesis of Iodoapatite by High-Energy Ball Milling," *RSC Adv.*, **4** [73] 38718–25 (2014).
- ¹⁹Y. Suetsugu, "Synthesis of Lead Vanadate Iodoapatite Utilizing Dry Mechanochemical Process," *J. Nucl. Mater.*, **454** [1–3] 223–9 (2014).
- ²⁰L. Campayo, et al., "Relevance of the Choice of Spark Plasma Sintering Parameters in Obtaining a Suitable Microstructure for Iodine-Bearing Apatite Designed for the Conditioning of I-129," *J. Nucl. Mater.*, **457**, 63–71 (2015).
- ²¹L. Zhang, et al., "A Tough Graphene Nanosheet/Hydroxyapatite Composite with Improved *In Vitro* Biocompatibility," *Carbon*, **61** [0] 105–15 (2013).
- ²²Z. Evis and E. Arcaklioglu, "Artificial Neural Network Investigation of Hardness and Fracture Toughness of Hydroxylapatite," *Ceram. Int.*, **37** [4] 1147–52 (2011).
- ²³D. Bregiroux, F. Audubert, E. Champion, and D. Bernache-Assollant, "Mechanical and Thermal Properties of hot Pressed Neodymium-Substituted Britholite $Ca_9Nd(PO_4)_5(SiO_4)_2F_2$," *Mater. Lett.*, **57** [22–23] 3526–31 (2003).
- ²⁴C. Y. Tan, et al., "Sintering and Mechanical Properties of MgO-Doped Nanocrystalline Hydroxyapatite," *Ceram. Int.*, **39** [8] 8979–83 (2013).
- ²⁵D. Lahiri, V. Singh, A. K. Keshri, S. Seal, and A. Agarwal, "Carbon Nanotube Toughened Hydroxyapatite by Spark Plasma Sintering: Microstructural Evolution and Multiscale Tribological Properties," *Carbon*, **48** [11] 3103–20 (2010).
- ²⁶J. Wang and L. L. Shaw, "Nanocrystalline Hydroxyapatite with Simultaneous Enhancements in Hardness and Toughness," *Biomaterials*, **30** [34] 6565–72 (2009).
- ²⁷W. C. Oliver and G. M. Pharr, "An Improved Technique for Determining Hardness and Elastic Modulus Using Load and Displacement Sensing Indentation Experiments," *J. Mater. Res.*, **7** [06] 1564–83 (1992).
- ²⁸G. R. Anstis, P. Chantikul, B. R. Lawn, and D. B. Marshall, "A Critical Evaluation of Indentation Techniques for Measuring Fracture Toughness: I, Direct Crack Measurements," *J. Am. Ceram. Soc.*, **64** [9] 533–8 (1981).
- ²⁹S. C. Liao, W. E. Mayo, and K. D. Pae, "Theory of High Pressure/Low Temperature Sintering of Bulk Nanocrystalline TiO_2 ," *Acta Mater.*, **45** [10] 4027–40 (1997).
- ³⁰N. P. Padture and B. R. Lawn, "Toughness Properties of a Silicon Carbide with an *In Situ* Induced Heterogeneous Grain Structure," *J. Am. Ceram. Soc.*, **77** [10] 2518–22 (1994).
- ³¹M. Aminzare, et al., "Hydroxyapatite Nanocomposites: Synthesis, Sintering and Mechanical Properties," *Ceram. Int.*, **39** [3] 2197–206 (2013).
- ³²D. Veljović, et al., "Processing of Dense Nanostructured HAP Ceramics by Sintering and Hot Pressing," *Ceram. Int.*, **35** [4] 1407–13 (2009).
- ³³J. Wang and L. L. Shaw, "Grain-Size Dependence of the Hardness of Submicrometer and Nanometer Hydroxyapatite," *J. Am. Ceram. Soc.*, **93** [3] 601–4 (2010).
- ³⁴S. Ramesh, C. Y. Tan, S. B. Bhaduri, W. D. Teng, and I. Sopyan, "Densification Behaviour of Nanocrystalline Hydroxyapatite Bioceramics," *J. Mater. Process. Technol.*, **206** [1–3] 221–30 (2008). □

Ge Yao, Jianwei Wang*

Department of Geology and Geophysics, Center for Computation and Technology, Louisiana State University, Baton Rouge, LA 70803

* Email: jianwei@lsu.edu

Abstract

Apatite-structured materials have been considered for incorporation of a number of fission products because of their chemical durability and compositional and structural flexibilities. It is hypothesized that the effect of beta-decay on the thermodynamic stability can be mitigated by introducing appropriate electron acceptors at the neighboring sites in the structure. Apatites with compositions of $\text{Ca}_{10}(\text{PO}_4)_6\text{F}_2$ and $\text{Ca}_4\text{Y}_6(\text{SiO}_4)_6\text{F}_2$ were selected as the model systems for $^{135,137}\text{Cs}$ and ^{90}Sr incorporations respectively, where Cs substitutes Ca and Sr/Zr substitutes Y. $\text{AgFePb}_8(\text{VO}_4)_6\text{I}_2$ was selected for ^{129}I incorporations. Decay series $^{135,137}\text{Cs} \rightarrow ^{135,137}\text{Ba}$, $^{90}\text{Sr} \rightarrow ^{90}\text{Y} \rightarrow ^{90}\text{Zr}$, and $^{129}\text{I} \rightarrow ^{129}\text{Xe}$ were investigated. Electron density of states, crystal and defect structure, and formation energies of before and after beta-decay were calculated using a spin-polarized DFT approach. Ferric iron was used as the electron acceptor. The beta-decay results in an extra electron in the structure and a change of chemical species: $\text{Cs}^+ \rightarrow \text{Ba}^{2+}$, $\text{Sr}^{2+} \rightarrow \text{Y}^{3+} \rightarrow \text{Zr}^{4+}$, and $\text{I}^- \rightarrow \text{Xe}$. Calculated electron density of states suggests that the ferric ion captures the electron, and changes its oxidation state and becomes ferrous iron. The crystal and defect structures were analyzed based on the volume, lattice parameters, radial distribution functions, metal to oxygen distances, and the metaprism twist angles of the crystal structure. The results show that there are only minor changes in the crystal structure and defect structure for $\text{Ca}_{10}(\text{PO}_4)_6\text{F}_2$ with Cs^+ and Fe^{3+} substitutions undergoing $\text{Cs}^+ \rightarrow \text{Ba}^{2+}$ transmutation, and for $\text{Ca}_4\text{Y}_6(\text{SiO}_4)_6\text{F}_2$ with Sr^{2+} and Fe^{3+} substitutions undergoing $\text{Sr}^{2+} \rightarrow \text{Y}^{3+} \rightarrow \text{Zr}^{4+}$ transmutations. The last decay change, from $\text{Y}^{3+} \rightarrow \text{Zr}^{4+}$, causes larger changes of the local defect structure around Zr involving the coordination environment. Significant distortions of the local defect structure were observed for

AgFePb₈(VO₄)₆I₂ undergoing I → Xe transmutation. The results on calculated total energy suggest that transmutations of Cs⁺ → Ba²⁺ and Sr²⁺ → Y³⁺ → Zr⁴⁺ in both apatite compositions are energetically favorable, consistent with the structural and compositional flexibility of apatite. In contrast, the I transmutation is not energetically favorable, largely due to the structure unable to accommodate the zero valance Xe in the structural channel. The study suggests that apatite structured materials could be promising waste forms to mitigate the beta-decay induced instability of the materials by incorporating ferric ion or other electron acceptors in the structure for some fission products. The study may demonstrate a methodology to evaluate the structural stability of waste forms incorporating fission products undergoing beta-decay.

Key words:

Apatite, fission products, beta-decay, Density Functional Theory, crystal structure, crystal defect, nuclear waste form

Introduction

Sustainable nuclear energy requires radioactive nuclear waste to be safely disposed. Currently, the long-term solution to high-level radioactive waste is to permanently place the waste in geological settings. During past decades, various nuclear waste forms have been developed to incorporate radionuclides from reprocessing of the used nuclear fuel and the defense processing programs. Among the radionuclides, the most problematic are those with weak affinity to engineering barriers and rocks in a disposal environment, including Cs, Sr, and I. Borosilicate glass has been developed and produced at industrial scale to immobilize high-level waste by a vitrification process.(Vienna, 2010; Weber et al., 2009) This is largely because of flexibility of the glass to incorporate a range of nuclear waste elements and the existing melting technology to produce the glass. In order to improve durability, increase waste loading, and reduce the waste volume, glass-ceramic waste form (Crum et al., 2014; Crum et al., 2012; Vienna et al., 2012) and ceramic waste form (Amoroso et al., 2014{Ringwood, 1979 #3021; Aubin et al., 2004) have been developed. Multiphase

ceramics, such as the synthetic rock (SYNROC) targeting an assemblage of crystalline phases have been successfully demonstrated to incorporate various radioactive waste elements into a number of crystalline phases. (Ringwood et al., 1979a; Ringwood et al., 1979b) The concept of SYNROCK is based on knowledge of naturally occurring minerals containing radioactive species similar to the radionuclides produced in wastes from fuel reprocessing. Those mineral analogs have desirable characteristics that demonstrate their long-term durability in the natural environment over geological timescales. Both glass-ceramic and ceramic waste forms are desired to incorporate radionuclides by targeting certain crystalline phases, such as zirconolite ($\text{CaZrTi}_2\text{O}_7$), perovskite (CaTiO_3), and hollandites ($\text{Ba}(\text{Al,Ti})_2\text{Ti}_6\text{O}_{16}$) in SYNROCK, and powellite (XMoO_4 , X= alkali, alkaline earths, lanthanides) and oxyapatite ($\text{Ca}_2\text{Ln}_8(\text{SiO}_4)_6\text{O}_2$) in glass-ceramic waste form. (Crum et al., 2014; Ringwood et al., 1979a; Ringwood et al., 1979b; Weber et al., 2009) Those phases incorporate radioactive fission products such as Cs and Sr at their lattice sites, and these fission products are beta emitters. Beta-decay emits an electron with energy in MeV range and the sudden increase in nuclear charge, resulting in modifications of the host phase chemistry and changes of the thermodynamic and mechanical properties. These changes can cause thermodynamic instability of those phases and microstructure changes, which may fundamentally degrade the performance of the waste forms incorporating these radionuclides.

Interactions of beta-decay with the host phase largely depends on the nature of the decay and the host material. (Dezerald et al., 2015; Jiang et al., 2010; Jiang et al., 2012; Marks et al., 2013; Stanek et al., 2012; Uberuaga et al., 2010; Weber, 1988) Recent density functional theory studies of the effects of beta decay of ^{137}Cs (Jiang et al., 2010) and ^{90}Sr (Jiang et al., 2010; Marks et al., 2013) in crystalline phases showed important chemical and structural modifications of the host phases as characterized by a process of radioparagenesis (Jiang et al., 2010; Marks et al., 2013), a structural and chemical transformation process resulting from radioactive decay of radionuclides in a solid phase. These studies enable the design of waste forms with improved mechanical properties by means of transmutation, thus opening a promising avenue for long-term nuclear waste containment. Chemical and valence change (e.g., $^{137}\text{Cs}^+$ to $^{137}\text{Ba}^{2+}$) may

lead to a volume change of the nuclear waste structure and decomposition of the crystalline waste form due to the valence and size changes from $^{137}\text{Cs}^+$ to $^{137}\text{Ba}^{2+}$. Thus, in addition to the heat and radiation from the MeV beta electron, effect of the chemical change on the integrity of the waste forms needs to be evaluated for the waste form design. In this regard, it is constructive to develop a strategy to evaluate and mitigate beta-decay induced instability of the nuclear waste forms that incorporate those fission products.

It is desirable that both the extra electron and increased nuclear charge from beta-decay are locally offset in the phase without causing phase decomposition or phase transition. This requires that the crystal-chemical substitutions must be electrically balanced and chemical bonding environment is flexible enough to accommodate transmutations involving changes in valence and atomic size. (Jantzen and Williams, 2008) When a monovalent cation (e.g., ^{137}Cs) transmutes to a divalent cation (e.g., ^{137}Ba), the substitutions must be coupled to electron acceptor (e.g., valence state reduced) to retain the electrical balance of the host phase without destroying the integrity of the phase, and the lattice site must be of suitable size and bond coordination to accept the transmutation. These requirements point to crystalline phases that have both chemical and structural flexibility with a wide range of chemical substitution. While chemical flexibility in glass is known and bonding in glass is considered short-ranges, the structure flexibility is unknown. Many natural minerals with potential interests to nuclear waste forms have structural and compositional flexibilities such as apatite $\text{A}_5(\text{XO}_4)_3\text{Z}$ ($\text{A} = \text{Na}^+, \text{K}^+, \text{Cs}^+, \text{Mg}^{2+}, \text{Ca}^{2+}, \text{Ba}^{2+}, \text{Sr}^{2+}, \text{Cd}^{2+}, \text{Pb}^{2+}, \text{Fe}^{2+}, \text{Fe}^{3+}, \text{REE}^{3+}, \text{and } \text{Ac}^{4+}$, $\text{X} = \text{P}^{5+}, \text{Si}^{4+}, \text{S}^{6+}, \text{V}^{5+}, \text{Cr}^{5+}, \text{As}^{5+}, \text{Mn}^{5+}, \text{Ge}^{4+}$, $\text{Z} = \text{OH}^-, \text{F}^-, \text{Cl}^-, \text{Br}^-, \text{I}^-, \text{O}^{2-}, \text{CO}_3^{2-}, \text{and } \text{IO}_3^-$), powellite related minerals – scheelite and fergusonite ABO_4 ($\text{A} = \text{Ca}, \text{Pb}, \text{Ba}, \text{Y}, \text{La}, \text{Ce}, \text{Nd}$, $\text{B} = \text{Mo}, \text{W}, \text{Nb}, \text{Ti}$), hollandite AB_8O_{16} ($\text{A} = \text{Cs}, \text{Sr}, \text{Ba}, \text{Rb}$, $\text{B} = \text{Al}, \text{Ti}, \text{Fe}, \text{Mn}$), crichtonite $(\text{Ca}, \text{Sr}, \text{La}, \text{Ce}, \text{Y})(\text{Ti}, \text{Fe}, \text{Mn})_{21}\text{O}_{38}$, murataite $(\text{Y}, \text{Na})_6(\text{Zn}, \text{Fe})_5(\text{Ti}, \text{Nb})_{12}\text{O}_{29}(\text{O}, \text{F})_{14}$, to name a few. Among these minerals, apatite shows great structural and compositional flexibilities, which are also demonstrated from the fact that the apatite structure can even be deviated from hexagonal symmetry while maintaining the topology of apatite structure. (Hughes et al., 1989; Wang, 2015; White et al., 2005; White and ZhiLi, 2003) Because its multiple crystallographic sites can be occupied by elements with different charges, changes associated with the

valance and identity of the radioactive elements resulting from radioactive decay of those beta emitters, e.g., ^{137}Cs and ^{90}Sr , could be potentially offset by a charge transfer between the sites and structural distortions within the same phase. This charge transfer and structural distortion, preferably local within a couple of bond distance, would prevent likely phase transition or decomposition due to radioactive decay without compromising the integrity of the phase. The emitted electron could be captured by a variable valance metal ion in the structure and transmuted element (e.g., ^{137}Ba , $^{90}\text{Y/Zr}$) remains in the lattice site. Thus, apatite-structured phases may be tolerant against or has potential to mitigate the aging effect of radionuclides from a process so-called radioparagenesis,(Jiang et al., 2009; Jiang et al., 2010; Marks et al., 2013; Uberuaga et al., 2010)

The purpose for this study is to test the hypothesis that apatite-structured phases with chemical and structural flexibility can tolerate structure and thermodynamic instability caused by beta-decay of some of important fission products, ^{137}CS , ^{90}Sr , ^{129}I , by introducing ferrous iron as electron acceptor in the structure. Electron density of states, crystal and defect structure, and formation energies of before and after beta-decay were calculated using a spin-polarized DFT approach. The results are expected to shed light on waste form designs and the evaluation of the structural stability of incorporating fission products undergoing beta-decay.

Methods

The Hamiltonian of crystals mainly includes terms for inter-electronic repulsion, spin-orbit coupling, and ligand field interaction. In the calculation, only iron ions have the open shell. As the first row transition metal, the spin-orbit coupling of iron ion is less important than other terms in the Hamiltonian and can be neglected.(Chibotaru, 2015) Therefore, a spin-polarized DFT approach(Yao et al., 2013) is appropriate in the calculations.

Density functional theory with the Perdew-Burke-Ernzerhof (PBE) exchange-correlation functional under generalized gradient approximation (GGA)(Perdew et al., 1996; Perdew et al., 1997)

implemented in the Vienna ab initio simulation package (VASP)(Kresse and Furthmüller, 1996a, b; Kresse and Hafner, 1993, 1994) was employed for the structural optimization and total energy calculations. Total energy $E_{TOT}[\rho_\alpha, \rho_\beta]$ is expressed in terms of $\rho_\alpha(\vec{r})$ and $\rho_\beta(\vec{r})$ which are the spin-up and spin-down electron densities, corresponding to the diagonal elements in spin space, and which play the same role as total electron density, $\rho(\vec{r})$. Calculations were done using PAW formalism,(Blöchl, 1994; Kresse and Joubert, 1999) which was developed using concept of pseudopotentials(Vanderbilt, 1990) in the plane-wave basis supplied by the VASP. A self-consistency cycle with a Pulay mixer and an iterative matrix diagonalization scheme was used to calculate the Kohn Sham (KS) state until the difference of the total energy less than 0.0001 eV, while the split-valence double- ζ plus polarization orbitals were chosen in calculation. The k-meshes are generated in the Brillouin zone with a $2 \times 2 \times 3$ Monkhorst–Pack grid in each direction. The energy cutoff was set as 520 eV.

$\text{Ca}_{10}(\text{PO}_4)_6\text{F}_2$ was selected for Cs^+ incorporation, since Cs incorporation in the $\text{Ca}_{10}(\text{PO}_4)_6\text{F}_2$ has been reported.(Chartier et al., 2001) Fe^{3+} induced at the neighboring site of Cs^+ as charge balance to remain the integrity of the phase have been discussed in perovskite.(Vance et al., 1982) Thus, Fe^{3+} was chosen as an electron acceptor coupled-substituted with Cs^+ in $\text{Ca}_{10}(\text{PO}_4)_6\text{F}_2$. For Sr^{2+} incorporation, Sr^{2+} and Fe^{3+} coupled-substitution requires a stoichiometric proportion of 1: 2 due to the two step decay. $\text{Y}_4\text{Ca}_2(\text{SiO}_4)_6\text{F}_2$ was selected where Sr^{2+} and Fe^{3+} could be substituted at Ca^{2+} and Y^{3+} position respectively. For iodide incorporation in the structural channel, size of the channel in the apatite structure has to fit the size of iodide ion. Currently, only a few iodide apatite compositions have been synthesized experimentally. $\text{Pb}_{10}(\text{VO}_4)_6\text{I}_2$ is a synthetic apatite inspired from vanadinite ($\text{Pb}_{10}(\text{VO}_4)_6\text{Cl}_2$) a chemically similar natural apatite.(Audubert et al., 1997; Stennett et al., 2011) $\text{AgPb}_9(\text{VO}_4)_6\text{I}$ and $\text{AgBa}_9(\text{VO}_4)_6\text{I}$ were synthesized as a potential waste form to immobilize radioactive iodine.(Uno et al., 2004) In the project. $\text{AgFePb}_8(\text{VO}_4)_6\text{I}_2$ was selected as the waste form for I⁻.

The cohesive energy (E_c), defined as the energy to pull a material apart into a collection of isolated atoms, was employed to compare the energetically preference of the transmutation product to its

parent.(Louis-Achille et al., 1998; Serway et al., 2005) For the A→B transmutation, the difference of the cohesive energy (ΔE_c) was calculated as

$$\Delta E_c = (\sum E_{B_{atom}} - E_{B_{apatite}}) - (\sum E_{A_{atom}} - E_{A_{apatite}}) \quad (1)$$

where $E_{B_{apatite}}$ and $E_{B_{atom}}$ denote to the total energy for the transmutation ion contained product and energy of the free transmutation atom. By that analogy, $E_{A_{apatite}}$ and $E_{A_{atom}}$ denote the parent. Since only the atom changes due to the beta decay after transmutation, equation (1) can be simplified as

$$\Delta E_c = (E_{prod_{atom}} - E_{B_{apatite}}) - (E_{rad_{atom}} - E_{A_{apatite}}) \quad (2)$$

where $E_{prod_{atom}}$ and $E_{rad_{atom}}$ represent the total energy of the transmuted free atom and its parent. Obviously, the higher ΔE_c , the more stable the transmutation product than its parent.

Radial distribution functions (RDF) were calculated to evaluate the structural changes involving the transmutation using the Interactive Structure Analysis of Amorphous and Crystalline Systems (ISAACS).(Roux and Petkov, 2010) The number of δr steps and the smoothing factor were set as 500 and 0.02 respectively.

Results and discussion

(1) Cs⁺ to Ba²⁺ β-decay

The main difficulty comes from the fact that multiple configurations are possible for the Cs⁺ and Fe³⁺ substitution in Ca₁₀(PO₄)₆F₂. In the project, Cs⁺ at Ca²⁺ site I with Fe³⁺ at site I or II, denoted as Cs⁺(I) - Fe³⁺(I) or Cs⁺(I) - Fe³⁺(II), and Cs⁺ at Ca²⁺ site II with Fe³⁺ at site I or II denoted as Cs⁺(II) - Fe³⁺(I) or Cs⁺(II) - Fe³⁺(II) were considered with the shortest distance between these two substitutions for electron transfer purpose (Figure 1). Ca₈Fe₁Cs₁(PO₄)₆F₂ (donated as Cs⁺-Fe³⁺) was set as supercell for Cs⁺ and Fe³⁺ substitution, in which the weight concentrations of Cs⁺ is 11.9% The transmuted product was set as Ca₈Fe₁Ba₁(PO₄)₆F₂ (donated as Ba²⁺-Fe²⁺) where Ba²⁺ is at the position of Cs⁺.

After $\text{Cs}^+ \rightarrow \text{Ba}^{2+}$ transmutation, Fe^{3+} is reduced to Fe^{2+} . The electron transfer process is demonstrated by comparing the changes in spin-polarized density of states (DOS) between $\text{Cs}^+\text{-Fe}^{3+}$ and $\text{Ba}^{2+}\text{-Fe}^{2+}$ in different configurations (Figure 2). The DOS appear as “sandwich-like” structures with the valence bands and the conduction bands filling with partial occupied d-like orbitals contributed by iron ion. For $\text{Cs}^+\text{-Fe}^{3+}$, the high spin state of Fe^{3+} (d^5) has been observed. The occupied spin α components of Fe^{3+} are delocalized with valence bands, while five unoccupied spin β components are localized between the valence and the conduct bands. After Cs^+ becomes Ba^{2+} , the high spin state remains. A few spin α d-like orbitals are localized, all spin β d-like orbitals keep the localization. One occupied d-like orbital appears in spin β projection, which indicates the emitted electron from β -decay has been “captured” during the $\text{Fe}^{3+} \rightarrow \text{Fe}^{2+}$ reduction process. Similar results were obtained in all configurations (Figure 2). The results demonstrate the variable valance iron cation behaves as a charge balancer during the Cs^+ β decay.

In order to compare the stability for these four different configurations, the total energy of the systems with $\text{Cs}^+\text{-Fe}^{3+}$ and $\text{Ba}^{2+}\text{-Fe}^{2+}$ were calculated after energy optimization (Table 1). A slight differences in total energy were observed between different configurations of $\text{Cs}^+\text{-Fe}^{3+}$, which indicates the Cs^+ and Fe^{3+} ions in the apatite may not have a specific site preference. However, the structure for Fe^{3+} at Ca^{2+} site I and Cs^+ at Ca^{2+} site II, $\text{Fe}^{3+}(\text{I})\text{-Cs}^+(\text{II})$, has the lowest total energy among all four configurations. After transmutation, Fe^{2+} located at site (I) and Ba^{2+} at site (II), i.e., $\text{Fe}^{2+}(\text{I})\text{-Ba}^{2+}(\text{II})$, has the lowest energy. Since the order of the Shannon-Prewitt Crystal Radius is $\text{Cs}^+ > \text{Ba}^{2+} > \text{Ca}^{2+} > \text{Fe}^{3+}$, (Shannon, 1976) this observation is consistent with the understanding that a larger ion preferentially enters the Ca-II site in the tunnel position rather than the Ca-I site in the framework site. (Lim et al., 2011)

The difference between cohesive energies of $\text{Cs}^+\text{-Fe}^{3+}$ and $\text{Ba}^{2+}\text{-Fe}^{2+}$ (ΔE_c) were calculated according to equation (2). The calculated results show the $\text{Ba}^{2+}\text{-Fe}^{2+}$ apatite is more energetically stable than the original waste forms (Table 1).

Beside the energetics, structural changes are also critical in nuclear waste-form designing. The volume and lattice parameters changing for the apatite from $\text{Cs}^+\text{-Fe}^{3+} \rightarrow \text{Ba}^{2+}\text{-Fe}^{2+}$ in different

configurations are listed in Table 2. The volumes become smaller with a reduction of 1.4 – 3.1%, as expected due to the smaller cation size of Ba^{2+} than Cs^+ . In all forms, the volume shrinking accompanies with the reducing of lattice constants in all dimensions with no exceptions, which may indicate small distortions during the β decay.

In all pairs RDF results, P-O bond distances for all configurations (first peak) remain the same within uncertainty, suggesting the rigid $(\text{PO}_4)^{3-}$ units are intact in the apatite structure. The most common Ca-O bond distances have small changes, which also supports the stability of the structure. Other pairs RDFs change gradually within the increase of pairs' distances (Figure 3). The cation to anion distances predominantly govern the lattice constants.(Jinmin et al., 1991) This relationship was demonstrated in apatite $\text{Ca}_5(\text{PO}_4)_3\text{F}$ as well.(Wu et al., 2004) The cation at site I is coordinated with nine O^{2-} , while cation at site II is coordinated to seven O^{2-} and to one F.(White and ZhiLi, 2003) The decrease in bond distances from Cs-O to Ba-O has been seen for all configurations with small changes in standard deviation, which suggests a volume contraction as a result of the transmutation without leading to increased local structure distortion (Figure 4). In general, iron ion's location gives less influence for the distribution in Cs-O or Ba-O bond distances. The bond distance change from Cs-O to Ba-O along with the total energy change shows changes in local structure and total energy after the transmutation event from Cs^+ to Ba^{2+} in $\text{Cs}^+-\text{Fe}^{3+}$ apatite occurs. The result shows a normal bond distance decrease while the structure being optimized (Figure 5).

The metaprism twist angle ϕ is quantitative measure of distortion in apatite structure from the ideal hcp packing, which can be calculated for any individual metaprism from the fractional coordinates of substituted cation at site I, O(1) and O(2).(White and ZhiLi, 2003) The metaprism twist angle for Cs^+ and Ba^{2+} contained species in different configurations are compiled and compared to the twist angle for $\text{Ca}_{10}(\text{PO})_6\text{F}_2$ (Figure 6).(Lim et al., 2011) In general, the shifts of the twist angles after the transmutation of $\text{Cs}^+(\text{I}) - \text{Fe}^{3+}(\text{I})$, $\text{Cs}^+(\text{I}) - \text{Fe}^{3+}(\text{II})$, and $\text{Cs}^+(\text{II}) - \text{Fe}^{3+}(\text{II})$ are less than 5 degree; the exception, $\text{Cs}^+(\text{II}) - \text{Fe}^{3+}(\text{I})$ changes to 6-8 degree. The result suggests that, in terms of the twist angle, only minor distortion is occurred after the β decay.

As a summary, $\text{Ca}_{10}(\text{PO}_4)_6\text{F}_2$ could be the qualified candidate for Cs^+ loading incorporated with the electron acceptor, Fe^{3+} . Besides the energetically favorable, the product of the transmutation does not change significantly including the volume, lattice parameters, radial distribution functions, metal to oxygen distances, and metaprisim twist angles.

(2) Sr^{2+} to Y^{3+} then Zr^{4+} β -decay

Since this decay series involved high changed species, apatite $\text{Ca}_4\text{Y}_6(\text{SiO}_4)_6\text{F}_2$ was selected for Sr^{2+} incorporation. In the structure, Ca^{2+} is at apatite site Ca-(I) and Y^{3+} is at site Ca-(II). (Villars, 2014) After a coupled substitution by Sr^{2+} and Fe^{3+} , the composition is $\text{Ca}_3\text{Sr}_1\text{Y}_4\text{Fe}_2(\text{SiO}_4)_6\text{F}_2$, donated as $(\text{Fe}^{3+}\text{-Sr}^{2+}\text{-Fe}^{3+})$, where one Ca^{2+} and two Y^{3+} substituted by Sr^{2+} and Fe^{3+} respectively, for the two steps in the Sr^{2+} β -decay series. Two possible configurations, two Fe^{3+} ions substituted for Y^{3+} at the same or different hexagonal channels (Ca-II), were considered in the calculations with Sr^{2+} and Fe^{3+} ions in neighboring sites. After the transmutations, the compositions are $\text{Ca}_3\text{Y}_5\text{Fe}_2(\text{SiO}_4)_6\text{F}_2$ ($\text{Fe}^{2+}\text{-Y}^{3+}\text{-Fe}^{3+}$) and $\text{Ca}_3\text{Zr}_1\text{Y}_4\text{Fe}_2(\text{SiO}_4)_6\text{F}_2$ ($\text{Fe}^{2+}\text{-Zr}^{4+}\text{-Fe}^{2+}$), where Y^{3+} then Zr^{4+} are changed from Sr^{2+} at the same position. Unlike the four configurations of Cs^+ and Fe^{3+} coupled substitution have similar total energies previously, the configuration with Fe^{3+} ions at the same hexagonal channel with Sr^{2+} has a significant lower in total energy (2.15 eV lower) than that Fe^{3+} at different channels, indicating Fe^{3+} and Sr^{2+} prefer in the same channel. Therefore, Sr^{2+} ion with two Fe^{3+} ions at the same hexagonal channel with a configuration of $\text{Fe}^{3+}\text{-Sr}^{2+}\text{-Fe}^{3+}$ was considered for the further discussion (Figure 7).

DOS for the systems with configurations of $\text{Fe}^{3+}\text{-Sr}^{2+}\text{-Fe}^{3+}$, $\text{Fe}^{2+}\text{-Y}^{3+}\text{-Fe}^{3+}$, and $\text{Fe}^{2+}\text{-Zr}^{4+}\text{-Fe}^{2+}$ were calculated to understand the transmutation induced electron transfers. In $\text{Fe}^{3+}\text{-Sr}^{2+}\text{-Fe}^{3+}$, two Fe^{3+} ions in the high spin state have the ferromagnetic order, which exhibits ten occupied spin-up (part delocalized) and ten empty spin-down (localized) d-like orbitals. (Figure 8-A). After Sr^{2+} decay to Y^{3+} (Figure 8-B) then to Zr^{4+} (Figure 8-C), the magnetic order and the spin state do not change, one electron fills in spin β orbital of $\text{Fe}^{2+}\text{-Y}^{3+}\text{-Fe}^{3+}$, and two electrons in spin β orbitals of $\text{Fe}^{2+}\text{-Zr}^{4+}\text{-Fe}^{2+}$. The charge balance is clearly seen in the changes of the DOS.

Same method for cohesive energy comparison in Cs^+ case was applied to calculate the cohesive energy differences from Y^{3+} to Zr^{4+} and from Sr^{2+} to Y^{3+} . The difference of the cohesive energy (ΔE_c) in the two step β -decay from Sr^{2+} to Y^{3+} then Zr^{4+} are 4.43 eV and 1.39 eV respectively, which indicates the structure is more energetically stable after the transmutations.

Unlike the volume decrease from Cs^+ to Ba^{2+} decay is due to shrink along all three axes, the Sr^{2+} decay series causes the lattice constant a and b increasing and c decreasing, which indicate nonlinear relationships between sizes of the lattice parameters and volume and substituting ions as a result of the transmutation (Table 3).(Wang, 2015) In RDF statistics, The Si-O peak positions remain during the transmutation (Figure 9). However. Other pairs' position including Ca-O change considerably. Metal cation to oxygen distances, Sr-O, Y-O, and Zr-O, are calculated for local structure changes. Sr^{2+} and its transmuted products are all located at site Ca-I, which is expected to have a coordination number of nine. The nine nearest metal to oxygen distances are calculated and plotted in Figure 10. From Sr^{2+} to Y^{3+} , all nine bond distances decreased nearly uniformly. From Y^{3+} to Zr^{4+} , the bond distances with its nearest seven neighbors decrease consistently, but the eighth and ninth bond distances increase. The result suggests a change of the coordination environment from Y^{3+} to Zr^{4+} .

A useful check for coordination is to employ the Grubbs' test(Grubbs, 1969) in one-sided (minimum) form for identifying the coordination number according to the relative contributions of the ligands to the total crystal field terms.(Yao et al., 2015) The crystal-field Hamiltonian has R^{-3} , R^{-5} ..., dependence, where R is the distance between metal cation to ligand. Mathematically, the R^{-3} dependence offers a convenient criterion to estimate the contribution to the crystal field from each ligand ion, in other words the coordinating ions to the central metal ion. The tested sample range was chosen from the top contributor down to include the proposed coordination number found plus one more. The G value was calculated for lowest contributor, as a suspected outlier, and compared to the Grubbs' critical value to determine the confidence interval. For the Fe^{2+} - Zr^{4+} - Fe^{2+} system, the test result shows that Zr^{4+} changes to

seven coordination at 99% confident interval, consistent with the results as shown in Figure 9. This observation may suggest that there may be a symmetrical change in the process of Y^{3+} decay to Zr^{4+} .

In summary, during the $Sr^{2+} \rightarrow Y^{3+} \rightarrow Zr^{4+}$ decay where Fe^{3+} acts as the electron acceptor, the products of the transmutation are energetically favorable. The tetrahedral $(SiO_4)^{3-}$ structure remains durable. However, the coordination number change in $Y^{3+} \rightarrow Zr^{4+}$ indicates a symmetrical distortion may occur in the process.

(3) I to Xe β -decay

Since the preference of the larger size ion to site (I) was found in previous simulation for $Ca_8Fe_1Cs_1(PO_4)_6F_2$, Ag^+ and Fe^{3+} are arranged to be located at site (I) and site (II) respectively in $AgFePb_8(VO_4)_6I_2$ (I- Fe^{3+}). After the I to Xe β -decay, the transmutation is signed as $AgFePb_8(VO_4)_6IXe$ (Xe- Fe^{2+}) where Fe^{3+} is reduced to Fe^{2+} . The electron transfer process is demonstrated by comparing the changes in spin-polarized density of states (DOS) between I- Fe^{3+} and Xe- Fe^{2+} . Similar to Cs^+ and Sr^{2+} cases, a reduction process from Fe^{3+} to Fe^{2+} has been observed during the I to Xe transmutation. As the noble gas, the releasing process of Xenon from the matrix is expected very fast unless under gigapascals of pressure. (Caldwell et al., 1997) Thus, the stability of $AgFePb_8(VO_4)_6I$ (vacancy- Fe^{2+}) was discussed as well. The iron ion oxidation state does not change after xenon gas flees (Figure 11).

From I to Xe β -decay, the difference of the cohesive energy (ΔE_c) is -40.3 eV due to the low Xe atom free energy (-27.26 eV) and high I atom free energy (10.44 eV). Although ΔE_c is 28.7 eV after xenon gas escapes, the overall ΔE_c is -13.0 eV. Unlike Cs^+ and Sr^{2+} β -decay, the product of I to Xe transmutation is more energetically unstable than its parent.

In Cs^+ and Sr^{2+} transmutations, tetrahedral $(PO_4)^{3-}$ and $(SiO_4)^{4-}$ structures, the “skeletons” of the apatite, does not change in terms of RDF (Figure 3 and Figure 9-A). In contrast, an increasing bond distance of V-O in $(VO_4)^{3-}$ has been observed during the I to Xe β -decay, and remains after xenon releasing (Figure 9-B). Under the background that the volume and lattice parameters decrease in $I-Fe^{3+} \rightarrow Xe-Fe^{2+} \rightarrow$

vacancy- Fe^{2+} processes (Table 4), the observation suggests a framework distortion may occur in I^- transmutation in $\text{AgFePb}_8(\text{VO}_4)_6\text{I}_2$.

In summary, $\text{AgFePb}_8(\text{VO}_4)_6\text{I}_2$ is not an ideal waste form for I^- , although it may be synthesized. The significant decrease of the cohesive energy in I^- to Xe β -decay indicates the energetically unstable. Furthermore, which is suggested from the contradictive observation, the decrease of volume and lattice parameters accompanied with the increasing V-O bond distance in $(\text{VO}_4)^{3-}$, suggests a structural distortion in $\text{I}^- \rightarrow \text{Xe}$ decay.

Conclusions

A library of mineral analogs could be candidates of nuclear waste forms. The theoretic research applies a convenient approach for potential waste forms picking and designing. In general, co-doping Fe^{3+} in the same waste form could be a practical solution for the purpose of the electron capture generated from a β -decay. The appropriation of selected apatites for wastes loading can be evaluated by comparing the features of the transmutation products and their parents. The energetic and structural studies show $\text{Ca}_{10}(\text{PO}_4)_6\text{F}_2$ is promising for $\text{Cs}^+ \rightarrow \text{Ba}^{2+}$ transmutation when coupled with Fe^{3+} as the electron acceptor at ~12% weight concentration at least. A structural unstable due to the change of the coordination number for Zr^{4+} to oxygen ligands in the $\text{Y}^{3+} \rightarrow \text{Zr}^{4+}$ process may occur in $\text{Ca}_4\text{Y}_6(\text{SiO}_4)_6\text{F}_2$ with Sr^{2+} and Fe^{3+} substitutions. In $\text{AgFePb}_8(\text{VO}_4)_6\text{I}_2$, the I^- decay causes the alteration of the tetrahedral $(\text{VO}_4)^{3-}$ which may induce a serve distortion for the transmuted production.

Acknowledgement

This research is being performed using funding received from the DOE Office of Nuclear Energy's Nuclear Energy University Programs under award DE-AC07-05ID14517.

References

- Amoroso, J., Marra, J.C., Tang, M., Lin, Y., Chen, F., Su, D. and Brinkman, K.S. (2014) Melt processed multiphase ceramic waste forms for nuclear waste immobilization. *J. Nucl. Mater.* 454, 12-21.
- Aubin, V., Caurant, D., Gourier, D., Baffier, N., Advocat, F., Bart, F., Leturcq, G. and Costantini, J.M. (2004) Synthesis, Characterization and Study of the Radiation Effects on Hollandite Ceramics Developed for Cesium Immobilization. *Mat. Res. Soc. Symp. Proc.* 807, 315-320.
- Audubert, F., Carpena, J., Lacout, J.L. and Tetard, F. (1997) Elaboration of an iodine-bearing apatite Iodine diffusion into a $\text{Pb}_3(\text{VO}_4)_2$ matrix. *Solid State Ionics* 95, 113-119.
- Blöchl, P.E. (1994) Projector augmented-wave method. *Phys. Rev. B* 50, 17953-17979.
- Caldwell, W.A., Nguyen, J.H., Pfrommer, B.G., Mauri, F., Louie, S.G. and Jeanloz, R. (1997) Structure, Bonding, and Geochemistry of Xenon at High Pressures. *Science* 277, 930-933.
- Chartier, A., Meis, C. and Gale, J.D. (2001) Computational study of Cs immobilization in the apatites $\text{Ca}_{10}(\text{PO}_4)_6\text{F}_2$, $\text{Ca}_4\text{La}_6(\text{SiO}_4)_6\text{F}_2$ and $\text{Ca}_2\text{La}_8(\text{SiO}_4)_6\text{O}_2$. *Phys. Rev. B* 64, 085110.
- Chibotaru, L.F. (2015) Theoretical Understanding of Anisotropy in Molecular, in: Gao, S. (Ed.), *Molecular Nanomagnets and Related Phenomena*. Springer, p. 198.
- Crum, J., Maio, V., McCloy, J., Scott, C., Riley, B., Benefiel, B., Vienna, J., Archibald, K., Rodriguez, C., Rutledge, V., Zhu, Z., Ryan, J. and Olszta, M. (2014) Cold crucible induction melter studies for making glass ceramic waste forms: A feasibility assessment. *J. Nucl. Mater.* 444, 481-492.
- Crum, J., Turo, L., Riley, B., Tang, M. and Kossoy, A. (2012) Multi-phase glass-ceramics as a waste form for combined fission products: Alkalis, alkaline earths, lanthanides, and transition metals. *J. Am. Ceram. Soc.* 95, 1297-1303.
- Dezerald, L., Kohanoff, J.J., Correa, A.A., Caro, A., Pellenq, R.J.M., Ulm, F.J. and Saúl, A. (2015) Cement As a Waste Form for Nuclear Fission Products: The Case of ^{90}Sr and Its Daughters. *Environmental Science & Technology* 49, 13676-13683.
- Grubbs, F.E. (1969) Procedures for Detecting Outlying Observations in Samples. *Technometrics* 11, 1-21.
- Hughes, J.M., Cameron, M. and Crowley, K.D. (1989) Structural variations in natural F, OH, and Cl apatites. *Am. Mineral.* 74, 870-876.
- Jantzen, C.M. and Williams, M.R. (2008) Fluidized Bed Steam Reforming (FBSR) Mineralization for High Organic and
- Nitrate Waste Streams for the Global Nuclear Energy Partnership (GNEP), Waste Management '08, Phoenix, AZ.
- Jiang, C., Stanek, C.R., Marks, N.A., Sickafus, K.E. and Uberuaga, B.P. (2009) Predicting from first principles the chemical evolution of crystalline compounds due to radioactive decay: The case of the transformation of CsCl to BaCl . *Phys. Rev. B* 79, 132110.
- Jiang, C., Uberuaga, B.P., Sickafus, K.E., Nortier, F.M., Kitten, J.J., Marks, N.A. and Stanek, C.R. (2010) Using "radioparagenesis" to design robust nuclear waste forms. *Energy & Environmental Science* 3, 130-135.
- Jiang, W., Van Ginhoven, R.M., Kovarik, L., Jaffe, J.E. and Arey, B.W. (2012) Superlattice Structure and Precipitates in O^+ and Zr^+ Ion Coimplanted SrTiO_3 : A Model Waste Form for ^{90}Sr . *The Journal of Physical Chemistry C* 116, 16709-16715.
- Jinmin, Z., Danian, Y. and Prewitt, C.T. (1991) Relationship between the unit-cell volumes and cation radii of isostructural compounds and the additivity of the molecular volumes of carbonates. *Am. Mineral.* 76, 100-105.
- Kresse, G. and Furthmüller, J. (1996a) Efficiency of ab-initio total energy calculations for metals and semiconductors using a plane-wave basis set. *Comp. Mater. Sci.* 6, 15-50.
- Kresse, G. and Furthmüller, J. (1996b) Efficient iterative schemes for ab initio total-energy calculations using a plane-wave basis set. *Phys. Rev. B* 54, 11169-11186.

- Kresse, G. and Hafner, J. (1993) Ab initio molecular dynamics for liquid metals. *Phys. Rev. B* 47, 558-561.
- Kresse, G. and Hafner, J. (1994) Ab initio molecular-dynamics simulation of the liquid-metal–amorphous-semiconductor transition in germanium. *Phys. Rev. B* 49, 14251-14269.
- Kresse, G. and Joubert, D. (1999) From ultrasoft pseudopotentials to the projector augmented-wave method. *Phys. Rev. B* 59, 1758-1775.
- Lim, S.C., Baikie, T., Pramana, S.S., Smith, R. and White, T.J. (2011) Apatite metaprisim twist angle (ϕ) as a tool for crystallochemical diagnosis. *J. Solid State Chem.* 184, 2978-2986.
- Louis-Achille, V., De Windt, L. and Defranceschi, M. (1998) Local density calculation of structural properties and cohesive energy for ScPO_4 , YPO_4 and the apatite $\text{Ca}_{10}(\text{PO}_4)_6\text{F}_2$. *Journal of Molecular Structure: THEOCHEM* 426, 217-224.
- Marks, N.A., D J Carter¹, M.S., Rohl, A.L., Sickafus, K.E., Uberuaga, B.P. and Stanek, C.R. (2013) Chemical evolution via beta decay: a case study in strontium-90 *J. Phys.: Condens. Matter* 25, 065504
- Perdew, J.P., Burke, K. and Ernzerhof, M. (1996) Generalized Gradient Approximation Made Simple. *Phys. Rev. Lett.* 77, 3865-3868.
- Perdew, J.P., Burke, K. and Ernzerhof, M. (1997) Generalized gradient approximation made simple (vol 77, pg 3865, 1996). *Phys. Rev. Lett.* 78, 1396-1396.
- Ringwood, A.E., Kesson, S.E., Ware, N.G., Hibberson, W. and Major, A. (1979a) Immobilization of high-level nuclear-reactor wastes in synroc. *Nature* 278, 219-223.
- Ringwood, A.E., Kesson, S.E., Ware, N.G., Hibberson, W.O. and Major, A. (1979b) The SYNROC process: A geochemical approach to nuclear waste immobilization. *GEOCHEMICAL JOURNAL* 13, 141-165.
- Roux, S.L. and Petkov, V. (2010) ISAACS - interactive structure analysis of amorphous and crystalline systems. *J. Appl. Cryst.* 43, 181-185.
- Serway, R., Moses, C. and Moyer, C. (2005) *Modern Physics*, third ed. Thomson Learning.
- Shannon, R.D. (1976) Revised effective ionic radii and systematic studies of interatomic distances in halides and chalcogenides. *Acta Crystallographica Section A* 32, 751-767.
- Stanek, C.R., Uberuaga, B.P., Scott, B.L., Feller, R.K. and Marks, N.A. (2012) Accelerated chemical aging of crystalline nuclear waste forms. *Current Opinion in Solid State and Materials Science* 16, 126-133.
- Stennett, M.C., Pinnock, I.J. and Hyatt, N.C. (2011) Rapid synthesis of $\text{Pb}_5(\text{VO}_4)_3\text{I}$, for the immobilisation of iodine radioisotopes, by microwave dielectric heating. *J. Nucl. Mater.* 414, 352-359.
- Uberuaga, B.P., Jiang, C., Stanek, C.R., Sickafus, K.E., Marks, N.A., Carter, D.J. and Rohl, A.L. (2010) Implications of transmutation on the defect chemistry in crystalline waste forms. *Nucl. Instrum. Methods Phys. Res., Sect. B* 268, 3261-3264.
- Uno, M., Kosuga, A., Masuo, S., Imamura, M. and Yamanaka, S. (2004) Thermal and mechanical properties of $\text{AgPb}_9(\text{VO}_4)_6\text{I}$ and $\text{AgBa}_9(\text{VO}_4)_6\text{I}$. *J. Alloys Compd.* 384, 300-302.
- Vance, E.R., Roy, R., Pepin, J. and Agrawal, D.K. (1982) Chemical mitigation of the transmutation problem in crystalline nuclear waste radiophases. *J. Mater. Sci.* 17, 947-952.
- Vanderbilt, D. (1990) Soft self-consistent pseudopotentials in a generalized eigenvalue formalism. *Phys. Rev. B* 41, 7892-7895.
- Vienna, J., Crum, J., Sevigny, G. and Smith, G. (2012) Preliminary technology maturation plan for immobilization of high-level waste in glass-ceramics. pp. 98.
- Vienna, J.D. (2010) Nuclear Waste Vitrification in the United States: Recent Developments and Future Options. *International Journal of Applied Glass Science* 1, 309-321.
- Villars, P. (2014) Material Phases Data System (MPDS), CH-6354 Vitznau, in: SpringerMaterials (Ed.), Switzerland.
- Wang, J. (2015) Incorporation of iodine into apatite structure: a crystal chemistry approach using Artificial Neural Network. *Frontiers in Earth Science* 03, 20.

- Weber, W.J. (1988) Radiation effects in nuclear waste glasses. Nucl. Instrum. Methods Phys. Res., Sect. B 32, 471-479.
- Weber, W.J., Navrotsky, A., Stefanovsky, S., Vance, E.R. and Vernaz, E. (2009) Materials Science of High-level Nuclear Waste Immobilization. MRS Bulletin 34, 46-53.
- White, T., Ferraris, C., Kim, J. and Madhavi, S. (2005) Apatite - An adaptive framework structure, in: Ferraris, G., Merlino, S. (Eds.), Micro- and Mesoporous Mineral Phases, pp. 307-401.
- White, T.J. and ZhiLi, D. (2003) Structural derivation and crystal chemistry of apatites. Acta Crystallographica Section B 59, 1-16.
- Wu, P., Zeng, Y.Z. and Wang, C.M. (2004) Prediction of apatite lattice constants from their constituent elemental radii and artificial intelligence methods. Biomaterials 25, 1123-1130.
- Yao, G., Berry, M., May, P.S., Wang, J. and Kilin, D.S. (2015) Relationship Between Site Symmetry, Spin State, and Doping Concentration for Co(II) or Co(III) in β -NaYF₄. Journal of Physical Chemistry C submitted.
- Yao, G., Berry, M.T., May, P.S. and Kilin, D. (2013) DFT Calculation of Russell–Saunders Splitting for Lanthanide Ions Doped in Hexagonal (β)-NaYF₄ Nanocrystals. The Journal of Physical Chemistry C 117, 17177-17185.

Figures

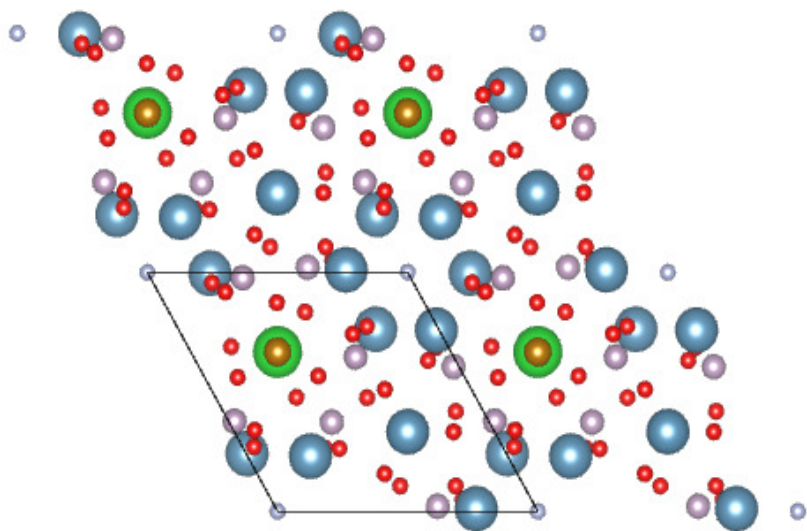


Figure 1. The optimized molecular structure of $\text{Cs}^+\text{-Fe}^{3+}$ (2x2x1), when both Fe^{3+} and Cs^+ as impurities replace two Ca^{2+} (I) in $\text{Ca}_{10}(\text{PO}_4)_6\text{F}_2$. Blue, golden, green, pink, red, and silver balls represent Ca^{2+} , Fe^{3+} , Cs^+ , P^{3+} , O^{2-} , and F^- respectively.

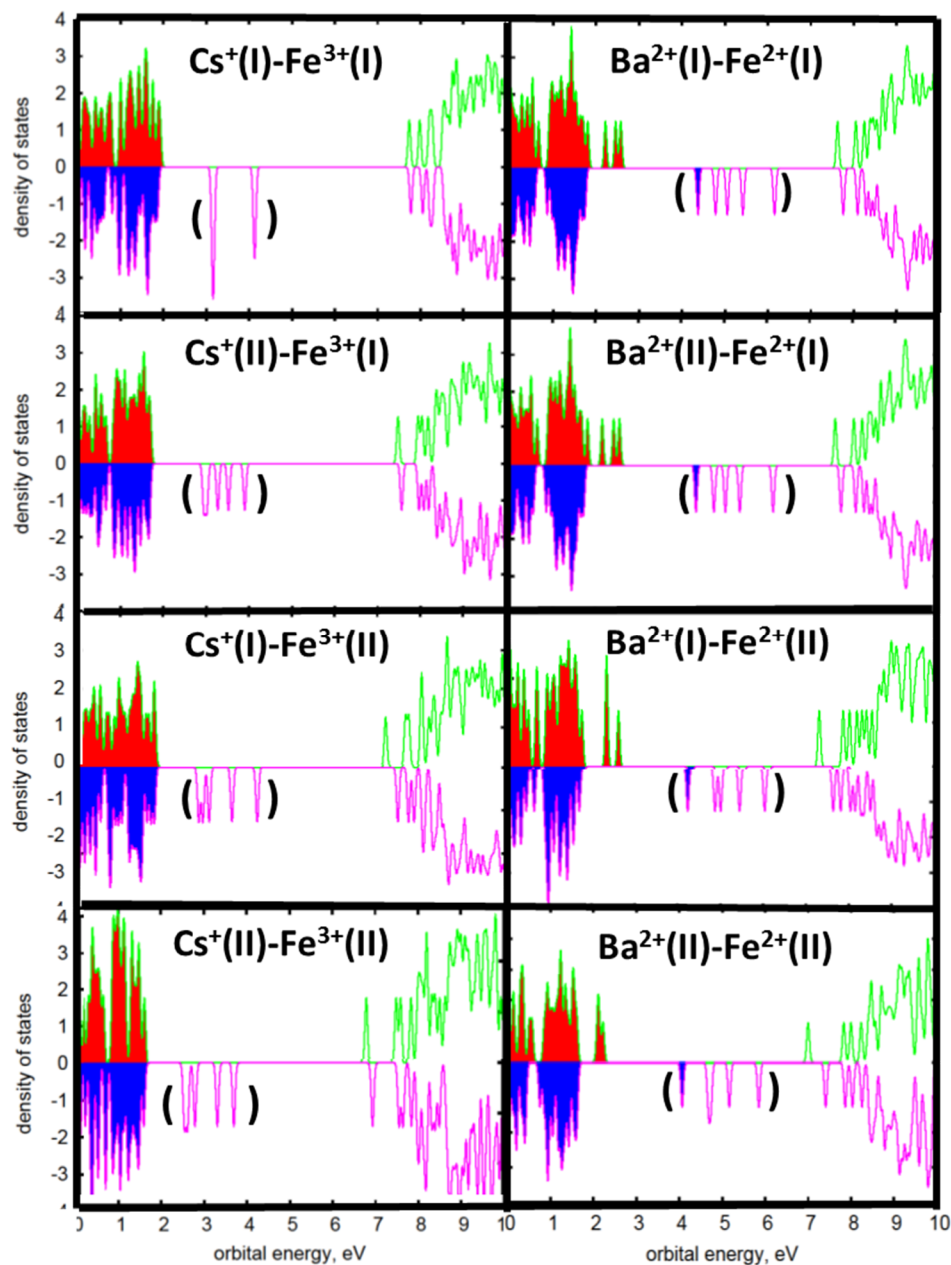


Figure 2. DOS of $\text{Cs}^+\text{-Fe}^{3+}$ (left panel) and $\text{Ba}^{2+}\text{-Fe}^{2+}$ (right panel) when $\text{Cs}^+/\text{Ba}^{2+}$ and $\text{Fe}^{3+}/\text{Fe}^{2+}$ locate at different Ca-site. Curves above and below the central line in each panel represent partial DOS for spin (α) (green) and spin (β) (pink) components. Filled portions of the curve represent occupied electronic states for spin (α) (red) and spin (β) (blue). High-spin configurations can be seen. The orbitals inside the black bracket are d-like orbitals contributed by Fe^{3+} (Fe^{2+}) ion.

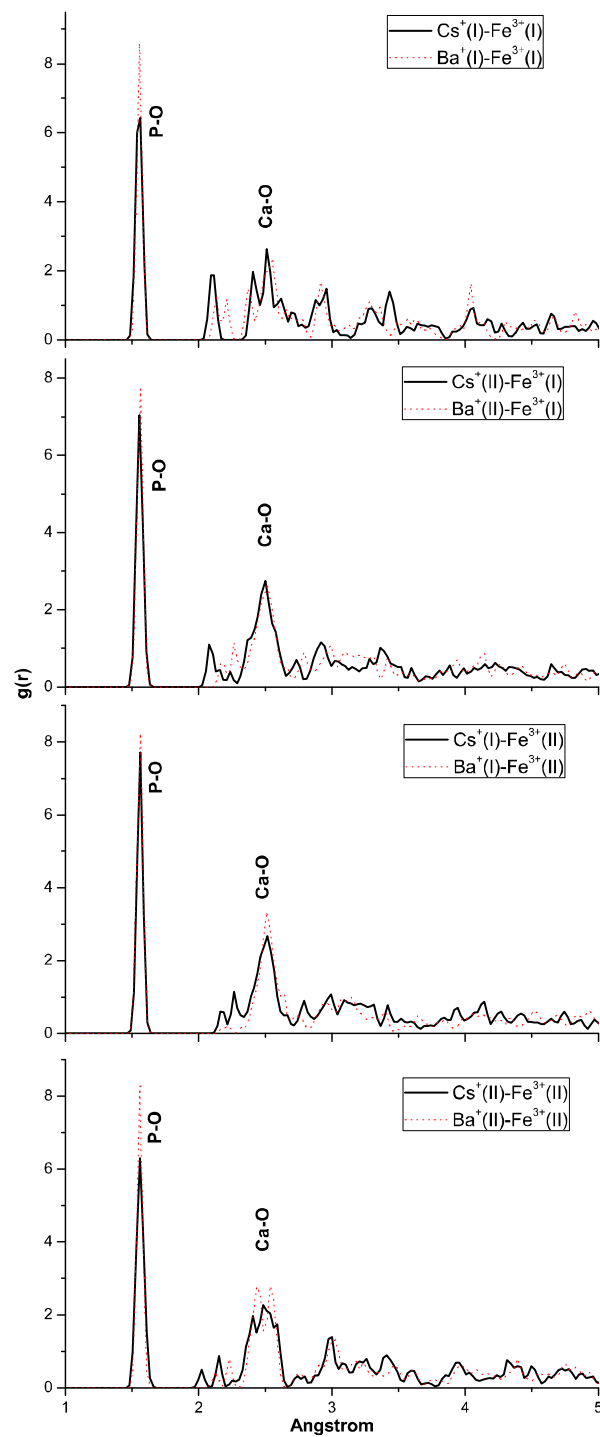


Figure 3. The radial distribution function for all pairs changes from $\text{Cs}^+ - \text{Fe}^{3+}$ species (black solid line) to $\text{Ba}^{2+} - \text{Fe}^{2+}$ (red dashes) decay. Figures are (A) $\text{Fe}^{3+}(\text{I})-\text{Cs}^+(\text{I})$, (B) $\text{Fe}^{3+}(\text{I})-\text{Cs}^+(\text{II})$, (C) $\text{Fe}^{3+}(\text{II})-\text{Cs}^+(\text{I})$, and (D) $\text{Fe}^{3+}(\text{II})-\text{Cs}^+(\text{II})$ decay from top to bottom. The P-O bonds remain same position, and Ca-O bonds exhibit a small shifts.

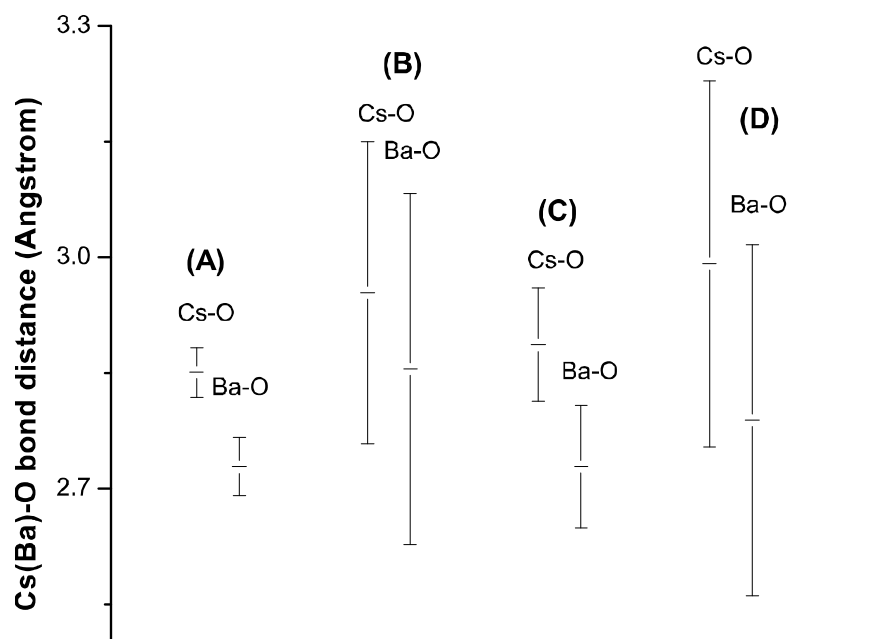


Figure 4. The average and standard deviation Cs-O and Ba-O bond distances for (A) $\text{Cs}^+(\text{I}) - \text{Fe}^{3+}(\text{I})$, (B) $\text{Cs}^+(\text{II}) - \text{Fe}^{3+}(\text{I})$, (C) $\text{Cs}^+(\text{I}) - \text{Fe}^{3+}(\text{II})$, and (D) $\text{Cs}^+(\text{II}) - \text{Fe}^{3+}(\text{II})$ decay.

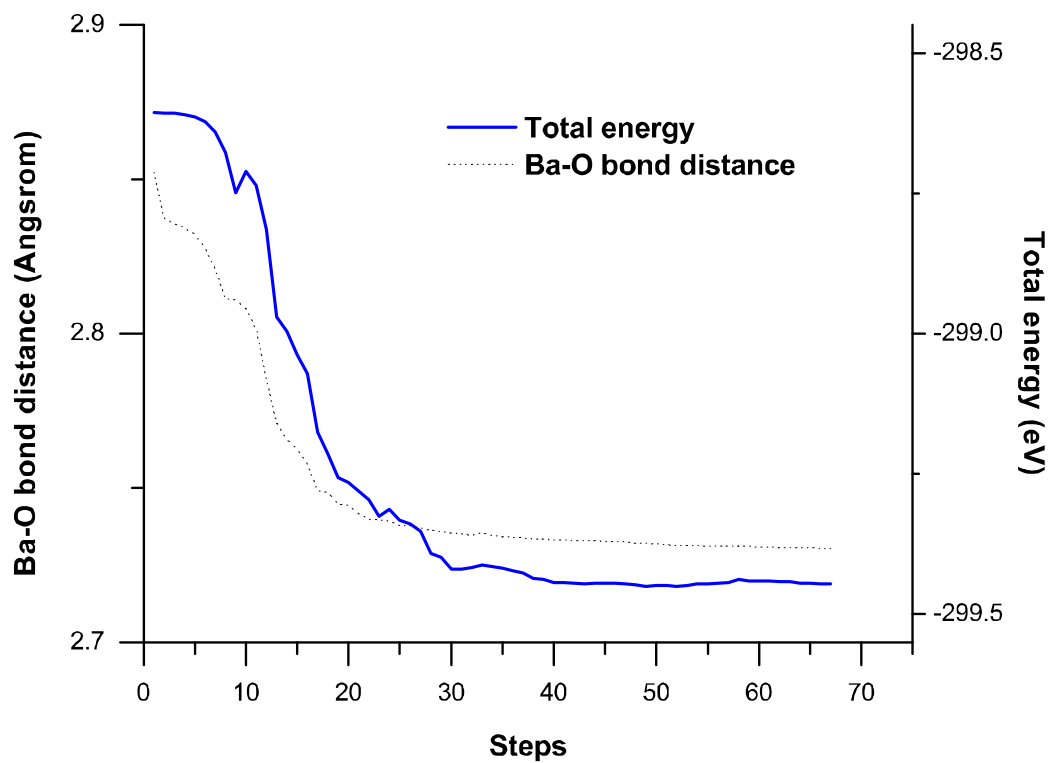


Figure 5. The evaluation of Ba-O band distance (Blue solid) and total energy (black dots) in the process of geometry optimization. The median of the Ba-O bond distances in $\text{Ba}^{+2+}(\text{I}) - \text{Fe}^{2+}(\text{I})$ was chosen in the figure as an example.

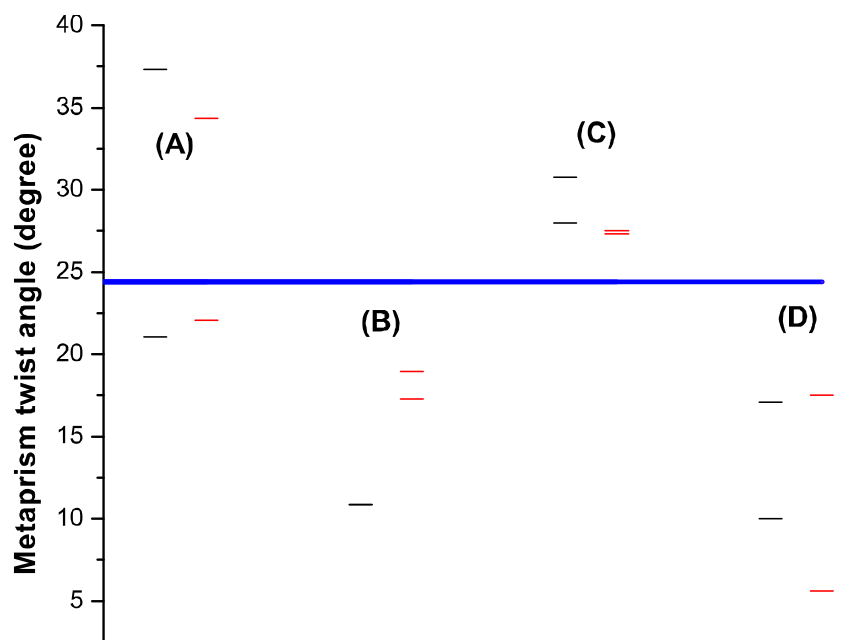


Figure 6. The metaprisism twist angle for Cs⁺ contained species (black bars) and the decay product Ba²⁺ contained species (red bars) for (A) Cs⁺(I) - Fe³⁺(I), (B) Cs⁺(II) - Fe³⁺(I), (C) Cs⁺(I) - Fe³⁺(II), and (D) Cs⁺(II) - Fe³⁺(II) decay. The blue line donates the twist angle for Ca₁₀(PO)₆F₂.

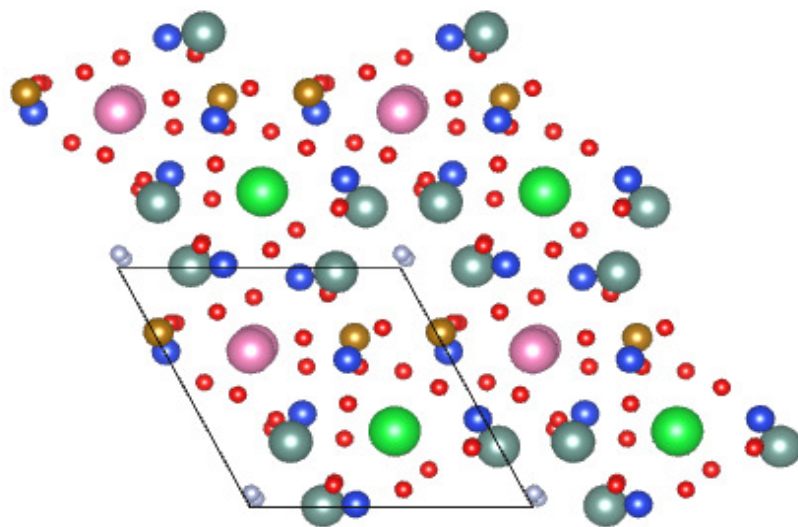


Figure 7. The optimized molecular structure of $(\text{Fe}^{3+}\text{-Sr}^{2+}\text{-Fe}^{3+})$ (2x2x1), when Sr^{2+} replaces Ca^{2+} at site (I) and two Fe^{3+} replace two Y^{3+} at same hexagonal channel. Green, golden, pink, grey, blue, red, and silver balls represent Sr^{2+} , Fe^{3+} , Ca^{2+} , Y^{3+} , Si^{4+} , O^{2-} , and F^- respectively.

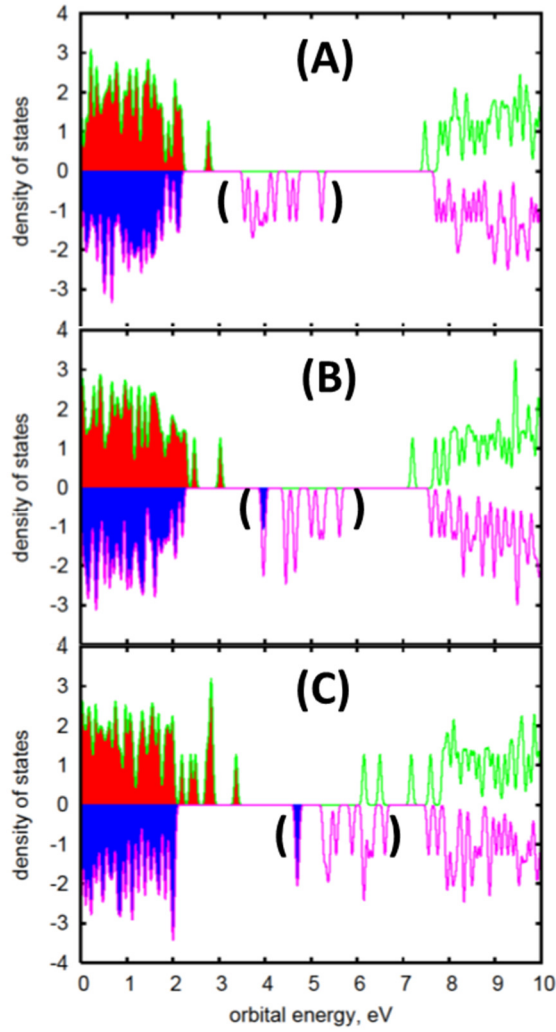


Figure 8. DOS of $\text{Fe}^{3+}\text{-Sr}^{2+}\text{-Fe}^{3+}$ (A), $\text{Fe}^{2+}\text{-Y}^{3+}\text{-Fe}^{3+}$ (B), and $\text{Fe}^{2+}\text{-Zr}^{4+}\text{-Fe}^{2+}$ (C). Curves above and below the central line in each panel represent partial DOS for spin (α) (green) and spin (β) (blue) components. Filled portions of the curve represent occupied electronic states for spin (α) (red) and spin (β) (blue). The ferromagnetic order of iron ions with high spin state can be seen. The orbitals inside the black bracket are d-like orbitals contributed by Fe^{3+} (Fe^{2+}) ion.

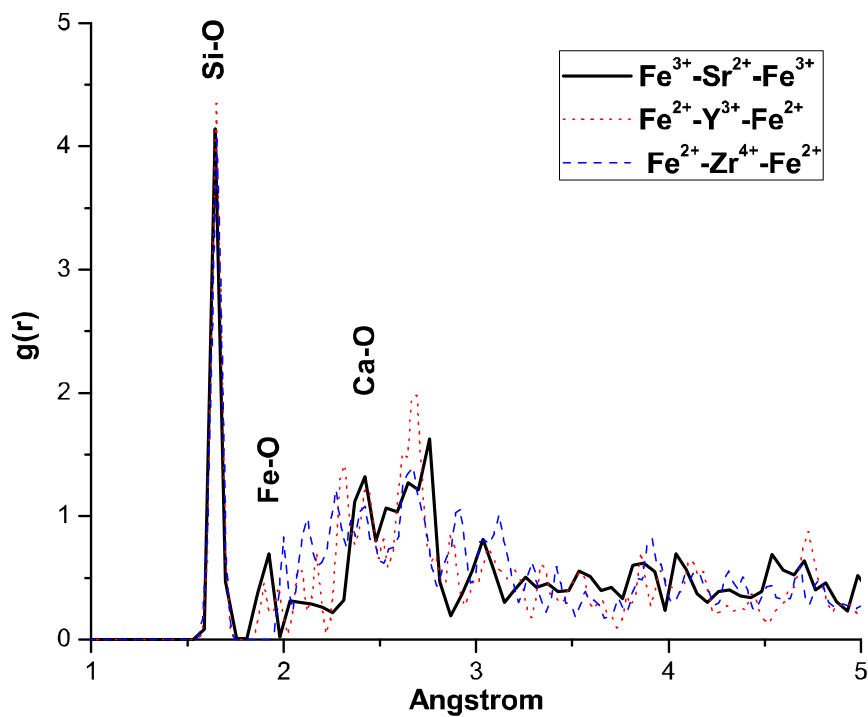


Figure 9. The radial distribution function for all pairs changes from $\text{Fe}^{3+}\text{-Sr}^{2+}\text{-Fe}^{3+}$ (black solid line) \rightarrow $\text{Fe}^{2+}\text{-Y}^{3+}\text{-Fe}^{3+}$ (red dots) \rightarrow $\text{Fe}^{2+}\text{-Zr}^{4+}\text{-Fe}^{2+}$ (blue dashes). From left, the first peak is the Si-O bond. The position of this peak remains in $\text{Sr}^{2+} \rightarrow \text{Y}^{3+} \rightarrow \text{Zr}^{4+}$ transmutation. Fe-O and Ca-O bonds are signed in the figure.

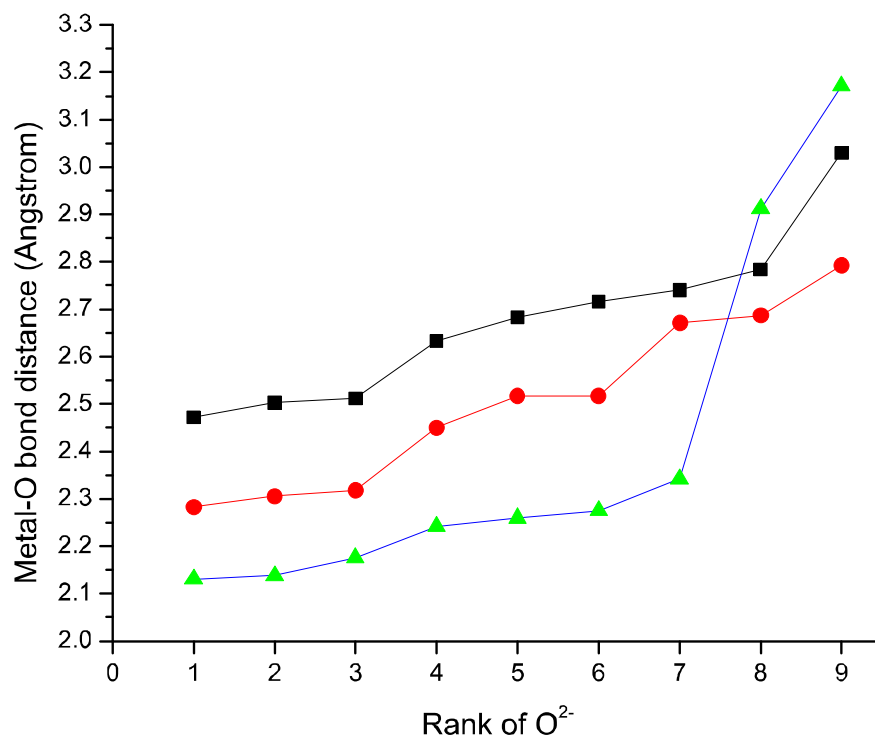


Figure 10. The nine nearest Metal-O bond distances for Sr-O (black squares), Y-O (red dots), and Zr-O.

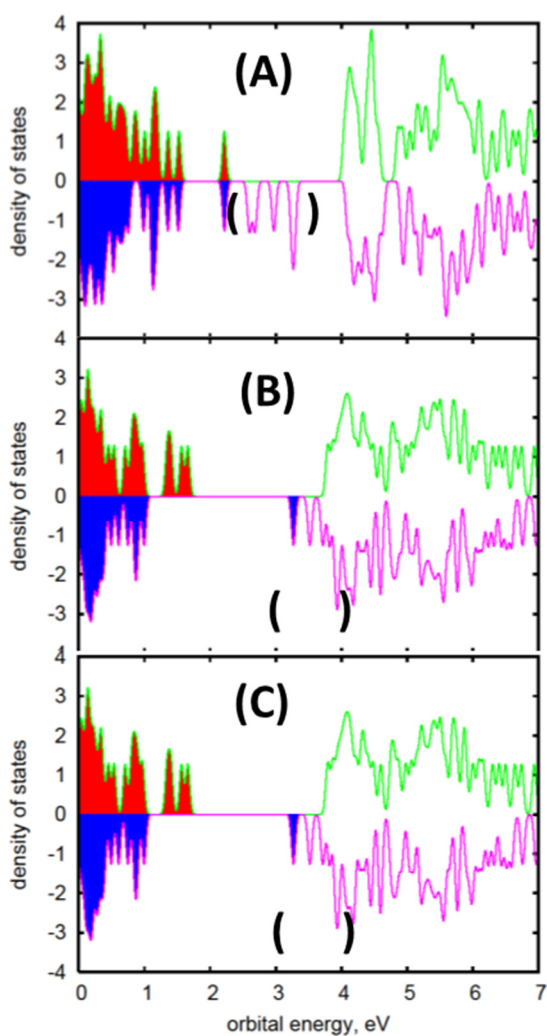


Figure 11. DOS of I-Fe³⁺ (A), Xe- Fe²⁺ (B), and vacancy- Fe²⁺ (C). Curves above and below the central line in each panel represent partial DOS for spin (α) (green) and spin (β) (blue) components. Filled portions of the curve represent occupied electronic states for spin (α) (red) and spin (β) (blue). The orbitals inside the black bracket are d-like orbitals contributed by Fe³⁺ (Fe²⁺) ion.

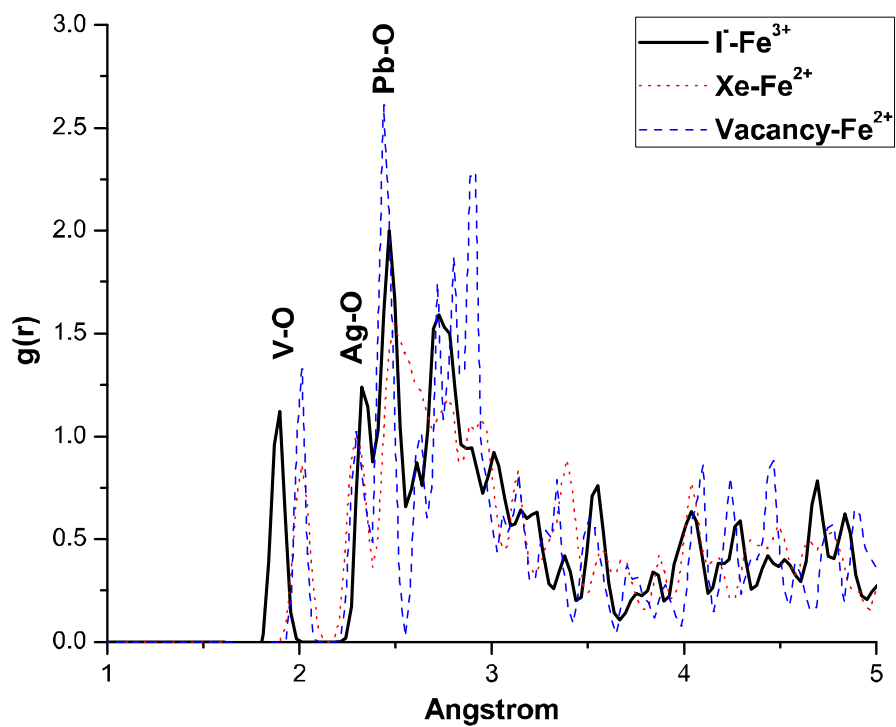


Figure 12. The radial distribution function for all pairs changes from I-Fe^{3+} (black solid line) \rightarrow Xe-Fe^{2+} (red dots) \rightarrow vacancy- Fe^{2+} (blue dashes). From left, the first, second and third peaks contribute by V-O, Ag-O, and Pb-O bonds respectively. A significant shift of V-O bond has been seen.

Tables:

Table.1 Total energies and the cohesive energy change when Cs and Fe are at different Ca sites

(unit: eV)

	Cs ⁺ (I) - Fe ³⁺ (I)	Cs ⁺ (II) - Fe ³⁺ (I)	Cs ⁺ (I) - Fe ³⁺ (II)	Cs ⁺ (II) - Fe ³⁺ (II)
Total energy	-295.61	-295.76	-295.47	-295.49
	Ba ²⁺ (I) - Fe ²⁺ (I)	Ba ²⁺ (II) - Fe ²⁺ (I)	Ba ²⁺ (I) - Fe ²⁺ (II)	Ba ²⁺ (II) - Fe ²⁺ (II)
Total energy	-299.38	-300.94	-300.71	-300.79
	Cs	Cs	Cs	Cs
Total energy	-2.41	-2.41	-2.41	-2.41
	Ba	Ba	Ba	Ba
Total energy	-1.23	-1.23	-1.23	-1.23
$\Delta E_c(\text{Ba-Cs})$	4.95	6.36	6.42	6.53

Table 2. The comparison of the volume and lattice parameters in Cs⁺-Fe³⁺ → Ba²⁺-Fe²⁺

	volume	a	b	c	α	β	γ
Cs ⁺ (I) - Fe ³⁺ (I)	550.2	9.497	9.497	7.043	90.0	90.0	120.0
Ba ²⁺ (I) - Fe ²⁺ (I)	542.4	9.486	9.486	6.961	90.0	90.0	120.0
Changing	-1.4%	-0.1%	-0.1%	-1.2%	0.0%	0.0%	0.0%
Cs ⁺ (II) - Fe ³⁺ (I)	559.7	9.796	9.656	6.827	90.7	90.1	119.9
Ba ²⁺ (II) - Fe ²⁺ (I)	550.6	9.656	9.550	6.896	90.2	89.4	120.0
Changing	-1.6%	-1.4%	-1.1%	1.0%	-0.6%	-0.7%	0.1%
Cs ⁺ (I) - Fe ³⁺ (II)	565.3	9.588	9.613	7.167	90.3	90.2	121.2
Ba ²⁺ (I) - Fe ²⁺ (II)	554.8	9.532	9.546	7.075	90.0	90.5	120.5
Changing	-1.9%	-0.6%	-0.7%	-1.3%	-0.4%	0.3%	-0.6%
Cs ⁺ (II) - Fe ³⁺ (II)	573.3	10.059	9.751	6.752	90.0	90.0	120.0
Ba ²⁺ (II) - Fe ²⁺ (II)	555.7	9.719	9.629	6.861	90.0	90.0	120.1
Changing	-3.1%	-3.4%	-1.2%	1.6%	0.0%	0.0%	0.0%

Table 3. The comparison of the volume and lattice parameters in $\text{Ca}_3\text{Sr}_1\text{Y}_6\text{Fe}_2(\text{SiO}_4)_6\text{F}_2 \rightarrow \text{Ca}_3\text{Y}_7\text{Fe}_2(\text{SiO}_4)_6\text{F}_2 \rightarrow \text{Ca}_3\text{Zr}_1\text{Y}_6\text{Fe}_2(\text{SiO}_4)_6\text{F}_2$ transmutation.

	Volume	a	b	c	α	β	γ
$\text{Fe}^{3+}\text{-Sr}^{2+}\text{-Fe}^{3+}$	538.4	9.257	9.333	7.040	89.8	90.7	117.7
$\text{Fe}^{2+}\text{-Y}^{3+}\text{-Fe}^{3+}$	531.0	9.370	9.443	6.860	89.7	89.7	119.0
change	-1.4%	1.2%	1.2%	-2.6%	-0.1%	-1.1%	1.1%
$\text{Fe}^{2+}\text{-Zr}^{4+}\text{-Fe}^{2+}$	530.5	9.548	9.464	6.683	89.3	90.1	118.6
Change	-0.1%	1.9%	0.2%	-2.6%	-0.5%	0.5%	-0.3%

Table 4. The comparison of the volume and lattice parameters in $\text{AgFePb}_8(\text{VO}_4)_6\text{I}_2 \rightarrow \text{AgFePb}_8(\text{VO}_4)_6\text{IXe} \rightarrow \text{AgFePb}_8(\text{VO}_4)_6\text{I}$ process.

	volume	a	b	c	α	β	γ
I-Fe^{3+}	742.9	10.726	10.938	7.443	93.5	90.7	121.4
Xe-Fe^{3+}	742.6	10.718	11.143	7.321	93.2	89.5	121.7
change	0.0%	-0.1%	1.9%	-1.6%	-0.3%	-1.3%	0.2%
vac- Fe^{3+}	705.0	10.572	10.863	7.314	93.2	88.7	122.8
change	-5.1%	-1.4%	-2.5%	-0.1%	0.0%	-0.9%	0.9%

Dual-Mode Mechanisms of Iodine Release and Long-term Chemical Durability of Iodine Apatite $\text{Pb}_{9.85}(\text{VO}_4)_6\text{I}_{1.7}$

Zelong Zhang and Jianwei Wang ^{1,*}, et al.

¹Department of Geology and Geophysics, Louisiana State University, Baton Rouge, Louisiana 70803

*Jianwei Wang
Department of Geology and Geophysics
Louisiana State University
Baton Rouge, Louisiana 70803, USA
Phone: 225-578-5532
Fax: 225-578-2302
Email: jianwei@lsu.edu

Key words: apatite, iodine, nuclear waste forms, leaching, diffusion, dissolution

Abstract

Iodine-129 is a volatile radionuclide that formed as a product of nuclear fission. Due to its long half-life (15.7×10^6 year) and high mobility in environment, it is imperative to develop suitable waste forms which are durable to retain I-129 in geological settings. Vanado-iodoapatite has been proposed as a candidate waste form for iodine immobilization because of the chemical durability of apatite structure. To evaluate the long-term performance of such waste form materials, it is necessary to examine the leaching behavior of iodine in the apatite in aqueous solution. A standard test method based on Accelerated Leach Test (ALT) was adopted to investigate the iodine leaching behavior. The ALT is a semi-dynamic leach test in which the matrix material is exposed in fresh leachant on a periodic schedule. The leachant is replaced completely after each interval. The experiments were carried out in cap-sealed Teflon vessels under constant temperature 90 ± 0.5 °C. Apatite samples ($\text{Pb}_{9.85}(\text{VO}_4)_6\text{I}_{1.7}$) were placed on Teflon mesh stands in the vessels, which were filled with deionized water as leachant. The leachates were collected and analyzed using ICP-MS. The results show that Pb and V were released stoichiometrically with a molar ratio Pb/V of 1.6, consistent with their stoichiometric ratio 9.8 / 6. However, the released iodine is significantly higher than its corresponding stoichiometric value (I/V) 1.7 / 6. In addition, at neutral pH with DI water, iodine leaching rate decreases with time, while at slightly acidic condition, the leaching rate becomes a constant after first day. The estimated long-term leach rate of iodine is ~ 2 mg/m/day, significantly lower than a number of candidate iodine waste forms. The leaching behaviors show that the release of iodine is controlled by diffusion and

dissolution processes. Our current study demonstrates the potential of vanado-iodoapatite as a waste form candidate to immobilize iodine-129.

Introduction

The disposal of radioactive waste is a technical challenge that inhibits the application of nuclear energy (Agency, 1987; Council, 2011; Gombert, Ebert, Marra, Jubin, & Vienna, 2008; Noyes, 1995; Peters & Ewing, 2007; Weber, Navrotsky, Stefanovsky, Vance, & Vernaz, 2009). The general accepted waste management strategy requires the immobilization of radionuclides in waste forms, stable solid host materials of high durability in disposal environment (Agency, 1987; Council, 2011). Waste forms is the primary barrier engineered to retain radionuclides into biosphere for a time scale of the order of a half-life. Therefore, developing appropriate waste forms is imperative to address this challenge, particular for radionuclides exhibiting long half-live and poor sorption on conventional materials (Council, 2011; Ewing, 1999, 2001; Ewing, Weber, & Clinard Jr, 1995; Noyes, 1995).

Iodine – 129 is one of an important radionuclides for assessing the disposal safety of radioactive waste (Kato, Kato, & Tanabe, 2002; Peters & Ewing, 2007), owing to the extremely long half-live, the high volatility of elemental iodine, the high corrosiveness of iodide salts, and the easy displacement of iodine by other common anions in nature (Agency, 1987; Council, 2011; Ewing et al., 1995; Fuge & Johnson, 1986; Gombert et al., 2008; Lide, 2005; Noyes, 1995). Iodine – 129 is also one of the prevailing radionuclides in terms of the maximum dose rate (Ewing et al., 1995), especially for nuclear waste bearing transuranic elements (Kato et al., 2002). Iodine ion exhibits low sorption property on conventional engineering barrier materials as well as the natural ones such as rock and soil (Council, 2011; Fabryka-Martin, 1988; Koch-Steindl & Pröhl,

2001). Moreover, iodine – 129, if treated conventionally, can be released rapidly from a geological repository and migrate to biosphere with insignificant decay loss due to its extremely long half-life 1.57×10^7 year (Agency, 1987; Council, 2011; Noyes, 1995). Thus, immobilizing iodine is one of the priority goals in nuclear waste management.

Several candidate waste form along with their respective treatment techniques have been proposed to immobilize iodine. Glass type waste forms can be obtained by Hot Isostatic Pressing (HIP) and low temperature vitrification. HIP method involves high temperature and pressure that convert amorphous silica gel into crystalline quartz solidificate. Iodine is confined among quartz grains in the form of AgI or AgIO₃. Therefore, the release of iodine, which retained by the quartz grain boundary layer in HIP treated solidificate, is dominated by diffusion process (Kato et al., 2002). Another glass waste form (e.g. AgI - Ag₂O - P₂O₅ and B₂O₃ - Si₂O – PbO) utilizes low temperature vitrification to confines radioactive iodine, which yields homogeneous glass without crystallization (Council, 2011). In addition to glasses, another type of waste forms is produced by consolidation treatments yielding cement, ceramics, and mineral crystalline waste forms with cage or tunnel structures. Hot-press of the spent filter methods solidify spent iodine filter and encapsulate iodine with physically and chemically stable metallic or mineral matrices, such as copper and apatite. The iodine release occurs with the matrix corrosion. High performance cement solidification has been developed as a high iodine retention waste form by mixing the IO₃⁻ with high sorption performance cement. A distribution coefficient about 900 ml/g has been reported for the IO₃⁻. Naturally occurred mineral structures with inherently low solubility and leachability have inspired the synthesis of mineral waste forms, which are composed of mineral lattices with iodine anion. Leach tests on the synthesized iodine sodalite Na₈(AlSiO₄)₆I₂ and lead

vanado-iodoapatite $\text{Pb}_{10}(\text{VO}_4)_6\text{I}_2$ revealed leach rates of $0.005 - 0.01$ and $0.398 \text{ g} \cdot \text{m}^{-2} \cdot \text{d}^{-1}$, respectively (Kato et al., 2002; Maddrell, Gandy, & Stennett, 2014). It also shows that the iodine released from sodalite was driven by congruent dissolution, whereas an incongruent release of iodine was observed in apatite waste form (Kato et al., 2002; Maddrell et al., 2014). Among these candidate waste forms, materials with apatite structure exhibit numerous advantages (Ewing & Wang, 2002; Oelkers & Montel, 2008). With geological record of over billions of years, naturally occurred apatite minerals $\text{Ca}_{10}(\text{PO}_4)_6\text{X}_2$ have demonstrated the mechanical and chemical durability of apatite structure (Ewing, 1999; Ewing et al., 1995). A wide range and high tolerance of substitutions at multiple crystallographic sites show a high degree of chemical and structural flexibility of apatite matrix (Council, 2011; Ewing, 1999; Weber et al., 2009), which can accommodate different elements generated from radioactive decay of iodine (Oelkers & Montel, 2008; Peters & Ewing, 2007; Wang, 2015). Therefore, apatite structured material $\text{Me}_{10}(\text{XO}_4)_6\text{Y}_2$ is a promising waste form candidate for iodine immobilization, given the inherited durability and flexibility from natural analogues.

To quantify the chemical durability, it is necessary to carry out robust leaching test on candidate waste form. Current leach test standards of material chemical durability are generally adapted from MMC series tests (MCC-1 through MCC-5) developed by the Materials Characterization Center (MCC) (Council, 2011). The successors Waste Form Test Protocols (C1174, 1220, C1285, C1662, C1663, and C1308), developed by the ASTM Subcommittee C26.13, provide mechanistic understanding of material durability (Council, 2011; Weber et al., 2009). In general, there are five types of approaches for testing chemical durability of waste forms: static leach test, Product Consistency Test (PCT), Soxhlet test, Single-Pass Flow-Through test (SPFT), and

Accelerated Leach Test (ALT). Static leach test is widely used to compare the dissolution behaviors of waste forms and to probe the reaction during static exposure to dilute solution, of which the solution feedback effect is assumed to be insignificant. The PCT is also a static test using crushed sample to determine the dissolution mechanisms of waste forms, particularly for glasses. Soxhlet test, mostly used in Europe, is designed to maximize the amount of leachable constituent in leachant by allowing a continuous contact between the waste and recycling leachant in a closed system. SPFT method, conducted in a constant-flow environment, is recommended to study the long-term dissolution of glass waste forms, which assumes that the leached species have negligible effects on the forward dissolution rate. The ALT is a semi-dynamic test in which the leachate solution is periodically replaced after a short interval (e.g. 1 day).

Soxhlet test on synthesized lead vanado-iodoapatite $\text{Pb}_{10}(\text{VO}_4)_6\text{I}_2$ by hot-pressing showed a release rate of iodine leached from apatite was two orders of magnitude higher than a typical glass waste and suggested apatite will be a good waste form if embedded in a suitable matrix material to overcome its vulnerability to leaching (Kato et al., 2002; Uno, Shinohara, Kurosaki, & Yamanaka, 2001). The release of iodine can be subjected to leaching model (diffusion) or solubility limit model (dissolution) (Kato et al., 2002). However, soxhlet test is not recommended to study the release mechanism of waste form due to the lack of control of model parameter values and the overlook of possible impact of the effective flow rate (Ebert & Fuhrmann, 2010). Several researchers performed static leach test on iodide vanadinite $\text{Pb}_{10}(\text{VO}_4)_6\text{I}_2$ obtained from solid state reaction or dry mechanochemical process (Maddrell et al., 2014; Suetsugu, 2014; Zhang, Maddrell, Abraitis, & Salje, 2007), from which an incongruent

release of iodine is observed with approximately an order of magnitude higher than matrix dissolution. A diffusion controlled iodine release model is proposed due to the exchangeability of I^- by OH^- (Suetsugu, 2014; Zhang et al., 2007). Due to the difference of leach test protocols implemented worldwide, it is difficult to compare the result reported in literatures. Thus, it is beneficial to apply a test protocol that enables the normalization of test system parameters, which can yield scalable result to compare previous study under different settings.

Considering the diffusion and possibility of multiple processes, conducting an appropriate leach test is necessary to characterize the iodine release behavior of apatite waste form. Here, the ALT test is proposed to monitor the species of interest released in successive test intervals, which can 1) determine the diffusion coefficients, temperature and other parameter dependences, to project the long-term release; 2) enhance the degree of overall reaction within a laboratory time frame; 3) evaluate the stability of waste form matrix, solution feedback, and solubility limit effects.

In this paper, the ALT leach test (ATSM C 1308-08) is performed to examine the occurrence of diffusion and necessary dependences for evaluating the long-term chemical durability of a synthetic apatite waste form: lead vanado-iodoapatite $Pb_{9.85}(VO_4)_6I_{1.7}$. In addition, dependencies on critical parameters such as time, surface to volume ratio, temperature, and pH are characterized and normalized for predicting the long-term leaching behavior of this apatite waste form.

2 Method

2.1 Leach Test

The lead vanadoapatite samples were synthesized by High Energy Ball Milling and Spark Plasma Sintering with a structure of $\text{Pb}_{9.85}(\text{VO}_4)_6\text{I}_{1.7}$ (Yao et al., 2014). All samples were prepared in a consistent manner to produce a uniform and reproducible surface finish. Sample surfaces were polished by a mechanical polishing wheel successively using 600, 2400, and 4000 grits paper with absolute ethanol lubrication.

Standard Test Method for Accelerated Leach Test (ALT), ASTM C-1308, was adopted to assess the long-term iodine immobilization of lead vanado-iodoapatite matrix. In the ALT leach test, the matrix material is exposed in fresh leachant on a periodic schedule. The leached solution is replaced completely after each interval. Based on the elemental analysis of successively collected leachates, the results can be quantitatively modeled to characterize the release mechanisms (e.g. diffusion, dissolution), solution saturation effect, species partitioning, and therefore the long-term performance behavior.

In this study, ALT experiments of lead vanado-iodoapatite samples were performed in cap-sealed vessels under standard pressure 1 atm and constant temperature ($20, 50, 70, \text{ or } 90^\circ\text{C} \pm 0.5$). Those apatite samples were placed on mesh stand in Teflon vessels which were filled with distilled-deionized water as leachant. The replacement times were 2, 5, and 17 hours for the first three intervals and 24 hours for the rest intervals. To test the pH effects, buffer solutions were obtained from Fluka of Sigma-Aldrich as the leachant solution, of which the main buffering compounds are potassium hydrogen phthalate / formaldehyde, sodium citrate, and disodium tetraborate for pH 4, 6, and 9, respectively. The increment of buffers' pH values is within 0.4

under temperatures ranging from 20 to 90°C. The surface area was measured with micrometer and caliber.

The total weight of vessel (including vessel, apatite sample, and solution) were recorded before and after each interval to evaluate the weight loss of leachant. Our record shows that weight loss during all leaching intervals is within 1 %. In addition, acid strip tests to the vessels were also performed at the end of ALT experiment, which confirmed the sorption on vessel is negligible for elements of interest.

Interestingly, a comparative test conducted on brand new samples shows that there is no difference to the long-term leaching behavior by changing the initial intervals and surface roughness as shown in supplement Fig 1.

2.3 Leachate Analysis

Leachate solutions were analyzed with a PerkinElmer Elan 9000 Inductively Coupled Plasma - Mass Spectrometry (ICP-MS) system. Internal standards Cesium (Cs), Manganese (Mn), and Bismuth (Bi) were utilized in the analysis of Iodine (I), Vanadium (V), and Lead (Pb) in leachate, respectively. Three standard solutions provided by Inorganic Ventures were used in ICP-MS calibration and analysis: i) a iodine standard containing $1.001 \pm 0.007 \mu\text{g/ mL}$ Iodide in H_2O solution, ii) a lead and vanadium standard containing $1.000 \pm 0.007 \mu\text{g/ mL}$ Pb and $1.000 \pm 0.006 \mu\text{g/ mL}$ V in 1% HNO_3 solution, iii) and an internal standard containing $1.000 \pm 0.009 \mu\text{g/ mL}$ Cs, $1.000 \pm 0.008 \mu\text{g/ mL}$ Mn, and $1.000 \pm 0.006 \mu\text{g/ mL}$ Bi in 2 % HNO_3 . For a typical leachate analysis, a 1 mL internal standard was added into a 14 mL leachate solution.

A schematic of experiment is listed in Fig 1.

2.4 Surface Characterization

Apatite sample surfaces were characterized by Scanning Electron Microscopy (SEM) and Energy Dispersive Spectroscopy (EDS). SEM imaging were performed by FEI Quanta SEM system with FEI Versa 3D DualBeam, while the EDS spectra were collected from integrated TEAM Pegasus – Integrated EDS and EBSD Analysis System.

Raman spectroscopy was performed on HORIBA Jobin Yvon's LabRAM system integrated with Olympus BX41 microscope. Raman spectra were referenced to the standard silicon wafer 520 cm^{-1} .

3. Results and Discussion

3.1 Release Rate

The release of species of interest is reported as the cumulative concentration over interval time, such as Fig 2a and 2b. The cumulative concentration ($\text{mg} \cdot \text{m}^{-2}$) is sum of the concentration of species of interest leached during all prior and current intervals divided by the surface area of sample, which is calculated by the following equation:

$$\text{Cumulative Concentration}_j (\text{mg} \cdot \text{m}^{-2}) = \frac{\sum_{n=1}^j a_n (\text{mg})}{S (\text{m}^{-2})}$$

where a_n (mg) is the quantity of species measured in the leachate from the n th test interval, and the A (m^2) is the surface area of sample. Because there is no visible change of surface geometry and insignificant weight loss after leach test, the surface area (S) of sample is assumed to remain intact during the whole ALT test.

The resulting figures typically show steady increase of cumulative concentration over time, which can be accurately modelled by linear regression with R square values over 0.9. The leach rates ($\text{mg} \cdot \text{m}^{-2} \cdot \text{d}^{-1}$) of species of interest can be obtained by calculating the slope value of regression line as is shown in the following equation:

$$\text{Leach Rate } (\text{mg} \cdot \text{m}^{-2} \cdot \text{d}^{-1}) = \frac{\text{Cumulative Concentration}_j (\text{mg} \cdot \text{m}^{-2})}{\text{Time (day)}}$$

In order to obtain reliable result, only data of the last 7 intervals were used for leach rate calculation. In addition, the iodine leaching data (rate and figure) in section 3.1 is normalized in order to offset the time dependence, which is discussed in 3.3a.

3.1a Effect of Surface Area to Solution Volume Ratio

By varying the sample surface to solution volume ratio (S/V), the dependence of leach rate on the S/V ratio is determined as shown in Fig 2a and 2b. Using deionized water (DIW) as leachant and under conditions of 90°C and interval of 1 day, ALT tests of different S/V ratios including 2/m, 5/m, 10/m, 16/m, and 50/m yielded leach rates of iodine are 6.9, 5.5, 2.5, 4.4, and 1.1 $\text{mg} / (\text{m}^2 \cdot \text{d})$, while the leach rates of lead are 38, 29, 10, 6.0, and 2.0 $\text{mg} / (\text{m}^2 \cdot \text{d})$, respectively.

Lower S/V ratio indicates a relative larger volume of the leachant solution from the dissolved species in leachate, a high release rate from a low S/V system would be expected, and vice versa.

3.1b Solution Exchange Interval

The effect of interval length on leach rate is evaluated by varying the interval time as shown in Fig 3a and 3b, under conditions of DIW, 90°C, and 10 m^{-1} (S/V ratio). The interval of 1 day, 3.5

days, and 7 days yielded release rates of 2.5, 0.79, and 0.47 mg / (m² · d) for iodine and 11, 4.1, and 1.8 mg / (m² · d) for lead, respectively. Frequent solution exchange reduces the feedback effect of dissolved species. Therefore, shorter interval results a higher release rate, and vice versa.

3.1c Temperature

As shown in Fig 4a and 4b, ALT tests under different temperatures were conducted under conditions of DIW, 5 m⁻¹, and 1-day interval. Experiment under 20, 40, 70, and 90°C yielded release rates of 0.98, 1.8, 4.0, and 5.5 mg / (m² · d) for iodine and 5.7, 11, 19, and 29 mg / (m² · d) for lead, respectively. The relationship between temperature and release rate is analyzed using Arrhenius equation:

$$k = Ae^{-E_a/(RT)}$$

where k is the rate constant, A is the pre-exponential factor, E_a is the activation energy, R is the gas constant, and T is the temperature in kelvin. Since temperature is the only variable in this ALT series, the leach rate is equivalent to the k . Therefore, increment of temperature will increase the overall reaction rate. In addition, the Arrhenius equation can be transformed as

$$\ln k = \ln A - E_a/(RT)$$

Therefore, the apparent activation energy E_a can be derived by the leach rates in mol / (m² · d) and the corresponding temperatures in kelvin. In Fig 5, plotting $\ln r$ versus $-1000/T$ exhibits a desirable linear regression with R square values over 0.99 for both iodine and lead profiles, indicating a single reaction mechanism. The derived apparent activation energies E_a for iodine and lead are 22.4 kJ · mol⁻¹ and 20.0 kJ · mol⁻¹, respectively. The difference is attributed to the initial diffusion of iodine, of which the detail is discussed in Section 3.2.

3.1d pH

Solution pH can have pronounced effect on leaching rates. The result of ALT tests using pH buffers as leachant is listed in Fig 6a and 6b. Buffers pH 4, 6, and 9 yielded significantly different leach rates. Under the conditions of 90°C, 5 m⁻¹, and 1-day interval, release rates of iodine 883, 1097, and 3.7 mg / (m² · d) were obtained, while the release rate of lead are 4019, 9590, and 0 mg / (m² · d) for pH 4, 6, and 9, respectively. Lead released from pH 9 ALT, however, is too low to be detected.

Interestingly, both samples leached with buffers pH 4 and 6 showed similarly roughened surfaces (Fig 8a), however, new phase of brown color and smooth texture occurred that was scattered all over the pH 4 leached surface (Fig 8b). Raman spectroscopy in Fig 7 revealed that the new phase is chervetite Pb₂V₂O₇, which was also consist with the SEM and EDX results (Fig 8a and 8c). In addition, the measured elemental release rates of pH 4 test are considerably lower than those of pH 6. For pH 4 leach test, the new phase and the relatively low content of dissolved species confirmed that the leached elements were partitioned into the precipitate and leachate.

Comparing with DIW ALT results, element release rates of apatite are slightly reduced in the basic leachant from 5.5 to 3.7 mg / (m² · d) for iodine and 29 to 0 for lead, whereas the element release rates show exponential increase in acidic solutions over two orders of magnitude from 5.5 to 800-1100 mg / (m² · d) for iodine and 29 to 400 - 9600 mg / (m² · d) for lead from neutral to pH 9 solution, respectively. In addition, the atomic ratios of leachate in Fig XX shows relative low V/Pb but congruent I/Pb ratios. Given that the V/Pb 0.6 in apatite matrix and 1 in chervetite, the low V/Pb < 0.6 dissolved in leachate confirms the complex process of pH 4. Similar effect is

also reported on the leach test of $\text{Pb}_{10}(\text{VO}_4)_{4.8}(\text{PO}_4)_{1.2}\text{I}_2$ in water, which yielded $\text{Pb}_2\text{V}_{1.16}\text{P}_{0.27}\text{O}_{7.66}$ as the alternation product (Guy et al., 2002).

3.2 Leaching Mechanisms

The relative ratios of constituents can distinguish whether the leaching is congruent. In Fig 9a, the atomic ratios of iodine versus lead (I/Pb) show an exponential decrease of I/Pb over time eventually approaching the stoichiometric value 0.17 of apatite mineral, whereas the ratios of vanadium versus lead (V/Pb) show a relative small fluctuation around the stoichiometric value 0.61 of apatite mineral.

Congruent release of V and Pb suggests dissolution controlled leaching, whereas the incongruent rate of iodine indicates additional release mode involved. In terms of DIW leach test, the exponential decrease of I/Pb ratio can attribute to the iodine diffusion, and the trend that approaches the stoichiometric value can be ascribed to the continuous dissolution of matrix, which became apparent as the diffusion process was diminishing over time probably because of the depletion of diffusive iodine in solid. Due to the pronounced effect of pH, the dissolution was significantly enhanced by acid leachants, allowing a rapid release of iodine by dissolution before diffusion took place. The element released in pH 6 solution shows steady atomic ratios over time complied with the mineral stoichiometry, suggesting dissolution dominated release. The release rate of iodine in pH 4 was significantly inhibited by the massive precipitate scattered on the sample surface protecting the surface beneath from dissolution. Therefore, the iodine release can be described as a two-mode leaching behavior controlled by dissolution and diffusion; and the release of lead and vanadium is controlled by dissolution.

3.3 Long-term Chemical Durability

3.3a Normalization on leach test parameters

To predict the long-term leaching behavior, key system parameters including S/V, Interval and pH, on which the leach rates depend, need to be quantitatively characterized and normalized.

The stoichiometric ratio of dissolved lead and vanadium in DIW suggest a congruent dissolution of mineral matrix. ALT in basic solution shows similar mechanism with those in DIW, whereas dissolution process is the dominant release mechanism in acid solutions. Due to the precipitation in pH 4 ALT, the dissolved content is only a fraction of total release and the overall release is arguably hindered by the surface precipitate. Therefore, the total release rate at pH 4 cannot be retrieved from the result. The result of leaching under different pH standalone is inconclusive to characterize the pH dependence of the release rate.

However, previous study showed a systematic change of systematic dissolution rate over pH in acid leachant (Guidry & Mackenzie, 2003; Guy et al., 2002; Valsami-Jones et al., 1998). Since the ALT result of pH 6 is suitable to characterize the dissolution due to the congruent release, having the data of pH 6 and DIW is sufficient to normalize the pH effect of acid.

3.3b Long Term Dissolution of Lead and Vanadium

Dependence normalization of a DIW leach environment is carried out based on the data obtained from the DIW leach test of different S/V and interval.

The dissolution is the primary process for most lead and vanadium as well as a small fraction of iodine released in DIW. The change upon a dissolution process by varying the interval time and

the S/V ratio is the manifestation of solution feedback of dissolved species. Therefore, a leaching system with infinitely small interval and/or infinitely small S/V is equivalent to a system of infinitely diluted solution, which annihilates the solution feedback of dissolved species; and a system with infinite large interval and/or infinite large S/V is a limiting case, giving zero leaching rate as shown in Fig 10a and 10b. Both lead and vanadium rates are, therefore, modeled by the following equation:

$$f(x) = a \cdot (1 - \exp(-b \cdot x))$$

where $f(x)$ is the release rate of elements of interest, a is the maximum rate in infinite diluted medium and is constrained to the same value for both interval and S/V, and b is the fitting variable. As shown in Figure 10a and 10b, maximum rate 47.9885 and 8.5688 mg / (m² · d) are obtained with over 0.99 R square for lead and vanadium, respectively.

3.3c Short Term Diffusion and Long Term Dissolution of Iodine

Unlike lead and vanadium, the normalization of iodine release rate is complicated by its dual-mode mechanism. The iodine diffusion is a time dependent process for each sample. The time dependence was normalized by treating the atomic ratios of I/Pb with the following fitting equation:

$$g(x) = 0.1726 + m \cdot \exp(-n \cdot x)$$

where $g(x)$ is the I/Pb ratio, 0.1726 is the stoichiometric value of I/Pb atomic ratio, m and n are the fitting variables.

As shown in Fig 10c, the fitting curve simulates the baseline of I/Pb ratios, reaching the stoichiometric value of I/Pb. It seems unreasonable to assume a congruent release of I and Pb of

long term, considering the high incongruity of initial release. However, the diffusion process only facilitates the short term release of iodine, the amount of iodine diffused is trivial to affect the dissolution. The long term release of iodine is dominated by the dissolution, which became apparent as the diffusion diminishes over time. This can also be demonstrated by the comparative ALT sets (Supplement Fig 1), showing no difference for the long term release of iodine in DIW under same conditions 90°C, 1-day interval, and 5m⁻¹ regardless of the surface condition and high initial release. Therefore, the iodine leach rates in section 3.1 are obtained from time normalized leaching profiles without diffusion.

Normalization of S/V and interval of iodine release is based on the dissolution data, which is obtained by stripping away the time-dependent diffusion release from the total iodine release. Since the time dependence of iodine release is given by the diffusion process, the residual by removing the time dependent release is contributed by the iodine dissolution. Similar to the lead and vanadium data, the normalization of S/V and interval on iodine release yields a maximum release rate of 7.676 mg / (m² · d) with a R square of 0.93 as shown in Fig 10d.

4. Concluding Remarks

This study adopted accelerated leach test method ASTM C-1308 to evaluate the long term chemical durability of apatite nuclear waste form, Pb_{9.85} (VO₄)₆ I_{1.7}. A mechanistic insight of element release from nuclear waste form material is also presented by determining the release mechanisms and quantifying the impacts of different system parameters. Through the normalization of variables, the result findings can accommodate the extrapolation of leaching behavior under different settings including those of field scale.

The result also indicates a dual-mechanism of iodine release, in which the diffusion release is considerable in short term but is diminishing with time and therefore become negligible over long term. Thus, determining and differentiating the mechanisms of element release is critical to evaluate the long term durability of nuclear waste form. Solution feedback effect of dissolved species is also quantified by S/V ratio and interval.

Acknowledgements

This research is being performed using funding received from the DOE Office of Nuclear Energy's Nuclear Energy University Programs under award DE-AC07-05ID14517.

Figure 1. Experiment Schematic. Successive leachates are collected upon each interval. Then, the elemental analysis of leachate solution is performed by inductively coupled plasma – mass spectrometry (ICP-MS).

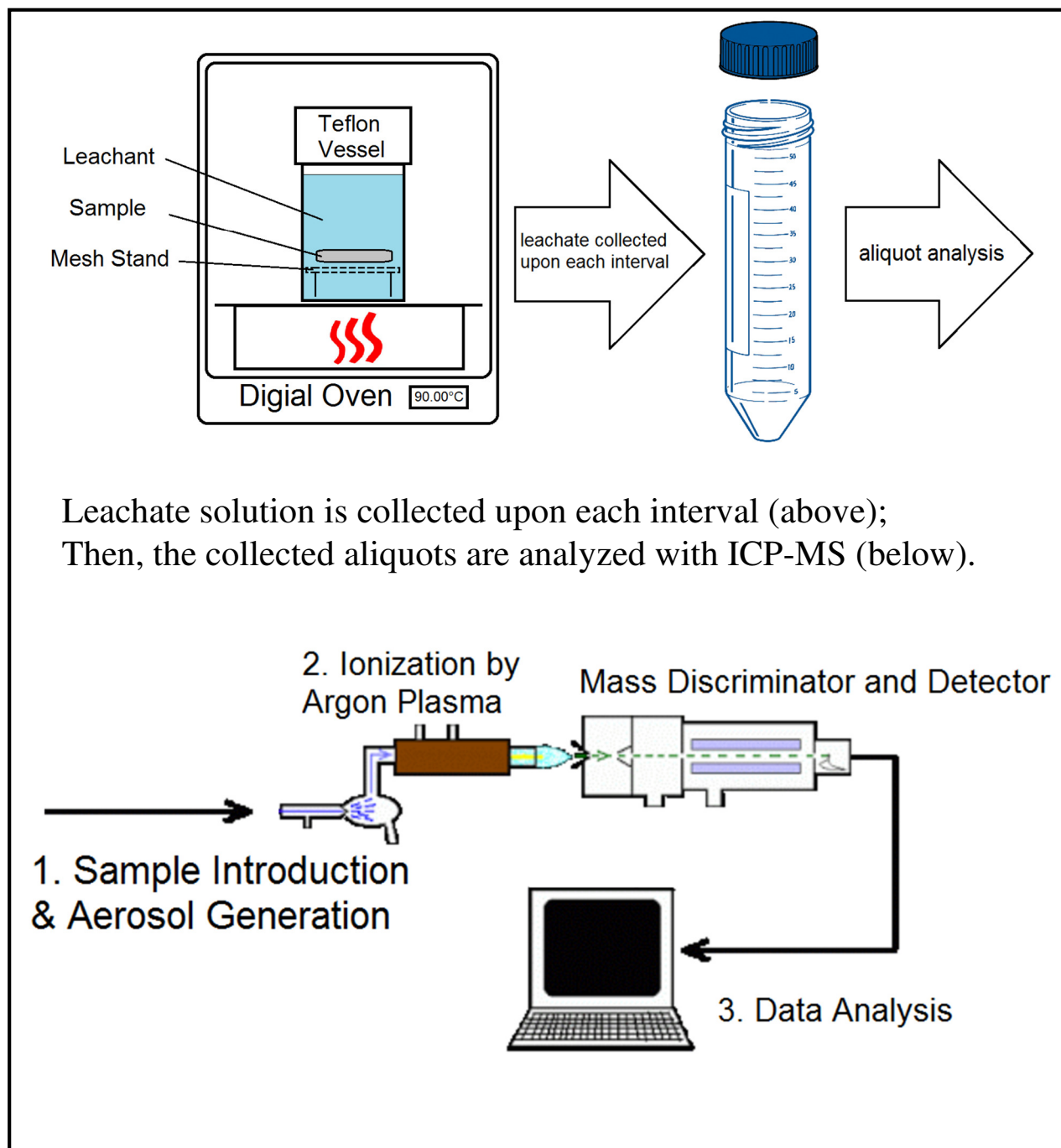


Figure 2a. Effect on iodine element release by varying sample surface to solution volume ratio (S/V) in deionized water under conditions of 90°C and 1-day interval. Below are the results of five leach tests with different S/V ratios of 2, 5, 10, 16, and 50 m⁻¹. The leaching rate is in unit of mg / (m² · d).

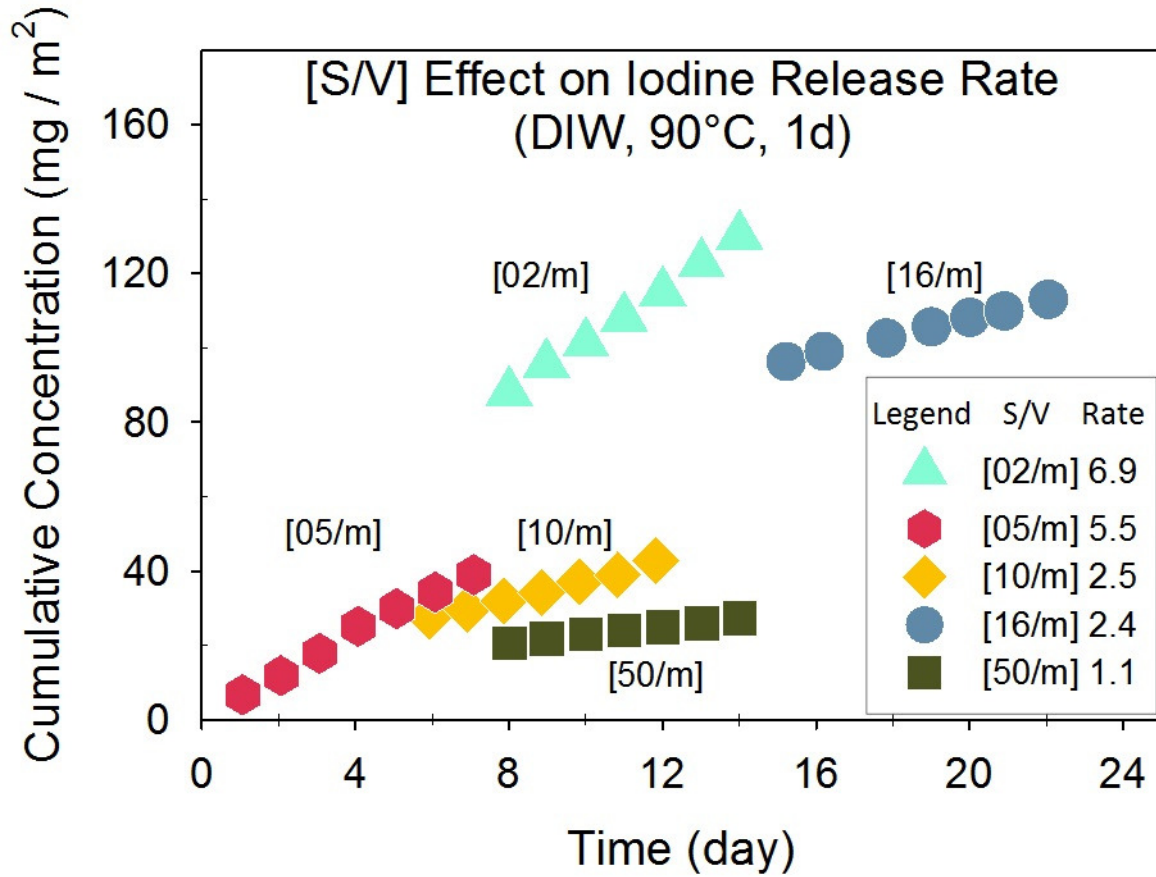


Figure 2b. Effect on lead element release by varying sample surface to solution volume ratio (S/V) in deionized water under conditions of 90°C and 1-day interval. Below are the results of five leach tests with different S/V ratios of 2, 5, 10, 16, and 50 m⁻¹. The leaching rate is in unit of mg / (m² · d).

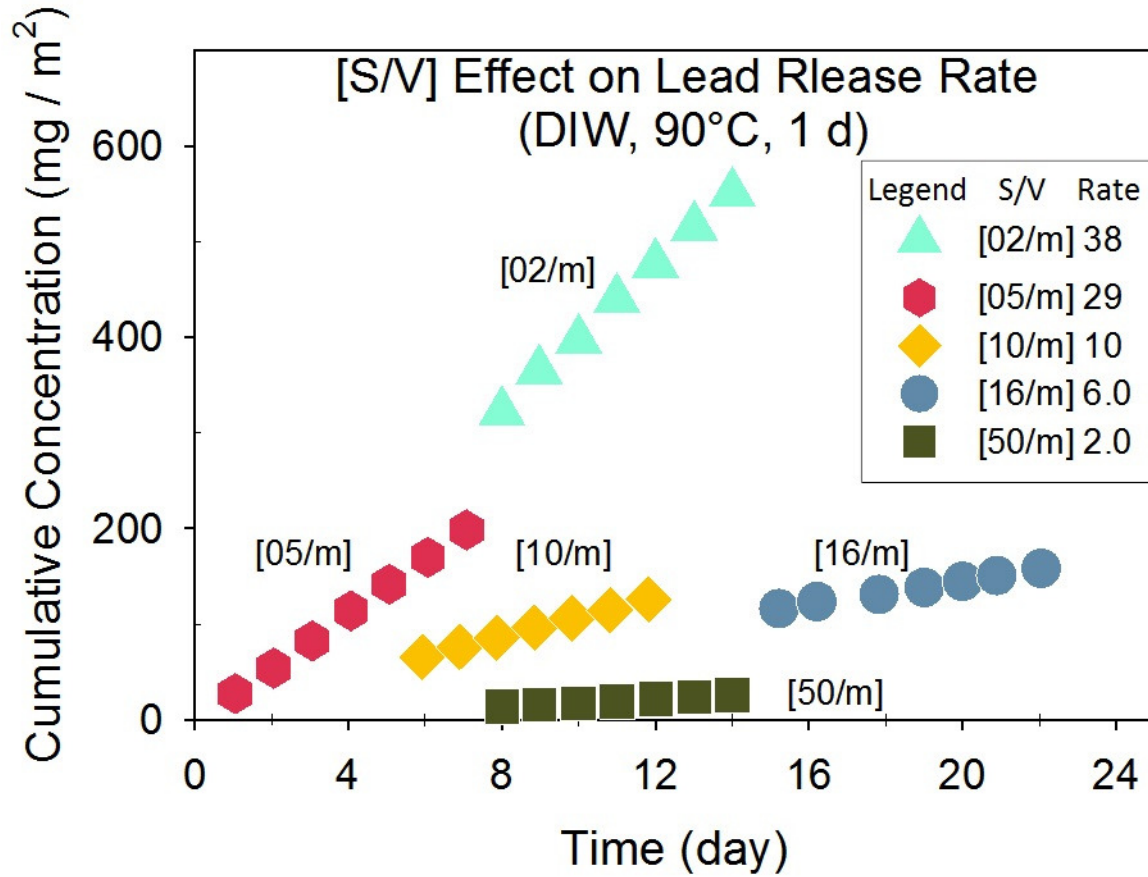


Figure 3a. Effect on iodine element release by varying interval time in deionized water under conditions of 90°C and S/V 10 m⁻¹. Below are the results of three leach tests with different intervals of 1, 3.5, and 7 days. The leaching rate is in unit of mg / (m² · d).

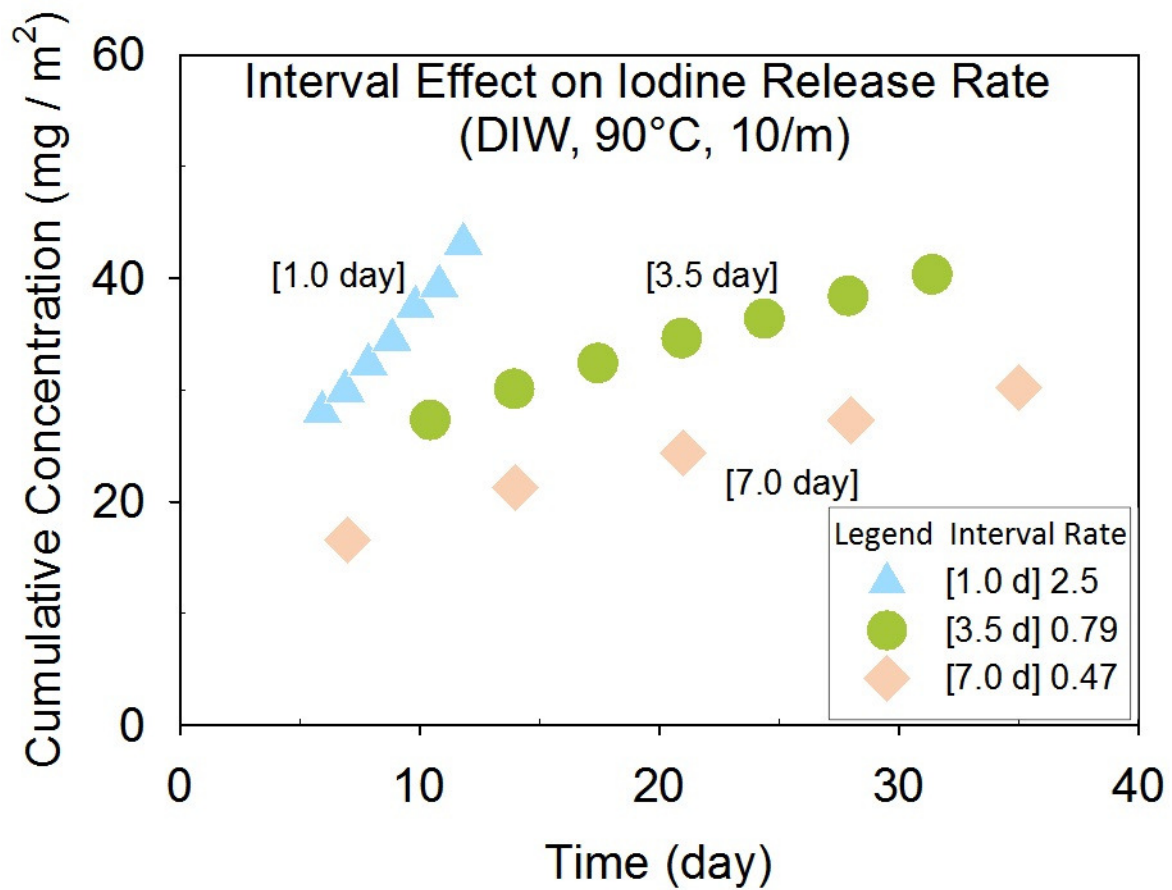


Figure 3b. Effect on lead element release by varying interval time in deionized water under conditions of 90°C and S/V 10 m⁻¹. Below are the results of three leach tests with different intervals of 1, 3.5, and 7 days. The leaching rate is in unit of mg / (m² · d).

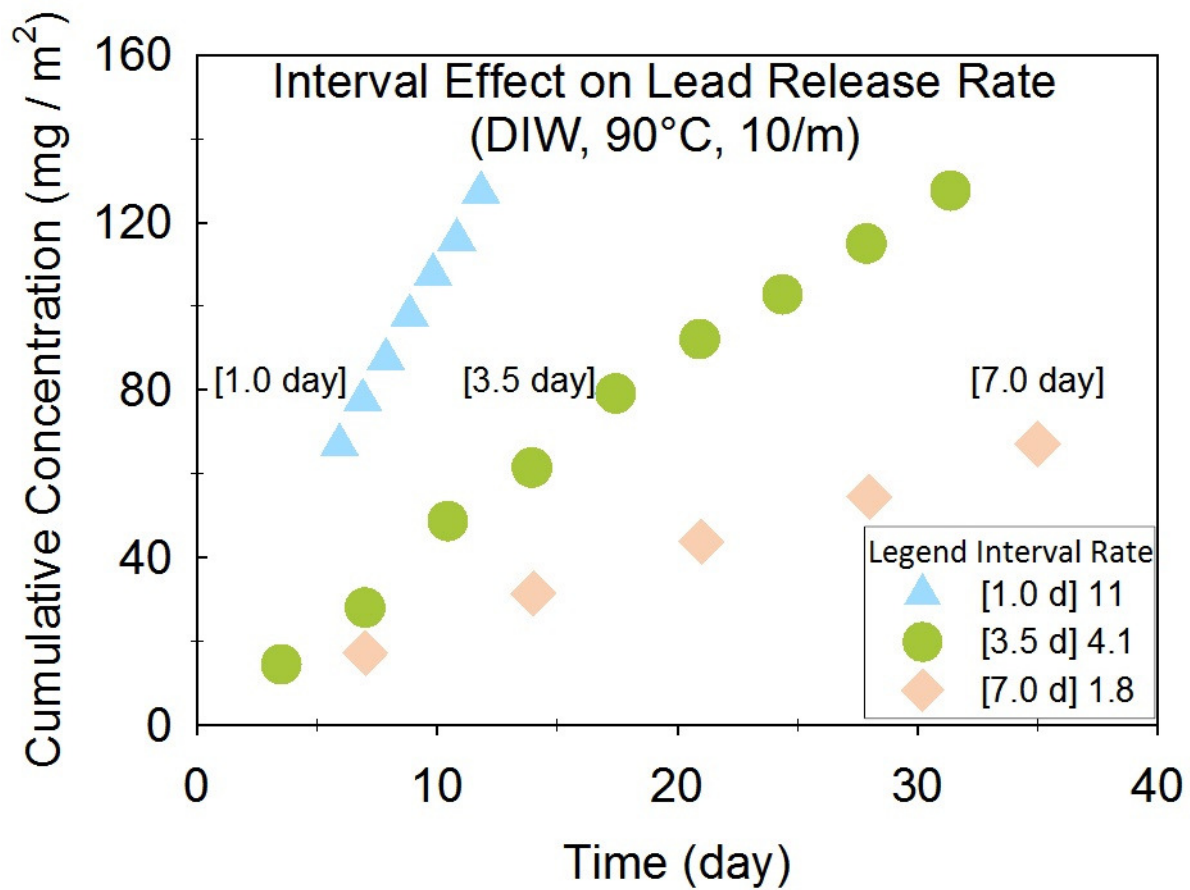


Figure 4a. Effect on iodine element release by varying temperature in deionized water under conditions of 1-day interval and S/V 5 m^{-1} . Below are the results of four leach tests at different temperature of 20, 40, 70, and 90 °C. The leaching rate is in unit of $\text{mg} / (\text{m}^2 \cdot \text{d})$.

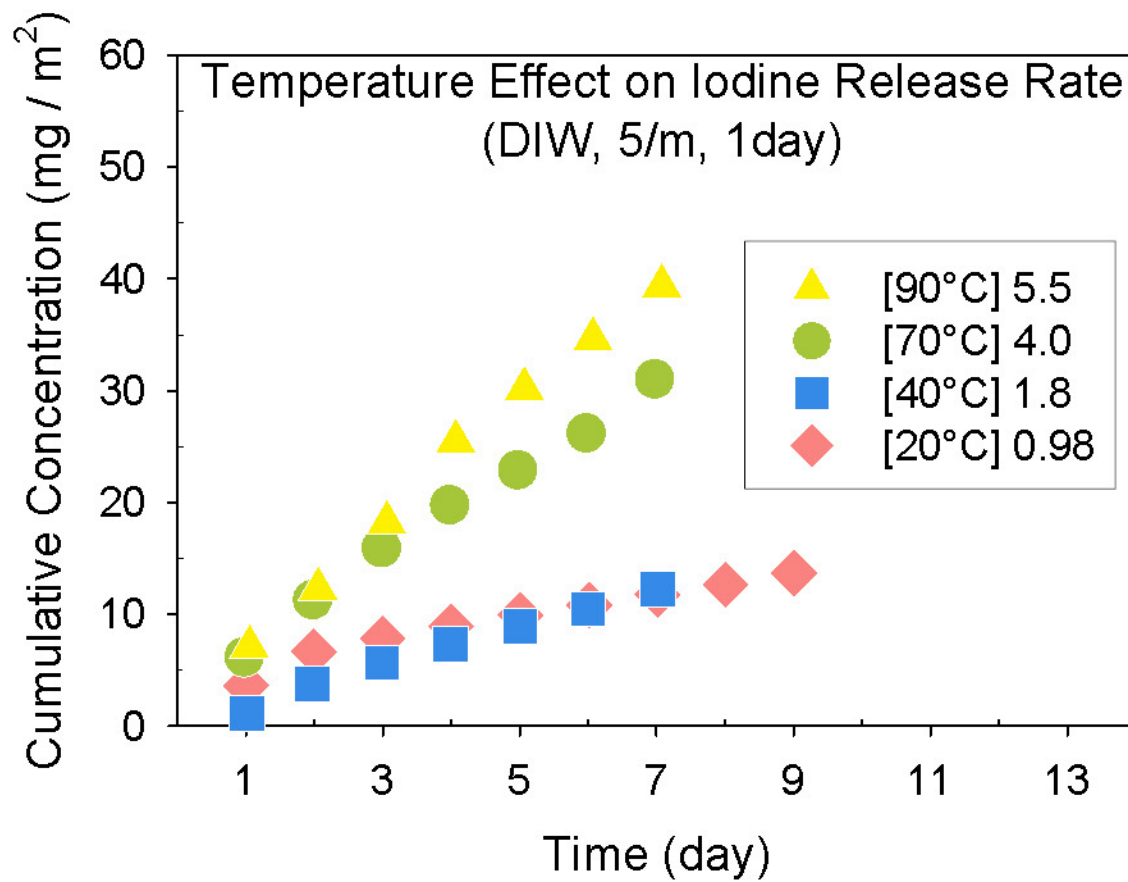


Figure 4b. Effect on lead element release by varying temperature in deionized water under conditions of 1-day interval and S/V 5 m^{-1} . Below are the results of four leach tests at different temperature of 20, 40, 70, and 90 °C. The leaching rate is in unit of $\text{mg} / (\text{m}^2 \cdot \text{d})$.

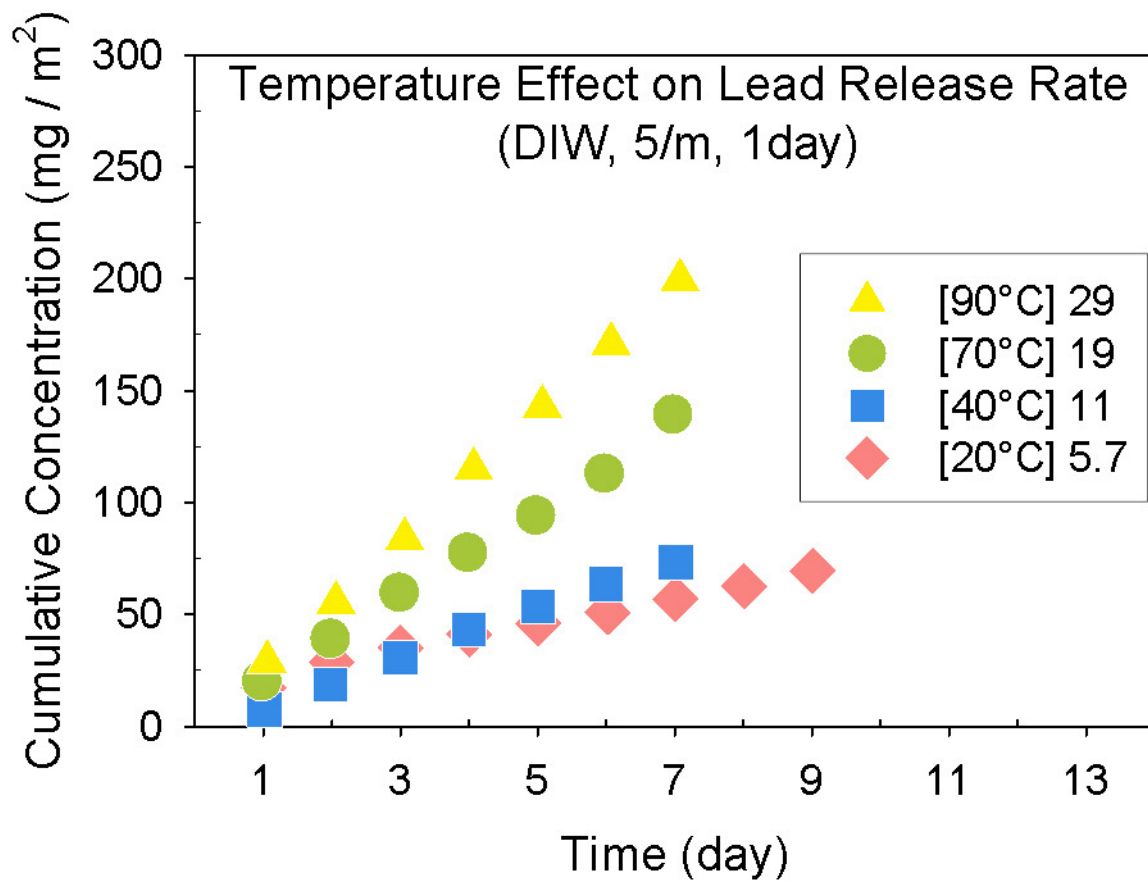
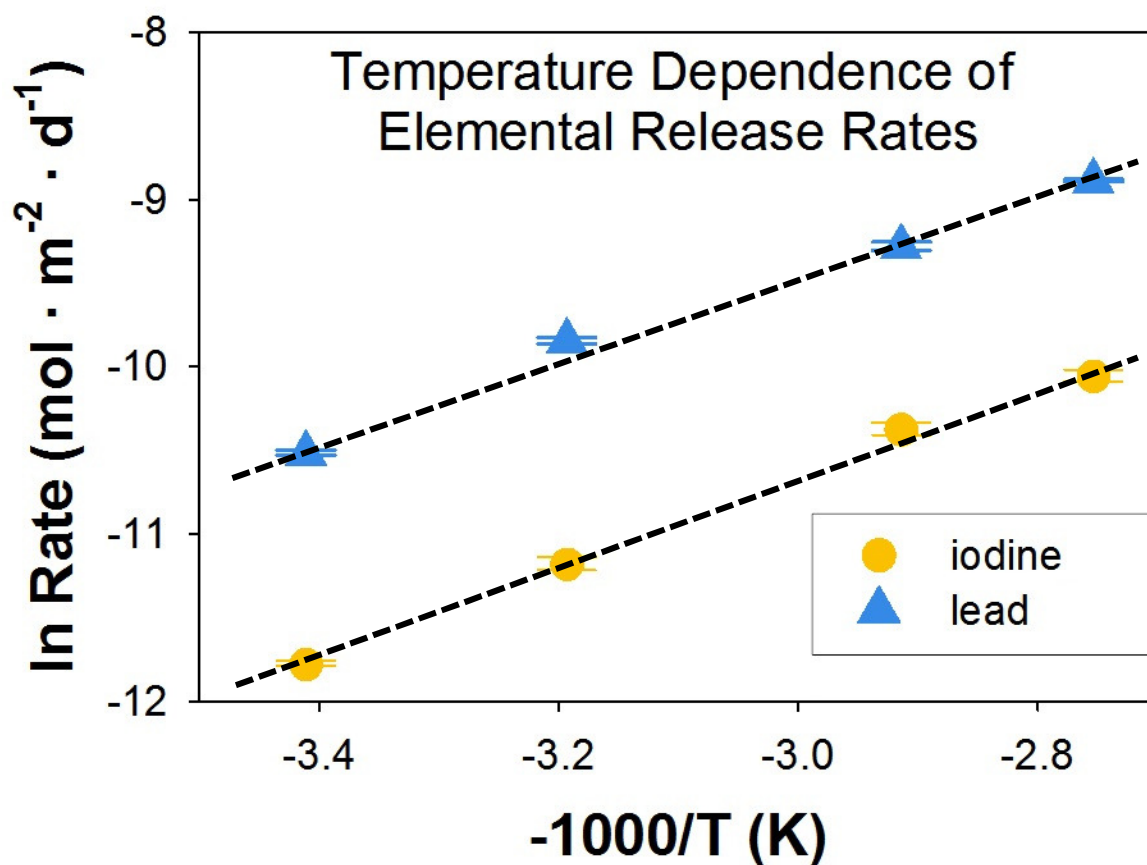


Figure 5. Temperature dependence of elemental release rate for iodine and lead. The plot is based on the result of Fig 4a and 4b. The apparent activation energy of iodine and lead can be derived from the corresponding linear regressions, as shown in the table below.



Element	Linear regression	R square	Apparent Activation Energy (kJ · mol ⁻¹)
Iodine (I)	y = 2.6647x - 2.6578	0.9964	22.4
Lead (Pb)	y = 2.3985x - 2.2658	0.9925	20.0

Figure 6a. Effect on iodine element release by using different pH buffer solutions at 90°C under conditions of 1-day interval and S/V 5 m⁻¹. Below are the results of three leach tests at pH 4, 6, and 9. The leaching rate is in unit of mg / (m² · d).

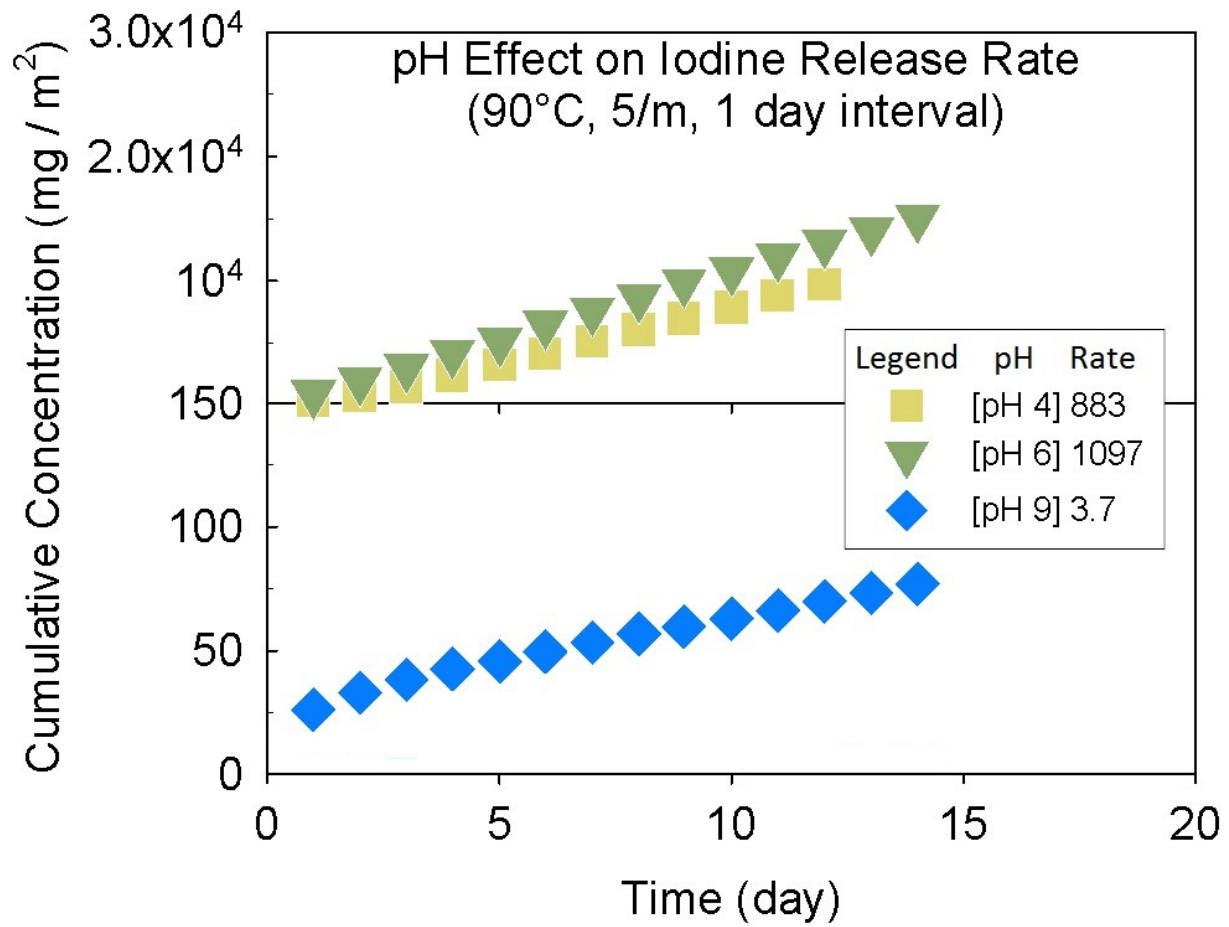


Figure 6b. Effect on lead element release by using different pH buffer solutions at 90°C under conditions of 1-day interval and S/V 5 m⁻¹. Below are the results of three leach tests at pH 4, 6, and 9. The leaching rate is in unit of mg / (m² · d).

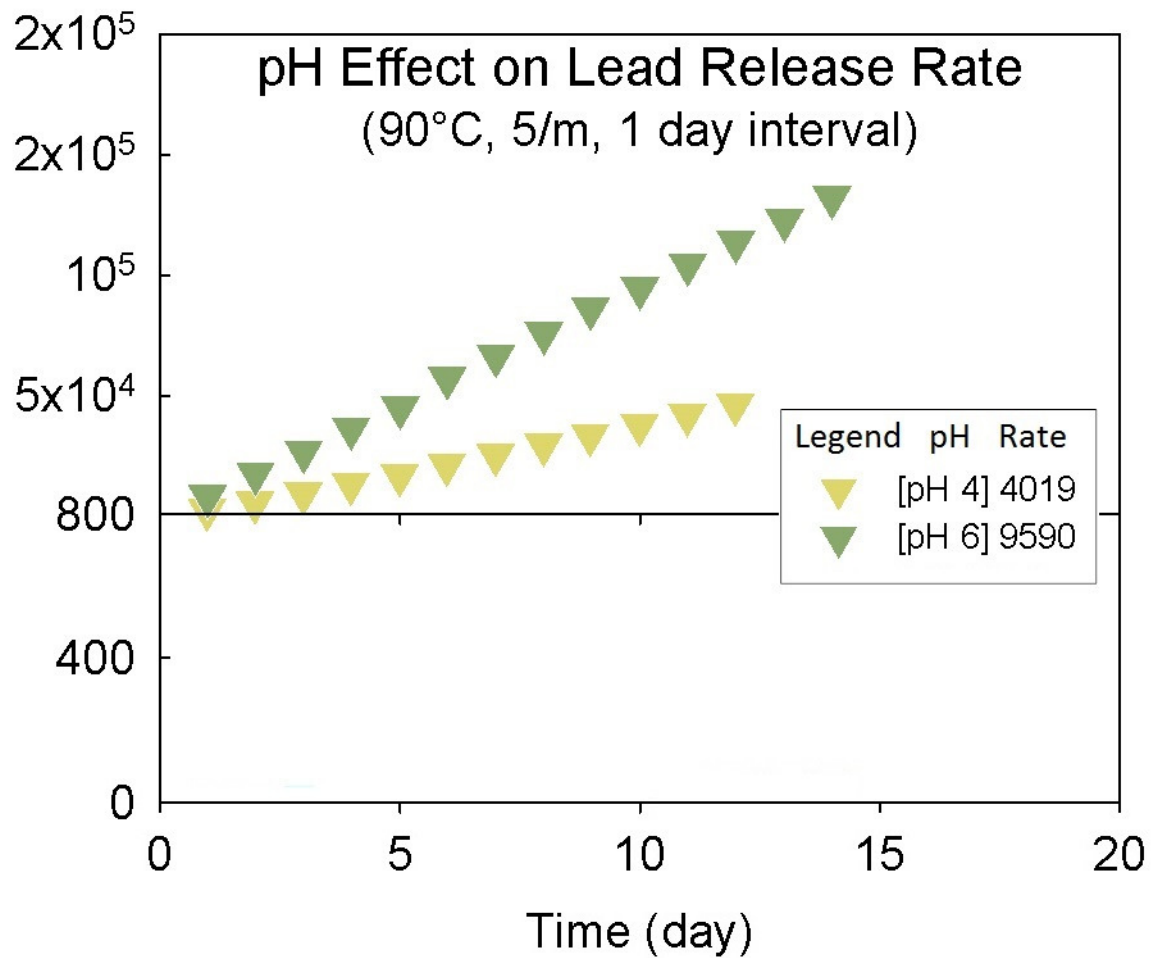


Figure 7. Raman spectroscopy of unleached surface and precipitate occurred on pH 4 leached surface.

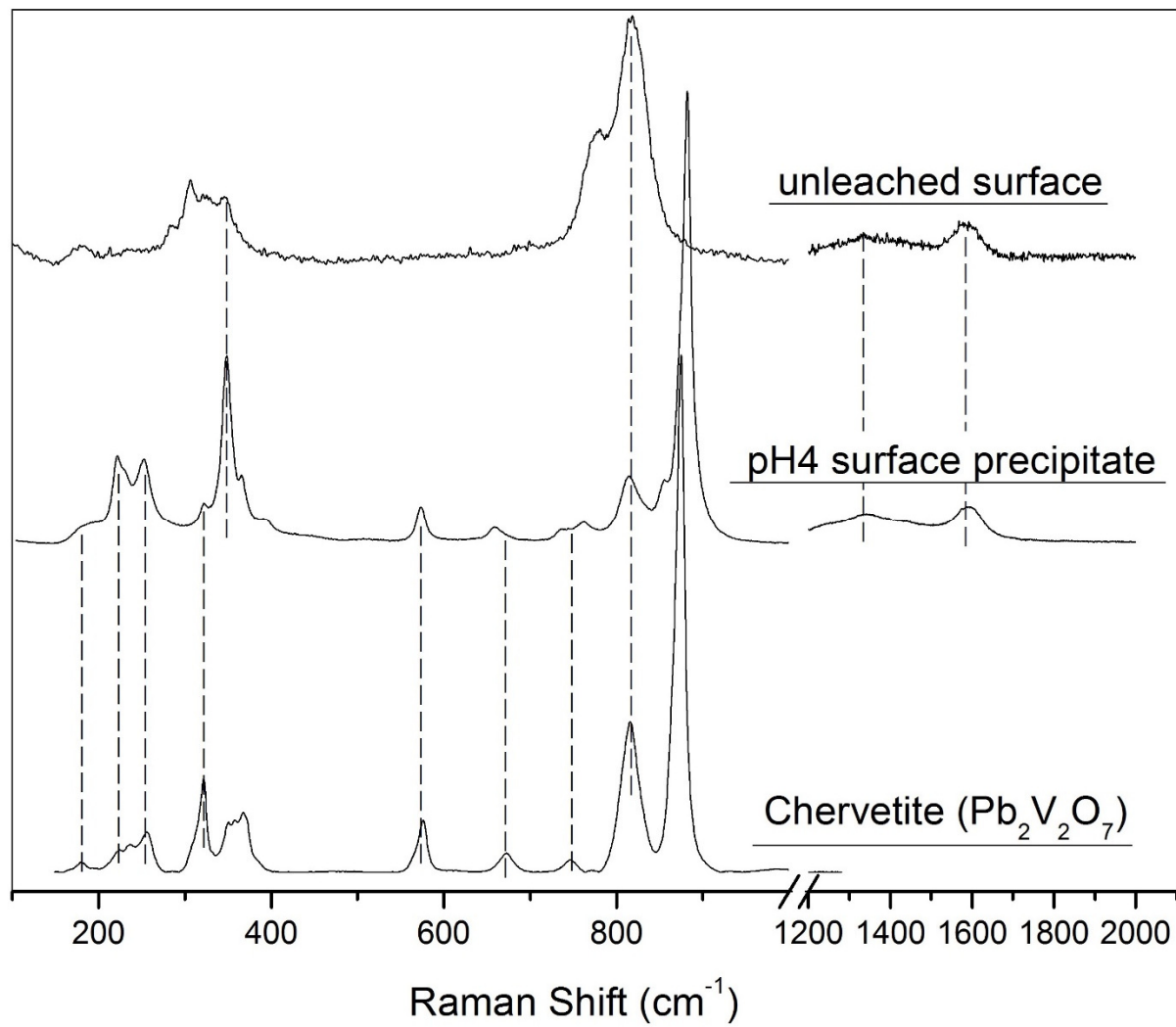


Figure 8a. SEM image of polished surface (unleached surface) and leached surface with deionized water, pH 4, pH 6, and pH 9 buffer solutions. “[]” denotes the S/V ratio in m^{-1} .

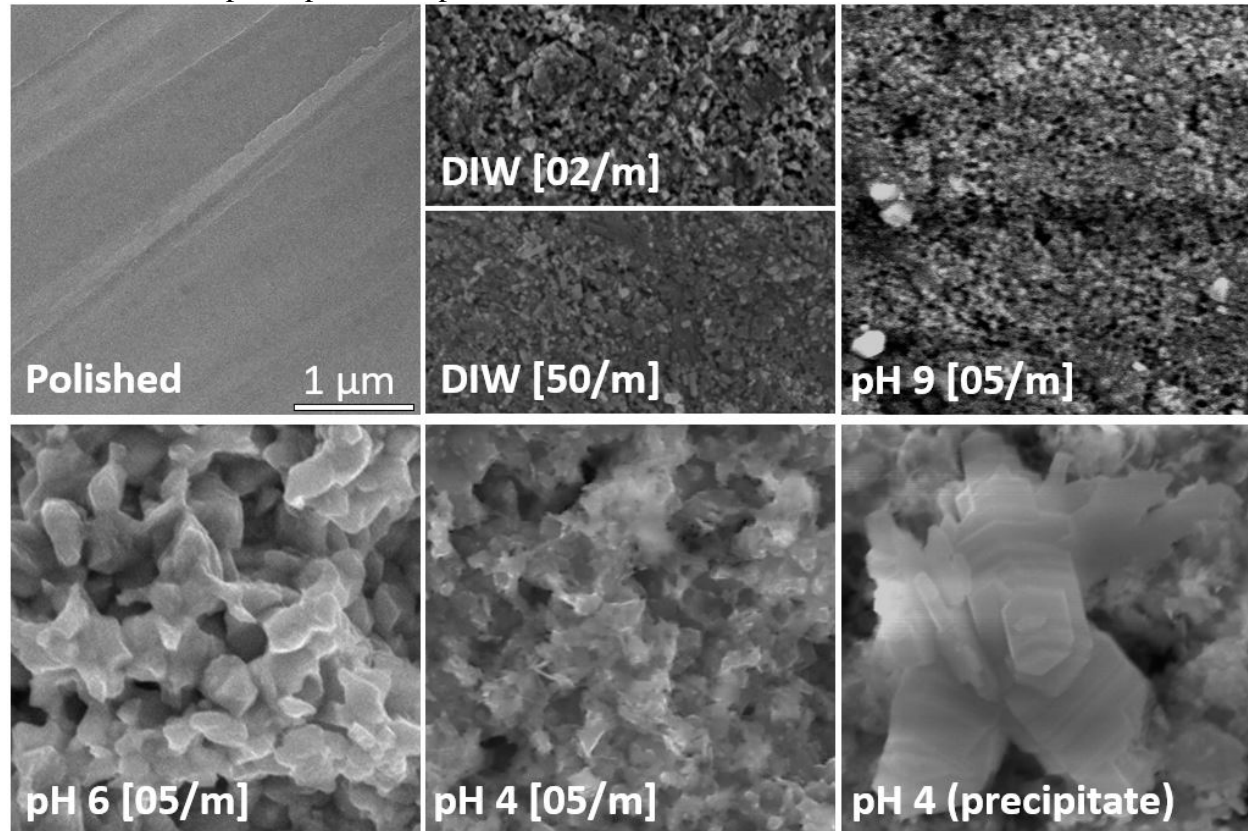


Figure 8b. Optical microscope image of leached surface by pH 4 buffer solution. The new phase (brown) is scattered all over the surface, which is characterized as chertite

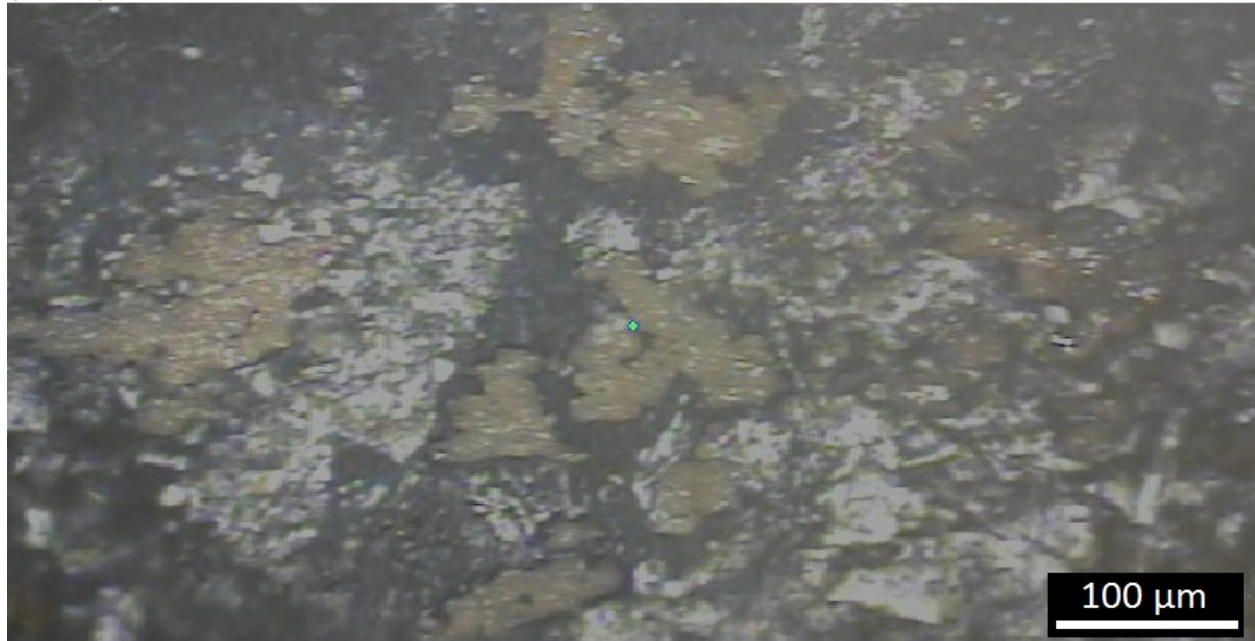


Figure 8c. Energy-dispersive X-ray spectroscopy of selected areas on leached surface by pH 4 buffer solution. Selected Area 1 is the leached surface, while the Selected Area 2 is the surface precipitate. The EDS analysis result shows the composition of precipitate is different to that of leached surface.

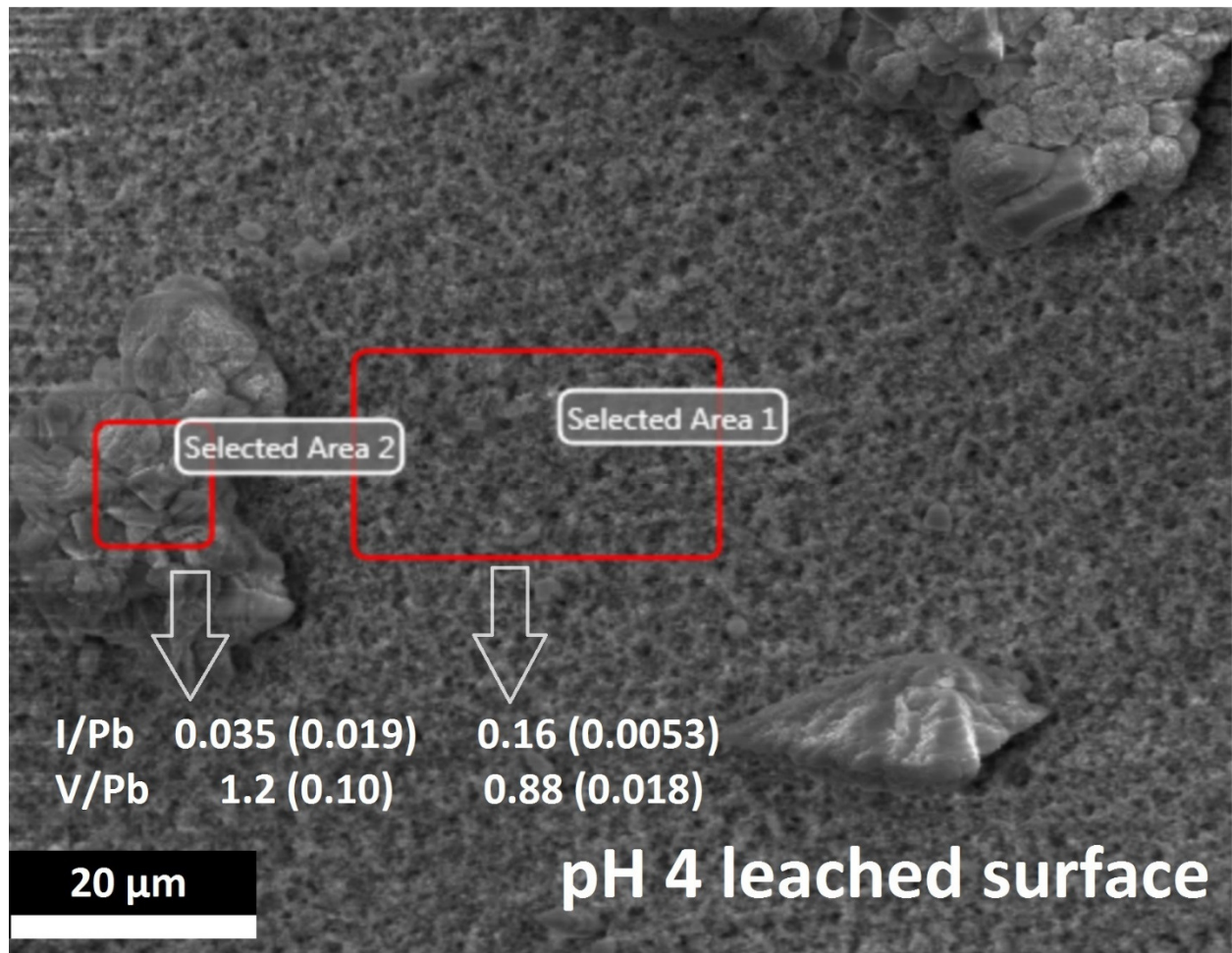


Figure 9a. Atomic ratio of iodine versus lead of test in deionized water at 90°C.

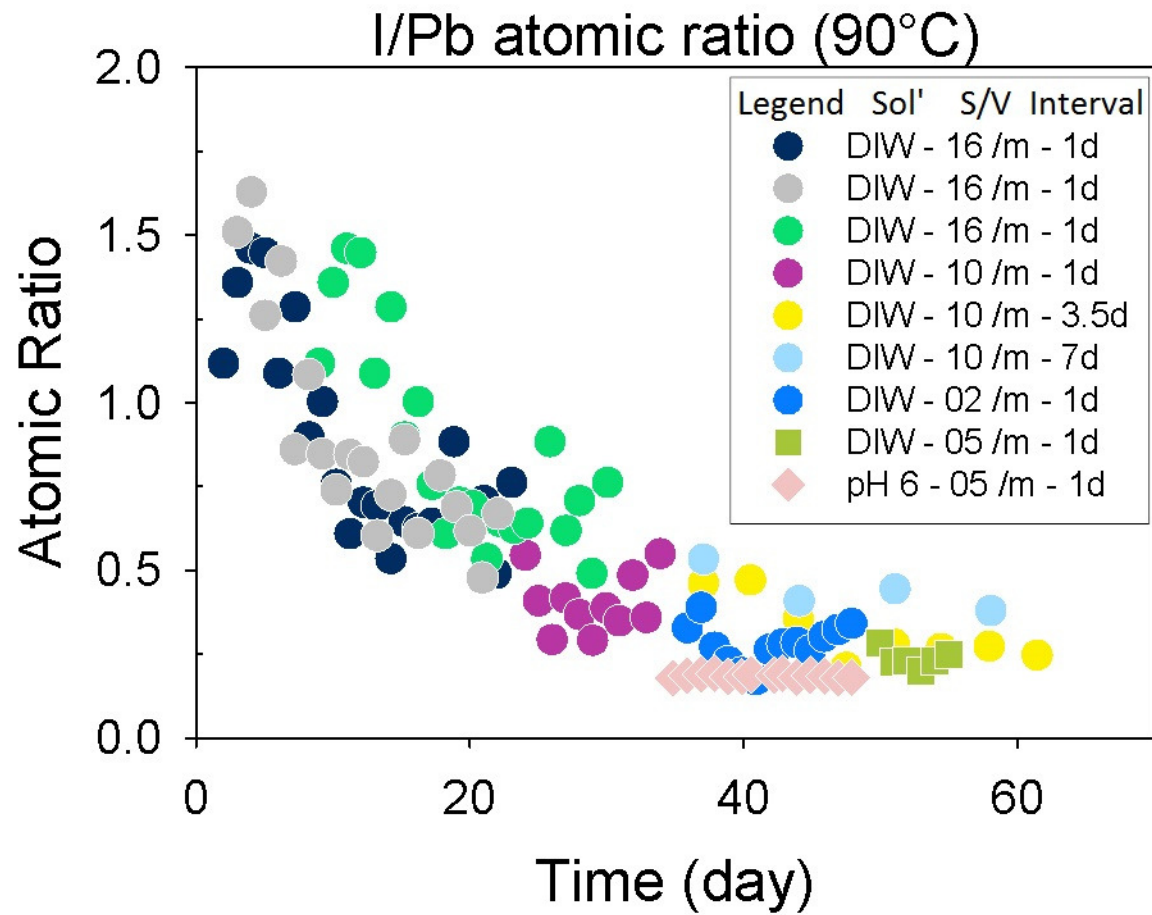


Figure 9b. Atomic ratio of vanadium versus lead of test in deionized water at 90°C.

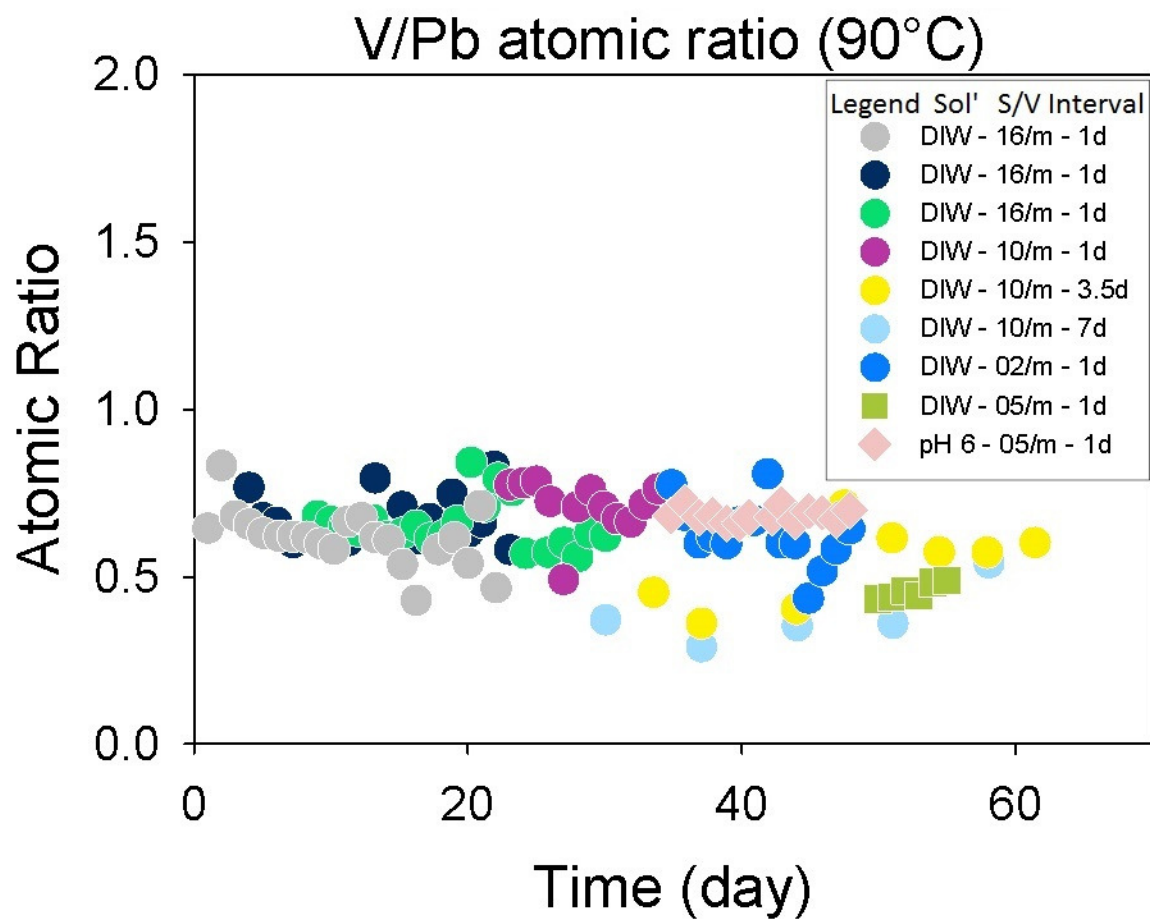


Fig 10a. Normalization on dependences S/V and Interval on lead release rate.

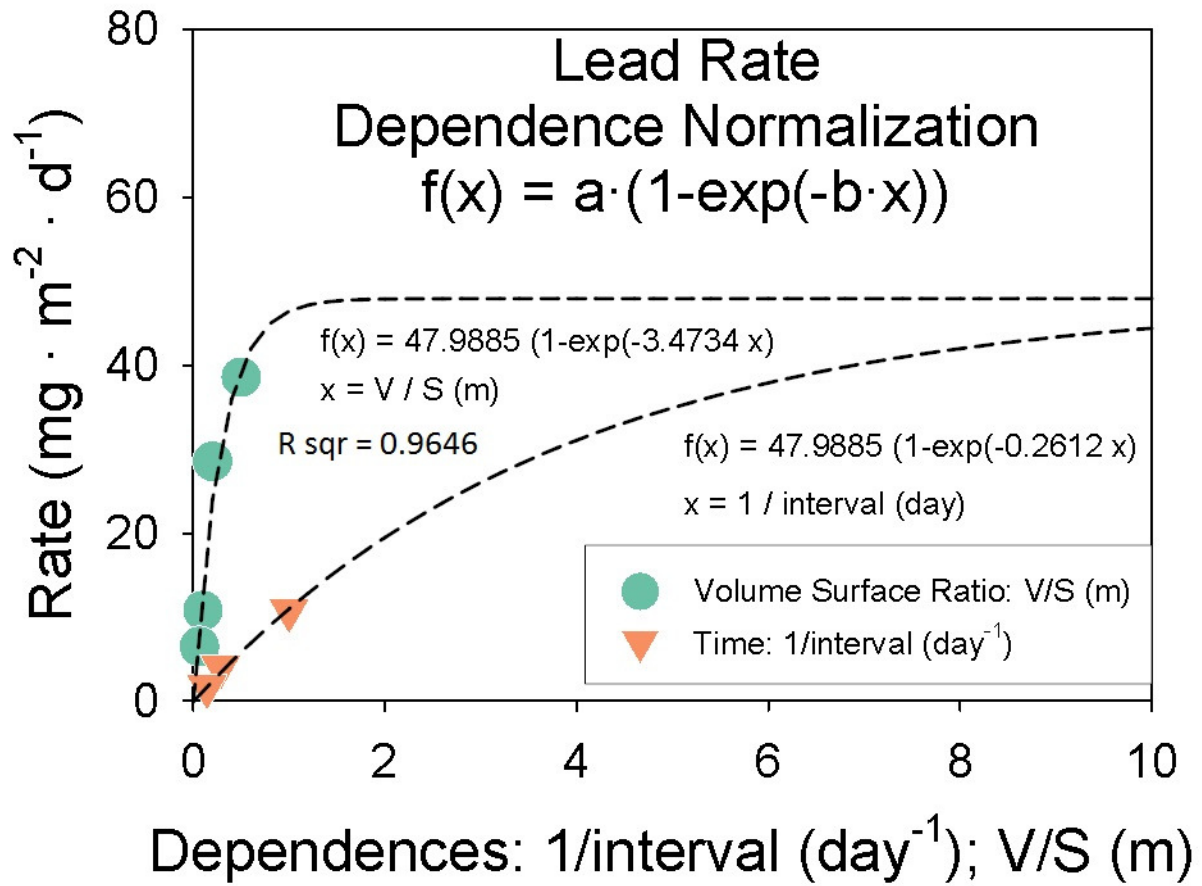


Fig 10b. Normalization on dependences S/V and Interval on vanadium release rate.

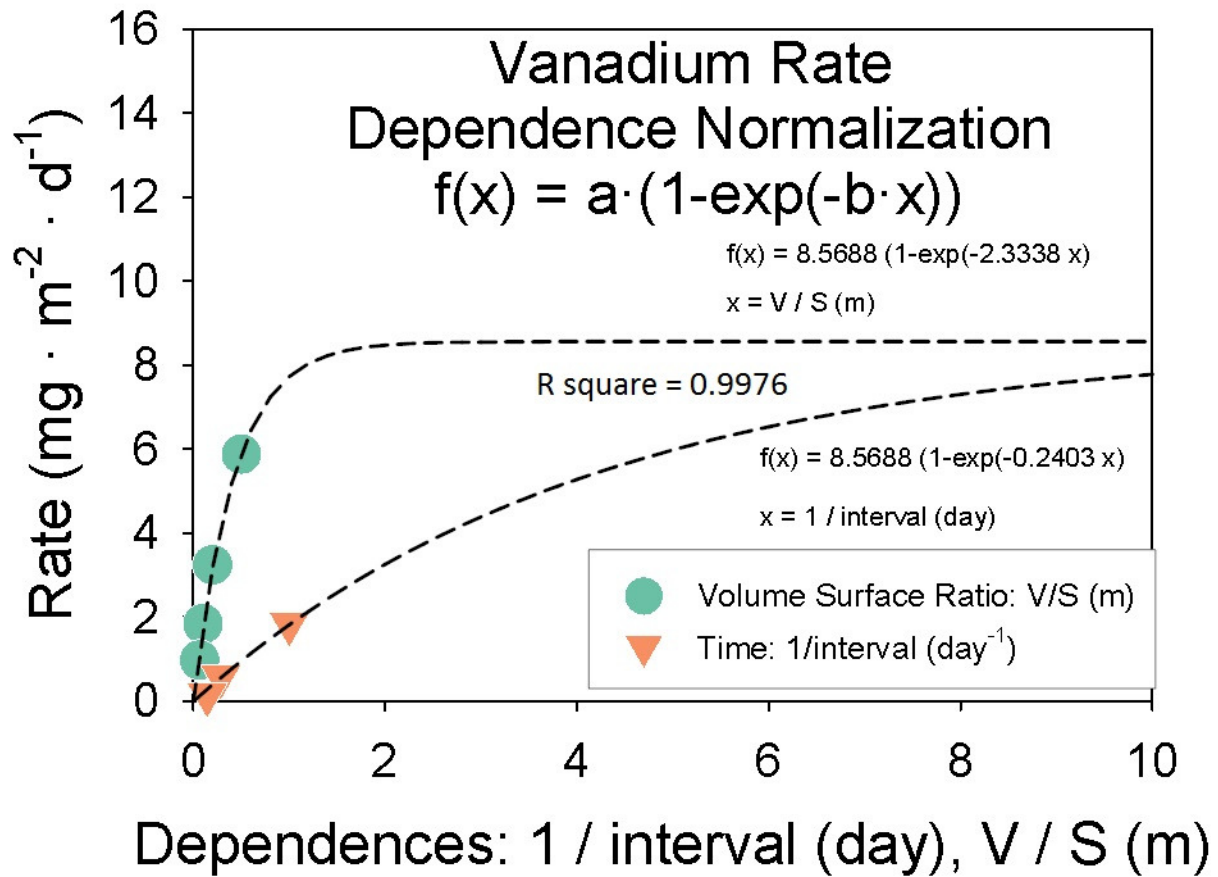


Fig 10c. Normalization on time dependence on iodine release.

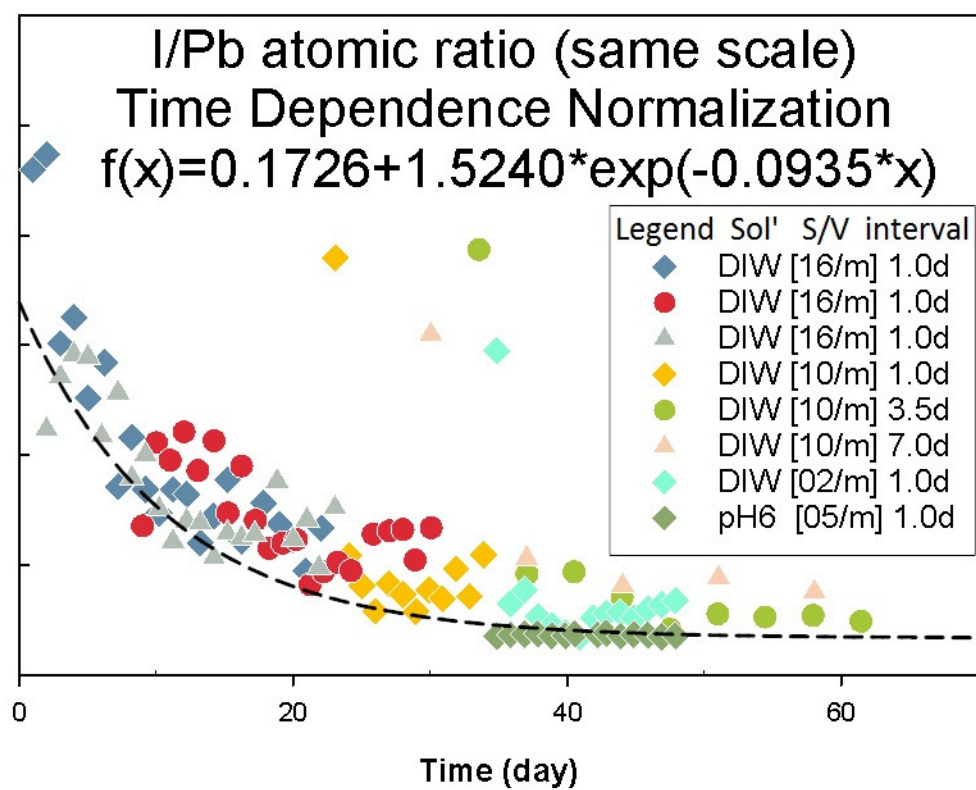
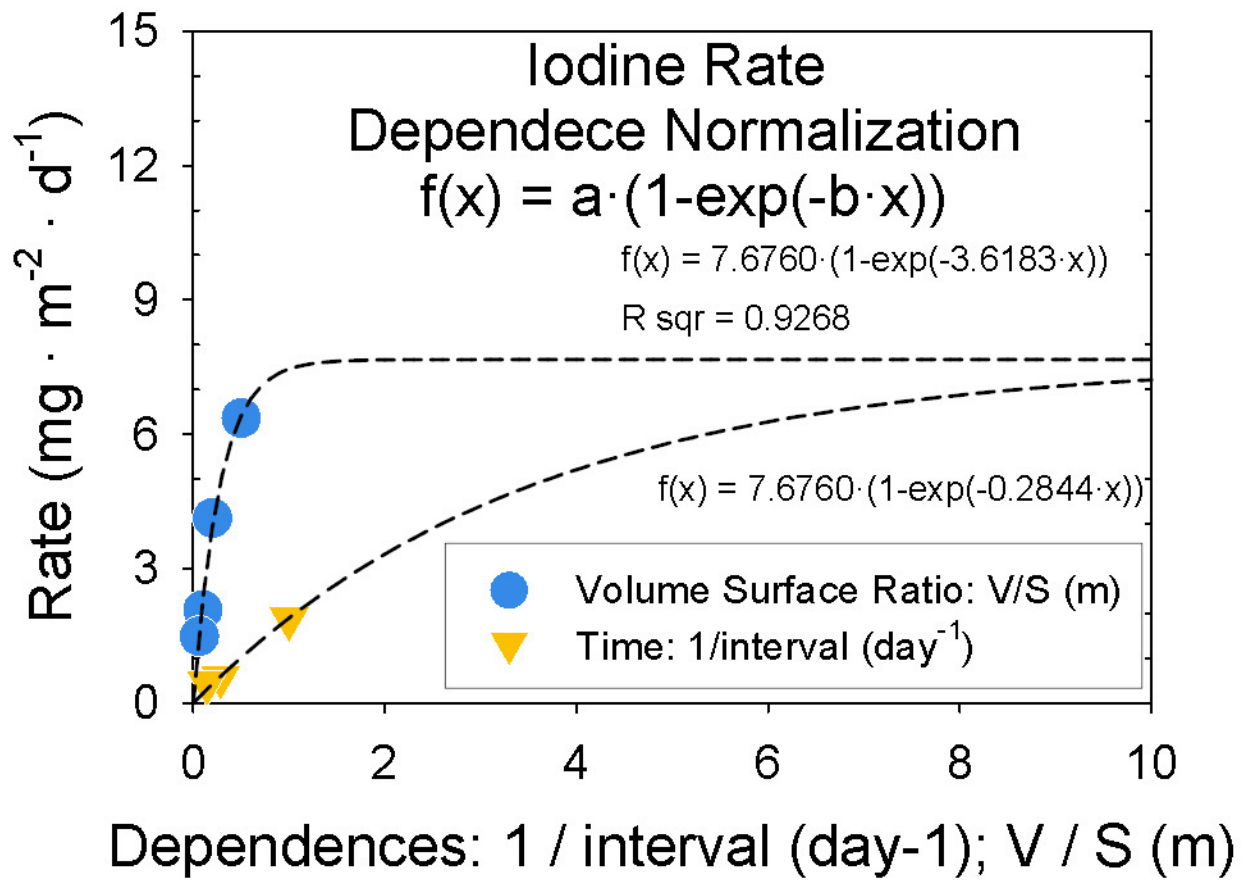
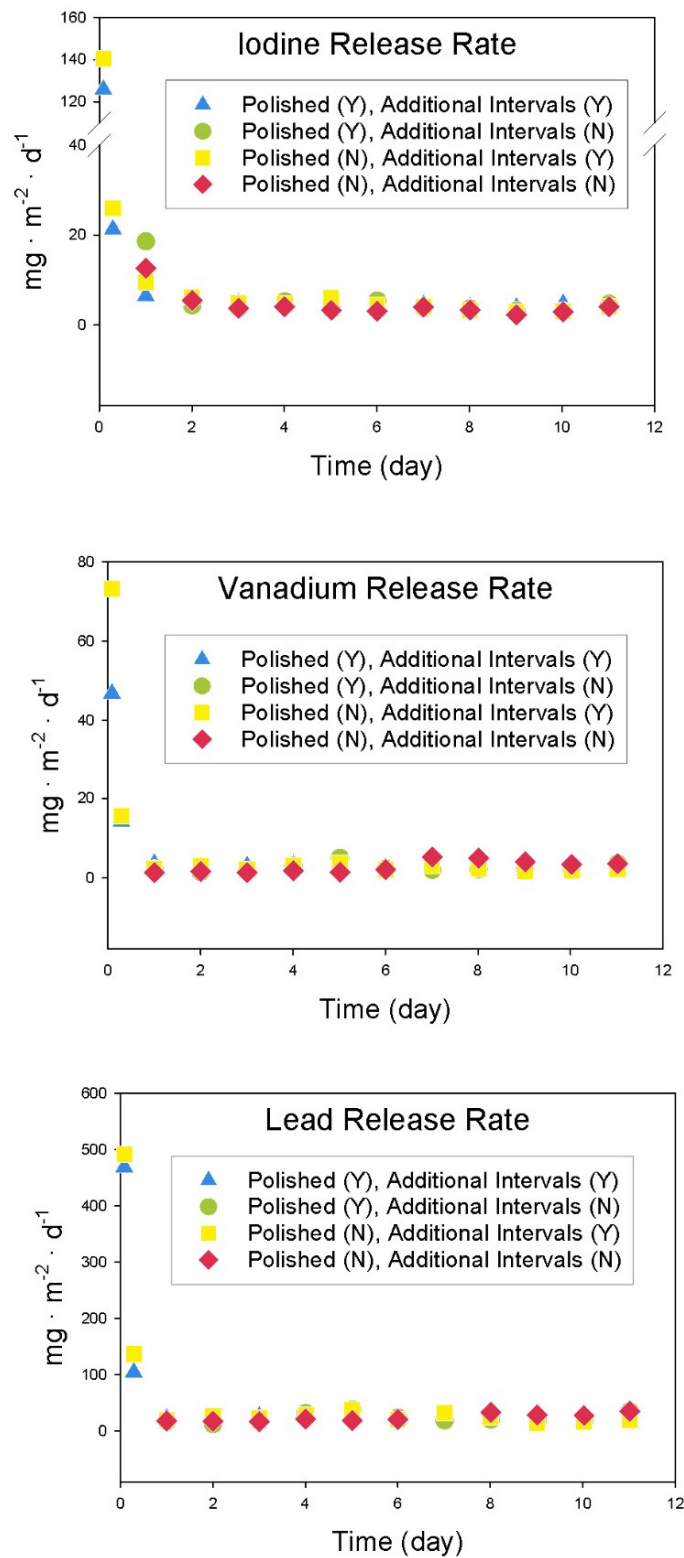


Fig 10d. Normalization on dependences S/V and Interval on iodine release rate of which the time dependence has been normalized.



Supplement Fig 1. Element release rate of comparative tests in terms of initial interval and surface roughness.



References:

- Agency, I. A. E. (1987). *Treatment, conditioning and disposal of iodine-129*: Vienna : International Atomic Energy Agency, 1987.
- Council, N. R. (2011). *Waste forms technology and performance final report*. Washington, D.C.: National Academies Press.
- Ebert, W., & Fuhrmann, M. (2010). *Radionuclide Release from Slag and Concrete Waste Materials. Part I: Conceptual models of leaching from complex materials and laboratory test methods*. Retrieved from
- Ewing, R. C. (1999). Nuclear waste forms for actinides. *Proceedings of the National Academy of Sciences*, 96(7), 3432-3439.
- Ewing, R. C. (2001). The design and evaluation of nuclear-waste forms: Clues from mineralogy. *Canadian Mineralogist*, 39, 697-715. doi:10.2113/gscanmin.39.3.697
- Ewing, R. C., & Wang, L. M. (2002). Phosphates as nuclear waste forms. In M. J. Kohn, J. Rakovan, & J. M. Hughes (Eds.), *Phosphates: Geochemical, Geobiological, and Materials Importance* (Vol. 48, pp. 673-699). Washington: Mineralogical Soc America.
- Ewing, R. C., Weber, W. J., & Clinard Jr, F. W. (1995). Radiation effects in nuclear waste forms for high-level radioactive waste. *Progress in Nuclear Energy*, 29(2), 63-127. doi:[http://dx.doi.org/10.1016/0149-1970\(94\)00016-Y](http://dx.doi.org/10.1016/0149-1970(94)00016-Y)
- Fabryka-Martin, J. T. (1988). *Production of radionuclides in the earth and their hydrogeologic significance, with emphasis on chlorine-36 and iodine-129*. Arizona Univ., Tucson, AZ (USA).
- Fuge, R., & Johnson, C. C. (1986). The geochemistry of iodine—a review. *Environmental Geochemistry and Health*, 8(2), 31-54.
- Gombert, D., Ebert, W., Marra, J., Jubin, R., & Vienna, J. (2008). *Global Nuclear Energy Partnership Waste Treatment Baseline* (INL/CON-08-13917; TRN: US0803760 United States TRN: US0803760 Thu Aug 27 07:24:39 EDT 2009 INL English). Retrieved from <http://www.osti.gov/scitech/servlets/purl/933184-X1hcco/>
- Guidry, M. W., & Mackenzie, F. T. (2003). Experimental study of igneous and sedimentary apatite dissolution: control of pH, distance from equilibrium, and temperature on dissolution rates. *Geochimica et Cosmochimica Acta*, 67(16), 2949-2963.
- Guy, C., Audubert, F., Lartigue, J.-E., Latrille, C., Advocat, T., & Fillet, C. (2002). New conditionings for separated long-lived radionuclides. *Comptes Rendus Physique*, 3(7-8), 827-837. doi:[http://dx.doi.org/10.1016/S1631-0705\(02\)01377-4](http://dx.doi.org/10.1016/S1631-0705(02)01377-4)
- Kato, H., Kato, O., & Tanabe, H. (2002). *Review of immobilization techniques of radioactive iodine for geological disposal*. Paper presented at the Proceedings of the International Symposium, NUCEF.
- Koch-Steindl, H., & Pröhl, G. (2001). Considerations on the behaviour of long-lived radionuclides in the soil. *Radiation and Environmental Biophysics*, 40(2), 93-104. doi:10.1007/s004110100098
- Lide, D. R. (2005). *CRC Handbook of Chemistry and Physics, Section 4*. Boca Raton, FL: CRC press.
- Maddrell, E., Gandy, A., & Stennett, M. (2014). The durability of iodide sodalite. *Journal of Nuclear Materials*, 449(1), 168-172.
- Noyes, R. (1995). *Nuclear Waste Cleanup Technologies and Opportunities*: Elsevier.

- Oelkers, E. H., & Montel, J. M. (2008). Phosphates and nuclear waste storage. *Elements*, 4(2), 113-116. doi:10.2113/gselements.4.2.113
- Peters, M. T., & Ewing, R. C. (2007). A science-based approach to understanding waste form durability in open and closed nuclear fuel cycles. *Journal of Nuclear Materials*, 362(2-3), 395-401. doi:<http://dx.doi.org/10.1016/j.jnucmat.2007.01.085>
- Suetsugu, Y. (2014). Synthesis of lead vanadate iodoapatite utilizing dry mechanochemical process. *Journal of Nuclear Materials*, 454(1), 223-229.
- Uno, M., Shinohara, M., Kurosaki, K., & Yamanaka, S. (2001). Some properties of a lead vanado-iodoapatite $\text{Pb}_{10}(\text{VO}_4)_6\text{I}_2$. *Journal of Nuclear Materials*, 294(1-2), 119-122. doi:[http://dx.doi.org/10.1016/S0022-3115\(01\)00462-7](http://dx.doi.org/10.1016/S0022-3115(01)00462-7)
- Valsami-Jones, E., Ragnarsdottir, K., Putnis, A. a. a., Bosbach, D., Kemp, A., & Cressey, G. (1998). The dissolution of apatite in the presence of aqueous metal cations at pH 2-7. *Chemical Geology*, 151(1), 215-233.
- Wang, J. (2015). Incorporation of iodine into apatite structure: a crystal chemistry approach using Artificial Neural Network. *Frontiers in Earth Science*, 3, 20.
- Weber, W. J., Navrotsky, A., Stefanovsky, S., Vance, E. R., & Vernaz, E. (2009). Materials science of high-level nuclear waste immobilization. *MRS bulletin*, 34(01), 46-53.
- Yao, T., Lu, F., Sun, H., Wang, J., Ewing, R. C., & Lian, J. (2014). Bulk iodoapatite ceramic densified by spark plasma sintering with exceptional thermal stability. *Journal of the American Ceramic Society*, 97(8), 2409-2412.
- Zhang, M., Maddrell, E., Abraitis, P., & Salje, E. (2007). Impact of leach on lead vanado-iodoapatite $[\text{Pb}_5(\text{VO}_4)_3\text{I}]$: an infrared and Raman spectroscopic study. *Materials Science and Engineering: B*, 137(1), 149-155.

Thermodynamic properties of iodide apatite from first-principles calculations

Jianwei Wang,^{1,*} Sanda M Botis,² Jie Lian,³ Fei Gao,⁴ Rodney C. Ewing⁵

¹Department of Geology and Geophysics, Center for Computation and Technology, Louisiana State University, Baton Rouge, Louisiana 70803-0001, USA

²Department of Earth and Environmental Sciences, University of Michigan, Ann Arbor, Michigan 48109-1005, USA

³Department of Mechanical, Aerospace, and Nuclear Engineering, Rensselaer Polytechnic Institute, Troy, NY 12180, USA

⁴Department of Nuclear Engineering and Radiological Sciences, University of Michigan, Ann Arbor, Michigan 48109-1005, USA

⁵Department of Geological and Environmental Sciences, Stanford University Stanford, California 94305-2115, USA

*Jianwei Wang

Department of Geology and Geophysics

Louisiana State University

E235 Howe-Russell Building

Baton Rouge, Louisiana 70803, USA

Phone: 225-578-5532

Fax: 225-578-2302

Email: Jianwei@lsu.edu

Abstract

Apatite structure provides a great potential for incorporating long-lived radioactive iodine from nuclear waste streams for long term storage because of its mechanical and chemical durability, high iodine content, and low leaching rate. Artificial Neuron Network simulations were used to predict unknown compositions of iodide apatite. First-principles calculations were carried out to calculate structure, vibrational spectroscopy and thermodynamics stability of known and unknown apatites predicted from the Artificial Neuron Network simulations ($A_5(XO_4)_3I$, with $A = Pb, Sr$; $X = V, As$). The calculated crystal structures of known apatite are comparable with available experimental results. Phonon density of states was calculated using the linear response theory and finite-difference approach, which was used to calculate free energy of the formation of the apatites. These results can be used to understand the thermodynamic stability of the apatites with respect to their decomposed phases. Results on $Sr_5(AsO_4)_3I$ show that the structure maintains the apatite structure and the interactions between iodide and strontium are mainly ionic character. The reaction to form $Sr_5(AsO_4)_3I$ either from the oxides (e.g., SrO , As_2O_5 , SrI_2) or arsenate (e.g., $Sr_3(AsO_4)_2$) is shown to be thermodynamically favorable. However, the Gibbs free energy decreases with temperature for the apatite formation from the oxides while the free energy increases with temperature for the formation from the arsenate. The formation energetics as a function of temperature provides insights on how to design experiments to efficiently synthesize the apatite. Our work on apatite demonstrates that first-principles methods can be used to provide insights on designing nuclear waste forms by predicting their thermodynamic stabilities.

1. Introduction

Production of nuclear energy generates radioactive nuclear wastes. One of the main concerns for the environment associated with nuclear energy is how to dispose the nuclear wastes and how their impact to the environment to be minimized. Depending on the fuel cycle options, novel chemical reprocessing and transmutation strategies can result in a complicated waste streams with a number of radionuclides. Among these nuclear waste elements, the radionuclides with a long half-life are particular problematic because they need to be immobilized in durable waste forms for long-term storage in a geological setting. Current efforts in this area are directed towards optimizing separation processes for complex nuclear waste streams and designing appropriate waste forms. Decades of research and development result in various nuclear waste forms for different nuclear wastes, including glass, glass ceramics, and single phase and multiphase ceramics waste forms. Among them, some waste forms such as borosilicate glasses have been put in practice in immobilizing radioactive wastes. For glass nuclear waste forms, although high chemical durability of some vitrified glasses has been proven by industry for centuries with an established verification technology, the longer-term durability beyond industrial practice is still not clear, which currently is of great research interest and essential for expanding glass waste forms applications. Ceramic waste forms, single phase or multiphase, on the other hand, are largely developed from the concept of synrock (1978, Ted Ringwood). Since ceramic phases often have natural analogies, their long-term durability can be checked or verified by studying their performances in the geological history. In addition, crystalline phases have well-defined crystal structures and their atomistic scale structures are better understood with respect to glasses, thus, their durability is relatively simpler to characterize as comparing with the glass waste forms. Among crystalline phases for nuclear wastes forms, apatite-

structured materials are unique and have a number of advantageous properties including mechanical and chemical durability and structural and chemical flexibility. Its mechanical and chemical durability can be demonstrated by the properties of natural apatite samples over billions of years in geological records [1]. Its structural and chemical flexibility offer the opportunity to incorporate multiple radionuclides in a single ceramic phase. For instance, apatite can incorporate one of more following radionuclides: Cs, Sr, I, rare-earth elements, and actinides (XX). In addition, because its multiple crystallographic sites can be occupied by elements with different charges, changes associated with valance and identity of radioactive elements could be potentially offset by charge transfer between the sites. Thus, apatite-structured phases may be tolerant against or has potential to mitigate the aging effect of radionuclides or a process named radioparagenesis [2, 3], structural and chemical transformation process resulting from a radioactive decay of radionuclides in a solid phase.

Apatite is a group of materials with the apatite structure. The general formula for apatite is $A_5(XO_4)_3Z$ with hexagonal $P6_3/m$ symmetry (space group number 176). The crystal structure is depicted in Figure 1. The A cation occupies two crystallographic sites Ca(I) and Ca(II). The molar ratio of Ca(I)/Ca(II) is 2:3. The A cation can be substituted by a number of ions including Na^+ , K^+ , Cs^+ , Mg^{2+} , Ca^{2+} , Ba^{2+} , Sr^{2+} , Cd^{2+} , Pb^{2+} , Fe^{2+} , Fe^{3+} , RE^{3+} , and Ac^{4+} . For $Ca_5(PO_4)_3F$, Ca(I) site has a coordination number of six at Ca(I)-O distance of 2.5 Å and nine at 2.8 Å, and Ca(II) site has a coordination number of six at Ca(II)-O/F distance of 2.5 Å and seven at 2.7 Å [6, 7]. The X cation often forms a tetrahedron with four oxygen atoms and can be substituted by P, Si, S, V, Cr, As, Mn, Ge, in some cases, by non-tetrahedron anions such as ReO_5 [8] and BO_3 [9]. The Z anion can be substituted by OH^- , F^- , Cl^- , Br^- , I^- , O_2^{2-} , CO_3^{2-} , and IO_3^- . The chemical substitutions are often coupled between multiple sites. For instance for Ca^{2+}

substitution by RE^{3+} , the tetrahedron cation is also involved (e.g., $\text{RE}^{3+} + \text{SiO}_4^{4-} = \text{Ca}^{2+} + \text{PO}_4^{3-}$). One of the unique properties of apatite is that it can simultaneously incorporate multiple radionuclides. For instance, $\text{Sr}_8\text{CsNd}(\text{PO}_4)_6\text{F}_{2.3}$, including both Sr and Cs in its structure, was synthesized by a precipitation reaction method [10]. For that reason, apatite materials have been proposed as a host material for storage of nuclear wastes [9, 11-23], including iodine [9, 11-13, 24-27]. These studies show that apatite has a great potential for storage of radioactive nuclear waste elements. Although materials with apatite structure show excellent chemical and mechanical properties as nuclear waste forms for various radionuclides, the durability also depends on chemical composition of apatites. In order to optimize the performance of apatite waste forms, there is a need to explore different apatite compositions with various radionuclides. Since chemical substitutions occur at all sites (i.e., A, X, and Z in $\text{A}_5(\text{XO}_4)_3\text{Z}$), the number of possible apatite compositions could easily reach over a few hundreds only for the end-members. Trying all the combinations experimentally will not only be expensive but also time consuming. Apparently, not all of them are thermodynamically stable and can be synthesized. Thus, it is necessary to be selective and to rule out those that do not meet the basic requirements of the structure and crystal chemistry of apatite. Artificial Neural Network (ANN) has been applied for that purpose using a crystal chemistry approach [28]. However, the ANN simulation only considers ionic radius and electronegativity of the constituent elements without any knowledge of their stabilities of the predicted apatite compositions. First-principles calculations in this regard can be used to provide essential thermodynamic data and their stabilities of the predicted but unknown apatite compositions.

Purpose of this study is to estimate the thermodynamic stabilities of the previously predicted apatite compositions with respect to their chemical constituents (i.e., simple oxides). Gibbs free

energies of the reactions that produce apatite are calculated using First-principles calculations. Phonon density of states is calculated and Statistical Quasi-Harmonic Approximation (QHA) is used to calculate zero point energy (ZPE) and entropic contribution to the free energy. In addition, crystal structures and mechanic properties of some apatite compositions are also calculated. As a case study, iodine apatite compositions are investigated. The results demonstrate that first-principles thermodynamics is an effective technique to estimate the stability of known and unknown apatite compositions, and may also shed light on other ceramic phases with novel chemical compositions for nuclear wastes designs.

2. Methods

Artificial Neural Network (ANN) approach was used to simulate crystal chemistry properties of unknown apatite compositions. ANN is inspired from biological neuron assemblies and their way of encoding and solving problems [54]. Because of the modular and non-linear nature of artificial neural networks, it is able to approximate any arbitrary function to an arbitrary degree of accuracy [54-56]. Nonlinearity makes the functions a natural choice for complex correlations between inputs and outputs. In this study for iodine apatite, the channel size of crystal structure is simulated based on the composition. The Artificial Neural network toolbox from Matlab program package was used [57, 58]. The Bayesian regulation backpropagation was employed using mean-square error with respect to weight and bias as the performance function. The method showed the best performance among other backpropagation algorithms. There are six input parameters, average radius and average electronegativity for each of the three cation sites. There is a hidden layer with four neurons and an output layer. The output has one parameter for the channel size. The dataset from experimental crystal structure data is divided to two, one for training the networks (44 apatites) and one for testing the networks (42 apatites). The training

dataset includes the end members of apatite compositions and some of the solid solutions, and the rest of them are included in the testing dataset. This strategy allows the ANNs to be well trained for the predictions of apatite compositions related to those compositions covered in the training dataset. Using Bayesian regularization (BR) algorithm, the training simulation runs until the algorithm is converged, which is indicated by the convergence of the effective number of simulation parameters, maximum MU (a parameter for controlling convergence algorithms), convergence of the summed square error, and sum squared parameter. The details of the simulations are described in a separated publication {Wang, 2015 #3002}.

Density Functional Theory with plane-wave basis sets using GGA PBE exchange-correlation functional as implemented CASTEP by Materials Studio was used for the calculations {Accelrys, 2013 #2856}. Norm-conserving pseudopotentials were used and represented in reciprocal space. The number of valence electrons is 6 for O, 22 for Pb, 10 for Ca, 5 for V, 5 for As, 10 for Sr, 7 for F, 7 for I. Monkhorst-Pack grid was used for k point grid and was found that 2x2x3 mesh is adequate for the convergences of the systems. The cutoff energy of 650 eV was used in all the calculations. The convergence criteria were set to 1.0×10^{-5} eV/atom and 0.03 eV/Å for the geometry optimization, and 2.0×10^{-6} eV/atom of the SCF cycles. These convergence criteria were shown to be adequate for the geometry optimizations. For the phonon density of states, the systems were first optimized and linear response theory was used to calculate the phonon density of states. The convergence tolerance was set to 1.0×10^{-5} eV/Å². The CASTEP total energy yields the total electronic energy at 0 K. The calculated phonon spectra were used to compute free energy (F) as functions of temperature based on statistical Quasi-Harmonic Approximation (QHA), using the following equation:

$$F(T,V)=E_{static}(V)+\int_0^{\infty}d\omega g(\omega)\left(\frac{1}{2}\hbar\omega+k_BT\ln(1-e^{-\frac{\hbar\omega}{k_BT}})\right)$$

Where $F(T,V)$ is free energy, $E_{static}(V)$ is the energy at zero kelvin.

3. Results and discussion

3.1 Structures and mechanical properties

The optimized crystal structure unit cell parameters are listed in Table 1. Comparing with the experimental results show that the calculated values are larger the experiments and the c values are smaller than the experiments. The results are in agreement with the experimental results.

The calculated bulk moduli are listed in Table 2for the three apatites. The calculated errors are around 10%, which is normal in calculating mechanic properties using DFT.

The calculated elastic constants are listed in Table 3. The errors vary, which depend on the These calculated values can be used for parameterizing the interatomic potentials of the three apatite compositions.

3.2 Calculations of phonon density of states

The phonon densities of states for each of the apatites are selected shown in Figure 2 for Pb-V-I and Sr-As-I apatites. These calculations are required for the thermodynamics calculations. Small values at negative frequencies are within the numerical errors of the calculations.

The results suggest that the phonon density of states are similar for the two apatite compositions, Pb-V-I and Sr-As-I apatites, with difference only in the details.

3.3 Thermodynamics of reactions for synthesis apatites

Thermodynamics (enthalpy, free energy, heat capacity) properties for each of the apatites are then calculated based on statistical Quasi-Harmonic Approximation (QHA) as shown in Figure 3. These results will be used to calculate thermodynamics of chemical reactions to syntheses the apatites.

There are two ways to synthesis the apatite and they are represented by the following two equations:

(a) Sr-As-I apatite formation from oxides



(b) Sr-As-I apatite formation from arsenate



Using the above equations and the calculated thermodynamic properties of all the reactants and products, the free energy of the reactions can be computed. The result for this system is plotted in Figure 4.

The reaction (a) is plotted in Figure 4a and the reaction (b) is plotted in Figure 4b.

The Figure 4a shows the free energy of the iodine apatite formation from the oxides as a function of temperature. And the Figure 4b shows the free energy of the formation from the arsenate intermediate phase. This result suggests that formation of the iodine apatite from the oxides is more favorable as temperature increase, less favorable from arsenate! A similar trend has been predicted for the Pb-V-I apatite reported in the last annual report of this project. However, the

stable temperature of the Sr-As-I apatite is predicted to be lower than the Pb-V-I apatite. This result provides important clues to designing experiments for the syntheses of the iodine apatites.

4. Concluding remarks

Availability of previous unknown iodine apatite compositions would provide more opportunities for designing iodine waste forms with optimal waste loading and performance by tuning the chemical compositions. The demonstration of using DFT calculations to estimate the thermodynamics stability of an unknown crystalline phase may also shed light on designing other waste forms using similar strategies.

Acknowledgement

This research is being performed using funding received from the DOE Office of Nuclear Energy's Nuclear Energy University Programs. The computational work was supported by NERSC (DE-AC02-05CH11231) and XSEDE (TG-DMR080047N and TG-DMR100034).

References

- [1] F. Gauthier-Lafaye, P. Holliger, P.L. Blanc, Natural fission reactors in the Franceville basin, Gabon: A review of the conditions and results of a “critical event” in a geologic system, *Geochim. Cosmochim. Acta*, 60 (1996) 4831-4852.
- [2] C. Jiang, B.P. Uberuaga, K.E. Sickafus, F.M. Nortier, J.J. Kitten, N.A. Marks, C.R. Stanek, Using "radioparagenesis" to design robust nuclear waste forms, *Energy & Environmental Science*, 3 (2010) 130-135.
- [3] C. Jiang, C.R. Stanek, N.A. Marks, K.E. Sickafus, B.P. Uberuaga, Predicting from first principles the chemical evolution of crystalline compounds due to radioactive decay: The case of the transformation of CsCl to BaCl, *Phys. Rev. B*, 79 (2009) 132110.

- [4] M. Pasero, A.R. Kampf, C. Ferraris, I.V. Pekov, J. Rakovan, T.J. White, Nomenclature of the apatite supergroup minerals, *European Journal of Mineralogy*, 22 (2010) 163-179.
- [5] Y.M. Pan, M.E. Fleet, Compositions of the apatite-group minerals: Substitution mechanisms and controlling factors, in: M.J. Kohn, J. Rakovan, J.M. Hughes (Eds.) *Phosphates: Geochemical, Geobiological, and Materials Importance*, 2002, pp. 13-49.
- [6] T.J. White, D. ZhiLi, Structural derivation and crystal chemistry of apatites, *Acta Crystallographica Section B*, 59 (2003) 1-16.
- [7] J.M. Hughes, M. Cameron, K.D. Crowley, Structural variations in natural F, OH, and Cl apatites, *Am. Mineral.*, 74 (1989) 870-876.
- [8] G. Baud, J.P. Besse, G. Sueur, R. Chevalier, Structure de nouvelles apatites au rhenium contenant des anions volumineux: $Ba_{10}(ReO_5)_6X_2$ ($X = Br, I$), *Mater. Res. Bull.*, 14 (1979) 675-682.
- [9] L. Campayo, A. Grandjean, A. Coulon, R. Delorme, D. Vantelon, D. Laurencin, Incorporation of iodates into hydroxyapatites: a new approach for the confinement of radioactive iodine, *J. Mater. Chem.*, 21 (2011) 17609-17611.
- [10] B.E. Burakov, Development of Fluorapatite as a Waste Form: Final Report, in, University of Nevada, Las Vegas, 2005, pp. 1-9.
- [11] F. Audubert, J. Carpena, J.L. Lacout, F. Tetard, Elaboration of an iodine-bearing apatite Iodine diffusion into a $Pb_3(VO_4)_2$ matrix, *Solid State Ionics*, 95 (1997) 113-119.
- [12] M.C. Stennett, I.J. Pincock, N.C. Hyatt, Rapid synthesis of $Pb_5(VO_4)_3I$, for the immobilisation of iodine radioisotopes, by microwave dielectric heating, *J. Nucl. Mater.*, 414 (2011) 352-359.

- [13] F.Y. Lu, Z.L. Dong, J.M. Zhang, T. White, R.C. Ewing, J. Lian, Tailoring the radiation tolerance of vanadate-phosphate fluorapatites by chemical composition control, *Rsc Advances*, 3 (2013) 15178-15184.
- [14] S.A.T. Redfern, S.E. Smith, E.R. Maddrell, High-temperature breakdown of the synthetic iodine analogue of vanadinite, $\text{Pb-5(VO}_4\text{)(3)I}$: an apatite-related compound for iodine radioisotope immobilization?, *Mineralogical Magazine*, 76 (2012) 997-1003.
- [15] J. Carpena, B. Donazzon, E. Ceraulo, S. Prene, Composite apatitic cement as material to retain cesium and iodine, *Comptes Rendus De L Academie Des Sciences Serie Ii Fascicule C-Chimie*, 4 (2001) 301-308.
- [16] S. Le Gallet, L. Campayo, E. Courtois, S. Hoffmann, Y. Grin, F. Bernard, F. Bart, Spark plasma sintering of iodine-bearing apatite, *J. Nucl. Mater.*, 400 (2010) 251-256.
- [17] M. Zhang, E.R. Maddrell, P.K. Abraitis, E.K.H. Salje, Impact of leach on lead vanado-iodoapatite $\text{Pb-5(VO}_4\text{)(3)I}$: An infrared and Raman spectroscopic study, *Materials Science and Engineering B-Solid State Materials for Advanced Technology*, 137 (2007) 149-155.
- [18] M. Uno, M. Shinohara, K. Kurosaki, S. Yamanaka, Some properties of a lead vanado-iodoapatite $\text{Pb-10(VO}_4\text{)(6)I-2}$, *J. Nucl. Mater.*, 294 (2001) 119-122.
- [19] J. Carpena, J.L. Lacout, Calcium phosphate nuclear materials: apatitic ceramics for separated wastes, *Actualite Chimique*, (2005) 66-71.
- [20] J.Y. Kim, Z.L. Dong, T.J. White, Model apatite systems for the stabilization of toxic metals: II, cation and metalloid substitutions in chlorapatites, *J. Am. Ceram. Soc.*, 88 (2005) 1253-1260.
- [21] R.C. Ewing, The design and evaluation of nuclear-waste forms: Clues from mineralogy, *Canadian Mineralogist*, 39 (2001) 697-715.

- [22] J. Rakovan, R.J. Reeder, E.J. Elzinga, D.J. Cherniak, C.D. Tait, D.E. Morris, Structural characterization of U(VI) in apatite by X-ray absorption spectroscopy, *Environmental Science & Technology*, 36 (2002) 3114-3117.
- [23] K. Popa, T. Shvareva, L. Mazeina, E. Colineau, F. Wastin, R.J.M. Konings, A. Navrotsky, Thermodynamic properties of $\text{CaTh}(\text{PO}_4)_2$ synthetic cheralite, *Am. Mineral.*, 93 (2008) 1356-1362.
- [24] M. Uno, A. Kosuga, S. Masuo, M. Imamura, S. Yamanaka, Thermal and mechanical properties of $\text{AgPb}_9(\text{VO}_4)_6\text{I}$ and $\text{AgBa}_9(\text{VO}_4)_6\text{I}$, *J. Alloys Compd.*, 384 (2004) 300-302.
- [25] W.J. Weber, Y.W. Zhang, H.Y. Xiao, L.M. Wang, Dynamic recovery in silicate-apatite structures under irradiation and implications for long-term immobilization of actinides, *Rsc Advances*, 2 (2012) 595-604.
- [26] W.J. Weber, Y.W. Zhang, L.M. Wang, Review of dynamic recovery effects on ion irradiation damage in ionic-covalent materials, *Nuclear Instruments & Methods in Physics Research Section B-Beam Interactions with Materials and Atoms*, 277 (2012) 1-5.
- [27] W.J. Weber, R.C. Ewing, A. Meldrum, The kinetics of alpha-decay-induced amorphization in zircon and apatite containing weapons-grade plutonium or other actinides, *J. Nucl. Mater.*, 250 (1997) 147-155.
- [28] J. Wang, Incorporation of iodine into apatite-structured materials: a crystal chemistry approach using Artificial Neural Network In preparation, (2014).

Table 1

Name	a(A)	c(A)	a _{exp} (A)	c _{exp} (A)	Error (%)	
Pb ₅ (VO ₄) ₃ F	10.109	7.261	10.319 ^a	7.337 ^a (1.03%)	2.03	
Pb ₅ (VO ₄) ₃ Cl	10.420	7.287	10.331 ^b (0.86%)	7.343 ^b (0.76%)		
Pb ₅ (VO ₄) ₃ Br	10.541	7.307	-	-		
Pb ₅ (VO ₄) ₃ I	10.675	7.351	10.397 ^c (2.6%)	7.501 ^c (1.99%)		
Sr ₅ (AsO ₄) ₃ I	10.807	7.268				
Ca ₅ (VO ₄) ₃ F	10.192	6.917	9.67	7.01		

Table 2

apatite	Calculated (GPa)	Experiment (GPa)
Pb ₅ (VO ₄) ₃ I	36.31914 ± 4.566	
Ca ₅ (VO ₄) ₃ F	45.39566 ± 4.057	
Sr ₅ (AsO ₄) ₃ I	42.29975 ± 1.454	

Table 3

apatite	Calculated (GPa)				Experiment (GPa)			
	C11	C33	C12	C13	C11	C33	C12	C13
Pb ₅ (VO ₄) ₃ I	40.49925 ± 7.969	100.50595 ± 8.512	32.14510 ± 3.673	35.87812 ± 9.969				
Ca ₅ (VO ₄) ₃ F	83.48020 ± 9.416	101.15585 ± 7.720	15.23800 ± 8.323	30.52952 ± 5.022				
Sr ₅ (AsO ₄) ₃ I	58.41620 ± 2.365	112.41430 ± 3.832	27.03015 ± 2.465	36.85103 ± 0.909				

Figure 1 crystal structure of apatite

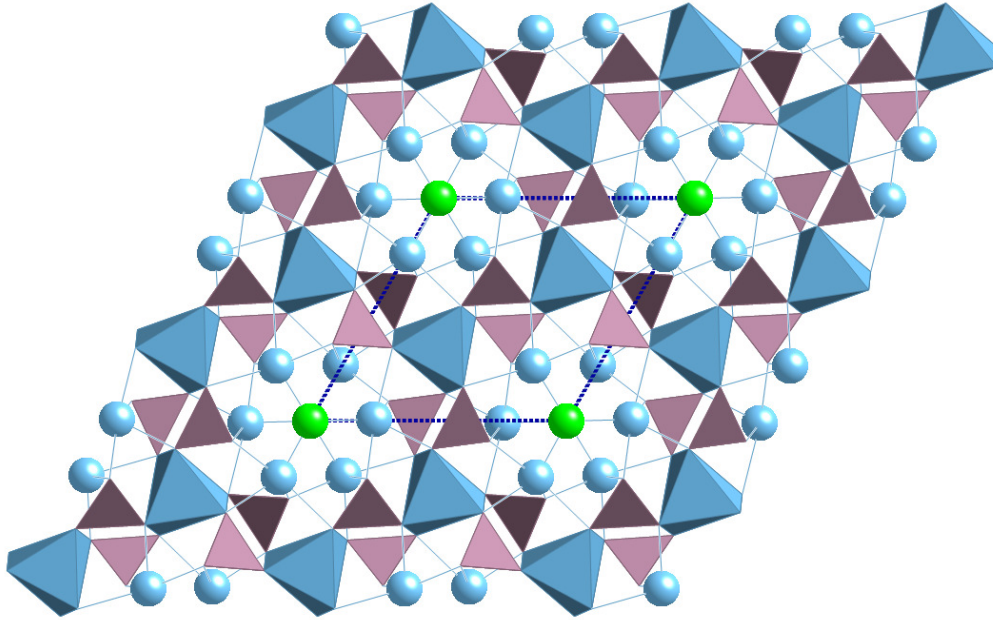


Figure 2 Phonon density of states of Pb-V-I and Sr-As-I apatites

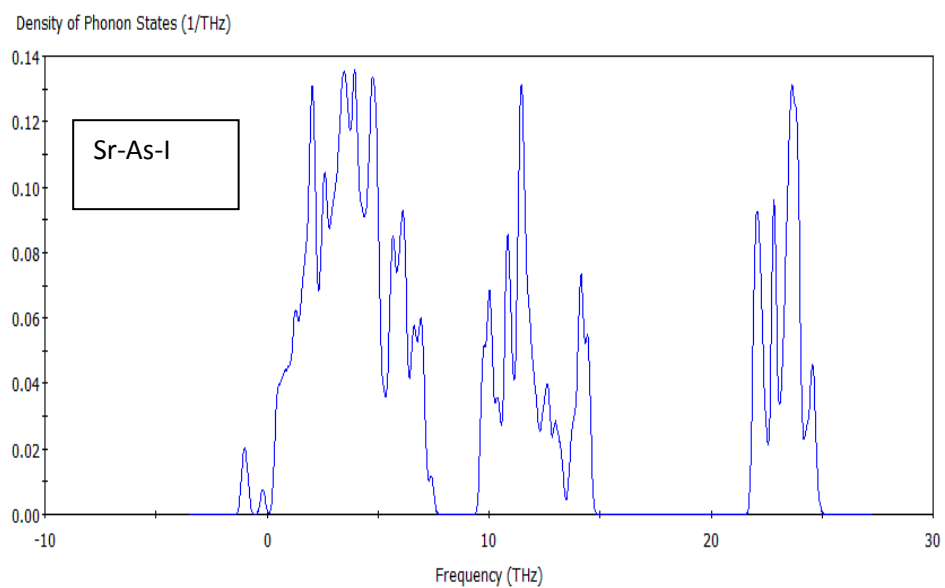
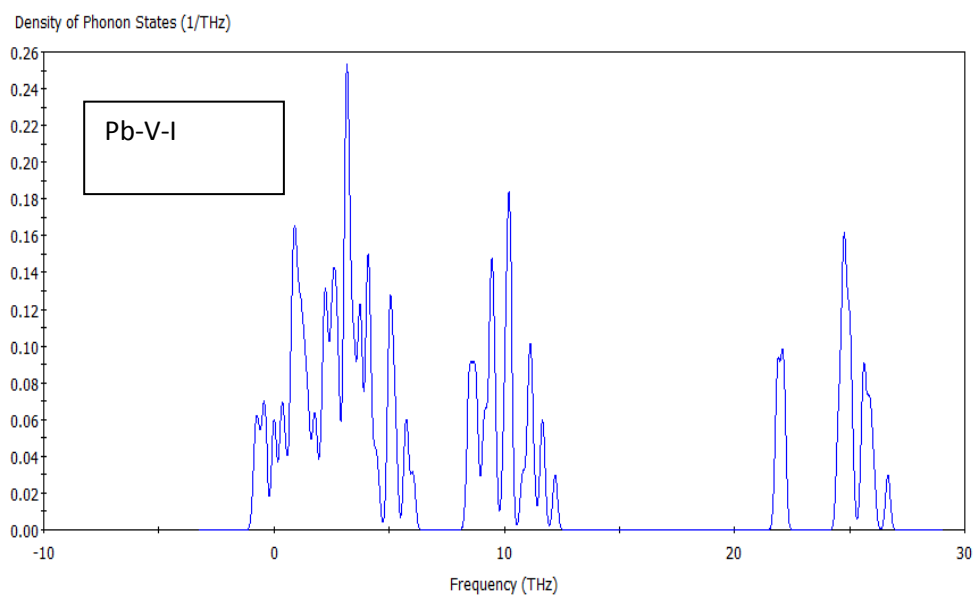


Figure 3 Enthalpy, entropy and free energy of Pb-V-I and Sr-As-I apatites

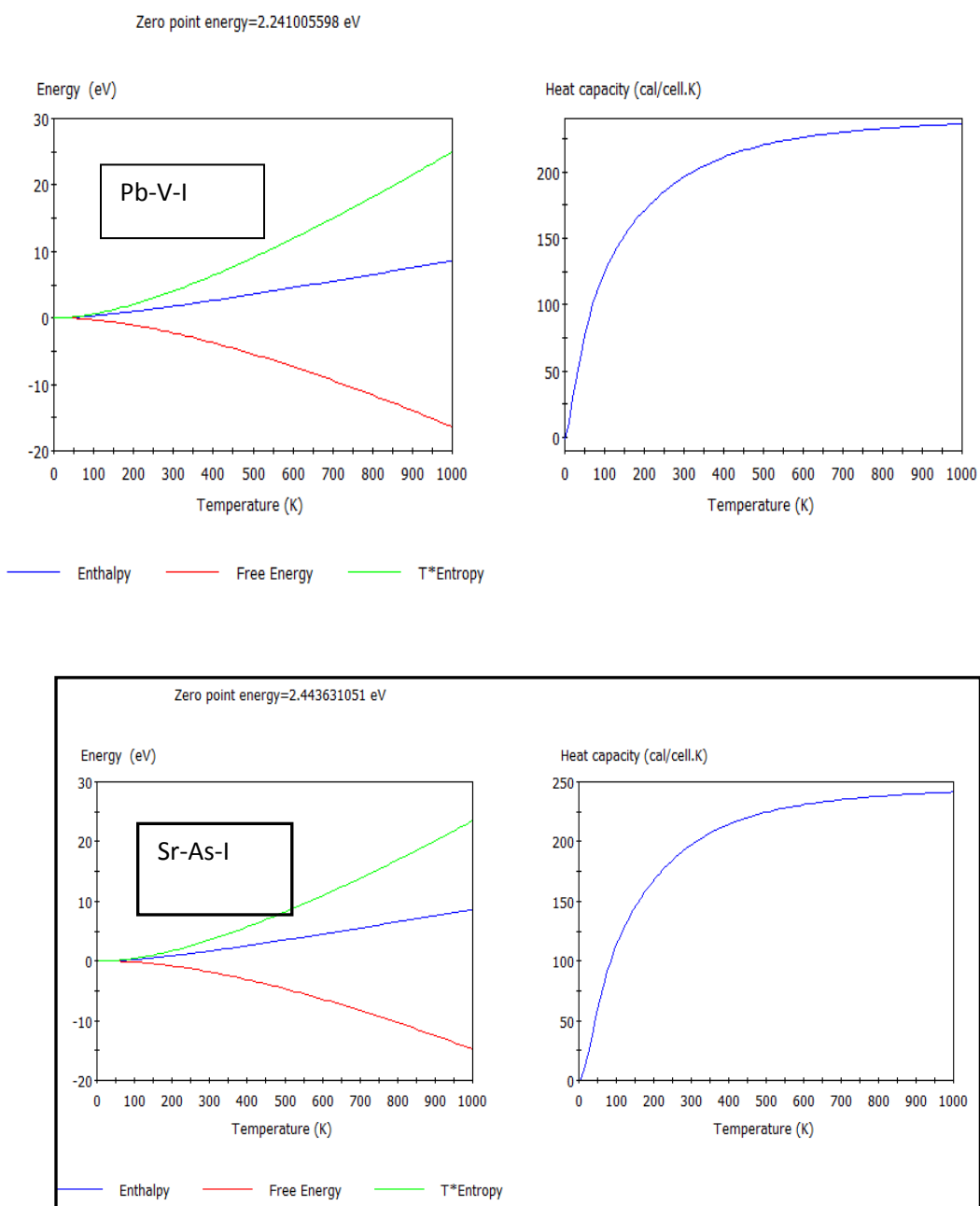


Figure 4 Free energy of reactions of Sr-As-I apatite formation

